EXPERIMENTAL INVESTIGATIONS OF FLOW BEHAVIOR INSIDE THE UPPER PLENUM OF TAMU AIR-COOLED REACTOR CAVITY COOLING SYSTEM

A Dissertation

by

SHAMSUL AMRI BIN SULAIMAN

Submitted to the Office of Graduate and Professional Studies of
Texas A&M University
in partial fulfillment of the requirements for the degree of

DOCTOR OF PHILOSOPHY

Chair of Committee,	Yassin A. Hassan
Committee Members,	Kalyan Annamalai
	Maria D. King
	William H. Marlow
Head of Department,	Yassin A. Hassan

August 2015

Major Subject: Nuclear Engineering

ABSTRACT

One of the candidates for advanced reactor designs identified for the Next Generation Nuclear Plant (NGNP) is the Very High Temperature Reactor (VHTR). The Reactor Cavity Cooling System (RCCS) is a promising passive decay heat removal system for the VHTR to ensure reliability of the transfer of the core decay heat to the environment whilst ensuring that the temperature of structures and concrete wall are under threshold limits during normal and off-normal operations, including accident conditions.

The experimental test facility reflects a ⅛ scale model of one conceptual passive decay heat removal system for advanced nuclear reactor designs. This ⅛ scale air-cooled RCCS experimental test facility was scaled, designed, constructed, and operated to study pertinent multifaceted thermal hydraulic phenomena based on the General Atomics (GA) concept for the Modular High Temperature Gas Reactor (MHTGR) during steady state and transient conditions. The experimental facility represents a portion of a full-scale air-cooled RCCS with an upper/hot plenum, four coolant risers and air as a coolant. The experimental facility is highly instrumented for measurement and analysis of highly chaotic spatial and temporal behavior of turbulent flows. The overall verification for the safe operation was achieved during the experimental facility shakedown.

Groundwork for experimental investigations focusing on the complex nature of turbulence mixing flow behavior and characteristics inside the upper/hot plenum have been carried out successfully. The steady-state condition was achieved and the experimental test facility capabilities were confirmed to permit flexibility for various

multi-parameter investigations for CFD-grade database verification. The experimental data of temperature and velocity flow fields during steady state and transient conditions showed the changes observed in the turbulent characteristics and mixing phenomena at the upper/hot plenum instigated by the parallel jets issued from the risers' outlets by means of movable thermocouple racks and 2D Particle Image Velocimetry (PIV). Several flow instabilities that have significant impacts on the cooling performance of the air-cooled RCCS were identified. Analysis of the evolution of coherent structures within the flow field for selected cases was performed using the Proper Orthogonal Decomposition (POD) technique.

DEDICATION

This dissertation is dedicated to my gracious parents, Sulaiman Amat and Saleha Adon; my lovely wife, Mehazatul-Amali Meor Hassan; and my sweetheart kids, Sofea Edrina Husna, Syaqil Affiq Haikal, Syahir Asyraff Danial, Syaqim Aariz Hakimi, Syamil Ariff Haziq and the newborn, Syabil Ariq Raif.

ACKNOWLEDGEMENTS

First and foremost, I would like to extend my deepest gratitude for the teaching, mentoring, guidance, support, and perseverance of my advisor, Professor Yassin A. Hassan. His knowledge and experience has allowed me to realize the primary objectives of this interesting project to its maximum prospective. He has served me not only as tutor in my studies and research, but most importantly as a knowledgeable personnel during my short time in graduate school, and I am very pleased to have him by my side. Not to forget to all the committee members, Professsor Kalyan Annamalai, Dr. Maria D. King and Professor William H. Marlow who have given some guidelines throughout my PhD. research.

Secondly, I would like to express my utmost love and appreciation to my wife, Mehazatul-Amali Meor Hassan for being supportive and for her perseverance during my absence from my duty as an overseas husband. Everything that I have learned is impossible without her sacrifice in ensuring well-being of the family, especially our kids. Millions thanks to my parents and parents-in-law for their infinite support of taking care of my family welfare throughout my PhD studies.

Thirdly, I would like to thank several important individuals for their continuous assistance during my research endeavors. I am very indebted to Dr. Elvis E. Dominguez-Ontiveros; my very good friend, for his technical savvy and guidance that allowed me to go further with the experiments. Without his assistance, the construction of the experimental facility and the experimental set-up would not have been possible. I am also

thankful for my wonderful project group members at TAMU who have assisted from beginning till the end; namely Tariq Alhashimi, John L. Budd, Hristo Goumnerov, Fatih S. Sarikurt, Matthew Garza, Mario Matos, and Nivyan Musavvir. Not to forget I would like to thank all my peers at Professor Hassan's laboratory for all their support and cooperation.

Finally, I am very grateful for the financial support from my sponsor, Yayasan Khazanah. The scholarship team members have stood by me since the beginning of my doctorate journey. I have become an improved individual by undergoing this graduate study and now I am more than ready to contribute for my nation-building in the immediate future.

TABLE OF CONTENTS

Page

LIST OF FIGURES

Page

LIST OF TABLES

Page

CHAPTER I

INTRODUCTION

I.1. Impetus and Rationale

Safety requirements for advanced reactor designs have been a hot topic for nuclear industries for many years. One of the leading safety concepts that has been investigated persistently is a fully passive decay heat removal system. Passive decay heat removal systems have caught special attention and have become a primary focus in the development of advanced reactor designs. Passive safety systems provide an avenue for an ultimate heat sink to remove the decay power from the system in the event of catastrophic circumstances, therefore inhibiting temperatures from extending to hazardous and unsafe levels and eventually deterring a reactor core meltdown. Natural circulation air loops have great prospects for a reliable operation and high degree of performance due to abundance of air and in-built safety features. As such, the reactor cavity cooling system (RCCS) has come forward as a chief safety system for the Next Generation Nuclear Plant (NGNP) gas-cooled thermal reactor, notably the Very High Temperature Gas-Cooled Reactor (VHTR). The VHTR concept was classified in the Generation IV technology roadmap (Generation IV International Forum, 2002 and 2005) as one of the candidates for the NGNP design. The VHTR is loosely defined as any reactor design with coolant outlet temperature of 1000 $^{\circ}$C or above (Chapin, Kiffer, and Nestell, 2004).

Passive decay heat removal systems furnish the prospect of a more reliable system to remove decay heat from a reactor pressure vessel (RPV) to an ultimate heat sink without the need of human (i.e. operator) intervention or external electrical power supply (i.e. off-site AC or on-site DC power). As such, passive heat removal systems present departure from the traditional overall safety concept of the nuclear industry of using active cooling via pumps driven by off-site AC or on-site DC power source (Figure 1). The Reactor Cavity Cooling System (RCCS) for the VHTR provides simplicity in design, maintenance and operation to guarantee the integrity of the RPV, the nuclear fuel, and other pertinent structures, preventing structural damage through overheating that could also lead to radioactive release. The RCCS provides an avenue to remove decay heat from the reactor core via reactor pressure vessel during accident events, which limits the reactor core and nuclear fuel temperatures from attaining unsafe levels and eventually prevents a core meltdown (Corradini, Feltus, and Wei, 2012). Nonetheless, maximum understanding of the RCCS necessitates thorough and full-fledged studies and investigations to comprehend its complex thermal hydraulic behavior, particularly flow instabilities (water-cooled) and turbulence mixing (air-cooled). Therefore, to shed some light on successful implementation of the RCCS to a full-scaled nuclear reactor design, the complications mentioned earlier must be fully comprehended. Since the focus of this dissertation is the air-cooled RCCS, the primary scope of work is knowledge of air flow thermal hydraulic characteristics, behavior and magnitude over a wide range of circumstances with greater emphasis on complex turbulence flow mixing inside the hot/upper plenum, with an eventual target from ambiguity to certainty. The new experimental data utilizing cutting

edge experimental set-up will furnish a CFD-grade database for the validation and promote advancement of CFD models.

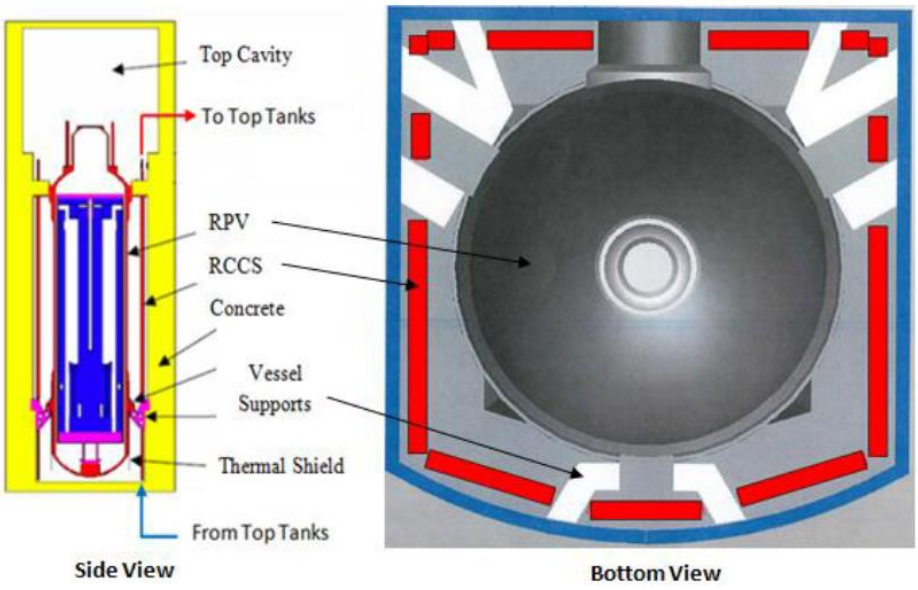

Figure 1. Typical RCCS Configuration

I.2. Existing and Previous Gas-Cooled Reactors Employing Passive Decay Heat Removal Systems

Historically, as early in 1950s, many high temperature gas reactors (HTGR) have incorporated passive decay heat removal systems in their designs. Both water-cooled and air-cooled designs have been considered for the RCCS (Table 1). The air-cooled RCCS is

designed to be totally passive in all operating situations and has no active components (e.g. blowers) to power the airflow through the heat exchangers (ducts or standpipes) (Frisani, Hassan, and Ugaz, 2010; Frisani, 2010). During normal operation, the RCCS is functioning to cool-off safety related cavity components such as the reactor pressure vessel (RPV), the vessel mechanical support structure and the surrounding concrete structure (IAEA Safety Series Report No. 54, 2008). Neither active component nor operator actions are needed to switch the RCCS from normal to accident, at least for very long periods of time (i.e. days) (IAEA Safety Series Report No. 54, 2008). However, the over-design of the RCCS system would be unacceptable since during normal operation, and in some cases for normal shutdowns, excessive parasitic heat losses would be undesirable (Oh, Park, and Davis, 2009). Significant variation of heat load distribution during accident conditions, which depend on the accident characteristics, also contribute to the difficulty in designing the RCCS.

The Japanese's first HTGR, the high temperature engineering test reactor (HTTR), is a 30 MWt test reactor operated by Japan Atomic Energy Research Institute (JAERI) (Figure 2). The HTTR achieved its first criticality in 1998 and full operation in 2001 (Fujimoto, Nojiri, Tachibana, and Mizushima, 2009). Its core is prismatic block type with coated fuel particles (TRISO), graphite moderated, helium gas cooled, 4 MPa pressure with maximum outlet temperature of 950 ^{o}C at the reactor outlet. Water-forced convection is employed for its RCCS via a set of water stand pipes and radiant fins (Corradini et al., 2012). After a reactor scram, auxiliary cooling system (ACS), which is on standby during normal operation, will be in operation. In the event the ACS is unable to cool the reactor

core in an efficient manner, the vessel cooling system (VCS), which is used to cool the biological shield during normal operation, will kick in to cool the reactor core under a no forced-cooling condition such as a primary pipe rupture accident (not a strictly passive design) (JAERI, 1994).

Table 1. Type and characteristics of RCCS in the HTGRs (Park, Cho, and Cho, 2006; Corradini et al., 2012).

Country	**Reactor**	**Power (MWt)**	**RCCS Coolant /Type**	**Secondary Coolant / Type**
Japan	HTTR	30	Water Forced Convection	Water Forced Convection
China	HTR-10	10	Water Natural Convection	Air Natural Convection
South Africa	PBMR	400	Water Natural Convection	Air Natural Convection
Russia	GT-MHR	600	Air Natural Convection	No Secondary Cooling
USA	MHTGR	450	Air Natural Convection	No Secondary Cooling

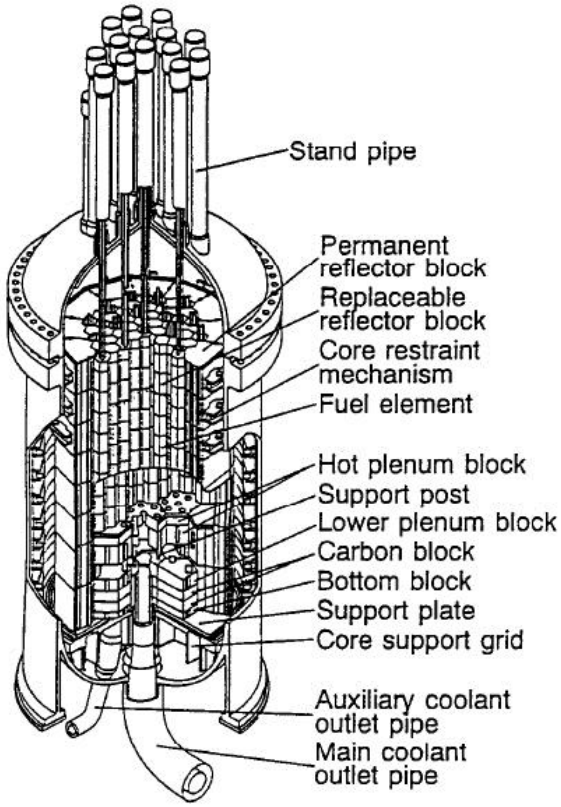

Figure 2. Reactor vessel and core schematic for HTTR (JAERI, 1994).

As part of a major project in the energy sector of the Chinese National High Technology Programme, Institute of Nuclear and New Energy Technology (INET) has been entrusted to design, license application, construct and operate the Chinese High Temperature Reactor (HTR-10) (Figure 3). The HTR-10, a 10 MWt module pebble bed HTGR reached its first criticality in 2000, full operation in 2003 with a core outlet temperature reaching 700 ^{o}C and the plant connected to the electrical grid (International Atomic Energy Agency, 2001 and 2013). The HTR-10 is adopting spherical fuel elements

with ceramic coated fuel particles, with a reactor core surrounded by graphite reflectors, helium coolant and 3 MPa primary helium pressure. The HTR-10 decay heat removal is a totally passive system. In the event of loss of pressure accident (no core cooling is anticipated), dissipation of the decay power is via the reactor core structures by means of heat radiation and conduction to the outside of the RPV (International Atomic Energy Agency, 2001). The decay heat will be dissipated into a surface cooling system positioned on the wall of concrete housing. This system operates using water natural circulation and releases the decay heat through air coolers to the atmosphere (International Atomic Energy Agency, 2001).

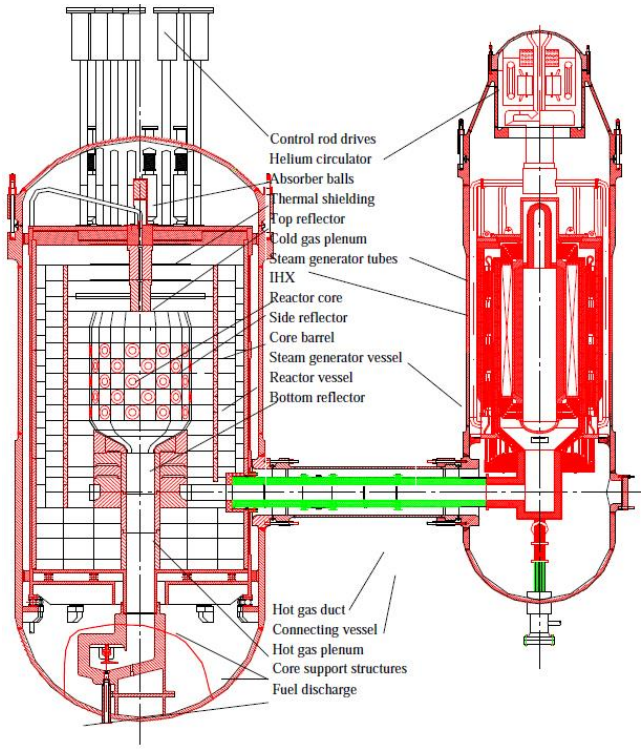

Figure 3. Primary system schematic of HTR-10 (International Atomic Energy Agency, 2013).

The pebble bed modular reactor (PBMR), a 400 MWt reactor from South Africa, utilizes TRISO ceramic fuel coated ^{235}U in graphite spheres (Figure 4). The PMBR is graphite moderated reactor having helium gas as a primary coolant operated at 9 MPa with the core outlet temperature of 900°C (International Atomic Energy Agency, 2013). Its RCCS is designed to dissipate the heat from the reactor cavity during normal operation, including shutdown. The PBMR RCCS encompasses 3 x 100% independent systems consisting of a low pressure, closed loop, natural-convection driven, self-acting water-based cooling system and an external water to an air heat exchanger (International Atomic Energy Agency, 2001). The RCCS also offers a heat sink for uninterrupted removal of decay heat transferred from the RPV during normal operation and during a postulated loss of forced cooling (LOFC) circumstance (International Atomic Energy Agency, 2013).

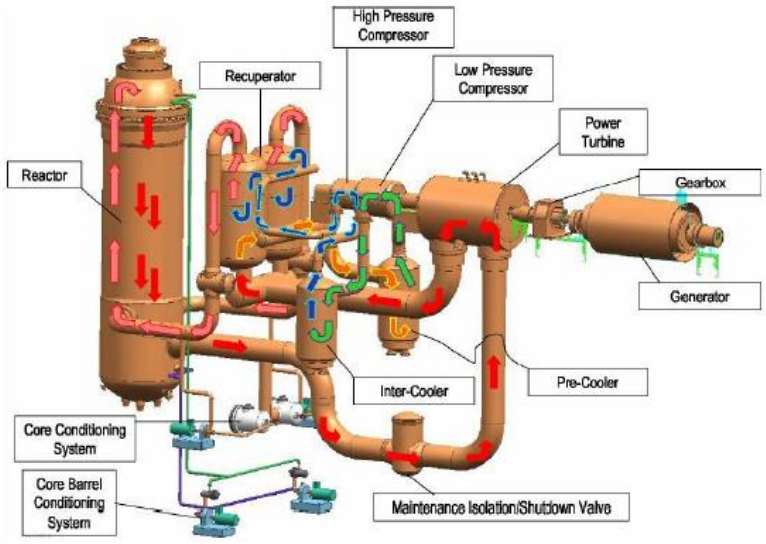

Figure 4. Primary system schematic of PBMR (International Atomic Energy Agency, 2013).

The gas turbine modular helium reactor (GT-MHR), a 600 MWt reactor, is amongst the most significant HTGR gas turbine plant designs currently under study in the world (Figure 5). The GT-MHR is an international effort which is led by Agency of Atomic Energy of Russia and other organizations such as US Department of Energy (DOE), GA and ORNL from the United States of America, Framatome of France and Fuji Electric of Japan (International Atomic Energy Agency, 2013). The GT-MHR employs hexahedral prismatic fuel assemblies, graphite moderated, and helium coolant with the core average outlet temperature of 850 ^{o}C.). Idaho National Laboratory (INL) in its report INEEL/EXT-03-00141 (Baccaglini, Ball, and Shaber, 2003) provided a very valuable graphic on the reactor building arrangement (Figure 6). The arrangement and placement of the RCCS inside the reactor building was incorporated in Figure 6. The GT-MHR RCCS has two functions: (1) a passive means of transporting core residual heat from the reactor cavity when neither the Power Conversion System (PCS) nor the Shutdown Cooling System (SCS) is available – thus avoiding the reactor vessel from surpassing design temperature thresholds, and (2) shields the concrete walls of the reactor cavity from surpassing design temperature thresholds for all types of operation (Blandford, Moheet, Seifried, and Thomas, 2007). The RCCS dissipates heat by radiation and natural convection from the uninsulated vessel and by conduction via through the graphite reflector. Heat is removed from the reactor cavity by natural circulation of outside air through the cooling panel placed around the reactor vessel. The RCCS system has multiple inlet/outlet ports and interconnected parallel flow paths to confirm continuous cooling in the case of blockage of any single duct or opening. The GT-MHR will be the first for a

full scale air-cooled RCCS design performance test (International Atomic Energy Agency, 2001).

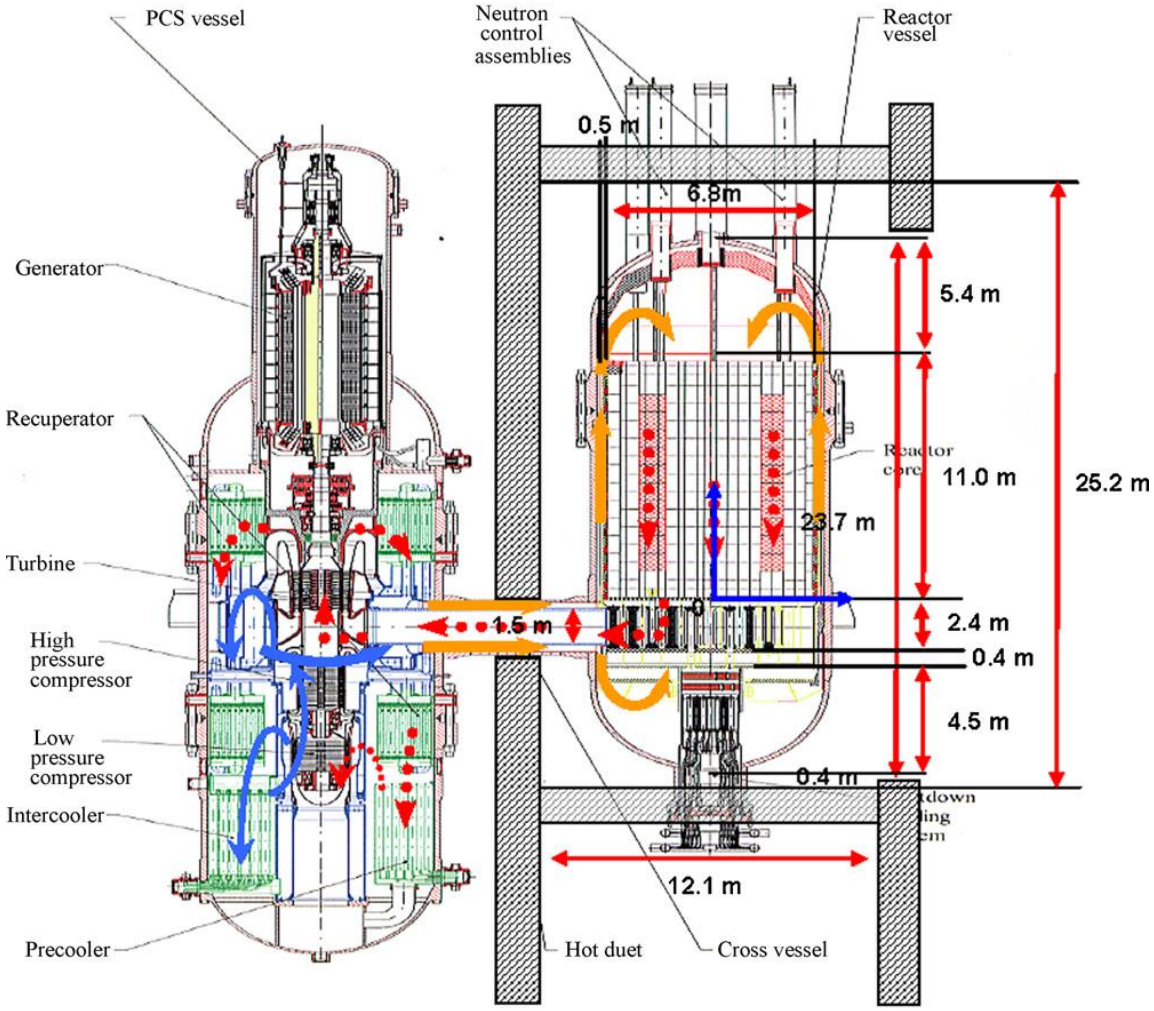

Figure 5. Primary system schematic of GT-MHR (International Atomic Energy Agency, 2013; Oh et al., 2010).

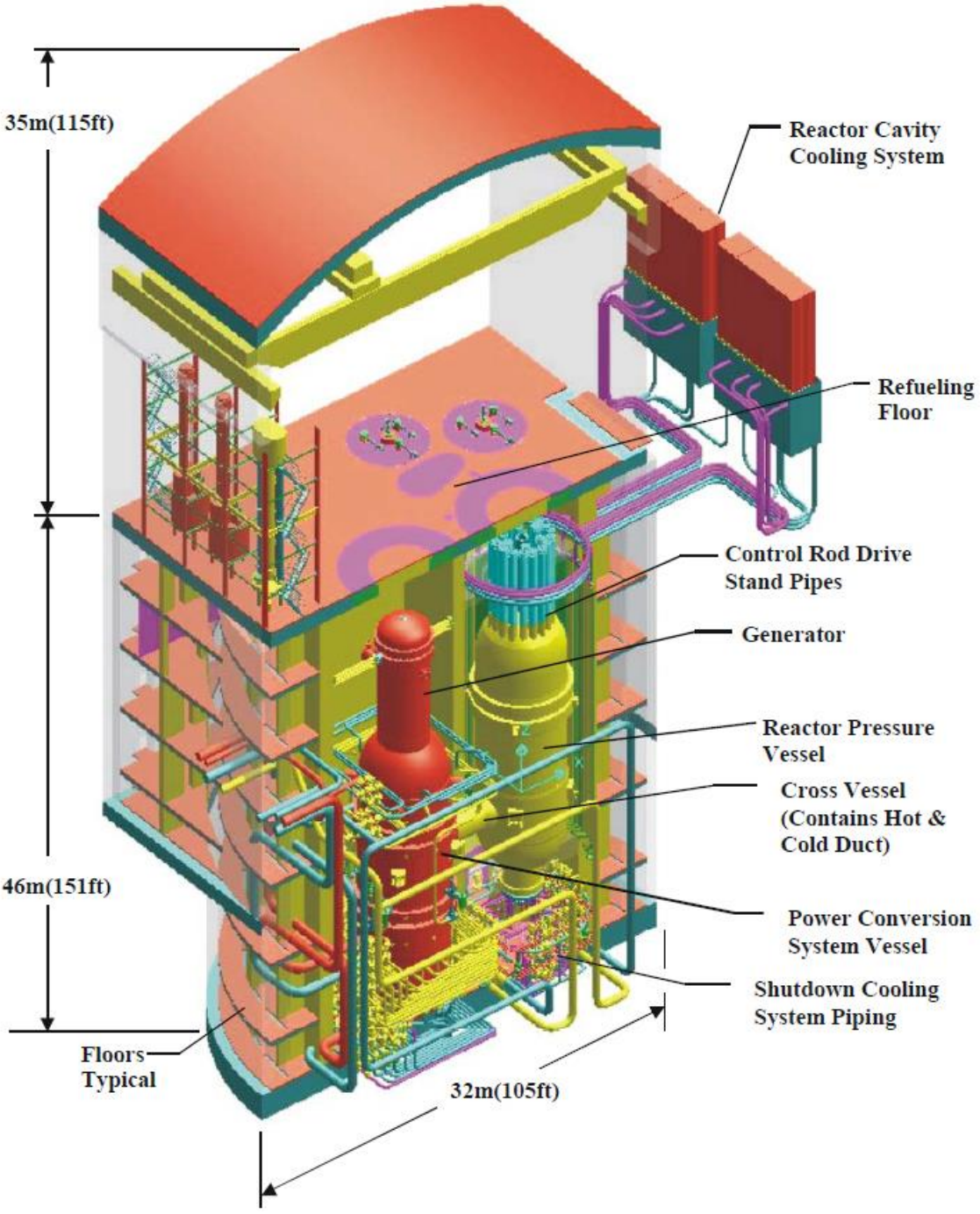

Figure 6. The reactor building cutaway of the GT-MHR (General Atomics, 1996; Baccaglini et al., 2003).

The General Atomics modular high temperature gas reactor (GA-MHTGR) is a 450 MWt HTGR reactor developed in the United States (Figure 7). The GA-MHTGR is a graphite moderated reactor having helium as a primary coolant operated at 7.07 MPa with the core outlet temperature of 850°C (Williams et al, 1994). As per other reactor design, the decay heat is approximately 6% of reactor power prior to shutdown, about 1% after an hour and approximately 0.002% after more than 100 hours. The GA-MHTGR RCCS removes heat from the reactor cavity in a passive manner by the outside air natural convection via the cavity cooling panel which is located next to and follows the interior contour of the reactor cavity wall. The cooling panel and ducting are responsible to accumulate the heat transferred from the RPV by radiative and natural convective heat transfer and carry the heated air to the ultimate heat sink, the environment. During normal operation, the cooling panel and ducting are functioning to guard the cavity walls from overheating. During accident and emergency condition (e.g. loss of force cooling systems such as the Heat Transport System (HTS) and the Shutdown Cooling System (SCS)), the cooling panel and ducting will offer an alternate means of decay heat removal.

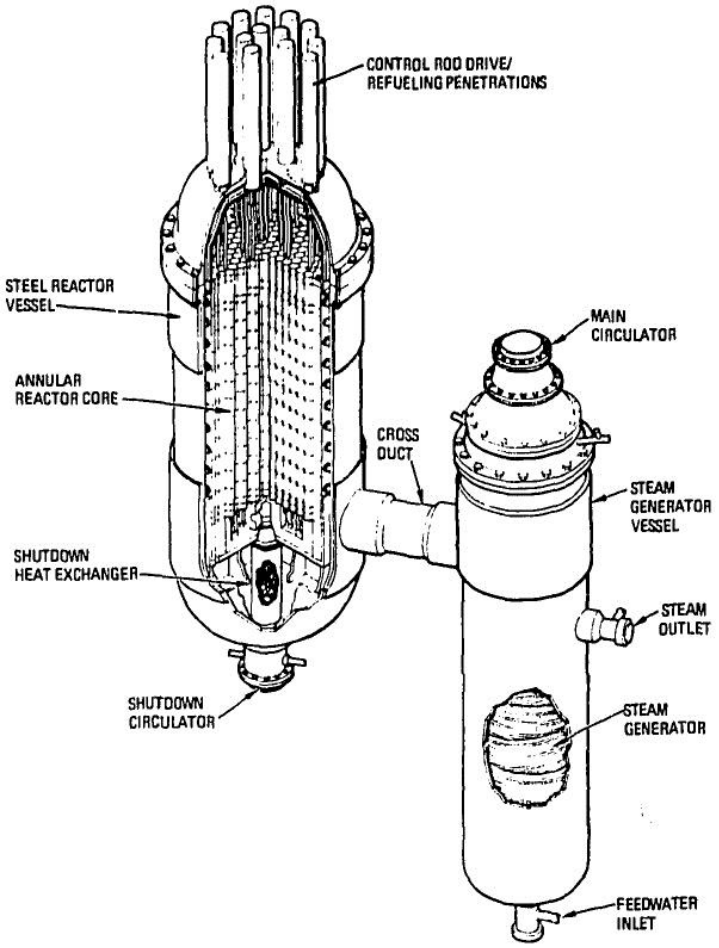

Figure 7. Primary system schematic of GA-MHTGR (Bechtel National, Inc., 1992).

I.3. The GA-MHTGR RCCS

For the GA-MHTGR design, the primary means of nuclear heat removal is Heat Transport System (HTS). HTS is also the principal method of removing decay heat during a normal shutdown. In the event of unavailability of the HTS, most probably due to maintenance needs or even due to its system failure, the RCCS would be available for the

heat removal. The RCCS will require several days for cooling and this will be detrimental to the plant availability. As such, the MHTGR is equipped with a Shutdown Cooling System (SCS), the second means to remove decay and residual heat and also limit the risk of investment loss. The SCS will circulate helium only in the reactor pressure vessel and transfer the heat via a closed water loop. Air blast heat exchanger is used to reject the heat to the atmosphere (Figure 8).

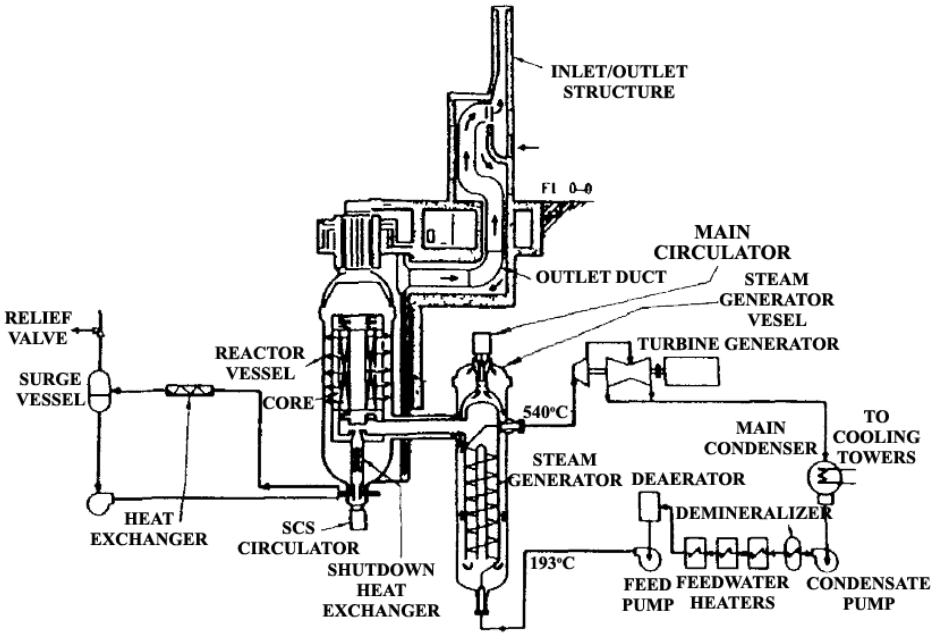

Figure 8. The GA-MHTGR heat removal systems (Dilling, Ghose, and Berkoe, 1992a and 1992b).

The Heat Transport System (HTS) is the primary means of removing nuclear heat from the core. It is also the primary means of removing decay heat during a normal

shutdown. If the HTS is unavailable because of its maintenance needs or because it has failed, the plant can be cooled down using the RCCS. However, this requires several days and subjects the vessel to a temperature excursion. To obtain the desired plant availability and to limit the risk of investment loss, the MHTGR is equipped with a Shutdown Cooling System (SCS). The heat exchanger and the circulator of the SCS are located at the bottom of the reactor vessel. The SCS circulates helium only within the reactor vessel. It rejects heat to a closed water loop which in turn rejects heat to the atmosphere via an air-blast heat exchanger. Normally, the SCS will be the second means of rejecting nuclear decay and residual heat. Both the HTS and SCS are active systems.

For the GA-MHTGR, one of the worst accident scenarios is Conduction Cooldown event. Conduction Cooldown is a scram-initiated event involving the failure of both main cooling systems, i.e. HTS and standby SCS core cooling systems. The GA-MHTGR reactor core heats up very slowly, owing to its huge thermal capacity following the scram event. As a result, the heat is conducted primarily in the radial direction via the outer graphite reflector. Thermal radiation and natural convection are the primary means of the heat transfer from the outside of the core barrel to the vessel wall, i.e. across the core annulus. Inside the reactor cavity, thermal radiation (~ 90%) and natural convection (~ 10%) (Bechtel National, Inc., 1992) are also responsible for the heat transfer from the reactor pressure vessel to the cooling panels that line up the reactor cavity wall (Figure 9).

The proposed GA-MHTGR power plant design is shown in Figure 10 (Hecht, 1989). The envisaged power plant comprises four MHTGR modules, each at 135 MWe, for a total power output of about 540 MWe, utilizing prismatic fuel elements within

hexagonal core, and utilizing helium as the coolant. The reactor module (nuclear island) is housed in a below-ground concrete silo, separated from the power generating unit. Every nuclear island is a stand-alone confinement structure, with its own exhaust system (Hecht, 1989).

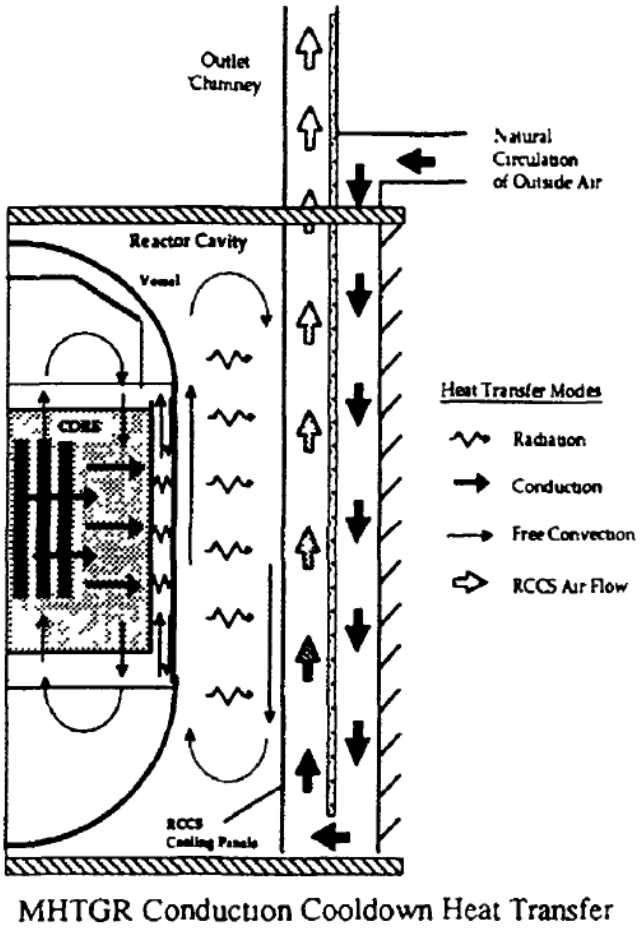

Figure 9. Schematic of heat transfer process during the Conduction Cooldown event (Dilling et al., 1992a and 1992b).

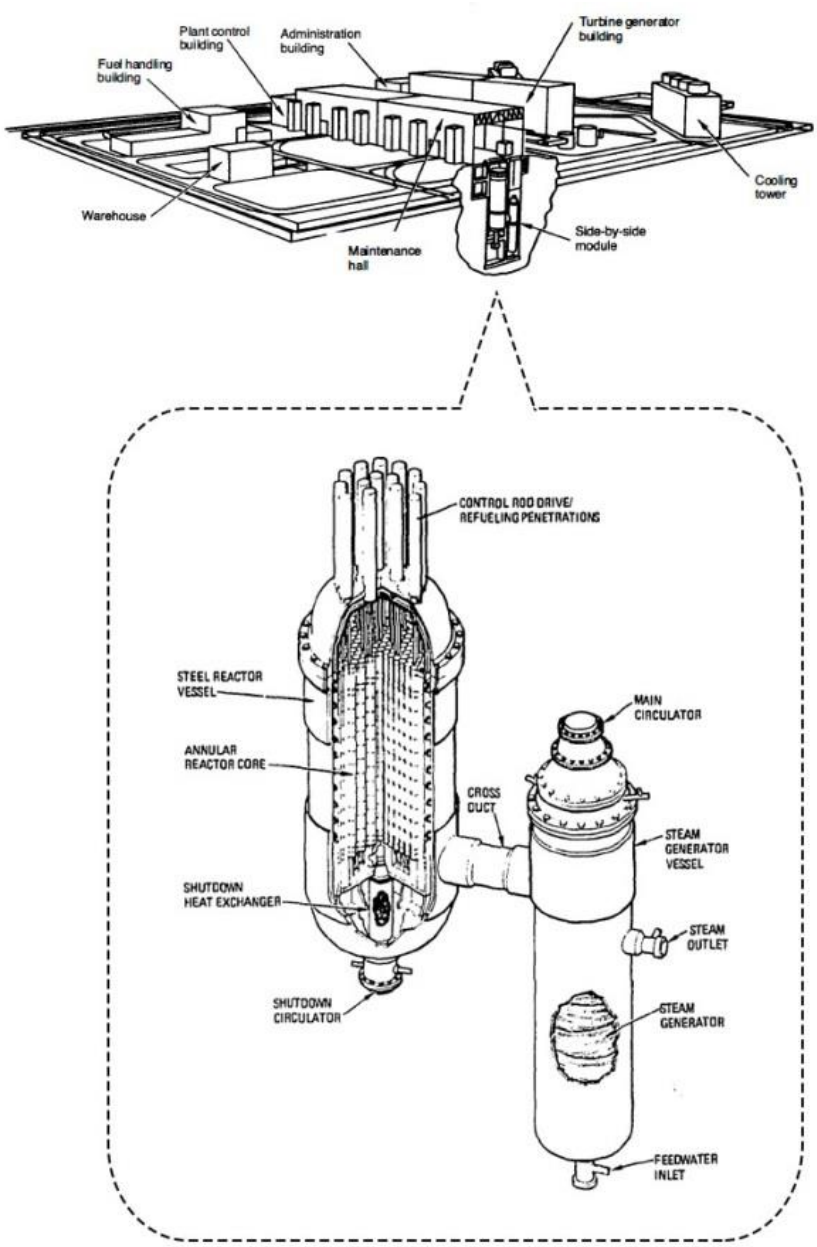

Figure 10. The proposed power plant for the GA-MHTGR (Bechtel National, Inc., 1992; Hecht, 1989).

However, a particular design that has comprehensive write-up is a 28.9 m tall, prismatic core, helium-cooled, 450 MWt reactor (Bechtel National, Inc., 1992). A series

of air ducts that follows the interior outline of the reactor cavity walls, 227 units in total, each having a rectangular cross sectional area of 5 cm x 25 cm (2" x 10") with a total length of 19.2 m in two redundant circuit, form the integral part of air-cooled RCCS system (Bechtel National, Inc., 1992). The planned total elevation right from the chimney inlet to the bottom of the air duct is over 55m. The incoming air of the inlet plenum is assumed to be 43 °C (110 °F). The air will travel in downward direction through a series of downcomers and then it changes to upward direction via a set of risers and finally it will be discharged to the atmosphere by the chimney (Corradini et al, 2012). An ANL study of air-cooled RCCS (ANL-GenIV-179) is a good source of information pertaining to the isometric view of the GT-MHR RCCS (Figure 11 to Figure 13).

Figure 14 and Figure 17 portray an illustration of the link between the RCCS and the RPV. The RPV transfers heat by two ways: first by radiation and/or convection to outside air via air cooling panels that line up the reactor cavity walls, and second by conduction to the earth surrounding the reactor building (Chapin et al., 2004). The cooling panels and relevant ducting accumulate the heat transferred from the RPV by radiation and natural convection and transport the hot air to the atmosphere external to the reactor building. During normal operation, the RCCS functions to shield the concrete cavity walls from overheating. In an emergency situation where forced cooling systems are lost and no electrical power connection, the RCCS is capable of removing the decay heat as a result of the stoppage of the reactor, since no active components associated with the RCCS design could inhibit the reactor cooling objectives.

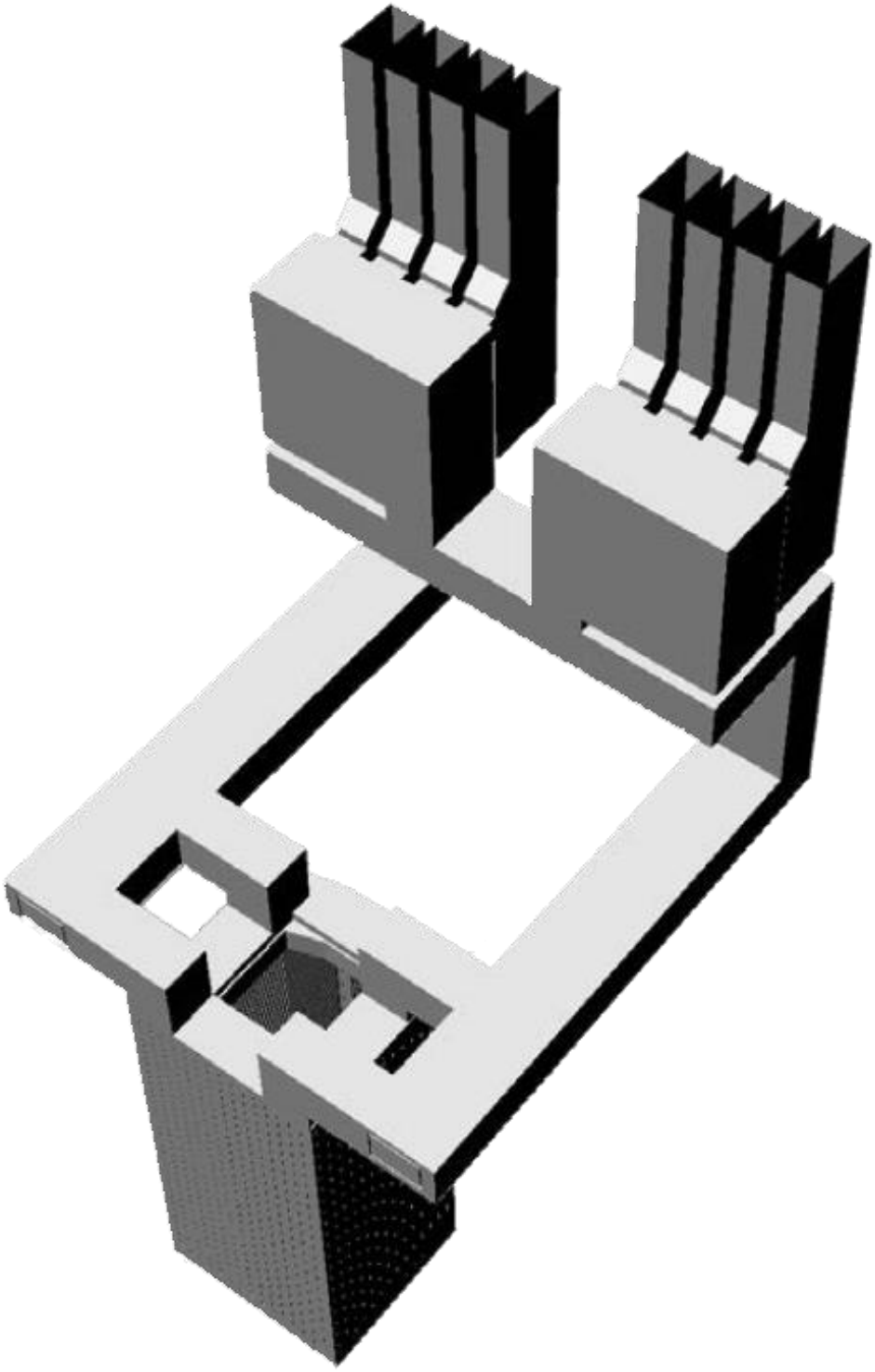

Figure 11. Isometric view of the full scale GA-MHTGR (ANL-GenIV-179).

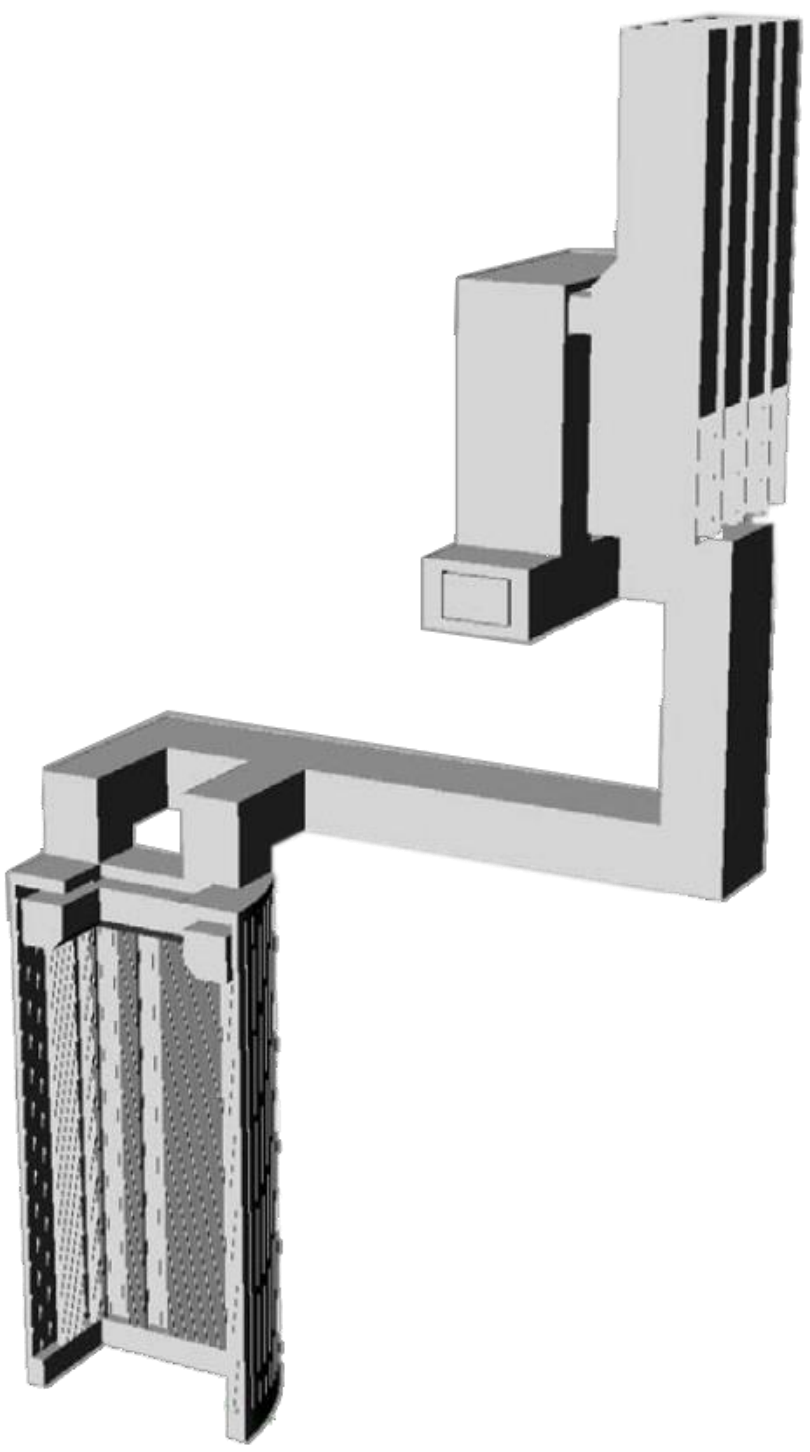

Figure 12. Full scale GT-MHTGR side cutaway view (ANL-GenIV-179).

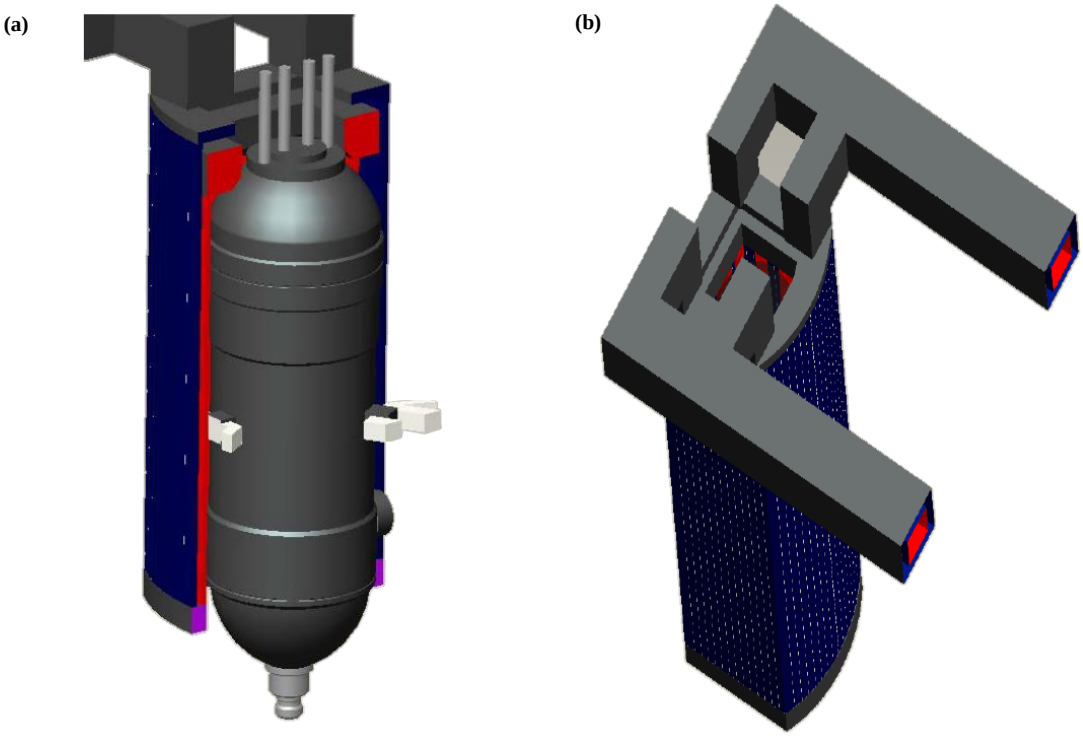

Figure 13. (a) Reactor cavity isometric view, (b) Ex-cavity RCCS outer cold duct/inner hot duct run (ANL-GenIV-179).

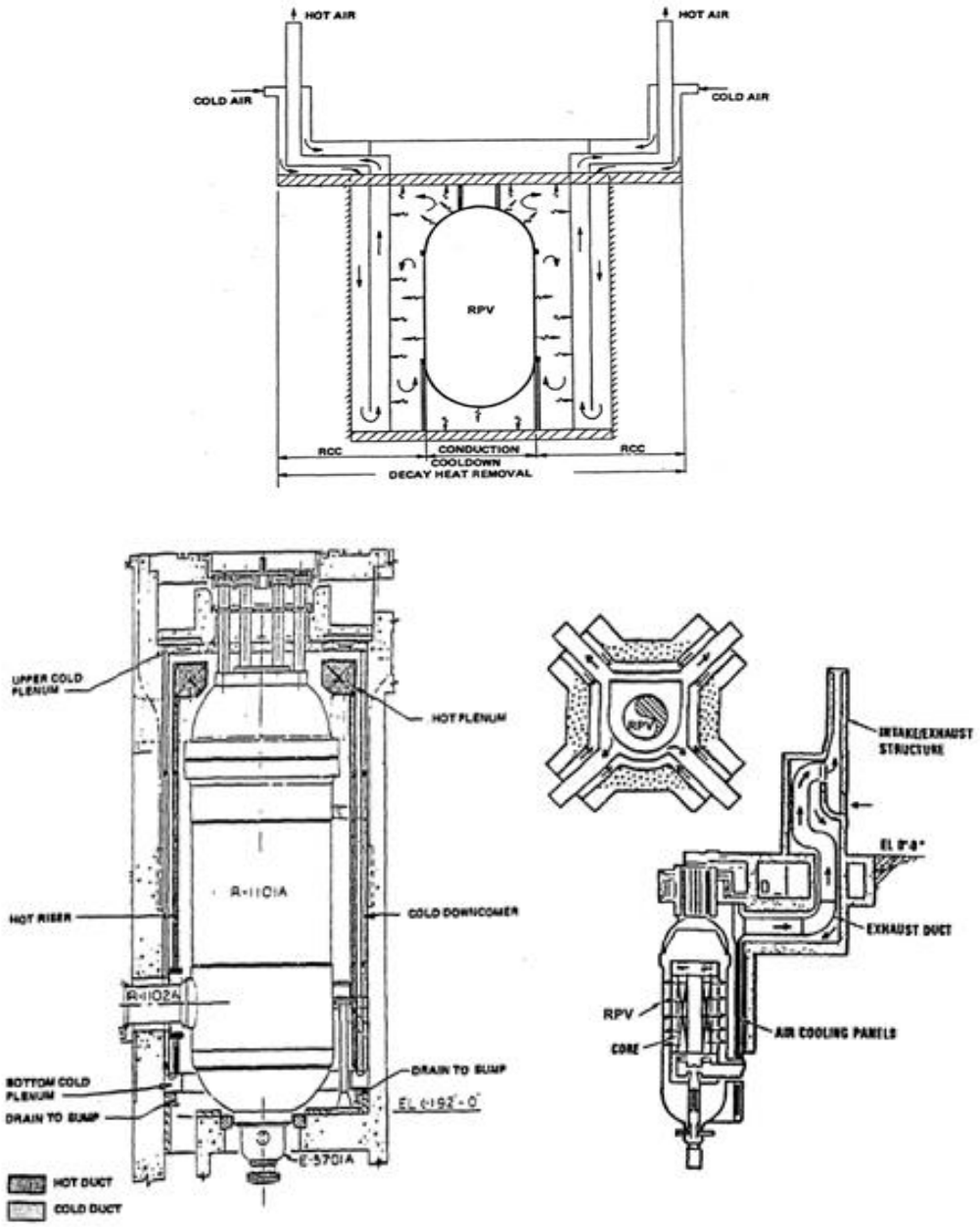

Figure 14. The passive air-cooled concept (side view) (IAEA-TECDOC-757; Bechtel National, Inc., 1992).

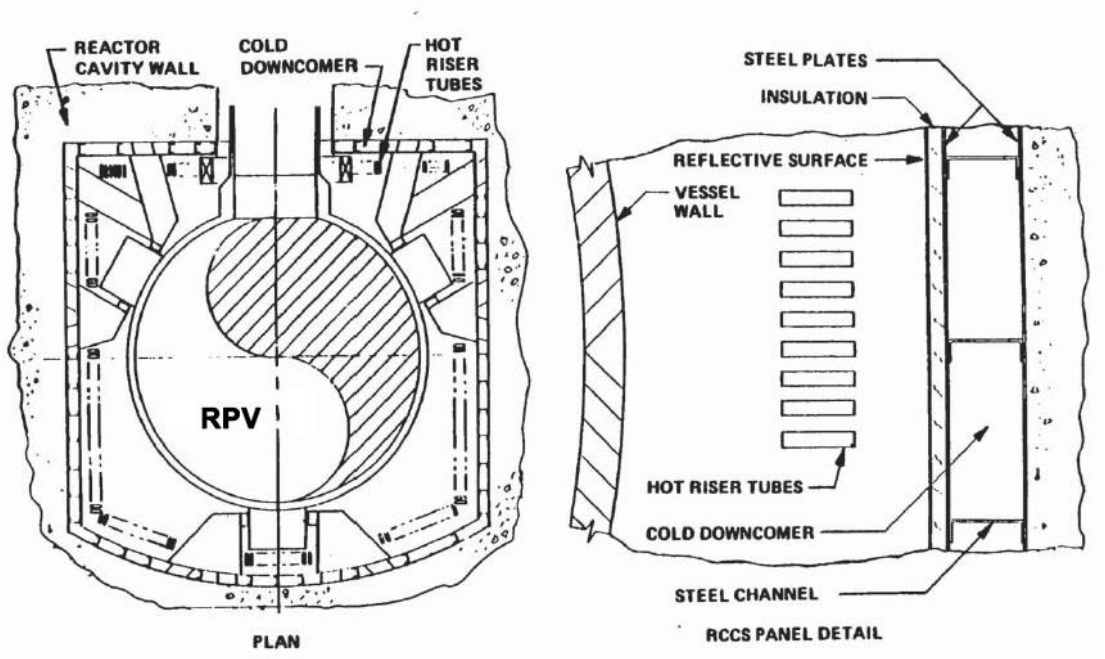

Figure 15. The GA-MHTGR RCCS cooling panel (plan view) (Bechtel National, Inc., 1992).

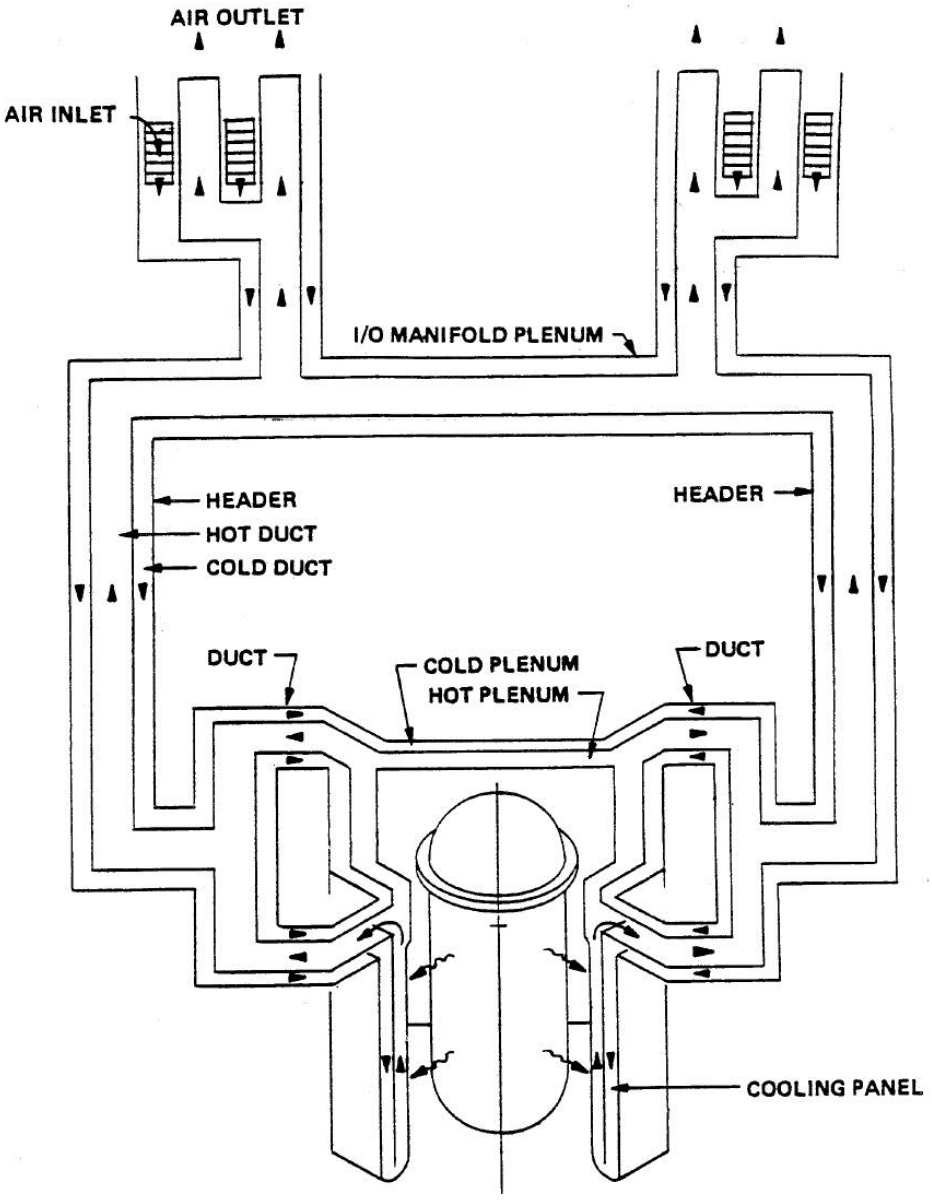

Figure 16. The GA-MHTGR RCCS overall pipings (Konefal et al., 2009).

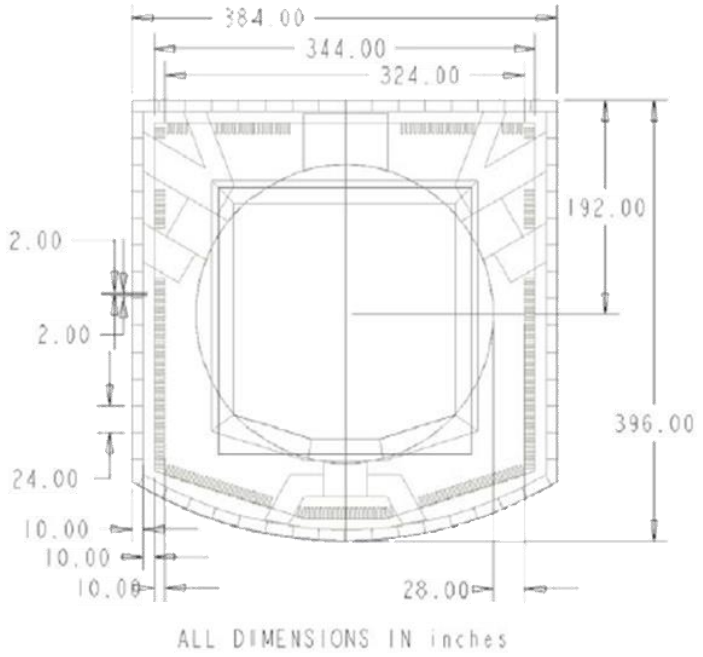

Figure 17. The GA-MHTGR RCCS top view with dimensions (Bechtel National, Inc., 1992).

During normal operation of the GA-MHTGR, it is anticipated that it can manage a heat loss rate of 0.7 MWt from the RPV at steady state. More importantly, the GA-MHTGR is expected to handle 1.5 MWt maximum decay heat during accident transient condition (with the absence of forced cooling system) (Bechtel National, Inc., 1992; Lisowski, 2013; Lisowski, Moses, Andersen, and Corradini, 2013).

CHAPTER II

RESEARCH PURPOSE

II.1. Research Purpose, Objectives, and Scope

The scope of this research, and the emphasis of the work presented in this dissertation, consists of the methodology used to design, construct, and evaluate an experimental RCCS facility at Texas A&M University. The virtue of the work may be defined not only by completion, but profundity in understanding, of four key objectives:

1. Construct a set of scaling laws based on previous available efforts to preserve wide parameters and key thermal hydraulic phenomena between a full scale concept and a reduced scale model;
2. Design and construct a scaled model experiment to accurately match the prototype design and permit flexibility for various multi-parameter investigations;
3. Characterize the experimental facility, verify repeatability, and evaluate the scaled model system performance during steady state and transient operations;
4. Investigate and characterize the behavior of turbulence flow at multiple conditions inside the hot/upper plenum, with a focus on identifying the patterns, character and magnitudes of flow in light of furnishing novel experimental data of CFD-grade database for the validation and promote advancement of CFD models utilizing cutting edge experimental set-up.

CHAPTER III

RESEARCH APPROACH

III.1. Experimental Research Activities

The plan experimental activities are as follows:

1. Development of computational fluid dynamics (CFD) model for the experimental facility design and instrumentations;
2. Measurement of boundary conditions' profiles for the upper plenum;
3. Measurement of temperature inside the upper plenum using custom-made vertical and horizontal thermocouple racks;
4. Measurement of velocity inside the upper plenum using Particle Image Velocimetry (PIV)
5. Proper Orthogonal Decomposition (POD) analysis at selected planes of interest based on the PIV data.

III.2. Overall Plan

In order to ensure smooth implementation, the entire research project was divided into several stages as the following:

- Stage 1: Data Collection and Literature Review;
- Stage 2: Experimental Test Facility Design and Material Selection;
- Stage 3: Vendor Selection and Experimental Test Facility Fabrication, Transportation and Construction;
- Stage 4: Instrument Selection, Procurement, Calibration and Installation;
- Stage 5: Experimental Test Facility Shakedown and Characterization;
- Stage 6: Development of Test Matrix and Experimental Research Activities;
- Stage 7: Experimental Data Analysis and Discussions.

A simplified Gantt chart that illustrates the overall project schedule was developed (Figure 18). The Gantt chart shows the start and finish dates of each stage. The stages will be described in details in the following chapters.

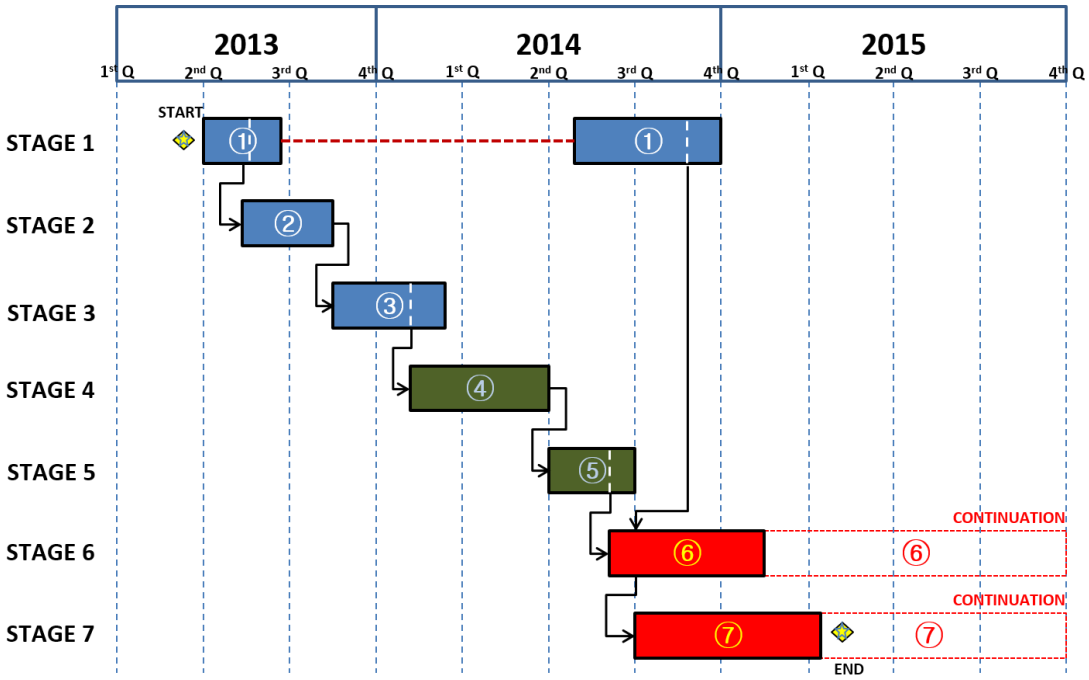

Figure 18. The simplified Gantt chart showing the overall research timeline.

CHAPTER IV

STAGE 1: DATA COLLECTION AND LITERATURE REVIEW

IV.1. Introduction

In order to understand the air flow behavior inside the hot/upper plenum of the air-cooled RCCS, an extensive literature review was carried out. Parallel turbulent jets for a single jet, dual jets, and multiple jets were presented. Review on pertinent measurement techniques for velocity was also carried out, namely particle image velocimetry, particle tracking velocimetry, and Laser Doppler velocimetry. Basic overview of POD method was studied including its brief mathematical formulation.

IV.2. Parallel Jets

For many years, parallel turbulent jets behaviors have been investigated by many researchers due to the fact that turbulent mixing of jets is applicable to wide variety of fields and numerous practical industrial applications. In multiple jets investigations, the reciprocal influence of the neighboring jets on each other and requirements of an optimum nozzles' spacing to achieve desirable condition necessitate comprehensive understanding. "Parallel jets" term is referring to jet issued from "parallel" nozzles (Nasr and Lai, 2010).

IV.2.1. Single Jet

Previous experimental, theoretical and numerical studies of vertical buoyant jets can be used as a preliminary tool and guideline to investigate the behavior of the multiple jet flows into the upper/hot plenum. The buoyant jet characteristics are strongly related to entrainment rate of the surrounding fluid, the decay of buoyant jet velocity, density, and temperature (Chen and Chen, 1979). The jet flow characteristics are classified into two distinct regions: (1) zone of flow establishment (ZFE), and (2) zone of established flow (ZEF) (Figure 19) (Chen and Nikitopoulos, 1979). The ZFE is the area within the shear layer developed at the edge of a jet, and is known to have a 'conical' shape, because of the shear layer dispersion towards the jet axis at the advancing of the jet (Chen and Nikitopoulos, 1979). It is the location where jet symmetry plane is not entered by turbulence near the exit of the jet flow. The ZEF is the area where the flow field is turbulent and it is divided by three sub-regions: (1) a non-buoyant region (an initial variable density region), (2) an intermediate region (a transition region), and (3) a buoyant region (a plume region) (Figure 19) (So and Aksoy, 1993). The densimetric Froude number, Fr (inertia/momentum force per gravity/buoyant force) is used as a parameter to determine the regions at the range between $\mathrm{Fr} = 0$ (buoyancy only driven flow) and $Fr = \infty$ (non-buoyancy only driven flow).

IV.2.2. Dual Parallel Jets

Parallel jets originated from neighboring nozzles into still surroundings have inclination to merge into a single jet at a particular downstream point of these jets. These turbulent jets interaction have a capability for speedy and thorough mixing of the fluids.

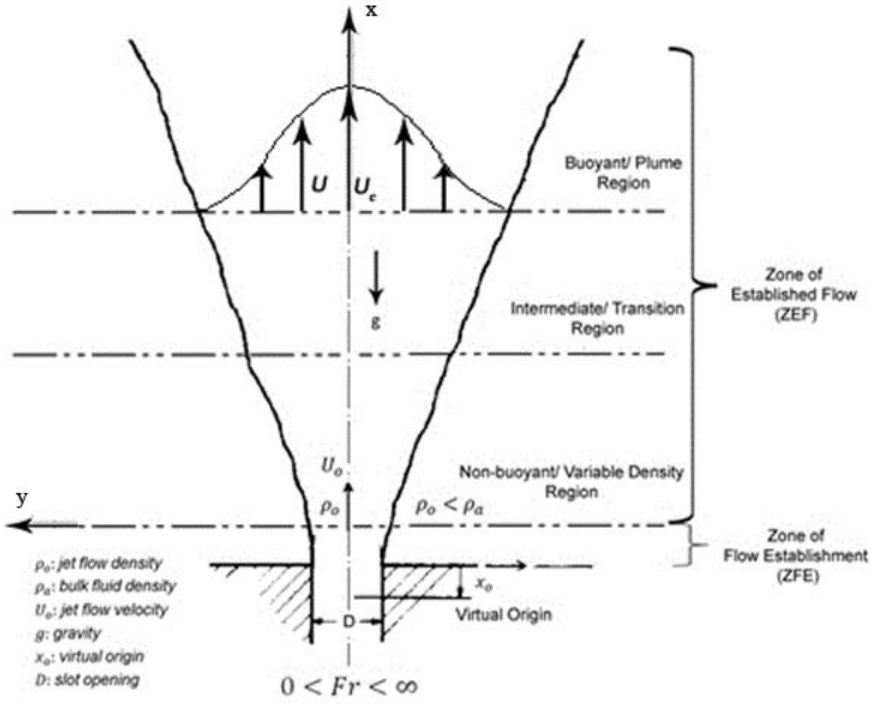

Figure 19. Two distinct regions of vertical jet flow (with three sub-regions for the ZEF) (Chen and Chen, 1979; Erdem and Atli, 2002).

The general flow field structure of two parallel jets in axial direction is characterized by three distinct regions; namely converging region, merging region, and

combined (free jet) region (Tanaka, 1970 and 1974; Erdem and Atli, 2002; Durve, Patwardhan, Banarjee, Padmakumar, and Vaidyanathan, 2011) (Figure 20).

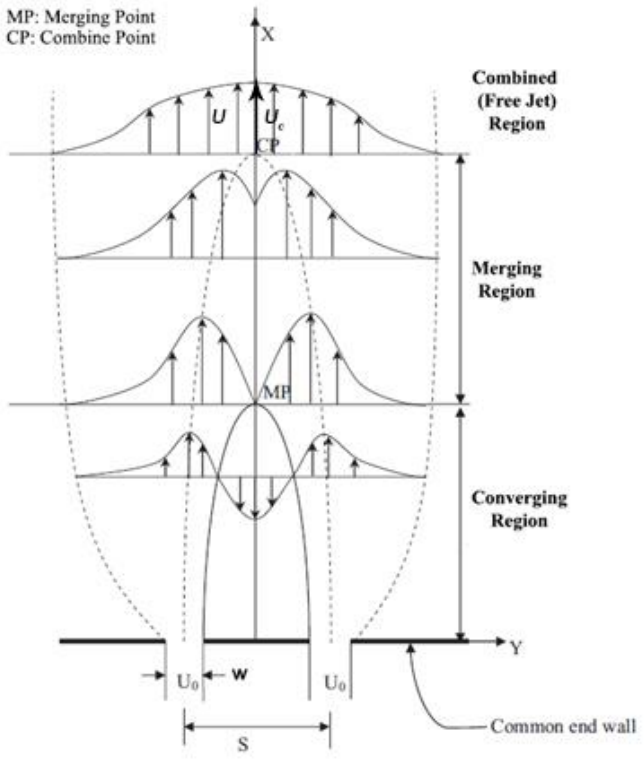

Figure 20. General flow field structure of twin parallel jets (Durve et al., 2011).

The first region, defined as the converging region, is the region from nozzle exit to the location where the jets merge (merge point). Entrainment of the surrounding fluid as a result of high fluid velocity occurs at the nozzle exit. High entrainment rate from the jet boundaries causes a negative region between jets. The depressurized region triggers

the jet trajectories deflection towards each other. Two converging jets, with the sub-atmospheric region in between, approach the symmetry plane X as they travel from the nozzle exit. The two converging jets merged at the merging point, MP. The MP is the location of which the mean velocity in the jet flow direction is zero and highest pressure value in the symmetry axis X. The high pressure at the MP is accountable for the axial mean velocity positive direction downstream of the MP (i.e. redirecting the flow in axial direction) as well as negative direction upstream of the MP (i.e. reversed part of the flow towards the entrainment or converging region). Therefore, the mean velocity changes its path beyond the MP. Beyond the MP, the actual mixing of the jet streams is taking place. This second region, in between the MP and the combine point, CP is defined as the merging region. The CP is the position of which the two jets join and the stream wise velocity reaches its peak value. After the CP, or the region downstream the CP, the two jets resemble a single jet behavior.

Lai and Lee (2012) in their proposed general semi-analytical model for the dynamic interaction of multiple buoyant jets in stagnant ambient condition demonstrate that the velocity field of multiple momentum jets after merging can be calculated by using the superposition technique based on Reichardt's hypothesis (Figure 21). Reichardt's inductive hypothesis for turbulent closure (based on a round jet momentum flux radial distribution follows an error function distribution) assumes that the lateral gradient of the shear stress is proportional to the transverse gradient of the x momentum (for a pure jet discharging in the x direction), which results in a linear equation in terms of the jet momentum flux u^2. The jet momentum linearity allows the usage of the superposition

method in multiple jets which implies the local momentum flux as the net summation of the momentum flux contributions from all the individual axisymmetric jets.

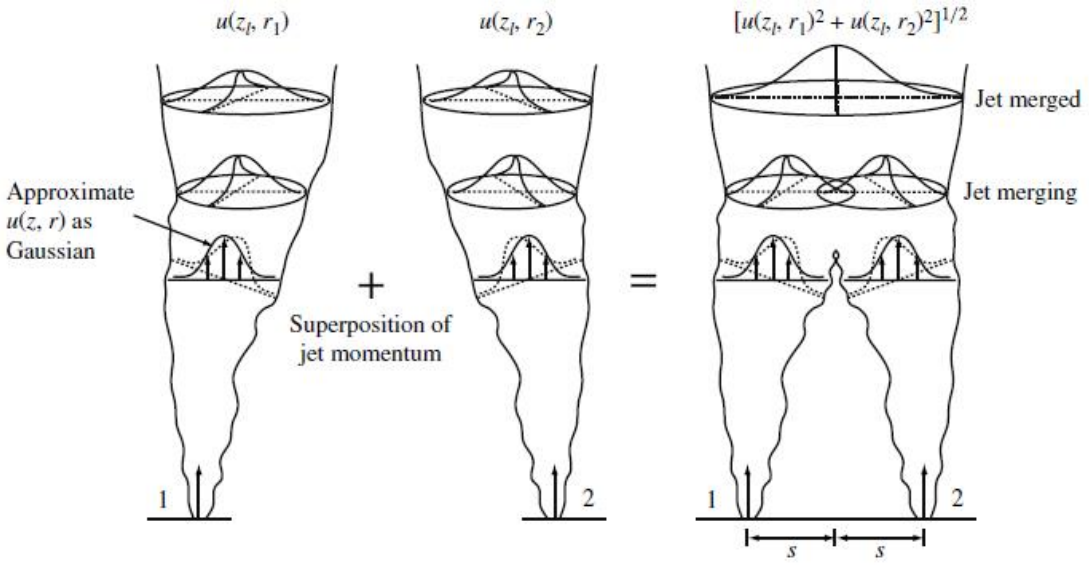

Figure 21. Momentum superposition for the velocity field of two interacting jet. Here r_1 and r_2 are the radial distances from the deflected jet centerline of jet 1 and jet 2, respectively (Lai and Lee, 2012).

IV.2.3. Triple Parallel Jets

Tokuhiro and Kimura (1999) investigated the thermal-hydraulic mixing of three quasi-planar, vertically flowing (water) parallel jets with the central jet at lower temperature (unheated or cold, non-buoyant) than the two adjacent jets (heated or hot, buoyant). The average exit velocity ratio, $r = V_{cold,exit}/V_{hot,exit}$ was equal to $r = 1.0$ (isovelocity), 0.7, or 0.5 (both non-isovelocity). The temperature difference between the

heated and the unheated jets was $\Delta T_{hc} = 5\,^{\circ}\text{C}$ or $10\,^{\circ}\text{C}$. An ultrasound Doppler velocimeter (UDV) was used to measure the velocity profiles while thermocouples were utilized to record the temperature. The velocity profiles were measure using ultrasonic velocity profiler while the temperature measurements were made using thermocouples. The authors showed that $r \neq 1$ delays onset of convective, thermal mixing. Nonetheless, the downstream distance at which mixing is complete continue unaffected.

Durve et al. (2011) performed numerical investigation of the mixing phenomenon in the two jet and three jet systems using CFD. The results from this work are useful for the design modifications of the hot/upper plenum since the mixing of the jets issued from the risers' exit could result in high temperature fluctuations at certain regions inside the hot/upper plenum. Approximation of the merge point and combine point are essential for the cooling effectiveness of the air-cooled RCCS since the merging region (mixing region) has high temperature fluctuation than the combine (free jet) region. The summary of the findings are as follows:

- The merge point of the two jet flow is affected by the nozzle diameter, the spacing between the jets, and the jet exit conditions (turbulent intensity) as per below relationship:

$$\frac{Y_{mp}}{D_n} = 0.721\left(\frac{S}{D_n}\right) + 2.06\,(I) - 2.453 \qquad \text{(IV-1)}$$

where

Y_{mp}: location of merge point on y-axis

D_n: nozzle diameter

S: spacing between two jets

I: turbulent intensity

- The combined point of the two jet flow depends primarily on the position of the merging point as the following:

$$\frac{Y_{cp} - Y_{mp}}{D_n} = 0.51\left(\frac{S}{D_n}\right) \qquad \text{(IV-2)}$$

where

Y_{cp}: location of combined point on y-axis

Y_{mp}: location of merging point on y-axis

D_n: nozzle diameter

S: spacing between 2 jets

- For two jet flow with $r \neq 1$, where $r = \frac{U_h}{U_c} = \frac{velocity\ of\ hot\ jet}{velocity\ of\ cold\ jet}$, the weaker jet is attracted towards the stronger jet. It was observed that the merging point shifts upstream for $r = 2$,. For $r = 1$, it was noticed that the variation in axial location of the merging point with spacing is higher than for $r \neq 1$. For $r \neq 1$, enhanced spacing pushes the merging point further towards stronger jet. For $r \neq 1$, mixing happens at much slower rate.

- The two-jet flow requires a larger region for complete mixing to occur compared with three-jet flow despite the mixing process in both the systems starting at similar downstream distance.
- The turbulent velocity fluctuations in two-jet and three-jet flows remain to be greater than the single-jet flow even past their combined points.
- The three-jet flow, having higher jet spread and more rapid velocity decay, implies mixing is more efficient than in the single-jet or two-jet flow.
- The existence of sturdy recirculation vortices and steeper deflection towards the plane of symmetry cause smaller turbulent fluctuations in two-jet flow as compared with the three-jet flow.

IV.2.4. Multiple Parallel Jets

Nasr and Lai (2010) utilized the superposition of Reichardt's solution for a single free jet to derive the velocity distribution for multiple parallel plane jets. Both ventilated (parallel jets issued from free-standing nozzles) and unventilated (parallel jets issued from nozzles with common wall in between) two parallel plane jets data available in the literature were used for comparisons with the theoretical results obtained from Reichardt's hypothesis. Nasr and Lai (2010) pointed out that for the cases of ventilated two parallel jets with small nozzle spacing ratio, the theoretical solution based on Reichardt's hypothesis was in agreement with experimental data. Large discrepancies existed between experimental results and those obtained based on Richardt’s hypothesis for the cases of

unventilated two parallel jets with large nozzle spacing ratio. However, provided the individual jet-center line deflection is small, low pressure gradient in the recirculation zone and merging region, and low flow collision, for closely spaced multiple parallel jets (small nozzle spacing ratio), there was reasonable agreement between experimental data (in the literature and unventilated five parallel with a nozzle spacing ratio of eight as per Figure 22) and theoretical results.

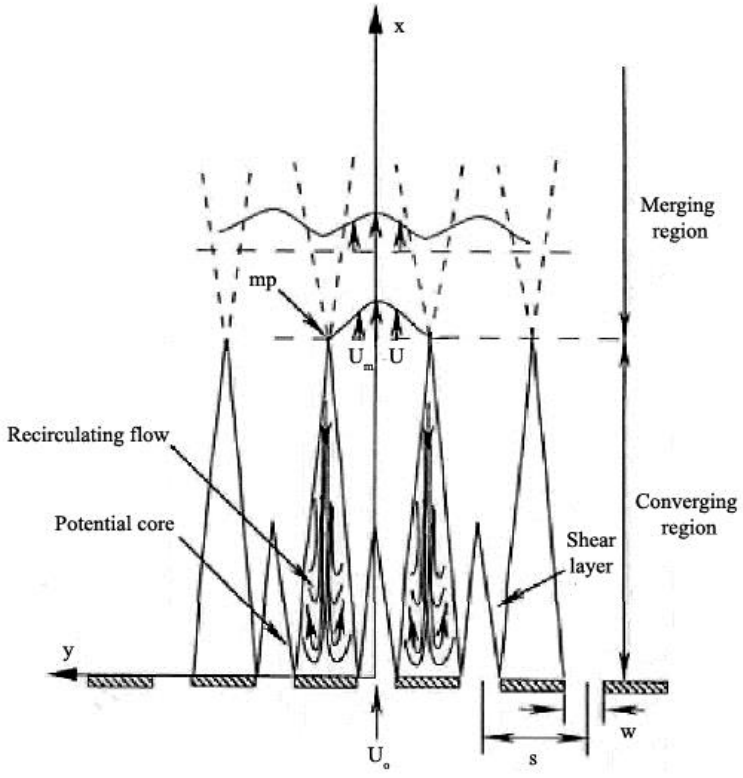

Figure 22. Schematic of five unventilated parallel jets (Nasr and Lai, 2010).

In separate investigations, Nasr and Lai (2011) found that for ventilated parallel jets with low nozzle spacing ratio, there was a good agreement between the calculations

based on theoretical and experimental data. For unventilated parallel jets with low nozzle spacing ratio (as low as 2.5), the superposition technique was found to be invalid in comparison with Laser Doppler Anemometry (LDA) measurement data. These findings were just primary and a more complete range of experiments is required in order to fully categorize the applicability of the superposition method of Reichardt's solution to the prediction of parallel plane jets.

The theoretical derivation of velocity distribution for multiple parallel jets is based on the analytical solution for a single free jet based on the work performed by Nasr and Lai (2010; 2011). The instantaneous governing equations of motion under the thin layer assumption, neglecting streamwise pressure gradient and molecular shear stress for a single jet flow are as follows:

$$U\frac{\partial U}{\partial x}+V\frac{\partial U}{\partial y}+\frac{1}{\rho}\frac{\partial \overline{uv}}{\partial y}=0 \qquad \text{(IV-3)}$$

$$\frac{\partial U}{\partial x}+\frac{\partial V}{\partial y}=0 \qquad \text{(IV-4)}$$

where u and v are the streamwise (x) and transverse (y) velocity components respectively.

Many turbulence models have been proposed in order to find velocity components and Reynolds shear stress of Eqs. (IV-3) and (IV-4) above. Reichardt (1942) proposed that an analogy exists between molecular and turbulent momentum transfer. As such,

Reichardt's hypothesis indicates that the pressure gradient and molecular viscosity effects are assumed negligible in the momentum equation. Assuming a momentum transfer length (analogous with Prandtl's mixing length) plus some mathematical operations, the transformed momentum equation for a single free jet is:

$$f'' + \eta f' + f = 0 \tag{IV-5}$$

where $f = U^2/U_m^2$, U_m is the mean streamwise centerline velocity for a single jet, $\eta = y/cx$, and c is a constant related to jet spreading rate.

U_m is related to the nozzle exit velocity, U_o by the following expression:

$$\frac{U_m}{U_o} = k\sqrt{\frac{w}{cx}} \tag{IV-6}$$

where k is a constant related to the velocity decay, c is a constant related to jet spreading rate and w is the nozzle width.

The solution of Eq. (IV-5) is:

$$f = \frac{U^2}{U_m^2} = e^{-0.5\eta^2} \tag{IV-7}$$

Due to the linearity of the transformed momentum equation for a single jet, Eq. (IV-5), the momentum distribution of multiple parallel plane jets for an even number of

nozzles $(2N)$ (where N is the number of nozzle(s), with equal separation distance s between each pair of nozzles) can be derived by superimposing the solution given by Eq. (IV-7) for individual jets. Note that a Cartesian coordinate in Figure 22 is adopted in this derivation (i.e. the coordinate origin is at the mid plane between two central nozzles and x-axis coincides the centreline of the central jet). Therefore, the superposition of Reichardt's solution for individual jets produces:

$$\left[\frac{U}{U_m}\right]^2 = \sum_{i=1}^{N}\left(e^{-0.5n_{it}^2} + e^{-0.5n_{ib}^2}\right) \qquad \text{(IV-8)}$$

where

$$\eta_{it} = \frac{y - 0.5is}{cx} \quad , \quad \eta_{ib} = \frac{y + 0.5is}{cx}$$

Inserting Eq. (IV-6) into Eq. (IV-8):

Even number of nozzles

$$\frac{U}{U_o} = k\sqrt{\frac{w}{cx}}\left[\sum_{i=1}^{N}\left(e^{-0.5n_{it}^2} + e^{-0.5n_{ib}^2}\right)\right]^{0.5} \qquad \text{(IV-9)}$$

The momentum distribution of multiple parallel plane jets for an odd number of nozzles $(2N + 1)$ (where N is the number of nozzle(s) with equal separation distance s between each pair of nozzles) is obtained by following the similar approach:

Odd number of nozzles

$$\frac{U}{U_o} = k\sqrt{\frac{w}{cx}}\left[e^{-0.5\eta_c^2} + \sum_{i=1}^{N}\left(e^{-0.5n_{it}^2} + e^{-0.5n_{ib}^2}\right)\right]^{0.5} \quad \text{(IV-10)}$$

where

$$\eta_c = \frac{y}{cx}$$

The streamwise velocity component, along the x-axis or symmetry axis ($y = 0$) for even and odd number of nozzles can be derived from Eqs. (2-7) and (2-8) respectively as:

Even number of nozzles

$$\frac{U_c}{U_o} = \sqrt{2}\,k\left[\frac{w}{cx}\sum_{i=1}^{N} e^{-0.5n_{it}^2}\right]^{0.5} \quad \text{(IV-11)}$$

Odd number of nozzles

$$\frac{U_c}{U_o} = k\left[\frac{w}{cx}\left(1 + 2\sum_{i=1}^{N} e^{-0.5n_{it}^2}\right)\right]^{0.5} \quad \text{(IV-12)}$$

IV.3. Parallel Jets Impinging on a Flat Surface

Literature reviews of several previous studies on impingement jets were conducted in order to gain a wide-ranging overview of the general pattern and behavior of the jet flow with a flat impingement surface. Most of the experimental test section arrangements

in the literatures were different from the set-up of the upper plenum, i.e. vertically downward jet flow instead axially upward flow (buoyancy and gravity effects would act differently). However, the finding of the literatures has furnished insightful information for adiabatic and heated experiments.

IV.3.1. Single Jet

Beitelmal, Shah, and Saad (2006) studied heat transfer relations for stagnation and wall jet region solutions for a two-dimensional jet normally impinging on a flat surface. The author mentioned that for exit Reynolds number > 700, a free submerged jet issuing from a nozzle becomes turbulent at a short distance from the point of discharge. As the fluid travels past a stagnant layer of fluid where a slipline is created, turbulence is formed. This slipline turns unstable causing the flow to change into a turbulent mixing zone due to entrainment of the surrounding fluid. Entrainment causes the surrounding fluid into the jet which results in the increase of the flow rate as the distance from the nozzle exit increases (Beitelmal et al., 2006). Prior to the impingement over a flat surface, the impinging jet may be effectively divided into four distinct regions: an initial mixing region, a free jet core potential core, an impinging region and a wall jet region (Figure 23) (Cartwright and Russell, 1967; Beitelmal et al., 2006). There are two sub-regions in the free jet potential core, namely the potential core with velocity equal to the jet exit velocity, and the lower-velocity mixing layer, which results from the surrounding fluid entrainment (Garimella and Rice, 1995). The maximum velocity is at the center of the free jet core and

decreases gradually to zero as the free jet approaches the stagnation point on the target surface. The static pressure is higher than the surrounding pressure at the time the free jet flow hits the target surface. The flow is deflected in the direction parallel to the flat surface to the pressure gradient and the wall jet is formed. The wall jet sticks to the target surface as it flows over the plate. It is expected that the wall jet region adherence to the flat surface will be different for the vertically upward jet flow as a result of the combined gravity and buoyancy influence. The heat transfer is highest at the stagnation point.

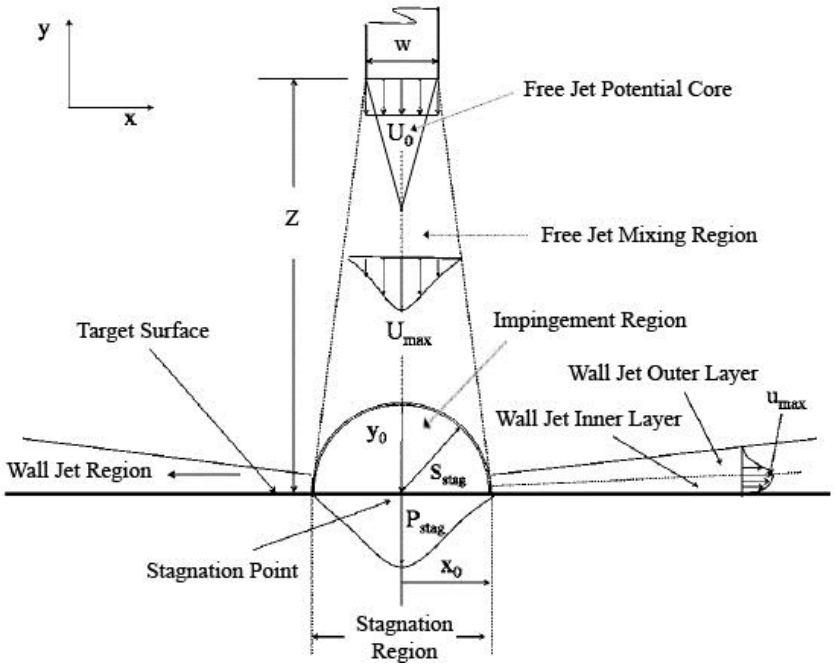

Figure 23. Schematic of impingement jet to a flat surface (Cartwright and Russell, 1967; Beitelmal et al., 2006).

The arrival velocity (i.e. the free jet maximum velocity at the stagnation point) and the external flow just outside the boundary layer affect the stagnation region. Pressure and velocity will decrease due to the surrounding pressure and temperature at the distance y_o and x_o from the stagnation point (Figure 23). The boundary layer flow in the close proximity of the stagnation point is almost certainly laminar in consideration of low local Reynolds number (Cartwright and Russell, 1967). It is safe to assume that the laminar flow is perpetuated for the entire stagnation region by the help of the positive pressure gradient in the region (Beitelmal et al., 2006). As the stagnation flow becomes a wall jet, the maximum velocity just outside the stagnation region recuperates to the maximum approach velocity. The wall jet is segregated into two layers; namely an inner layer and an outer layer (Figure 23). It is a turbulent boundary layer with zero-pressure gradient in the direction of the flow (Beitelmal et al., 2006). Viscous and entrainment effects will reduce the wall jet velocity. The heat transfer of the wall is affected by the turbulence intensity in the outer layer and the maximum velocity just outside the outer layer.

San and Chen (2014) discussed the earlier work by Garimella and Rice (1995) and Fitzgerald and Garimella (1998) on single-jet impingement heat transfer whereby the entrainment effect for a jet of FC-77 (a perfluorinated dielectric liquid) emanating from a round nozzle would cause the surrounding fluid to be sucked into the jet (Figure 24). For a confined impinging jet, Garimella and Rice (1995) discovered that the entrainment effect stimulates a recirculation flow between the jet and a location extending to a distance of several jet diameters from the jet centerline.

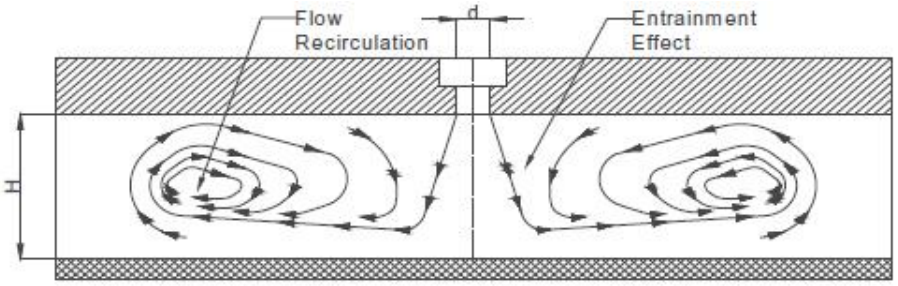

Figure 24. Entrainment effect of a confined impinging jet (Garimella and Rice, 1995; San and Chen, 2013).

IV.3.2. Multiple Parallel Jets

Another important factor that can affect the fluid flow and heat transfer for multiple-jet system is jet deflection and interaction on impingement plate (Figure 25). Flow visualization of twin-jet water flow impinging on a flat plate (equal jet diameters and momenta) performed by Saripalli (1983) observed that a fountain up-wash flow was generated by the colliding wall jets (jet deflection) (Figure 26). San and Chen (2014) pointed out that jet interference which disturbs the fluid motion of the jets in the jet array prior to impingement could affect the heat transfer as well (Figure 27). Stan and Chen (2014) also mentioned that the cross flow resulting from the expelled fluid of the upstream jets will disturb the downstream jets. Through the entrainment effect, part of the cross flow mixes with the downstream jets which causes a reduction of local heat transfer.

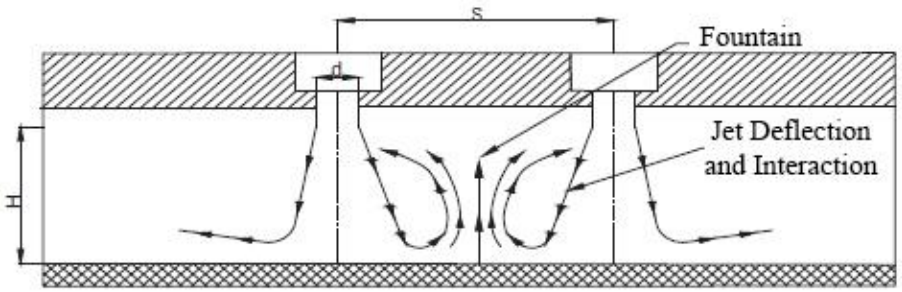

Figure 25. Jet deflection and interaction between the target surface and the twin jets (San and Chen, 2013).

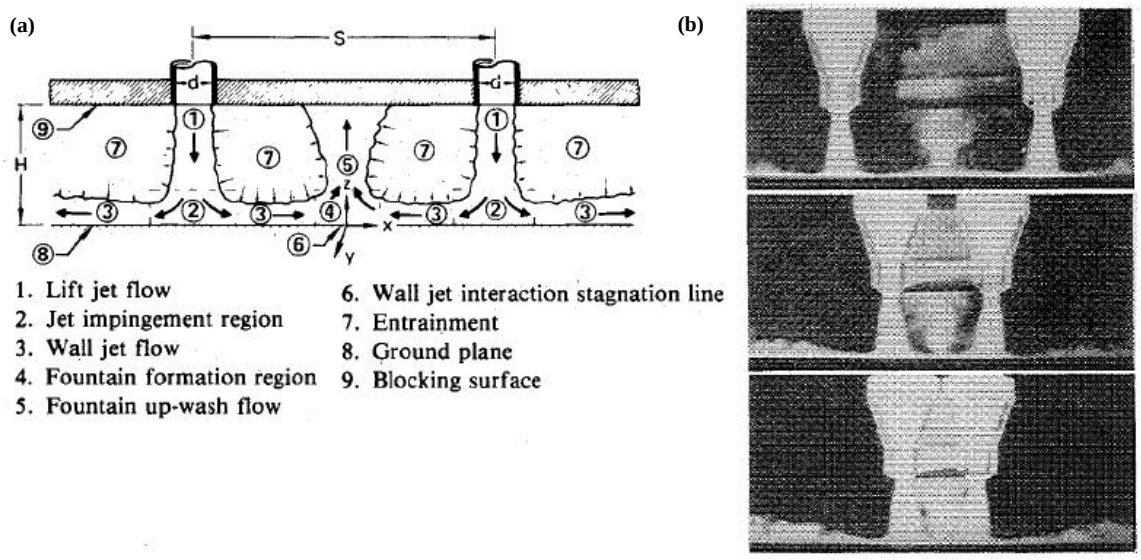

Figure 26. Twin-jet impingement flow: (a) Schematic of twin jet impingement flow, (b) Top picture shows the free jets, the wall jets, and the fountain, middle and bottom pictures illustrate the interaction of the fountain with the main jets for a closed-spaced jets (Saripalli, 1983).

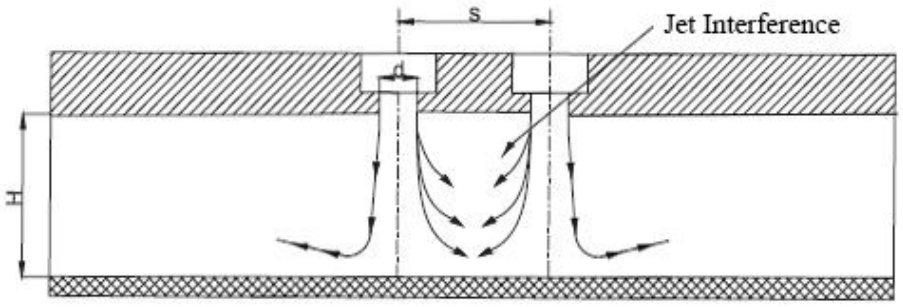

Figure 27. Jet interference between two adjacent jets (San and Chen, 2013).

IV.4. Measurement Techniques

Several measurement techniques for velocity will be employed in the experiments. Review of fundamentals of these measurement techniques were carried out in order to comprehend the overall system focusing on air as the medium.

IV.4.1. Particle Image Velocimetry (PIV)

PIV is a non-intrusive measurement technique that makes an instantaneous velocity measurement in a plane across the whole-flow-field based on the light scattered by small tracer particles in the flow illuminated by a laser light sheet. A high intensity, multiple-pulsed laser is utilized for a short period (approximately 0.1-100 ns) to create a thin 2-D light sheet positioned in the desired plane of the seeded flow (Sun and Zhang, 2007). For a basic 2-D PIV system, a high speed digital video camera synchronized with

the thin laser light sheet can be used to record the displacements of small tracer particles in an identified time interval between two laser pulses. The cross-correlation function can be used to evaluate the image displacement between pairs of frames. From the fundamental definition of velocity, the local velocity value can be computed by dividing the displacement by the time interval between two exposures (Adrian, 1991; Hassan, Blanchat, and Seeley, Jr., 1992). PIV is a robust technique for industrial applications since it unites whole-field visualization with the instantaneous capture of the data. The huge advantage of the PIV technique is its ability to carry a quantitative and instantaneous measurement of the velocity global-wise, i.e. over a whole plane simultaneously (both visualization and quantification of the 2-D flow structure become available), unlike point-wise measurement techniques (obtain the velocity information at the point of the probe), e.g. Laser Doppler Velocimetry (LDV) (Brossard et al., 2009; Sun and Zhang, 2004).

In general, PIV systems can be segregated into two major parts, namely hardware (imaging) and software (image analysis), respectively. Hardware (imaging acquisition) encompasses tracer particles, a light source, light sheet optics, and camera(s). This part will generate a double-exposed photographic image of the tracer particles in the flow field. Software (image analysis) comprises interrogation and post-processing systems. The interrogation system will extract and portray the velocity field information included in the photographs. Measurement settings for the PIV systems are in between these two major parts (Figure 28).

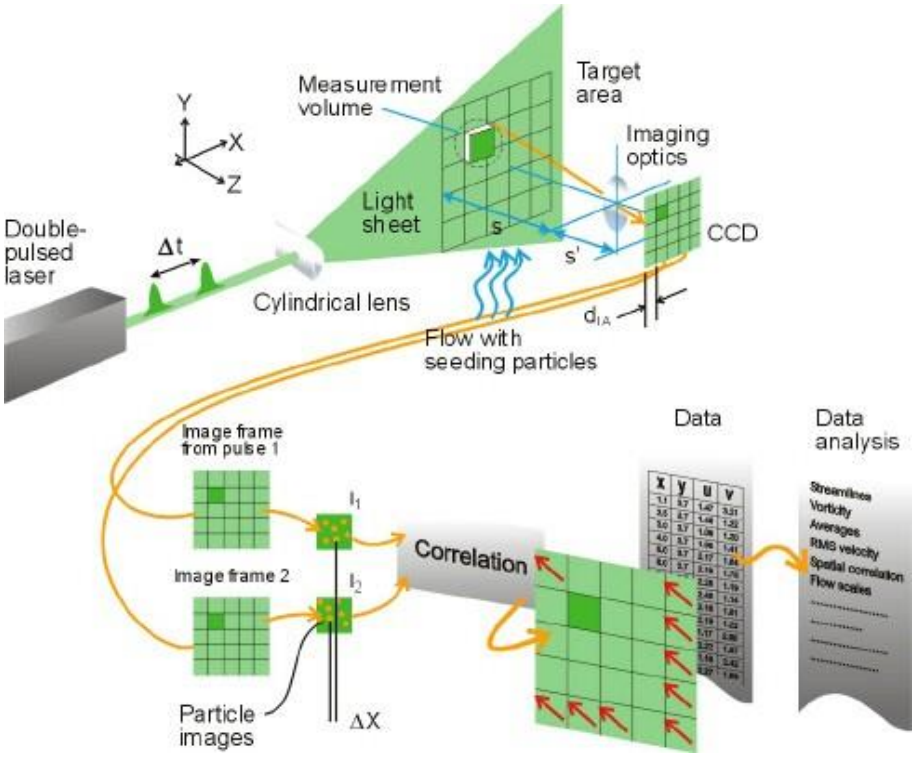

Figure 28. Schematic flow for PIV (Jahanmiri, 2011).

In order to image the whole-flow field, the flow must be seeded with light reflecting particles with appropriate concentration. It is assumed that the seeded particles are small enough to faithfully follow the flow and their velocity represents the flow. It is also assumed that these particles are homogenously distributed, uniform displacement within interrogation region and sufficient size to reflect the required amount of light. In addition, these particles physical density should be equivalent to the working fluid, have spherical shape and highly reflective surface (Sun and Zhang, 2007). In this dissertation, since the working fluid for the experiments is air, seeding materials for gas flows are

utmost importance. Raffel, Willert, Wereley, and Kompenhans (2007) listed a number of different particles that can be used for flow visualization (Table 2).

Very scarce information can be obtained in the literature on practical methods to supply the seed particles into the flow under investigation. Most of the time tracers need to be added in order to get adequate image contrast and also to control particle size. Solid particles are hard to disperse and are inclined to lump together. Liquid droplets are inclined to evaporate in a very fast manner. The seed particles sometimes must be injected without significantly causing flow perturbation at a location that guarantees homogeneous distribution of the tracers and fully developed flow. Numerous techniques have been developed to produce and provide particles for the gas flow. Amongst the available techniques are: (1) atomizers to disperse solid particles suspended in evaporating liquid; (2) atomizers to produce minute droplets of vapor pressure liquids (e.g. oil) that have been mixed with vapor pressure liquids (e.g. alcohol) which evaporate before entering in the experimental test section; (3) air jets or fluidized beds to disperse dry powders; (4) smoke generators and monodisperse polystyrene or latex particles injected with water-ethanol (wind tunnel flows condensation generators) (Raffel et al., 2007).

Table 2. Seeding materials for gas flows (Raffel et al., 2007).

Type	Material	Mean diameter (µm)
Solid	Polysterene	0.5-10
	Aluminum Al_2O_3	0.2-5
	Titania TiO_2	0.1-5
	Glass micro-spheres	0.2-3
	Glass micro-balloons	30-100
	Granules for synthetic coating	10-50
	Dietylphathalate	1-10
	Smoke	<1
Liquid	Different oils	0.5-10
	Di-ethyl-hexyl-sebacate (DEHS)	0.5-1.5
	Helium-filled soap bubbles	1000-3000

Lasers are commonly used in PIV as a light source due to their capability to emit monochromatic light with high energy density. This ability enables lasers to be easily shaped into thin light sheets for illuminating and recording the tracer particles without chromatic aberrations (Raffel et al., 2007). Every laser comprises three components: (1) laser material: an atomic or molecular gas, semiconductor or solid material; (2) pump source: excites the laser material by the introduction of electro-magnetic or chemical

energy; and (3) mirror arrangement: i.e. the resonator allows an oscillation within the laser material (Figure 29).

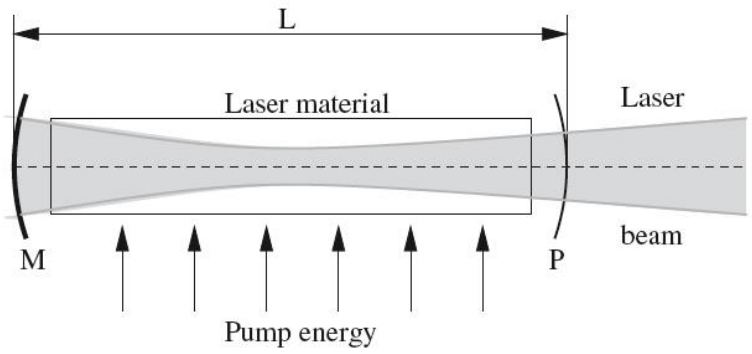

Figure 29. Typical schematic diagram of a laser (Raffel et al., 2007).

Two types of lasers are utilized in PIV, namely continuous wave (CW) lasers, e.g. a few watts of argon-ion lasers or low-powered helium-neon lasers, or pulsed lasers, respectively (Jahanmiri, 2011). Typical pulsed lasers are frequency-doubled Nd:YAG (neodymium yttrium aluminum garnet) lasers producing 100 to 400 mJ/pulse, repetition rate on the order of 10 Hz, and 5-10 ns duration (Jahanmiri, 2011; Törnblom, 2004) (Figure 30) (Table 3). Nd:YAG lasers emit light in the infrared range (1064 nm). A harmonic generator is used to make the Nd:YAG into half (532 nm) since most cameras have their maximum sensitivity in the blue-green part of the spectrum and it is inconvenient for not being able to see the light sheet when placing it in the measurement section (Törnblom, 2004). A cylindrical lens is required to shape the axisymmetric shape

coming out from the laser beam so that a planar sheet formation is possible. The laser light sheet is in the order 1–3 mm (0.04–0.125 in.) thick. Using a thin laser sheet as the illumination can present a challenge, particularly in a strong three-dimensional flow field of which the captured images by the camera at the first laser pulse includes many particles travelling out of the thin-depth measurement volume and therefore are invisible to the camera at the next laser pulse (Sun et al., 2004).

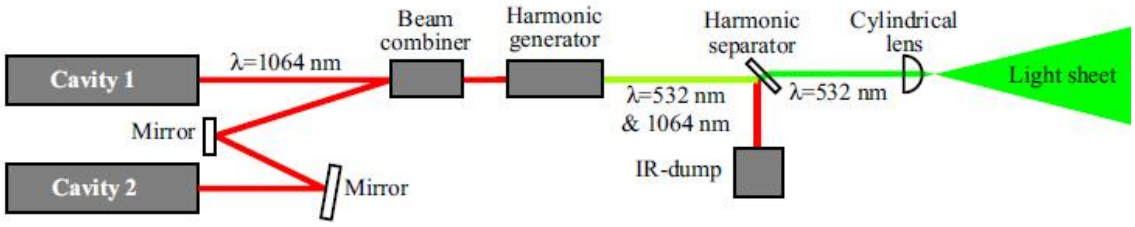

Figure 30. Typical schematic diagram of a double cavity, Nd:YAG laser (Törnblom., 2004).

Table 3. Properties and specifications of modern Nd:YAG PIV-laser systems (Raffel et al., 2007).

Parameter	Value
Repetition rate	10 Hz
Pulse energy for each two pulses	320 mJ
Roundness at 8 m from laser output	75%
Roundness at 0.5 m from laser output	75%
Spatial intensity distribution at 8 m from laser output	< 0.2
Spatial intensity distribution at 0.5 m from laser output	< 0.2
Line width	1.4 cm^{-1}
Power drift over 8 hours	< 5%
Energy stability	< 5%
Beam pointing stability	100 μrad
Deviation from colinearity of laser beams	< 0.1 mm/m
Beam diameter at laser output	9 mm
Divergence	0.5 mrad
Jitter between two following laser pulses	2 ns
Delay between two laser pulses	0 to 10 ms
Resolution	5 ps
Working temperatures	15^{o} - $35^{o}C$
Cooling water	10^{o} - $25^{o}C$
Power requirements	220-240V, 50 Hz

The three most common solid state electronic image sensors are charge coupled devices (CCD), charge injection devices (CID) and complementary metal-oxide semiconductor (CMOS). CCD sensors, which converts light (i.e. photons) to electric charge (i.e. electrons) based on the photoelectric effect (Figure 31), has found the most widespread use for PIV systems due to their convenience of data transmission and image processing, despite lower resolution than those of professional film cameras (Sun and Zhang, 2007). The CCD sensor encompasses many single sensors that are organized in a rectangular array where each pixel has a size on the order of 10x10 μm with their repetition rate (in PIV double frame mode) in the order of 10 Hz (Brossard et al., 2009).

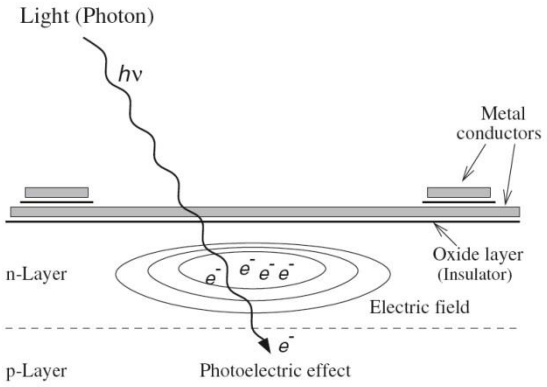

Figure 31. Simplified model of a CCD pixel (Raffel et al., 2007).

For assessment, the digital PIV recording is subdivided into small "interrogation windows". Each interrogation window consists of multiple pixels. For each interrogation

window, the local displacement vector of the particle images between the two illuminations is determined by a spatially statistical cross-correlation function (Brossard et al., 2009).

The first exposure image intensity is given by the following:

$$I_1(\boldsymbol{x}) = \sum_{i=1}^{N} V_1(\boldsymbol{X_i})\mu\,(\boldsymbol{x} - \boldsymbol{x_i}) \tag{IV-13}$$

where $\boldsymbol{X_i}$ is the position vector, $\boldsymbol{x_i}$ is the image position vector of particle i in the first exposure, $V(\boldsymbol{X_i})$ is the transfer function giving the light energy of the image of an individual particle i inside the interrogation volume and its conversion into an electronic signal, and i is the point spread function of the imaging lens.

The second exposure image intensity is defined in the expression below (assuming all particles inside the interrogation window have travelled with a same displacement vector $\boldsymbol{\Delta X}$ between the two exposures):

$$I_2(\boldsymbol{x}) = \sum_{j=1}^{N} V_2\big(\boldsymbol{X_j} + \boldsymbol{\Delta X}\big)\mu\left(\boldsymbol{x} - \boldsymbol{x_j} - \boldsymbol{\delta x}\right) \tag{IV-14}$$

where $\boldsymbol{\delta x}$ is the particle image displacement (approximated by $\boldsymbol{\Delta X} \cong \boldsymbol{\delta x}/M$, where M is the magnification vector).

The cross-correlation function of the two interrogation windows is:

$$R(\boldsymbol{s}) = \langle I(\boldsymbol{x})\, I(\boldsymbol{x}+\boldsymbol{s}) \rangle \tag{IV-15}$$

where $\boldsymbol{s}$ is the separation vector in the correlation plane, and $\langle\ \rangle$ is the spatial averaging operator over the interrogation window.

The cross-correlation can be decomposed into three components (Keane and Adrian, 1992):

$$R(\boldsymbol{s}) = R_C(\boldsymbol{s}) + R_F(\boldsymbol{s}) + R_D(\boldsymbol{s}) \tag{IV-16}$$

where R_C is the correlation of the mean image intensities, R_F is the fluctuating noise component ($\boldsymbol{i} \neq \boldsymbol{j}$ terms), and R_D is displacement-correlation peak ($\boldsymbol{i} = \boldsymbol{j}$ terms).

R_D is the highest when $\boldsymbol{s} = \boldsymbol{\delta x}$**.** As such**,** finding the location of this maximum yields $\boldsymbol{\delta x}$ and also $\boldsymbol{\Delta X}$**.** This location is normally found via orderly exploration inside the interrogation window by utilizing Fast-Fourier Transform algorithms for computing cross-correlation. The separation vector in the correlation plane $\boldsymbol{s}$ is obtained with sub-pixel accuracy from correlation data interpolation (Figure 32).

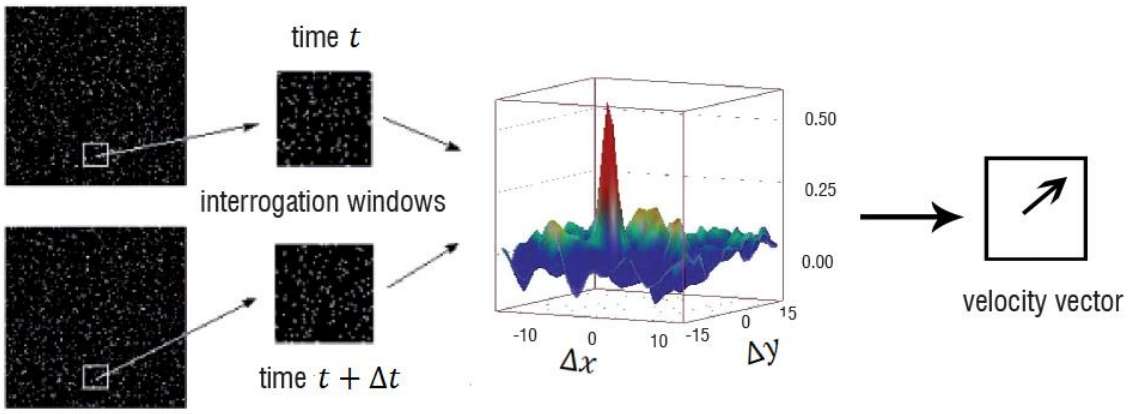

Figure 32. Cross-correlation of a pair of two singly exposed recordings (Brossard et al., 2009).

IV.4.2. Particle Tracking Velocimetry (PTV)

Particle tracking velocimetry (PTV) determines particles' trajectories and velocities by catching and examining each particle image to locate its center and connecting image tracks (possibly multiple exposures) (Adrian 1996; Sun and Zhang, 2007). The low-image-density mode of PIV is also known as PTV due to possibility to measure displacements by tracking individual images (since the number of images per unit area is small) (Adrian, 1991).

A PTV system has similar set-up to PIV system by having image acquisition hardware (one or multiple cameras to record the images/videos of the particle motion), data processing software, seed with tracer particles, and a light source, i.e. a laser for illumination on the observation section. Combination of the data processing software and the images is required to determine the image of an individual particle, track the particle

image in the temporal dimension, harmonize the images of the particle from all of the camera(s), and finally compute the particle velocity (Sun and Zhang, 2007). Table 4 shows the comparison between PIV and PTV.

Table 4. Comparison between PIV and PTV

Visualization Technique	Tracking	Image Density
PIV	Interrogation cell	High
PTV	Individual particle	Low

IV.4.3. Laser Doppler Velocimetry (LDV)

Laser Doppler Velocimetry (LDV) or Laser Doppler Anemometry (LDA) refers to a technique to measure the velocity of the flowing fluid at a point by detecting the Doppler shift of a laser light that has been scattered by small particles (typically 1~10 μm) (Adrian 1996; Menon, 1999; Sun and Zhang, 2007). The LDV technique is also known as dual beam, differential Doppler or fringe mode technique (Menon, 1999).

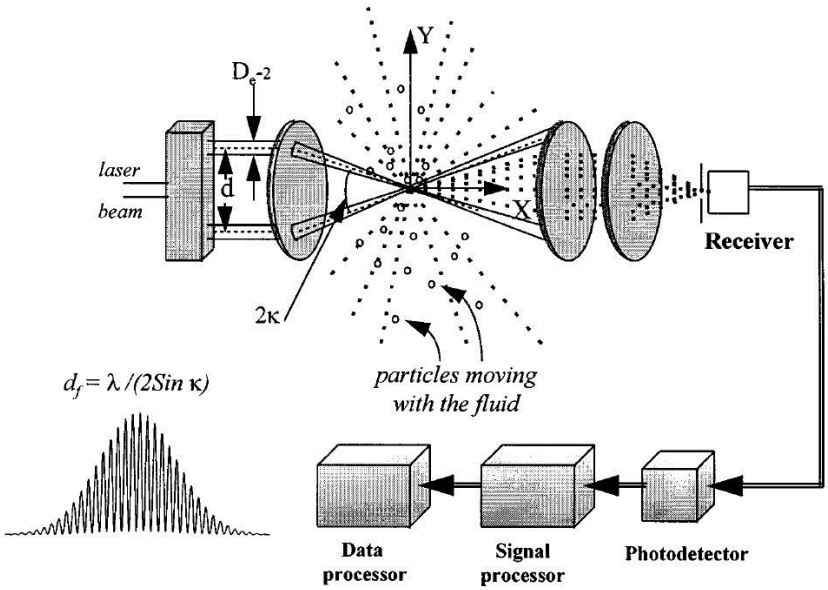

Figure 33. Schematic of a dual-beam system (Menon, 1999).

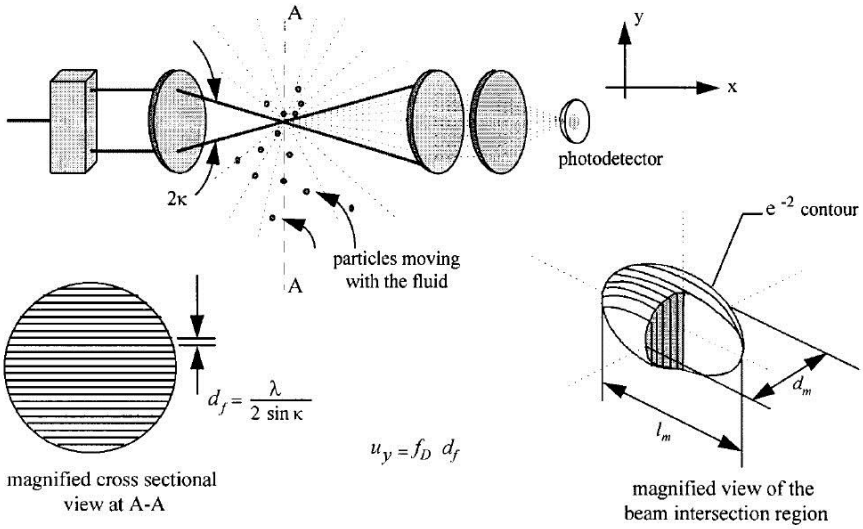

Figure 34. Details of the beam crossing (Menon, 1999).

Figure 33 shows the basic components of a complete LDV system using a dual-beam optical arrangement (Menon, 1999). A beam splitter is used to split the original laser beam into two parallel beams. The transmitting optics are utilized to focus and cross the two parallel beams onto a small control volume, which is the measuring region (Figure 34). The small particle will scatter the light from both beams when it moves from the small volume (measuring region). The scattered light has wavelength difference (which is determined by the particle velocity) from the incident light wavelength or known as Doppler shift principle (Sun and Zhang, 2007). The receiving optics receive part of the light scattered by the particles and send the light to a photodetector. The photodetector collects and converts the scattered light intensity to an analog electrical signal. A signal processor processes the frequency (which is proportional to the particle velocity) from the photodetector output and provides this as a digital number corresponding to the instantaneous velocity of the particle. The data processor acquires the complete flow properties from these instantaneous velocity measurements.

IV.5. Proper Orthogonal Decomposition (POD) Method and Its Mathematical Background

Proper Orthogonal Decomposition, commonly abbreviated as POD, is a multi-variate statistical tool which allows for the isolation and consolidation of numerical data. The POD is a linear procedure that takes a given collection of input data and generates an orthogonal basis constituted by functions estimated as the solutions of an integral

eigenvalue problem known as a Fredholm equation (Nobach et al., 2007). As such, order reduction by projecting high-dimensional data into lower-dimensional space as well as feature extraction of dominant and less dominant characteristics in the data can be sought (Kerschen, Golinval, Vakakis, and Bergman, 2005). In fluid mechanics, and particularly in the field of CFD, the POD technique was originally introduced by Lumley (1967) as a method to extract structures from turbulent flow (Berkooz, Holmes, and Lumley, 1993; Biagioli, Lachaux, and Narendran, 2014) so that the coherent structures of the flow can be characterized. Individual POD modes or a combination of POD modes designates different coherent flow structures. The method of snapshots proposed by Sirovich (1987) is popular in contemporary research due to its advantages over the classical (or direct) method in dealing with data comprising a large spatial resolution (Figure 35). Despite of the assumption of the snapshots being uncorrelated, this method has become extremely widespread.

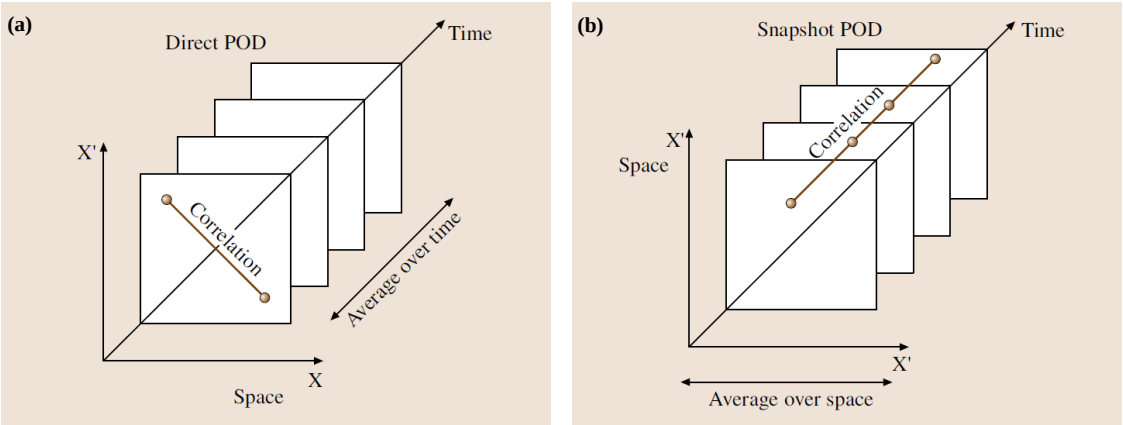

Figure 35. (a) Direct or Classical POD method (correlation over space, average over time) originally introduced by Lumley (1967), (b) Snaphot POD method (correlation over time, average over space) originally introduced by Sirovich (1987) (Nobach et al., 2007).

On one hand, a good spatial resolution can be obtained by numerical simulations such as direct numerical simulation (DNS) or large-eddy simulation (DNS) but normally at a very short time due to the cost consideration. PIV technique can have a highly resolved in space but it has a poor temporal resolution. The two-point temporal correlation tensor is statistically well converged under a moderate time history and high spatial resolution. On the other hand, experimental techniques such as hot-wire anemometry (HWA) or laser Doppler anemometry (LDA) have long time history and moderate spatial resolution which enabled the two-point spatial correlation tensor to statistically converge. In a nutshell, HWA and LDA data can be analyzed using direct POD method and snapshot POD method is more suitable for DNS, LES, and PIV.

The POD is also known by different names such as Karhunen-Loeve Decomposition (KLD), Principle Component Analysis (PCA) (when restricted to a finite dimensional case and truncated after a few terms), and Singular Value Decomposition (SVD). The mathematical background of the POD method is reproduced in this section (Sirovich, 1987; Nobach et al., 2007; Tirunagari, S., 2011; Amini, 2011; Biagoli et al., 2014).

Lumley (1967) proposed the POD method to evaluate turbulent flows and to identify large-scale coherent structures in turbulent velocity fields. In the POD method, the velocity field is decomposed into a finite expansion of orthonormal functions, or eigenfunctions (ϕ_n), and orthonormal amplitude coefficients a_n:

$$U(x,t_n) = \sum_{n=1}^{N} a_n(t)\phi_n \qquad \text{(IV-17)}$$

Sirovich (1987) introduced the method of snapshots which effectively reduces the calculation time of the eigenfunctions; therefore, one can perform a detailed analysis of velocity data with high spatial resolution, i.e. PIV. In such cases, the spatial resolution is significantly larger than the temporal resolution. Mathematically, this concept is captured by the inequality $N_t \ll M$, where N_t is the number of ensemble members deemed adequate for a description of the process and M is the number of spatial points in each instantaneous data set (Nobach et al., 2007).

Each instantaneous PIV fluctuating velocity field (i.e. snapshot) is denoted by

$$u^n = u(x,t_n) \qquad \text{(IV-18)}$$

In order to obtain the POD modes, the following Fredholm integral eigenvalue problem must to be solved:

$$\int_{\Omega} R(x,x')\,\phi(x')dx' = \lambda\phi(x') \qquad \text{(IV-19)}$$

where Ω is the domain of interest and $R(x,x')$ is the two-point spatial correlation tensor or the auto-covariance of the fluid variable, x.

In the algorithm used for the current POD analysis, the auto-covariance matrix is computed using the following definition of the two-dimensional velocity field:

$$U = \left[u^1 u^2 u^3 \dots u^N \right] = \begin{bmatrix} u_1^1 & u_1^2 & \dots & u_1^N \\ \vdots & \vdots & \vdots & \vdots \\ u_M^1 & u_M^2 & \dots & u_M^N \\ v_1^1 & v_1^2 & \dots & v_1^N \\ \vdots & \vdots & \vdots & \vdots \\ v_M^N & v_M^N & \dots & v_M^N \end{bmatrix} \tag{IV-20}$$

The snapshots method suggests that the autocovariance matrix can be approximated by a summation of sufficiently high number of snapshots, N:

$$R(x,x') = \frac{1}{N} \sum_{n=1}^{N} u^n(x)\, u^n(x') \tag{IV-21}$$

The autocovariance matrix is degenerate; therefore, it has eigenfunctions of the form:

$$\Psi = \sum_{i=1}^{N} A^i\, u^i \tag{IV-22}$$

where A^i are the constants to be estimated. The eigenvalue problem for the matrix reads as the following:

$$CA^i = \lambda^i A^i \tag{IV-23}$$

The i^{th} eigenvector A^i corresponds to the eigenvalue λ^i of C. The components of the temporal correlation tensor C is:

$$C = \frac{1}{N} u^T u \tag{IV-24}$$

Since C is a symmetrical matrix, all the eigenvalues are real and positive numbers. The eigenvectors are arranged in descending order of eigenvalues of which the first POD eigenvalue has the most energy.

$$\lambda^i > \lambda^{i+1} = \lambda^1 > \lambda^2 > \lambda^3 \cdots \lambda^N = 0 \tag{IV-25}$$

The magnitude of these eigenvalues is an indication of the kinetic energy of the POD modes. The total energy of the system is characterized by the sum of all of the eigenvalues.

$$\mathbb{E} = \sum_{i=1}^{N} \lambda^i \tag{IV-26}$$

The relative energy (R.E.) stored in each POD mode is denoted by

$$\mathbb{E}_i = \frac{\lambda^i}{\mathbb{E}} \tag{IV-27}$$

The POD modes (eigenfunctions) can be obtained by using the eigenvectors of Eq. (IV-23):

$$\phi^i = \frac{\sum_{n=1}^{N} A_n^i \, u^n}{\left\| \sum_{n=1}^{N} A_n^i \, u^n \right\|} \tag{IV-28}$$

The POD coefficients or amplitude coefficients are defined as follows:

$$a^n = \Psi^T u^n \tag{IV-29}$$

The snapshots of the flow field can be represented in the form of

$$u^n = \sum_{i=1}^{n} a_i^n \phi^i \qquad \text{(IV-30)}$$

where n is the number of modes to be used in the reconstruction. When $n = N$ the reconstruction uses all the modes and the output velocity equals the input velocity. The first few POD modes encompass the large-scale structures of the flow field and reconstructed snapshots with few modes will represent the dominant characteristics of the original flow field.

CHAPTER V

STAGE 2: EXPERIMENTAL TEST FACILITY DESIGN AND MATERIAL SELECTION [*]

V.1. Scaling

A small scale experimental test facility has been constructed at TAMU to study pertinent multifaceted thermal hydraulic phenomena in the air-cooled RCCS. The TAMU experimental facility is ½ scale from the experimental test facility of University of Wisconsin (UW) or ⅛ scale of the GA-MHTGR. In turn, the UW experimental facility is ¼ scale of the GA-MHTGR. There is another facility constructed by Argonne National Laboratory (ANL), Natural convection Shutdown heat removal Test Facility (NSTF), which is ½ scale of the proposed GA-MHTGR.

A scaling evaluation of the TAMU Air-Cooled RCCS system was carried out based on detailed analysis and analytical derivation from earlier efforts by ANL and UW (Tzanos and Farmer, 2006; Lomperski, Pointer, Tzanos, Wei, and Krauss., 2011; Lisowski et al., 2013). Scaling methods enable the study of thermal hydraulic phenomena and

[*] Part of the data reported in this chapter is reprinted with permission from "Design considerations and experimental observations for the TAMU air-cooled reactor cavity cooling system for the VHTR" by Sulaiman, S. A., Dominguez-Ontiveros, E. E., Alhashimi, T., Budd, J. L., Matos, M. D., & Hassan, Y. A., 2015. *AIP Conference Proceedings*, 1659, 030002. http://dx.doi.org/10.1063/1.4916850-. Copyright [2015] by AIP Publishing LLC.

behavior in the lateral (radial) and vertical (axial) for a system integral performance of the GA-MHTGR, using a practicable sized experimental facility with reasonable cost.

V.1.1. Integral (Top-Down) Scaling

A top-down scaling methodology was adopted for the non-dimensional conservation equations illustrating transient and steady state behavior of the RCCS, based off a reduced axial height, l_R, and a unity in structural thickness (Tzanos and Farmer, 2006; Lomperski et al., 2011; Lisowski et al., 2013). These parameters outline a system for the TAMU Air-Cooled RCCS that is one eighth in axial dimensions and one half in radial dimensions compared with the GA-MHTGR. The chief criterion of this scaling was preservation of the temperature rise across the risers. As such, scaling laws that were established is intended to preserve thermal hydraulic phenomena and behavior in the GA-MHTGR for the TAMU ⅛ scale experimental facility.

For the scaled TAMU Air-Cooled RCCS (the model) to be similar to the GA-MHTGR (the prototype), the ratio of any given similarity group must be equivalent at one. In the analysis that was carried out, the subscript *R* indicates the ratio of the value of a parameter in the model or experimental facility to the value of the identical parameter in the prototype or concept facility. Therefore the similarity relationship is

$$\psi_R = \frac{\psi(model)}{\psi(prototype)} = \frac{\psi_M}{\psi_P} \tag{V-1}$$

The scaling correlations were established in a similar manner to the previous efforts by ANL and UW (Tzanos et al, 2006; Lisowski et al, 2013). The essences of the derivations are reproduced here in the following paragraphs.

The total heat transferred to the riser tubes during normal operation is equivalent to the amount of the convective and radiative heat flux exerted on the riser tube walls and cooling panels inside the cavity.

$$\dot{Q} = h_{cavity} A (T_{RPV} - T_{riser}) + \epsilon \sigma_B A \left({T_{RPV}}^4 - {T_{riser}}^4 \right) \quad \text{(V-2)}$$

At steady state,

$$\dot{Q} = \dot{Q}_o = \dot{m} c_p (T_{RPV} - T_{riser}) = \rho A_o U_o c_p \Delta T_o \quad \text{(V-3)}$$

In order to preserve the density ratio, taking the heated section as the point of reference, at steady state conditions, the temperature rise, ΔT_o, along the heated section is

$$\Delta T_o = T_{RPV} - T_{riser} = \frac{Q_o}{\rho A_o U_o c_p} \quad \text{(V-4)}$$

Assuming the system is having constant thermal properties, the similarity relationship for the temperature rise along the heated section reduces to

$$\Delta T_{oR} = \frac{\dot{Q}_R}{A_{oR} U_{oR}} \quad \text{(V-5)}$$

The non-dimensional Froude, Fr number requires a similarity relationship equal to 1.

$$N_{Fr} = \frac{{U_o}^2}{gL_r} = \frac{\rho_f}{\Delta\rho} = 1 \tag{V-6}$$

Assuming the system is having same thermodynamic reference values, the similarity relationship for a reference velocity decreases to

$$U_{oR} = {l_R}^{1/2} \tag{V-7}$$

The time ratio number requires a unity similarity relationship.

$${T_R}^* = \frac{L_{hR}}{U_{oR}{\delta_{ir}}^2} = 1 \tag{V-8}$$

Making the scaling of the reference thickness to the length scaling, the similarity relationship for the time ratio lessens to

$${T_R}^* = \frac{l_R}{U_{oR}} = {l_R}^{1/2} \tag{V-9}$$

The non-dimensional Richardson number, Ri becomes unity based upon the similarity requirements for U_{oR} and ΔT_{oR}.

$$Ri_R = \frac{\dot{Q}_R L_{hR}}{{U_{oR}}^3 A_{oR}} = 1 \qquad \text{(V-10)}$$

The heat flux, $q_R" = {l_R}^{-1/2}$ and $\delta_{yR} = 1$, the similarity relationship for the power is

$$\dot{Q}_R = {l_R}^{1/2} \; or \; {l_R}^{1/2} \qquad \text{(V-11)}$$

Using $A_{oR} = 1$ and substitute Eqs. (3-7) and (3-11) into Eq. (3-5) yields a unity value for the similarity relationship of the temperature rise, ΔT_{oR}.

$$\Delta T_{oR} = \frac{\dot{Q}_R}{A_{oR} U_{oR}} = 1 \qquad \text{(V-12)}$$

As such, the temperature between scales is preserved.

By substituting $\psi_R = l_R =$ reduced axial length scale into Eq. (1), the correlation parameters for the reference velocity (U), time ratio (T_R^*), temperature rise (ΔT), power $(\dot{Q})$, and heat flux $(q")$ were summarized in Table 5.

V.1.2. Bottom-Up Scaling

The top-down scaling is the generic non-dimensionalization analysis functional to the 1-D conservation equations to acquire the important similarity parameters concentrated on a 1-D loop/circuit (Tzanos et. al, 2006). This implies that 3-D thermofluid

phenomena in the hot/upper plenum are not taken into account. For the GA-MHTGR hot/upper plenum, there is a possibility of thermal stratification occurrence via incomplete mixing of parallel jet flow originated from multiple parallel ducts of varying temperature, which calls for 3-D treatment. In addition, the parallel channel flow stability phenomena from the multiple ducts with varying outlet temperature could result in recirculation flow patterns between adjacent ducts, which also triggers for 3-D considerations (Tzanos et al., 2006).

Table 5. Summary of scaling parameters for ½ scale ANL, ¼ scale UW and ⅛ scale TAMU Air-Cooled RCCS.

		ANL	**UW**	**TAMU**
Parameter	**Scaling Ratios**	**Values for $l_R = 0.50$**	**Values for $l_R = 0.25$**	**Values for $l_R = 0.125$**
Lateral (radial)	-	1.00	1.00	0.50
Velocity, U	$U_{oR} = {l_R}^{1/2}$	0.707	0.50	0.35
Time ratio, T_R^*	$T_R^* = \frac{l_R}{U_{oR}} = {l_R}^{1/2}$	0.707	0.50	0.35
Temperature rise, ΔT	$\Delta T_{oR} = \frac{\dot{Q}_R}{U_{oR} A_{oR}}$	1.00	1.00	1.00
Power, $\dot{Q}$	$\dot{Q}_R = U_{oR} = {l_R}^{1/2}$	0.707	0.50	0.354
Heat flux, q"	$q_R^{"} = {l_R}^{-1/2}$	1.414	2.00	2.828

The bottom-up scaling approach as a result of anticipated thermal stratification in the hot/upper plenum and local phenomena within the riser ducts paid close attention to

the behavior of the jet in the hot/upper plenum. The hot jet penetration issued from the outlet of the hot riser ducts should influence the patterns of thermal stratification in the hot/upper plenum. The conditions for potential recirculation between the different hot riser ducts are also affected by the thermal stratification patterns. As such, the maximum ceiling height, X_m, of which the phenomena of jet entrainment, laminar-to-turbulent transition and ambient stratification are embedded inside it, is the chief parameter for the bottom up scaling. Experiments carried out by (Turner, 1966) on a negative buoyant jet for the axisymmetric case was a considerable simplification over a hot riser jet (which is initially positive buoyant until it reaches neutral or even negative buoyancy). Turner's data indicated that

$$\frac{X_m}{D_j} \alpha F_j^{1/2} \tag{V-13}$$

For the selected TAMU Air-Cooled RCCS experiment scaling, $D_{jR} = 0.50$, which has one half of radial dimensions, and $l_R = 0.125$, which lessens axial dimensions by one eighth, giving

$$X_m = {D_{jR}}^{1/2} {l_R}^{1/2} = 0.25 \tag{V-14}$$

Therefore, to cater for bottom-up scaling of jet penetration and turbulence mixing phenomena in the hot/upper plenum, the scaling of the hot/upper plenum height was designed to be 0.25 of the GA-MHTGR.

V.2. Design Considerations and Experimental Facility Overview

The design of the experimental facility was based upon the design of ¼ scaled air-cooled RCCS experimental facility at University of Wisconsin (UW). On the other hand, the concept design of UW facility was based on NSTF design at ANL. Reference to openly available literature particularly to HTGR-86-024 (Bechtel National, Inc., 1992) and other literatures by ANL was also made to the design of the ⅛ scale TAMU Air-Cooled RCCS. Numerous meetings, exchange of emails, conference calls, and personal conversations between researchers at TAMU and UW were carried out during the design stage.

V.2.1. Design Features

The TAMU experimental facility represents ½ scale of the experimental test facility of UW or equivalently ⅛ scale of the GA-MHTGR. The TAMU Air-Cooled RCCS experimental test facility was built in the Optical Multiphase Flow Research Laboratory of Nuclear Engineering ("the laboratory") at TAMU, College Station, Texas. The TAMU Air-Cooled RCCS stands at an overall height of 7.20 m (including 1.47 m support base). Primary components encompass blowers, heaters, riser tubes, hot/upper plenums, and exhaust pipes/chimneys. The experimental test facility consists of four risers ①, one hot/upper plenum ②, two symmetric exhaust pipes ③, four air blowers ④ and four air heaters ⑤ (Figure 36) (Sulaiman, Dominguez-Ontiveros, Wang, and Hassan, 2014; Sulaiman et al., 2015).

Figure 36. The TAMU experimental test facility (TAMU Air-Cooled RCCS) (Sulaiman et al., 2014 and 2015).

The air-cooled RCCS design based on the GA-MHTGR relies completely on the natural circulation (i.e. without any active pumps or any other forced flow conditions) to remove the heat from the reactor cavity. The ½ scale NSTF facility at ANL (represents 19.03^{o} slice) and the ¼ scale experimental facility at UW (represents 10^{o} slice) were designed based on the similar concept. Nonetheless, for the TAMU Air-Cooled RCCS, an open once-through forced circulation flow was adopted instead of natural circulation (Sulaiman et al., 2014 and 2015). The key advantage of this forced circulation set-up is its ability to simulate multiple cases that necessitate flexibility of the inlet boundary

conditions of the upper plenum (i.e. velocity and temperature), which can be furnished by the other experimental facilities, i.e. ANL and UW. As such, thorough understanding of flow mixing behavior inside the hot/upper plenum can be gained by investigation under different boundary conditions and scenarios. Another feature of the TAMU Air-Cooled RCCS is that it is located in controlled environment (i.e. inside the building). This implies that the experiment is less influenced by the outside temperature and more importantly, the surrounding temperature is known and constant. The TAMU Air-Cooled RCCS is also complementary to the other two experimental test facilities in the sense that its experiments will augment the findings of the experiments that will be carried by those two experimental test facilities.

V.2.2. Key Design Parameters

Data from the GA-MHTGR and UW ¼ scale experimental facility were utilized to determine the central parameters for the TAMU Air-Cooled RCCS design. The GA-MHTGR full scale design will employ 227 riser tubes. These tubes will be able to maintain an outlet temperature of 152 °C at a power of 1.5MW_t ($\dot{Q}_{acc}$) during an accident scenario, with the corresponding peak accident heat flux of 10 kW/m^2 ($q"_{max}$) (Lisowski et al., 2013; Sulaiman et al., 2014 and 2015).

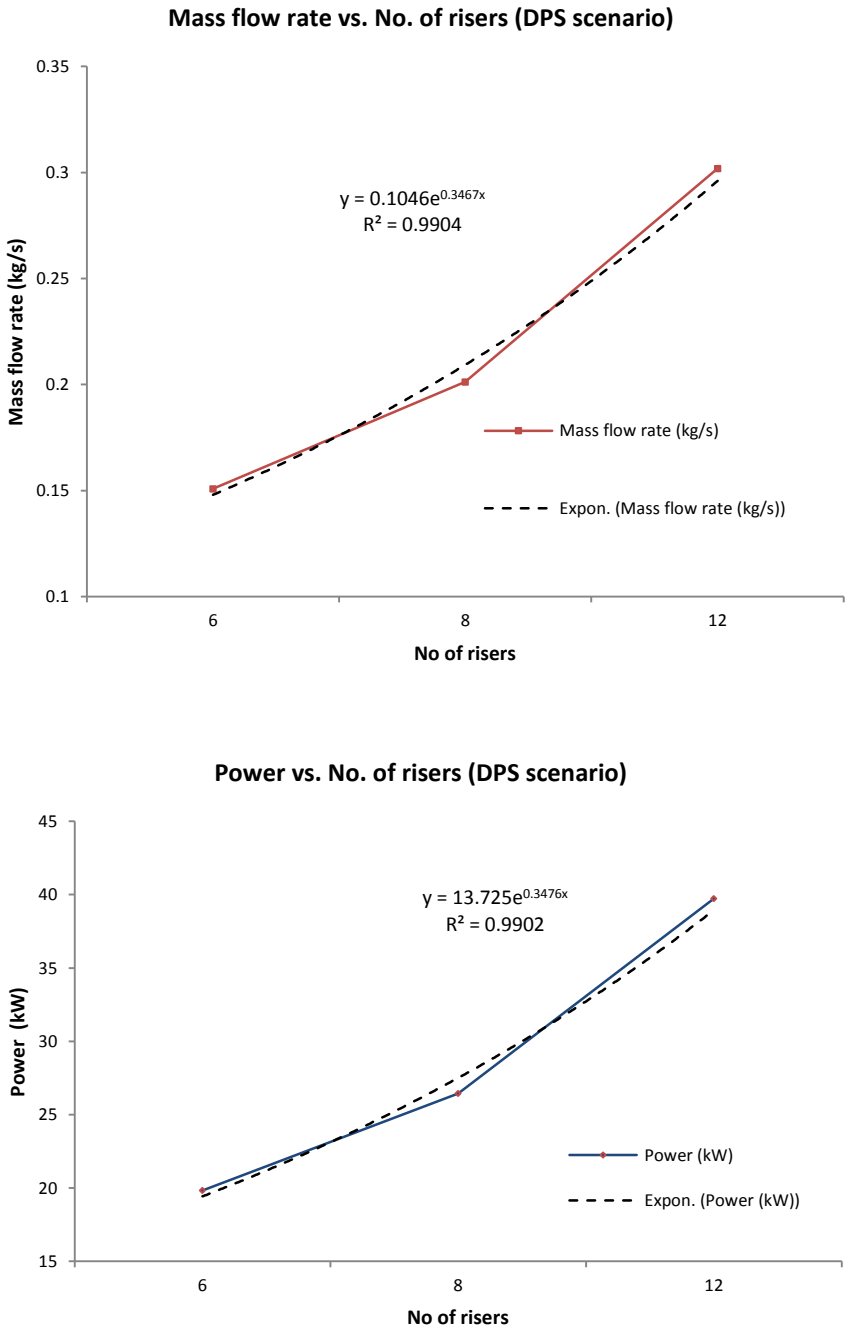

Figure 37. Mass flow rate and power based on UW data (DPS scenario) (Sulaiman et al., 2014 and 2015).

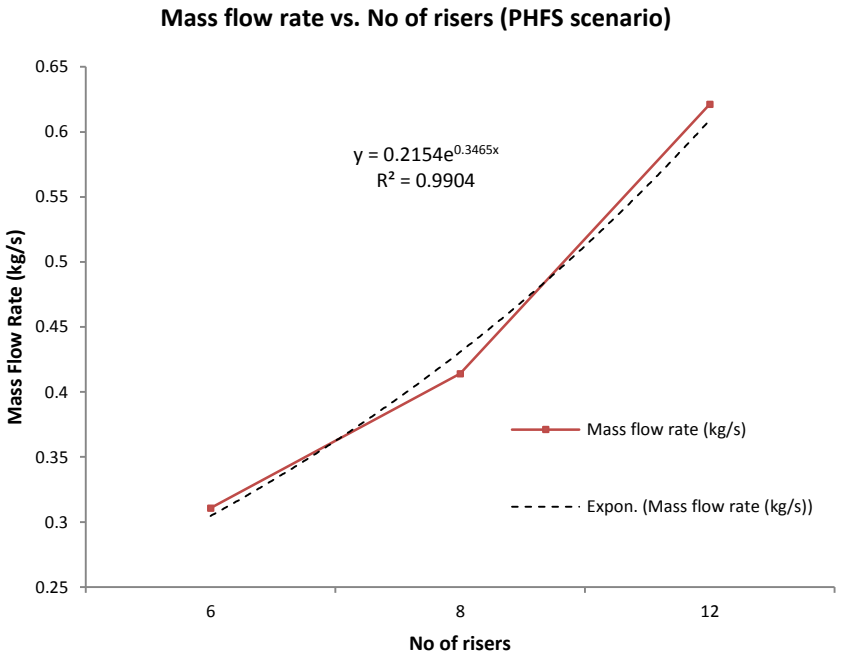

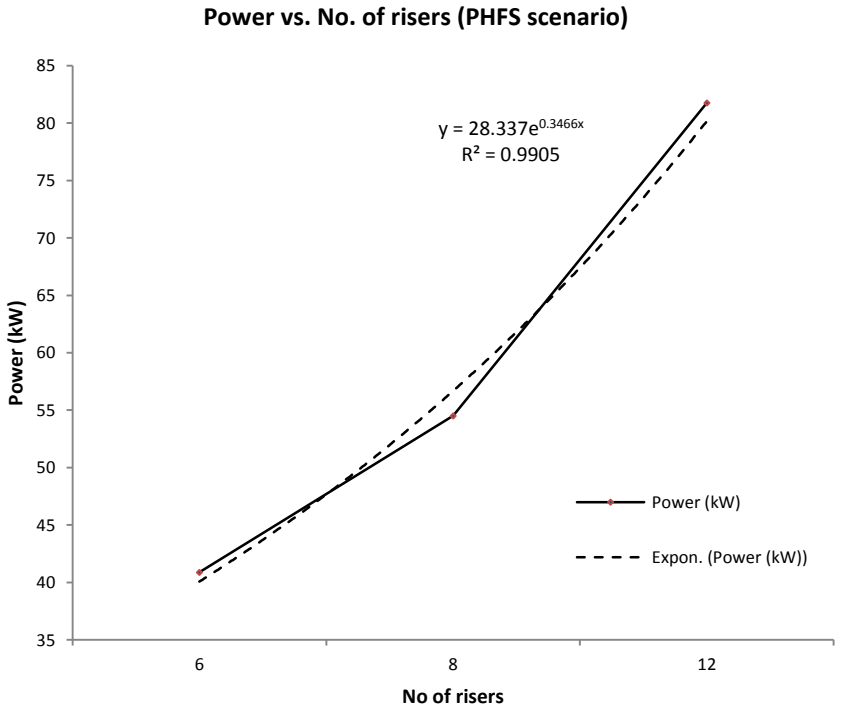

Figure 38. Mass flow rate and power based on UW data (PHFS scenario) (Sulaiman et al., 2014 and 2015).

Table 6. DPS data (assumed $\dot{Q}_{acc} = 1.5MW_t$ for GA-MHTGR (227 riser tubes) (Sulaiman et al., 2014 and 2015).

Data	No of risers	$\dot{m}_{total}$ kg/m^3)	P (kW)	q" (kW/m^2)
Extrapolated	4	0.1255	16.33	9.7
UW	6	0.1509	19.82	9.7
	8	0.2012	26.43	9.7
	12	0.3019	39.7	9.7

Table 7. PHFS data (assumed $q"_{max} = 10kW/m^2$ for GA-MHTGR (227 riser tubes) (Sulaiman et al., 2014 and 2015).

Data	No of risers	$\dot{m}_{total}$ kg/m^3)	P (kW)	q" (kW/m^2)
Extrapolated	4	0.2561	33.70	20.0
UW	6	0.3107	40.87	2 .0
	8	0.4142	54.50	20.0
	12	0.6213	81.7	20.0

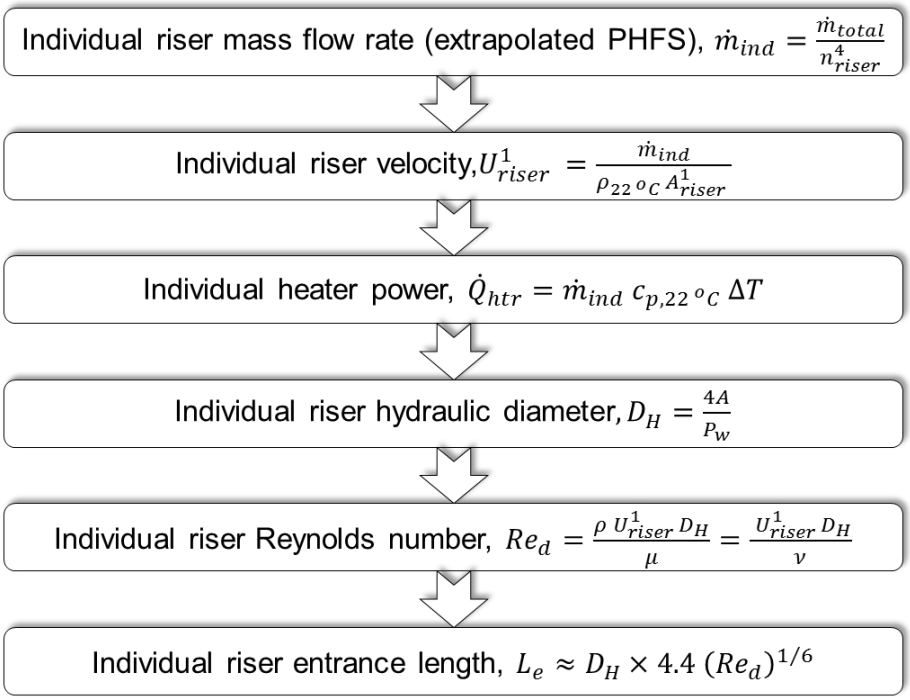

Figure 39. Design flowchart for the key design parameters of the TAMU Air-Cooled RCCS.

Four risers (1" x 5" rectangular cross section - outer dimension) were selected for the TAMU Air-Cooled RCCS in order to maintain flow symmetry based on UW design (six risers design). The separation between each riser (rectangular cross section - outer dimension) was 0.0254 m (1") or 0.03556 m (1.4") for rectangular cross section - inner dimension. The design data from UW ¼ scale experimental facility for 6, 8, and 12 risers were used in order to approximate the necessary mass flow rate and power required for decay power scaling (DPS) and peak heat flux scaling (PHFS) scenarios, respectively. UW DPS data were derived by assuming maximum accident decay power of 1.5 MWt whereas PHFS data were established by assuming peak accident heat flux of 10 kW/m^2.

The UW were plotted and extrapolated to obtain the desired result (Figure 37 and Figure 38) (Sulaiman et al., 2014 and 2015). Exponential trendline was adopted to obtain the desired results since it closely resembles the curve of UW data (Table 6 and Table 7) (Sulaiman et al., 2014).

The mass flow rate of individual riser for DPS and PHFS scenarios were computed in order to determine the heater power requirement. It was found that the mass flow rate of individual riser for PHFS was higher than DPS. As such, the mass flow rate for PHFS was utilized for the computation of each riser velocity and the required heater power. The corresponding hydraulic diameter of each riser was computed to determine the Reynolds number for the individual heater. Based on the computed Reynolds number, the required length of riser for fully developed flow was determined. The whole design process is depicted in Figure 39. The required parameters for the individual riser was produced and used as the chief design values of the TAMU Air-Cooled RCCS (Table 8) (Sulaiman et al., 2014 and 2015). The hot/upper plenum was designed to be transparent to allow direct visual observation of the flow structures and mixing patterns (two transparent glass window on each side and also the top portion). This configuration was adopted for the ease of pertinent flow visualization experiments.

Table 8. Summary of each riser required parameter (Sulaiman et al., 2014).

Parameter	Value
Temperature difference, ΔT	130 ˚C
Cross-sectional area, A_{riser}^{1}	0.003 m^2
Hydraulic diameter, D_H	0.04 m
Velocity, U_{riser}^{1}	17 m/s
Mass flow rate, $\dot{m}_{ind}$	0.06 kg/s
Heater power, $\dot{Q}_{htr}$	8.5 kW
Entrance length, L_e	1.1 m

CHAPTER VI

STAGE 3: VENDOR SELECTION AND EXPERIMENTAL TEST FACILITY FABRICATION, TRANSPORTATION AND CONSTRUCTION [*]

VI.1. Construction Purpose

The scaling, design and construction of a scaled water cooled RCCS served to assist in determination of thermal hydraulic characteristics, behavior, and magnitude of the air flow over a wide range of circumstances during normal, off-normal, and accidents operations placing a greater emphasis on complex turbulence flow mixing inside the hot/upper plenum. The TAMU Air-Cooled RCCS experimental facility is the third facility pertinent to the RCCS investigations that is currently in operation in the United States. The first facility is the Natural Convection Shutdown Heat Removal Test Facilities (NSTF) at Argonne National Laboratory (ANL). The NSTF represents a 19.03^{o} sector slice at a reduced ½ scale (Tzanos et al., 2006). It aims to address complexities associated with the RCCS buoyancy driven systems with multiple parallel flow paths that are challenging to envisage by computational fluid dynamic (CFD) models solely. Experimental verification and validation data for thermal-hydraulic system codes is necessary for flow

[*] Part of the data reported in this chapter is reprinted with permission from "Design considerations and experimental observations for the TAMU air-cooled reactor cavity cooling system for the VHTR" by Sulaiman, S. A., Dominguez-Ontiveros, E. E., Alhashimi, T., Budd, J. L., Matos, M. D., & Hassan, Y. A., 2015. *AIP Conference Proceedings*, 1659, 030002. http://dx.doi.org/10.1063/1.4916850-. Copyright [2015] by AIP Publishing LLC.

instabilities caused by minor perturbations which can deteriorate the performance and effectiveness of the RCCS. The second facility is the ¼ scale University of Wisconsin (UW) RCCS facility which is used to provide experimental assistance to the NSTF. The experimental facility at TAMU is playing a role as a complementary facility to the first two facilities in the sense that it will furnish experimental and CFD-grade database simulation analyses. These analyses are primarily on the anticipated thermal stratification as a result of multiple parallel jet flow paths with varying temperature inside the hot/upper plenum. Natural circulation driven flow might be inhibited by the establishment of stratified layers inside the upper plenum, which in turn could diminish the overall effectiveness of decay heat removal. As such, a number of criteria must be met in order for the TAMU Air-cooled RCCS experimental facility to accomplish its objectives, such as:

1. Prove pertinent and true to the GA-MHTGR prototype concept design;
2. Permission to record chief thermal hydraulics parameters that will produce a comprehensive and overall understanding of the air flow, particularly inside the hot/upper plenum;
3. Robust design that will allow investigations of multiple scenarios at various boundary conditions.

VI.2. Solidworks Drawings

Solidworks computer aided design (CAD) version 2013 software was utilized for the drawings of the experimental facility. The experimental facility drawings for each assembly and its parts illustrating standard views (i.e. top, side, front, and isometric views), detailed dimensions and specifications including precise locations of flow measurement port, which were sent to the steel manufacturer in Houston for fabrication (Appendix A). Made Well was selected as the vendor since the company has provided a competitive price and more importantly, it has a good track record with the laboratory. The fabrication of the experimental test facility was divided into two phases; namely Phase I and Phase II. Phase I comprises components such as the twin exhaust pipes, the upper plenum with glass windows, and the risers with support plates (able 9). Phase II encompasses all the circular pipings from each blower (including its enclosure) to the riser connectors. All the parts were made from carbon steel except for the upper plenum glass windows. Carbon steel was chosen for its strength, durability, and cost effectiveness. The fabrication of the parts took more than four months due to iterations of design details for some critical parts. For the ease of direction standardization and primary components identification, front, rear, right, and left directions were introduced to the experimental facility (Figure 40 to Figure 42).

Table 9. Assemblies and parts for Phase I drawing using Solidworks.

Assembly	Part
A-1: Exhaust pipe (2 units)	A-1 P-1: 90^{o} bend pipe (2 units)
	A-1 P-2: 45^{o} bend pipe (2 units)
	A-1 P-3: 45^{o} bend pipe (2 units)
	A-1 P-4: Horizontal pipe (2 units)
	A-1 P-5: 90^{o} elbow (2 units)
	A-1 P-6: Vertical pipe (2 units)
	A-1 P-7: Exhaust cap (2 units)
A-2: Upper plenum with glass windows	A-2 P-1: Upper plenum (1 unit)
	A-2 P-2: Window flange (front/rear) (1 unit each)
	A-2 P-3: Window flange (top)(1 unit)
	A-2 P-4: Glass window (front/rear) (1 unit each)
	A-2 P-5: Glass window (top) (1 unit)
	A-2 P-6: Thin metal sheet (front/rear) (1 unit each)
	A-2 P-7: Thin metal sheet (top) (1 unit)
A-3: Risers with support plates	A-3 P-1: Riser (4 units)
	A-3 P-2: Risers support plate (2 units)
	A-3 P-3: Riser connector (4 units)

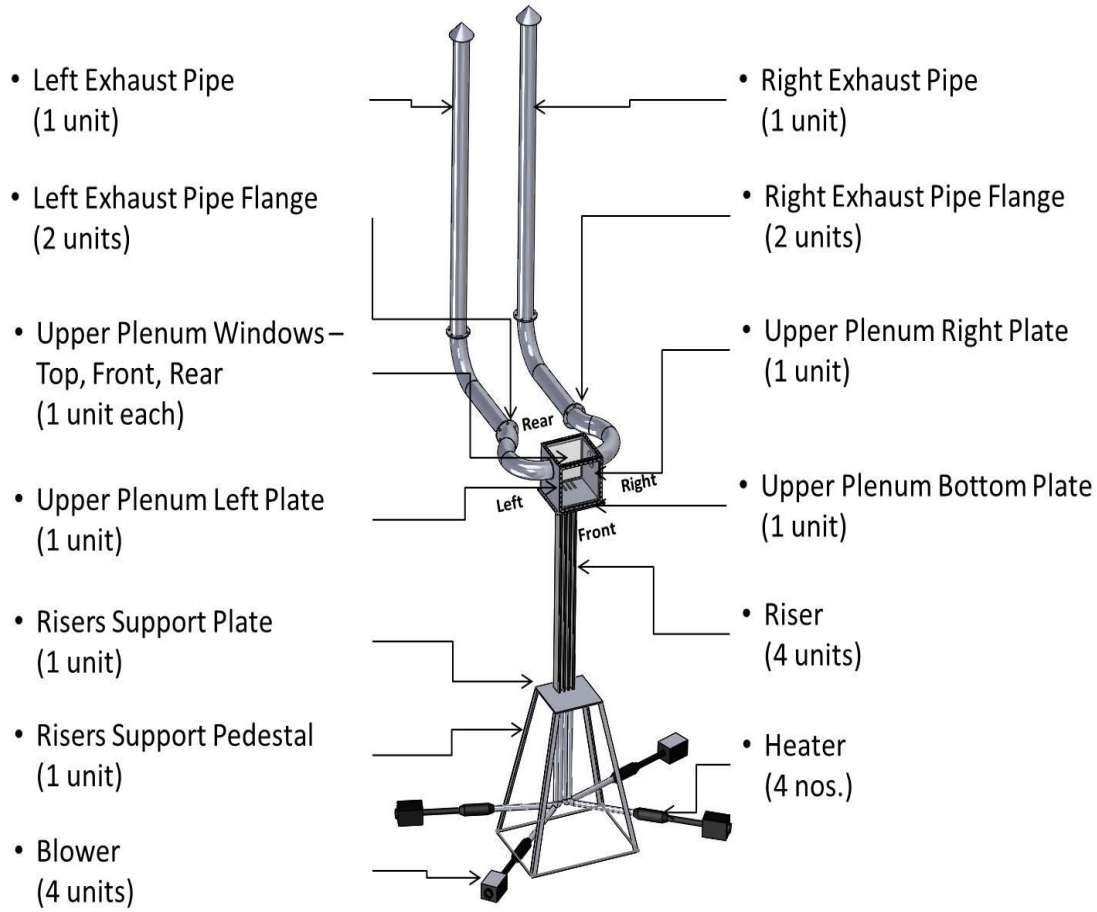

Figure 40. Primary components and direction standardization of the TAMU experimental test facility (TAMU Air-Cooled RCCS).

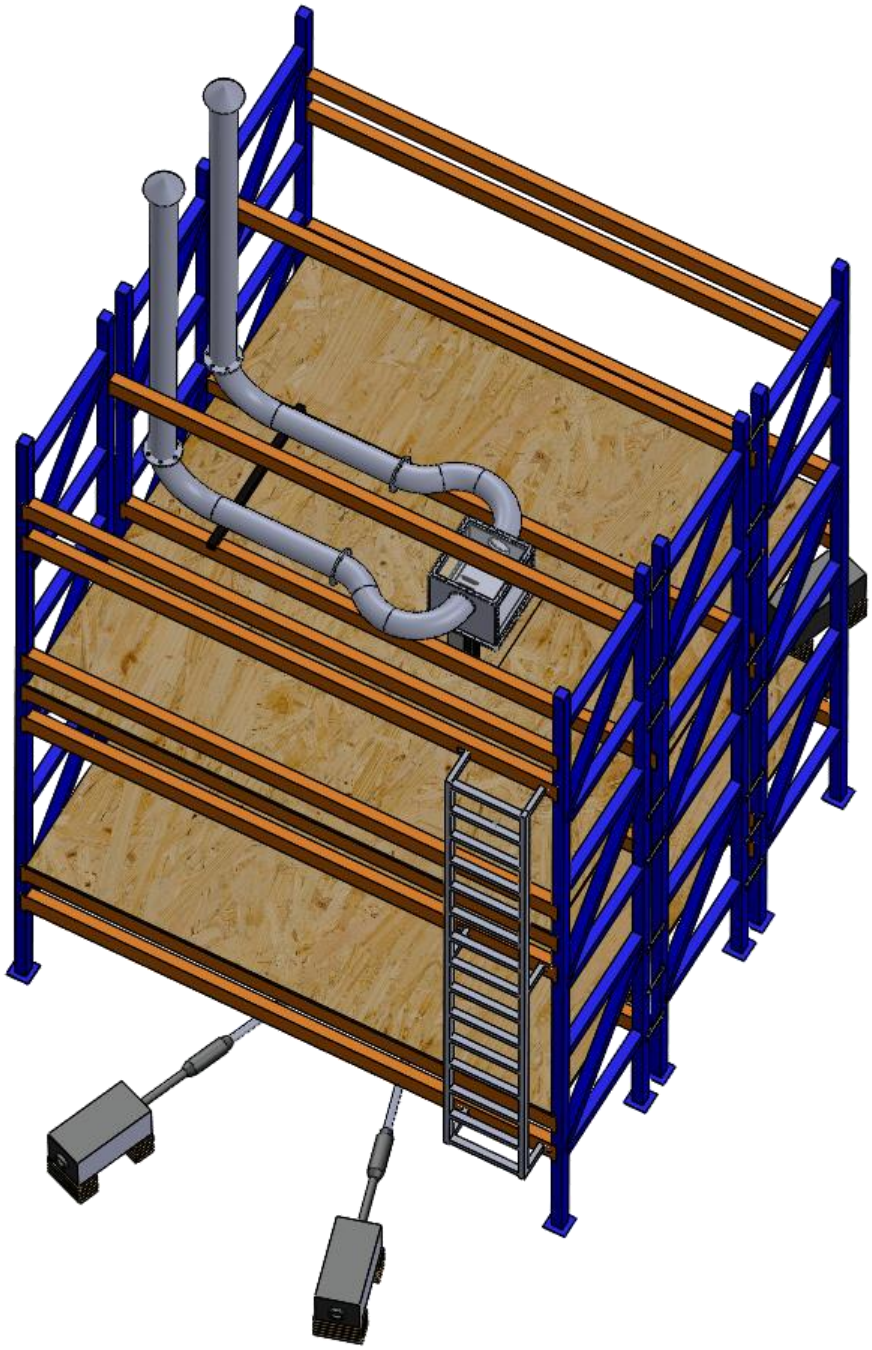

Figure 41. Isometric drawing of the experimental test facility (TAMU Air-Cooled RCCS).

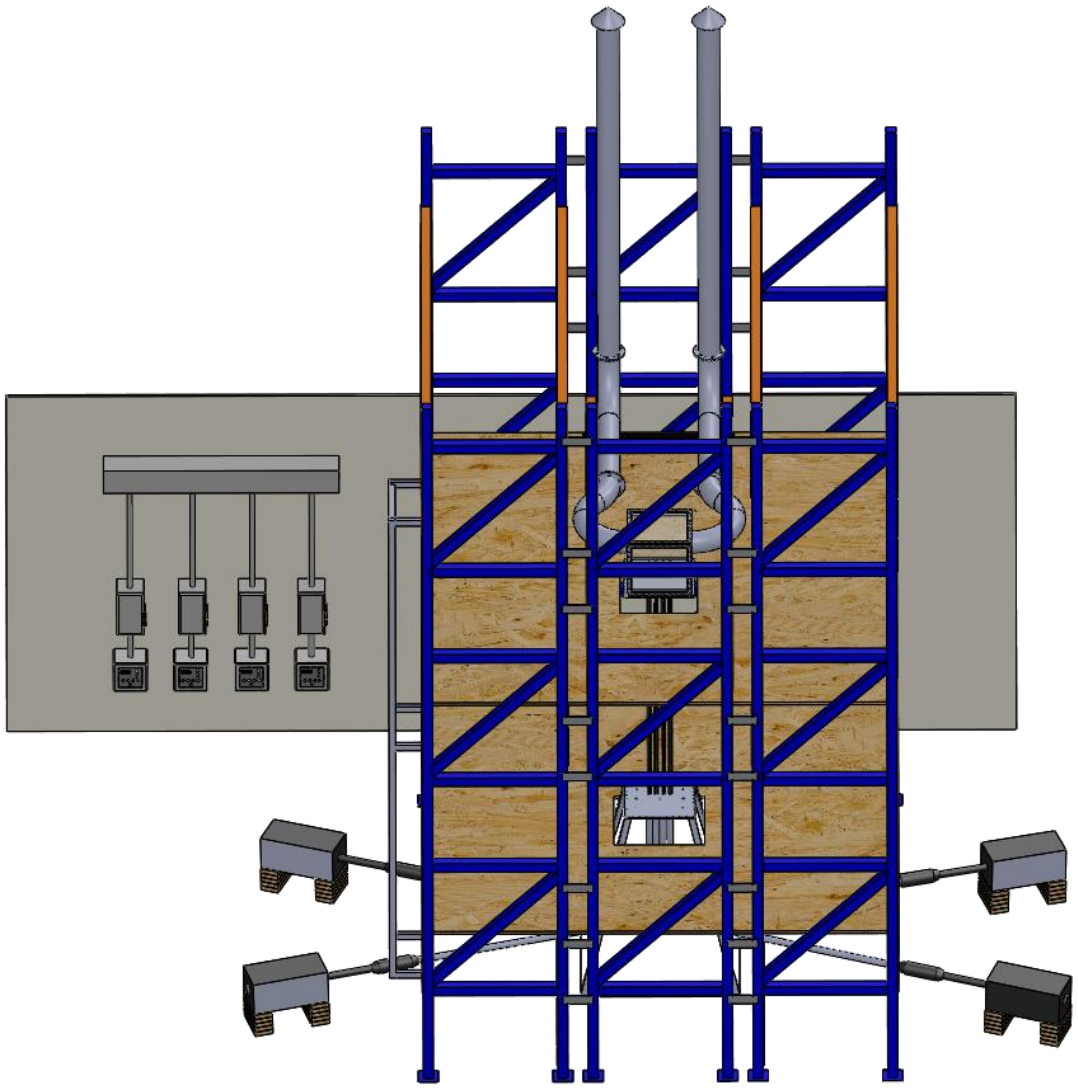

Figure 42. Another view of the experimental test facility showing the breakers and the process heater controllers.

VI.3. Fabrication and Transportation

At the fabrication shop, concerted efforts were made to ensure the finished product would adhere to the specifications. Frequent visits to the fabrication shop and exchange of information through telephone and email were utilized to update the status. Visits at specific time based on the progress of the parts fabrication have resolved many design issues. Some pictures of the parts at the fabrication shop are illustrated Figure 43 to Figure 47.

Figure 43. The twin exhaust pipes at the fabrication shop: (a) The left exhaust pipe, (b) The right exhaust pipe.

Figure 44. The exhaust pipes flanges at the fabrication shop.

Figure 45. Support plates at the fabrication shop: (a) The upper plenum bottom plate and the riser support plate, (b) The upper plenum left and right faces.

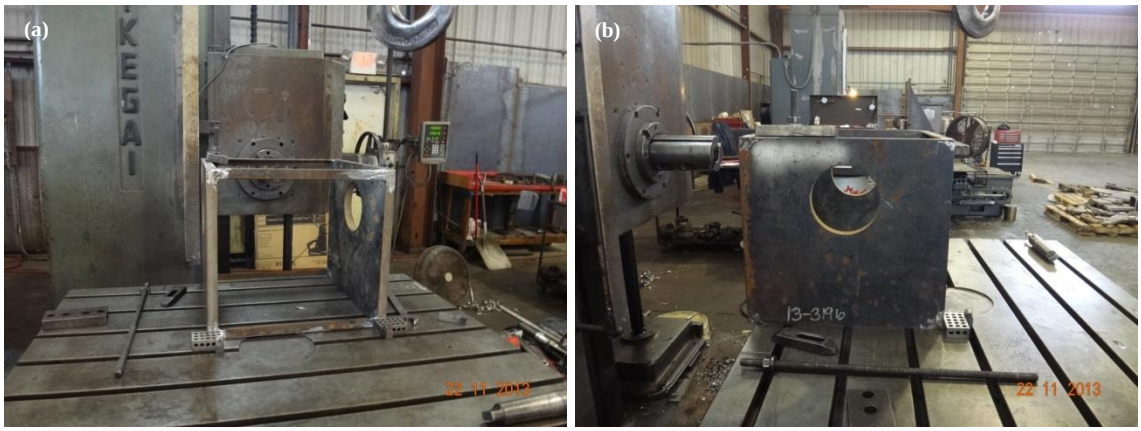

Figure 46. The upper plenum assembly at the fabrication shop: (a) The front view of the upper plenum, (b) The side view of the upper plenum.

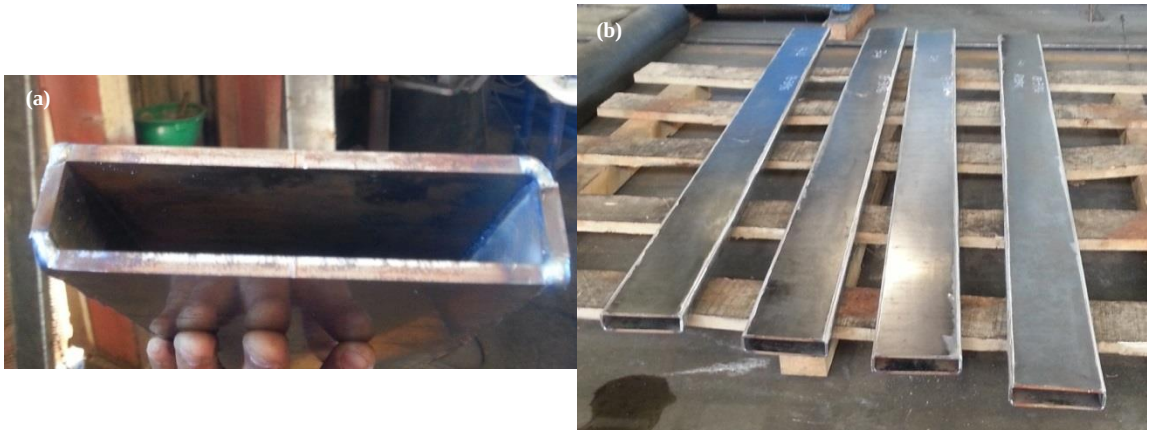

Figure 47. Risers assembly at the fabrication shop: (a) The cross section of one of the risers, (b) All four risers.

Since the TAMU Air-Cooled RCCS section is custom-built with carbon steel, segregation of components is highly necessary for the ease of transportation and installation. As such, in order to facilitate the installation, for Phase I, the primary components were segregated into three segregated assemblies as per Table 9. The first segregated assembly consisted of the hot/upper plenum (including its base support stand), the four risers (including their base plate and square-to-circular fittings) and the curve section of the twin exhaust pipes, i.e. combination of A-2 and A-3 assemblies in Table 9 (Figure 48). All joined parts were welded together in order to prevent any problem resulting from the air leakage. The second and third segregated assemblies comprised the remaining parts of the twin exhausts pipes, i.e. A-1 assembly in Table 9. These parts are connected with the four flanges (Figure 49). All components of Phase I were sand blasted and painted for smooth surfaces prior to delivery to the laboratory. Phase II components were delivered slightly later than Phase I components (Figure 50 and Figure 51) and those components were painted in the laboratory.

Figure 48. First segregated assembly of Phase I at the laboratory.

Figure 49. Second and third segregated assemblies of Phase I at the laboratory.

Figure 50. Phase II at the laboratory.

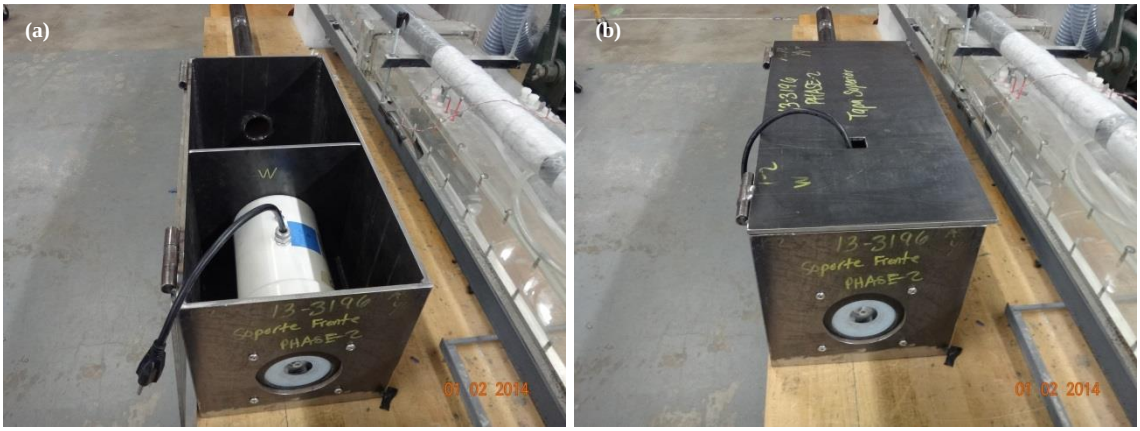

Figure 51. A blower enclosure of Phase II at the laboratory: (a) A blower in its custom-made compartment, (b) A custom-made blower compartment.

VI.4. Construction and Installation

The support structure for Phase I components was constructed using warehouse pallet racks (Figure 52). The pallet racks design was selected due to its robustness, flexibility, easy to assemble, and competitive price. Pallet racks configuration would enable suitable placement of flow visualization and data acquisition equipment in the vicinity of the experimental facility. More importantly, pallet racks arrangement allowed sufficient space for the researchers to maneuver during experiment. Teardrop style pallet racking was chosen for the structure. Six 3B80 teardrop uprights (240" height x 42" width x 2-11/16" thickness) were used as the anchor structures. Those teardrop uprights were connected by teardrop beams (144" length x 5-15/16" width x 1-⅝" thickness). One complete warehouse pallet rack consisted of two teardrop uprights and a number of teardrop beams. For the experimental facility, three complete warehouse pallets rack were utilized (left, center, right). 6" galvanized steel row spacers were placed in between the left, center, and right warehouse pallet racks. The installation of the row spacers was crucial for stability and sturdiness of the structure considering the height of the teardrop uprights. The strength of stability and durability of the structure was augmented by bolting each teardrop uprights to the ground using anchor bolts.

Two floors for the experimental facility; namely 1st floor and 2nd floor, respectively, were constructed by placing the teardrop beams at 5' and 11' elevation from the ground level (Figure 53). The 1st floor was intended for access to the risers and the upper plenum thermocouples installation and maintenance, operation of vertical insertion

thermocouples into the upper plenum, two cubicles for a desktop and a workbench (Figure 54). The 2nd floor was designed to accommodate the needs for the upper plenum related experiments and equipment, horizontal insertion frame operation, primary data acquisition, installation and maintenance of thermocouples, and so on (Figure 55). The space in between the ground floor and the 1st was planned for installation and access to Phase II components.

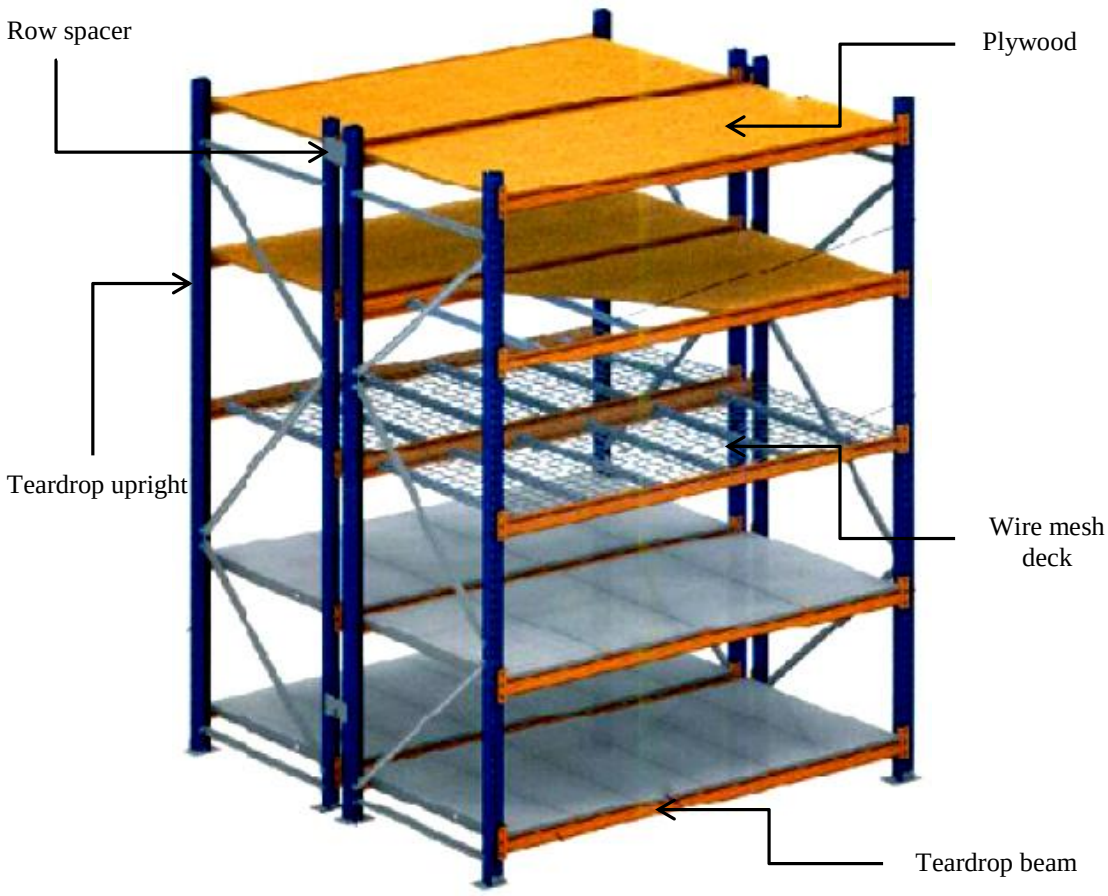

Figure 52. Generic warehouse pallet rack configuration.

Heavy duty wire mesh decks (42” wide and 46” length) were installed in between teardrop beams at both the 1st and 2nd floors, respectively. Smooth finished plywoods (42” wide 144” length x 1/2”) with neoprene rubber meshes (36” wide) were installed on top of each wire mesh deck. Neoprene rubber meshes installation was envisioned to minimize any falling and tripping hazards for personnel, equipment and tools. A slot opening near the middle of the center warehouse pallet rack was intended for the experimental facility installation.

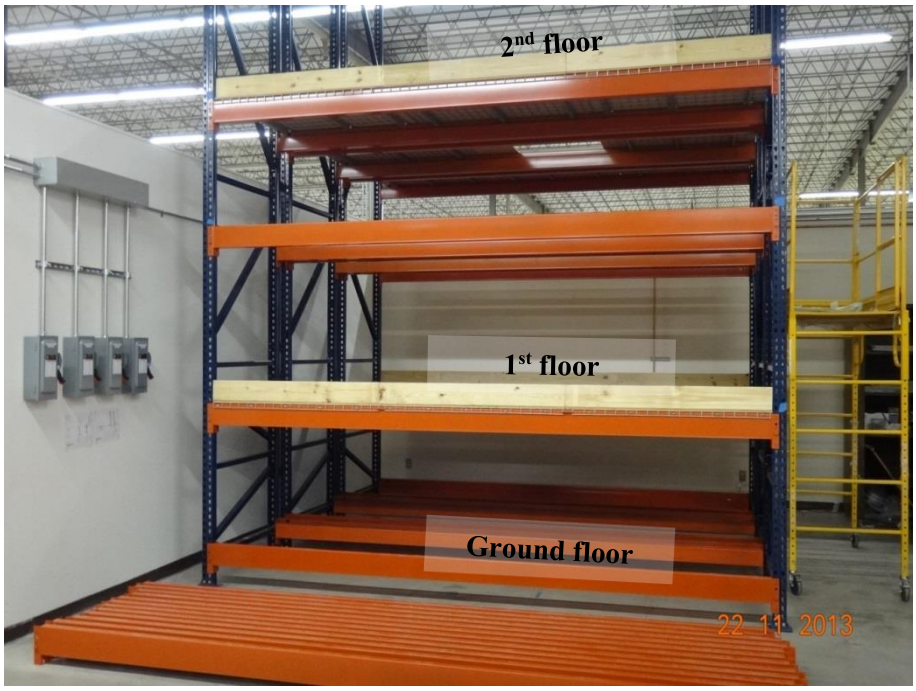

Figure 53. Palette racks structure for the TAMU Air-Cooled RCCS. The structure is divided into three floors; namely ground floor, 1st floor, and 2nd floor.

Figure 54. Views of the 1st floor from different angles.

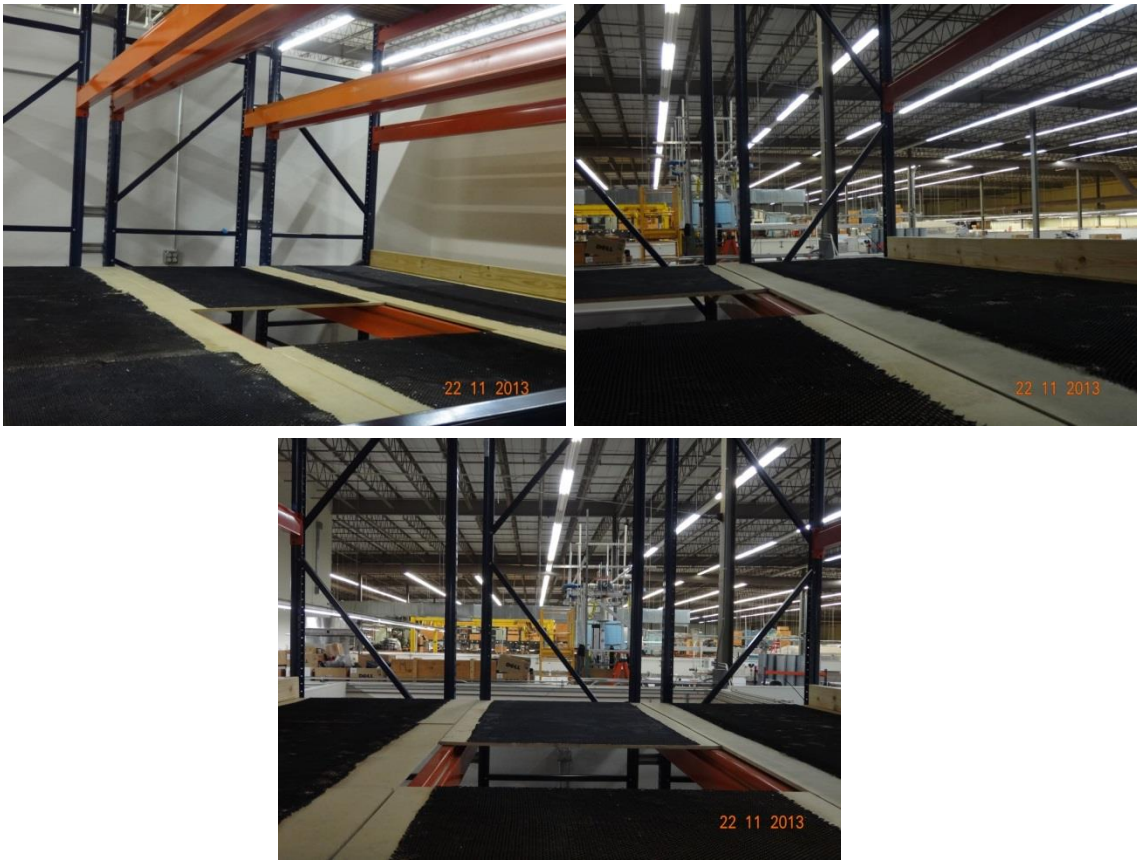

Figure 55. Views of the 2nd floor from different angles.

Lumber beams were placed at the edges of each floor to prevent any falling tools and equipment. Additional teardrop beams were installed at the 1st and 2nd floors as a precautious measure to curb falling and tripping hazards. These teardrop beams also increase rigidity of the structure. A wall-mount, side-step steel dock ladder with 9' 5" maximum climbing height was mounted in between the ground floor and the 2nd floor for safety and easy access.

Installation of the Phase I components was performed using a forklift, a chain and pulley system and a boom. A forklift was used to lift the boom above the 2nd floor. The boom was placed across the left and center pallet racks. A chain and pulley were used to lift the first assembly of Phase I components through the opening in the middle of the center pallet rack. The first assembly was placed on top of the custom-built 1.7 m height of the steel risers support pedestal (Figure 40) prior to connection with the second assembly using flanges. The second assembly of Phase I was rested on the crossbar in between teardrop of the center pallet rack. The third assembly was joined together with the second assembly using flanges connection.

A welded steel bar was put in between the second and third assemblies (each left and right components) to ensure even load distribution of the experimental facility. Pertinent pictures showing the sequence installation of the experimental facility are illustrated in Figure 56. Installation of Phase II components commenced right after the completion of Phase I installation. Two cubicles complete with chairs and tables were also installed at each floor (Figure 57 and Figure 58). Each riser was labeled for easy

identification (Figure 57). The pipings downstream of the in-line heaters up to the upper plenum were insulated to reduce the heat loss (< 1%) to the surrounding.

Figure 56. Sequences of the experimental facility installation.

Figure 57. The completed 1st floor of the experimental facility.

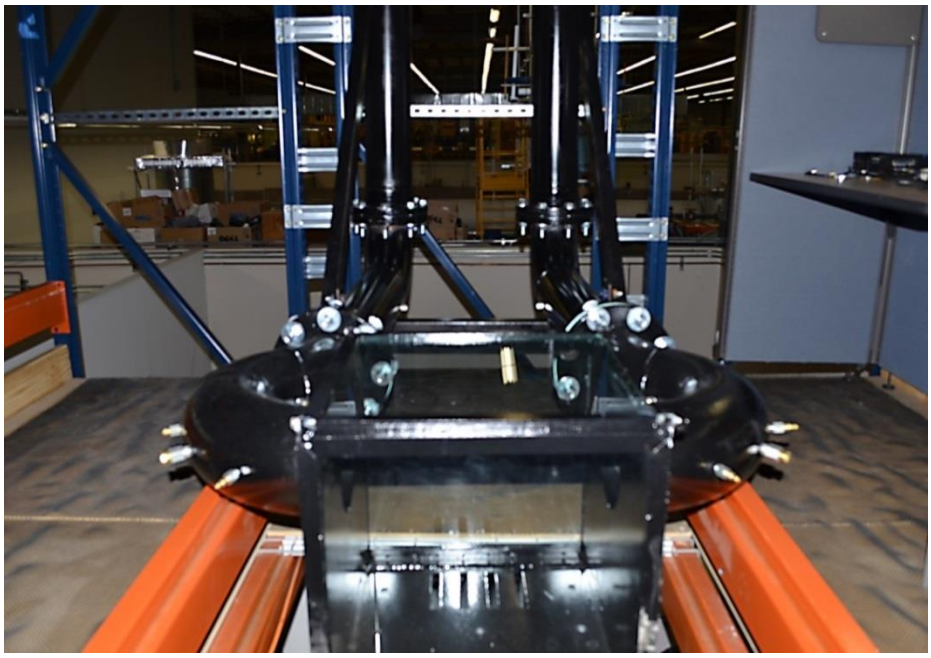

Figure 58. The completed 2nd floor of the experimental facility.

CHAPTER VII

STAGE 4: INSTRUMENT SELECTION, PROCUREMENT, CALIBRATION AND INSTALLATION [*]

VII.1. CFD Simulations

VII.1.1. Introduction to CFD

CFD is the science of illustrating fluid flows by generating numerical solutions to a system of partial differential equations (PDEs) (Johannessen, 2012). Discrete methods are used to have insightful understanding on physical phenomena present in different kinds of flows both qualitatively and quantitatively. Looking at the history, the aircraft industry was the first to use CFD. Capitalizing the experience of the aircraft industry plus realization of huge economic advantage of being able to describe fluid flows, the automotive and petroleum industries have also taken steps to venture into CFD applications.

CFD software codes are an advanced mathematical method of computing velocity, density, pressure and temperature flow fields and distributions in three dimensional space

[*] Part of the data reported in this chapter is reprinted with permission from "Design considerations and experimental observations for the TAMU air-cooled reactor cavity cooling system for the VHTR" by Sulaiman, S. A., Dominguez-Ontiveros, E. E., Alhashimi, T., Budd, J. L., Matos, M. D., & Hassan, Y. A., 2015. *AIP Conference Proceedings*, 1659, 030002. http://dx.doi.org/10.1063/1.4916850-. Copyright [2015] by AIP Publishing LLC.

problems. They are built on fundamental laws of fluid mechanics and thermodynamics based on the conservation of physical quantities such as mass, momentum, and energy. CFD also draws on the application of computer science, mathematics (classical and numerical analysis), and geometric modeling and meshing in the quest to perform a good CFD calculation and obtain reasonable results.

VII.1.2. CFD Process

One of the incentives for using CFD is the fact that extensive investigations of fluid flows by experiments are costly and time consuming. Another motivation includes the fact that CFD permits the investigation of minute scales and time development (in slow motion) of phenomena that otherwise would not be visible. To achieve these ends, computers are necessary to solve the PDEs since the equations governing fluid flows of practical importance are very complicated. More importantly, only a few and simple cases of fluid flow problems have analytical solutions, whereas for most of them, numerical solutions are needed to describe the fluid flows. In computational techniques the governing PDE's are substituted with systems of algebraic equations solvable by a computer. The process of getting practical and useful information on the problems associating with fluid motion is described in Table 10. Johannessen (2012) suggested the generic procedure for solving a fluid flow problem using CFD (Figure 59).

The continuity, momentum, and energy equations can be obtained in various forms. The boundary conditions determined the flow fields. These situations dictate the

particular solution to be found from the governing equation. Two stages require appropriate definition for numerical solution; namely the discretization and the equation solver (Figure 60). In the first stage, the continuous PDEs complete with their boundary conditions and initial conditions are transformed into a discrete system of algebraic equations. The initial point for the discretization is the governing PDEs equations. Integral or differential form of the equations can be applied.

Table 10. The process of getting practical, useful information on problems associating with fluid motion (Johannessen, 2012).

Conservation of mass	⇒	Continuity equation
Newton's second law	⇒	Euler/Navier-Stokes equations
Conservation of energy	⇒	Energy equation

Solve the above equations plus boundary conditions) using CFD

Velocity distribution	:	$u(x,y,z,t)$, $v(x,y,z,t)$, $w(x,y,z,t)$
Density distribution	:	$\rho(x,y,z,t)$
Pressure distribution	:	$P(x,y,z,t)$
Temperature distribution	:	$T(x,y,z,t)$

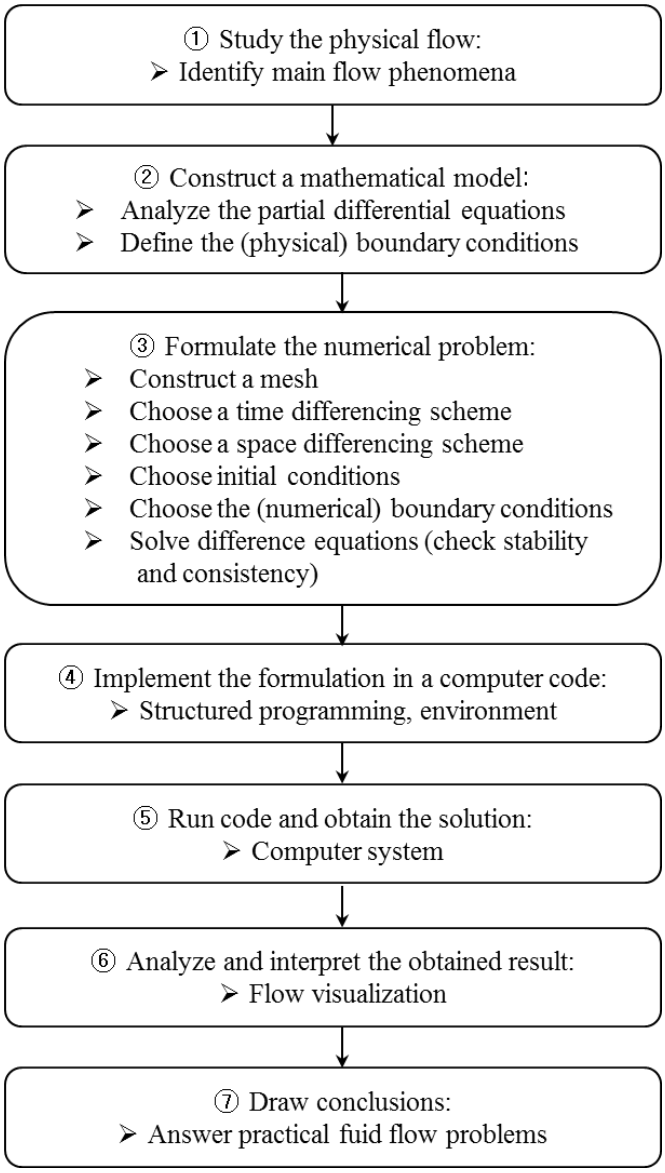

Figure 59. The generic work flow of solving fluid flow problems using CFD (Johannessen, 2012).

Most of CFD software codes encompass a pre-processor, equation solver and post-processor. The pre-processor is responsible to define the building geometry, fluid and solid region grids, boundary conditions, computational solvers as well as the selection of fluid

and solid material properties. The equation solver utilizes the pre-processed inputs and performs the selected computational models to simulate the fluid flow problems and produce a numerical representation of the required physical parameters.

An equation solver is required in order to obtain the solution of discrete system of algebraic equations. The following form is normally being used:

$$a_{11}x_1 + a_{12}x_2 + a_{13}x_3 + \cdots + a_{1i}x_i = b_1$$
$$a_{21}x_1 + a_{22}x_2 + a_{23}x_3 + \cdots + a_{2i}x_i = b_2$$
$$a_{31}x_1 + a_{32}x_2 + a_{33}x_3 + \cdots + a_{3i}x_i = b_3$$
$$\vdots$$
$$a_{i1}x_1 + a_{i2}x_2 + a_{i3}x_3 + \cdots + a_{ii}x_i = b_i$$

In a brief notation:

$$\mathbf{Ax} = \mathbf{b}$$

where A is a $i \times i$ -matrix of known coefficients, **x** is the column vector containing the unknowns and b is a column vector of known quantities.

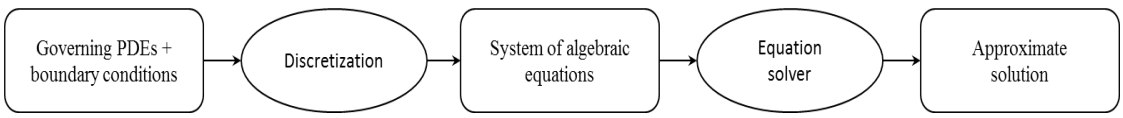

Figure 60. CFD stages (Johannessen, 2012).

Direct solvers and iterative solvers are two kinds of equation solver that is available for use. The solution of the linear system can be obtained precisely in a finite time whereas the accurate solution cannot. As the number of iterations rises, the solution of the iterative solver is approaching to the exact solution. The numerical solution must exhibit several key properties in order to succeed in solving the equations. Five essential properties are consistency, stability, convergence, conservation, and accuracy. Details of these properties can be found in Johannessen (2012). In addition, any CFD simulation accuracy is relying on elements such as grid resolution and grid quality, initial and boundary conditions, temporal discretization and to a certain extent the selection of true physics processes represented via the selection of solvers.

The post-processor utilizes the data produced from the equation solver and presents the obtained solution in the form identified by the user. Measurements of thermal hydraulic properties, i.e. velocity, density, pressure, and temperature can be taken at discrete points or displayed on a scalar or vector field over the entire geometry or selected plane of interest.

CFD can zoom into specific flow field phenomena, i.e. thermal, momentum or chemical properties at any point within the grid geometry. The grids with finer resolution will display the flow field phenomena much better than coarser grids.

VII.1.3. STAR-CCM+

STAR-CCM+, developed by CD-Adapco since 2004, is a powerful commercial CFD software code with an intention to introduce easy to use, all-in-one software package tool that is not only reserved for the CFD experts but also for novice users. Apart from being a CFD solver, STAR-CCM+ consists is a whole engineering process for solving problems involving flow, heat transfer and stress. STAR-CCM+ has developed a suite of integrated components, CAD creation to post processing to CAE, all in a single, easy-to-use environment which produce a powerful package that can address a wide variety of modeling needs. These components include:

- 3D-CAD modeler
- CAD embedding
- Surface preparation tools
- Automatic meshing technology
- Physics modeling
- Turbulence modeling
- Post-processing
- CAE Integration

STAR-CCM+ implements a stringent workflow when numerically solving a CFD problem (Figure 61). The STAR-CCM+ program is based on a finite volume method, a method for representing and evaluating partial differential equations in the form of algebraic equations. This implies that by using the divergence theorem, volume integrals

in a partial differential equation (that contain a divergence term) are transformed to surface integrals. Together with suitable initial and boundary conditions, and also by means of a number of discrete approximations, an algebraic equation system solvable on a computer is obtained. In the following section, a simple description of the solution method, workflow and physics in STAR-CCM+ will be furnished.

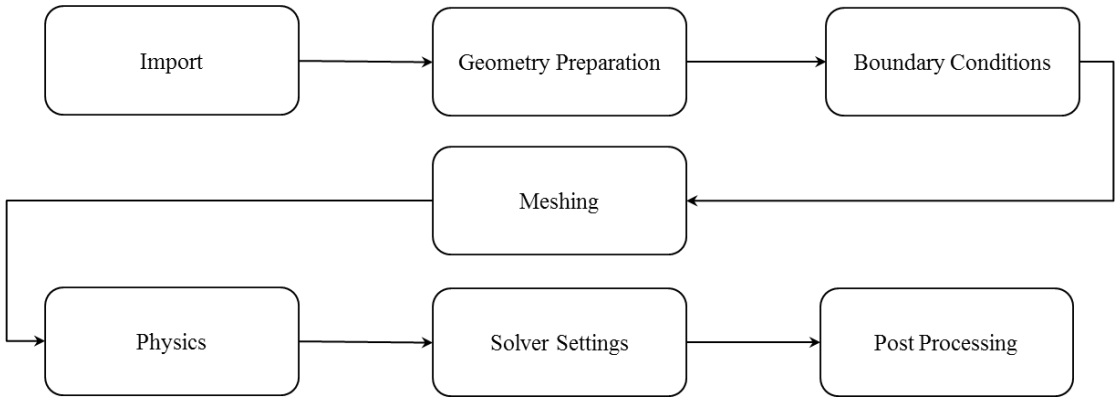

Figure 61. STAR-CCM+ workflow (CD-Adapco, 2014).

VII.1.4. STAR-CCM+ Methods and Model

This section is to furnish the reader with some insights in simple methods and physical models behind CFD simulation using STAR-CCM+ version 8.06.005. The purpose was for the author to become a proficient user of these programs to run only the necessary simulations; it was not necessary to become experienced and skilled in all aspects of the code. Basic steps as indicated by Figure 61 are followed when performing CFD simulations and these are summarized in the following paragraphs.

VII.1.4.1. CFD Model and Boundary Conditions

The computational fluid domains were generated using the commercial CAD software, SolidWorks version 2013. Production of a CAD drawing encompasses fluid domain not only eases the surface and volumetric meshes generation in STAR-CMM+ but more importantly saves computing time as well.

The SolidWorks CAD file was then exported into STAR-CCM+ (using .iges format). The computational fluid domains comprised three major parts, namely four risers, upper/hot plenum, and twin exhaust chimneys (Figure 62). The hot air moves from the upstream in-line heaters (not modeled in here) into the four risers, then enters the upper/hot plenum via multiple parallel jet flows, mixes inside the upper/hot plenum and finally exits through the twin exhaust pipes.

A part is the geometric definition in physical space. It can be a geometry part or derived part. The imported CAD surfaces were split into several parts, especially to those surfaces where individual boundary conditions need to be assigned. Inlet of each risers (for inlet velocity boundary condition), outlet of each exhaust pipe (for outlet pressure boundary condition), each riser outer walls (for near wall boundary condition), and each face of the hot/upper plenum (for near wall boundary condition) were assigned to be dedicated parts using split by patch command.

A region is a volume in 3D space (surface in 2D). STAR-CCM+ differentiates geometry parts from simulation relevant regions. Simulation relevant parts need to be transferred into the regions folder. After defining all the geometry parts, all of the parts

were assigned to regions (one region per part and one boundary per part surface). Assigning parts to regions produced a relationship between the meshed part and the physics region. This action permitted STAR-CCM+ to transform the volume mesh to a finite volume representation that the solver could use to obtain a solution.

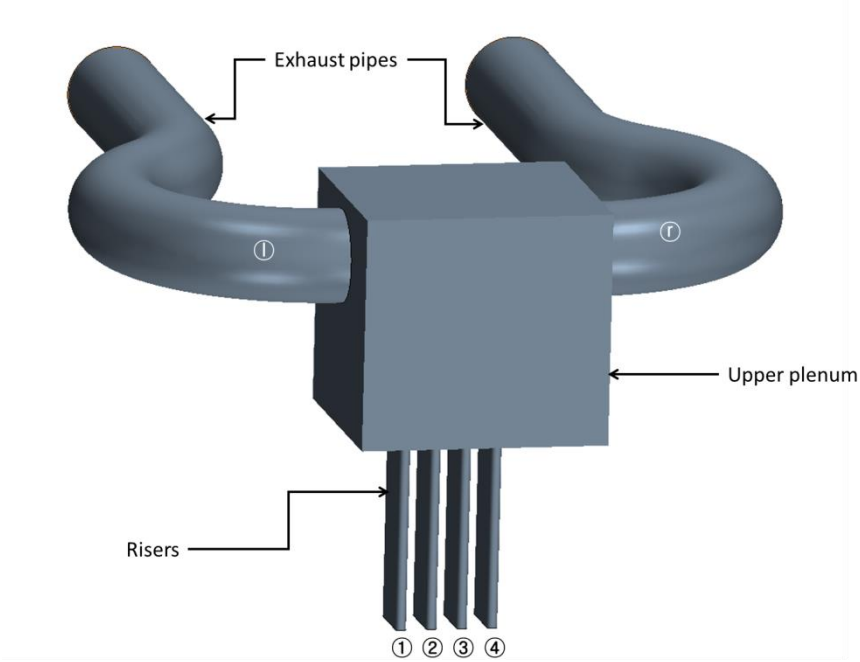

Figure 62. Computational fluid domain scene in STAR-CCM+ simulations (Sulaiman et al., 2014 and 2015; Wang and Sulaiman, 2014)**.**

Next, for each region, types of boundary conditions were specified since they affect the meshing (Table 11).

Table 11. Boundary conditions for the TAMU Air-Cooled RCCS.

Item	Boundary	Type
Riser (x4)	Inlet Face	Velocity Inlet
	Outer Wall Faces	Wall
Hot/Upper Plenum (x1)	All Faces	Wall
Exhaust (x2)	Outer Wall Faces	Wall
	Outlet Face	Velocity Inlet

VII.1.4.2. Fluid Domain Meshing and Discretization

A mesh is the discretized representation of the computational domain, which the physics solvers use to provide a numerical solution (CD-Adapco, 2013). STAR-CCM+ furnishes meshers and tools that are capable to produce a quality mesh for numerous geometries and applications. CD-Adapco Meshing recommended specific workflow for ensuring successful meshing generation in STAR-CCM+ (Figure 63).

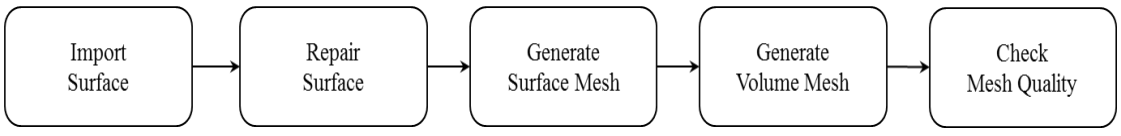

Figure 63. Meshing workflow in STAR-CCM+.

The first step of meshing in STAR-CCM+ is importing surface from third party software (e.g. SolidWorks). Direct CAD format import requires additional license. The second step is surface preparation for meshing. Since the imported CAD surface has too many details, presence of surface errors such as volume is not closed, surfaces overlay each other, surfaces intersect each other, volume is not manifold, etc. are likely (Figure 64). Ensuring closed surfaces is necessary in order to get good surface meshes. Manual repair or surface wrapper (automatic repair) is available for repairing the surfaces. Problems associated with free edges, non-manifolds, intersecting surfaces, imprint surfaces and edges onto target surfaces/bodies, and others can be repaired manually. The surface wrapper should be utilized when manual repair would be time consuming but care must be exercised when adopting this function since the probability of losing details in the original geometry of the imported CAD, e.g. .g. specification of a large cell size in the grill of a car, can result in closing of the grill openings, resulting in no flow to the engine compartment, is likely.

The surface wrapper is a powerful procedure used for obtaining a closed connected surface, starting from a poor quality or too complex CAD surface. The surface wrapper will provide a closed, manifold, non-intersecting surface. Some of the problems that are commonly fixable by surface wrapping include multiple intersecting parts, surface mismatches, double surfaces, overly complex details, and so forth. The surface wrapper is the top choice if the free edges, non-manifold edges and vertices together amount to a large number of errors.

The third step is surface mesh generation. The surface remesher is utilized to re-triangulate the imported CAD surfaces in order to improve the total quality of the surface and optimize the surfaces for the volume mesh models. The surface remesher is used prior to volume meshing. Part based meshes (PBM) was used in this work for several reasons, amongst others are: (1) the PBM improved ease of use (CAD aware meshing processes and simplified simulation tree via reduced entity count), (2) allow better control (flexible and extended mesh capabilities with simple set-up and surfaces and boundaries can be organized individually following different meshing and physics requirements), and (3) permit full automation and reduced turnaround time (replay sophisticated sequences of operations and re-mesh only parts that are modified or replaced).

Tetrahedral mesher uses a Delaunay based method to construct the mesh, which iteratively inserts points into the domain. The initial quality of the surface must be good in order to ensure a good quality volume mesh. Polyhedral mesher adopts dualization scheme based on an underlying tetrahedral mesh which is automatically created as part of the process. Typically, 14 cell faces are generated from polyhedral cells. Trimmed mesher uses a template mesh constructed from hexahedral cells from which it cuts or trims the core mesh based on the starting surface (Table 12). Prism layer mesher is comprised orthogonal prismatic cells grown next to the wall boundaries in the volume mesh. These cells are needed to accurately simulate the turbulence and heat transfer close to the walls. The thickness, number of layers and distribution of the prism layer mesh is dictated primarily by the adopted turbulence model. The prism layer mesher properties are

specified by the author. Prism layers are by default only generated at boundaries of type wall. Prism layer mesher is essential to turbulent flows.

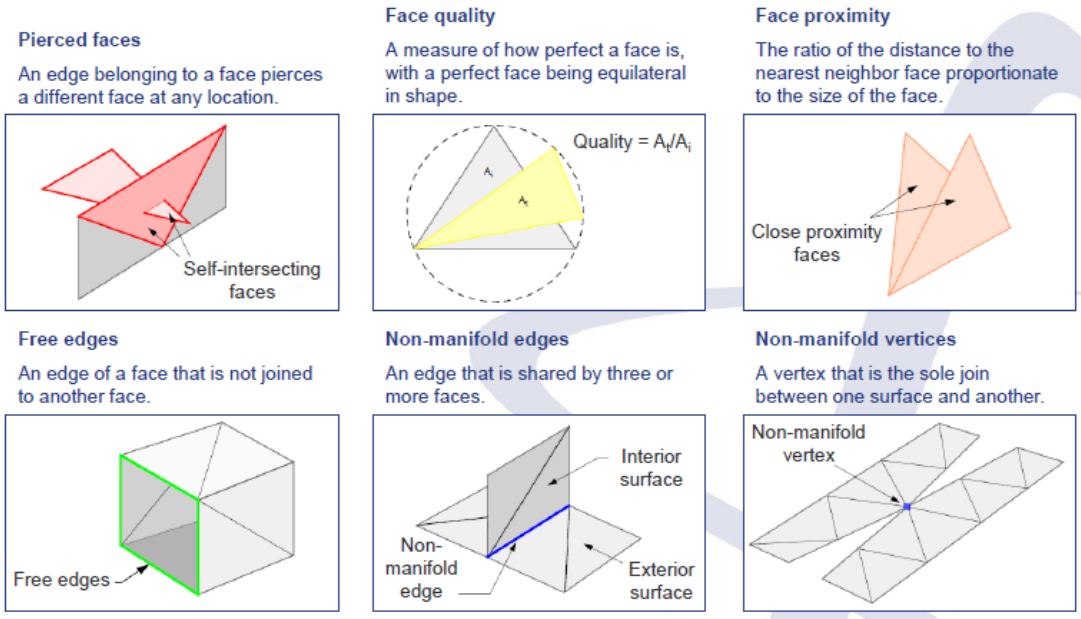

Figure 64. Repair surface diagnostics in STAR-CCM+ (CD-Adapco, 2014).

Table 12. Mesher characteristics.

Mesher	Characteristic
Tetrahedral 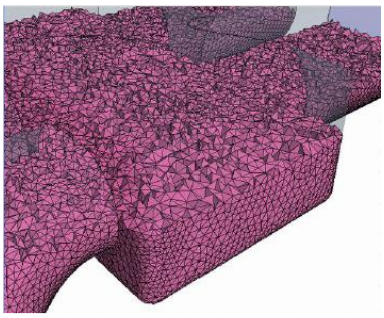	▪ Very dissipative ▪ Slow convergence
Polyhedral 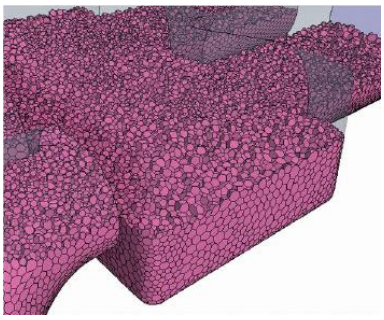	▪ General purpose, reliant, robust ▪ More accurate than tetrahedral meshes ▪ Faster convergence than tetrahedral meshes ▪ Give a conformal mesh at the interface between separate regions (capable of multi-region conformal meshing) ▪ Suitable for conjugate heat transfer simulations
Trimmed Cell 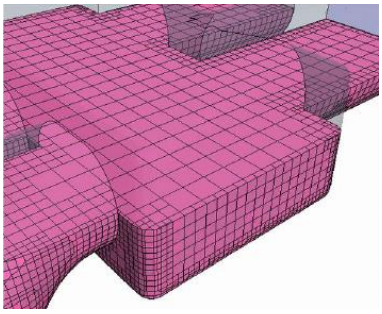	▪ Fast and high quality ▪ Perfect for large domains ▪ Require less memory to generate than polyhedral meshes ▪ Do not give conformal mesh at the interface between separate regions ▪ To be used for cases that have large Cartesian aligned flow directions

Surface remesher, polyhedral mesher, and prism layer mesher were the selected meshing models for the simulations. Automated mesh operation enabled STAR-CCM+ to automatically generate surface meshes, followed by volume meshes with prism layers on the walls.

An object can be meshed in multiple ways. The first method, most probably the simplest approach is a base mesh interval size can be assigned for a volume, which generates an even mesh throughout the whole volume. The second method is to specify specific locations, i.e. finer mesh near walls and coarser mesh in the center of volumes in order to have higher capability to analyze the fluid flow phenomena happening near walls (while not having too many points) but still be able to solve the flow fields with limited computing power. Both of these methods were utilized at times for different CFD computations discussed in this section. The mesh base size, a characteristic size used in mesh generation of which all other values can be set relative to this size, was set to 3.0 mm. At the riser outlets and the upper plenum, smaller mesh was necessary to resolve the flow. As such, the mesh was set those locations were set at 30% and 50% of the base mesh size. The total generated volumetric cells were 65.37 million (Figure 65 and Figure 66).

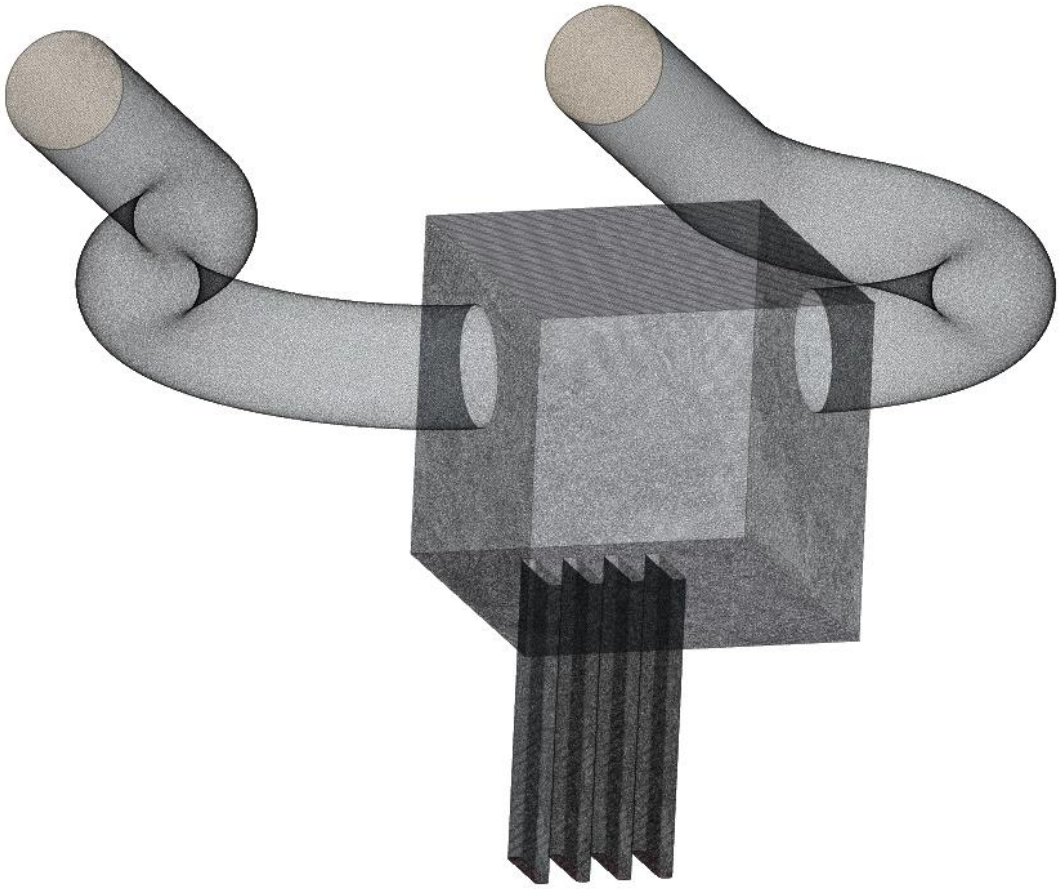

Figure 65. Generated volume meshes scene in STAR-CCM+ simulations.

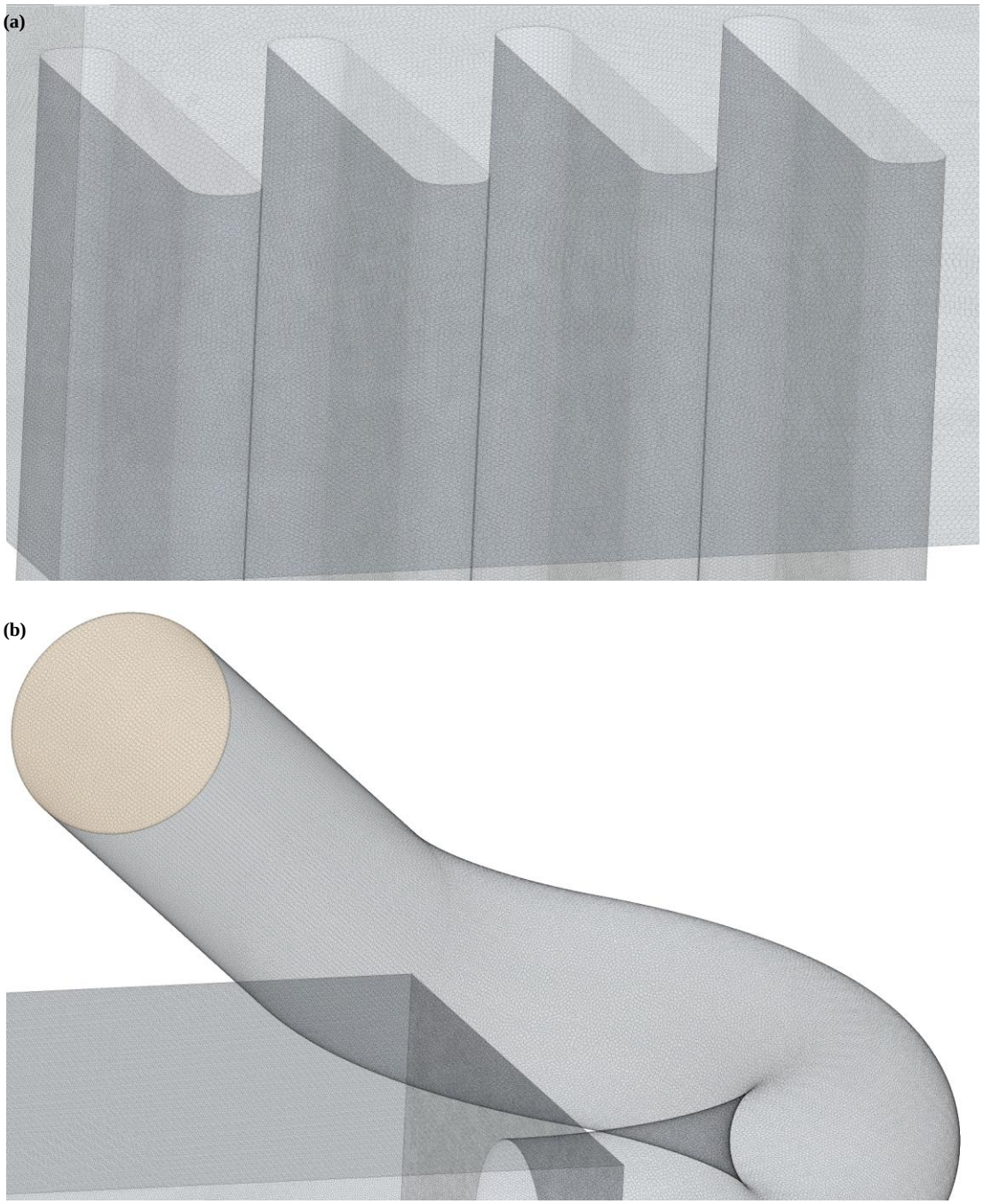

Figure 66. Generated polyhedral meshes scene in STAR-CCM+ simulations: (a) Near the four risers, (b) Near the right exhaust pipe.

The last step is to check mesh quality metrics. Poor quality cells can be visualized and removed from the meshes. As such, the quality of the created mesh was checked using the full mesh diagnostic report. For all meshes created for this work, regardless of the interval size, it was important to ensure that minimum face validity is unity as well as no elements were highly skewed. Therefore, it was decided that for this dissertation, every element should have a maximum skewness angle < 85 degrees. This is essential since the presence of highly skewed elements within a mesh has proven to produce a challenging simulation, and perhaps an inability to converge on a solution all together. Cell Quality Remediation model can be used to enhance convergence.

VII.1.4.3. Physics of the Model

STAR-CCM+ has a wide range of computational solvers for the simulation set-up in order to replicate the physical behavior of the experiments. Depending on what kinds of simulations are required and the level of which real world physics are to be modeled, the user has many choices to activate. The physics modeling realism level often has to be traded against the added computational expense. Below are various physics models that are available in STAR-CCM+ (CD-Adapco, 2013):

- Space, time, and motion
- Materials

- Flow and energy
- Species
- Turbulence and transition
- Radiation
- Aeroacoustics
- Combustion
- Multiphase flow
- Dynamic fluid body interaction
- Harmonic balance
- Solid stress
- Electromagnetism
- Electrochemistry
- Casting

The following physics models were adopted for the preliminary simulations (Figure 67). A brief explanation has been incorporated with each solver indicating which models it has been used.

- Three dimensional

  There are four Space models available in STAR-CCM+: (1) Axisymmetric Model, (2) Shell Three-Dimensional model, (3) Two-Dimensional Model, and (4) Three-

Dimensional Model. The Three-Dimensional solver is designed to work on three-dimensional meshes which imply that the fluid geometry is three-dimensions and picks the three dimensional form of all subsequent solver selections.

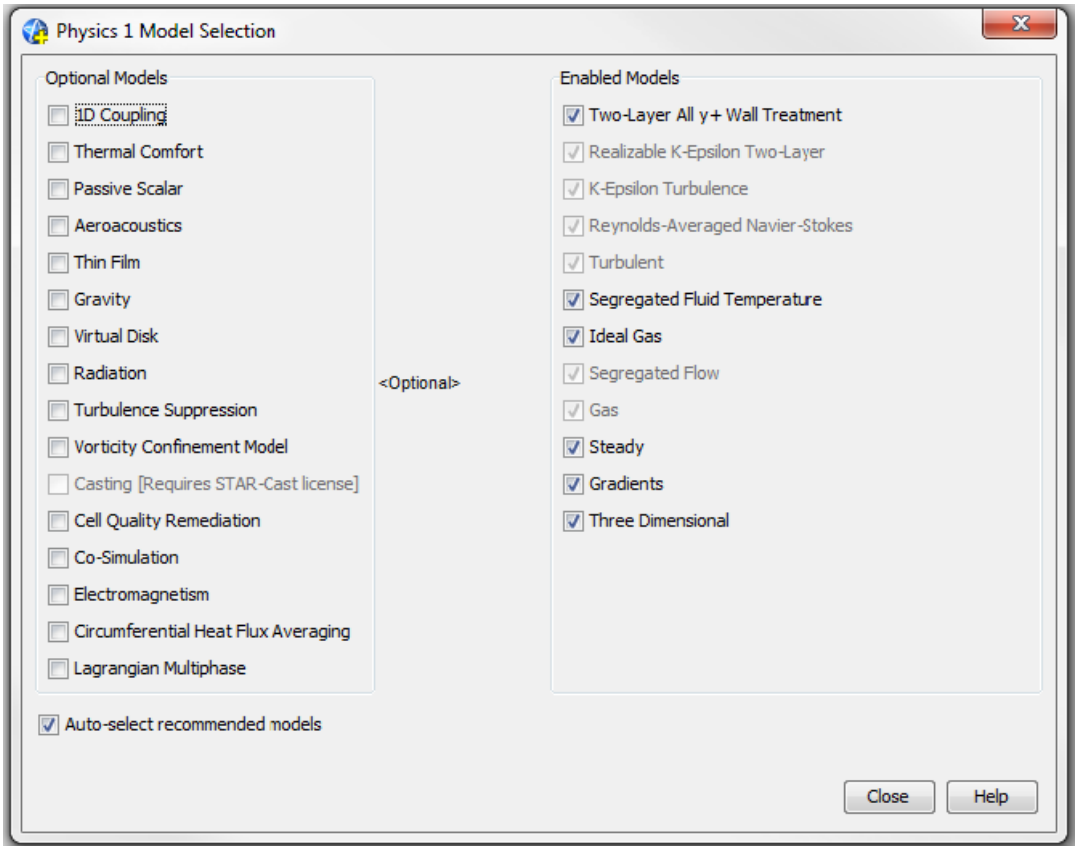

Figure 67. Physical model used in the STAR-CCM+ simulations.

- Steady

There are three Time models available in STAR-CCM+: (1) Steady, (2) Implicit Unsteady, and (3) Explicit Unsteady. The Steady model is utilized for all steady-state

calculations and the concept of a physical time-step is meaningless when this model is activated.

- Gravity

  The Gravity model accounts for the action of gravitational acceleration in STAR-CCM+ simulations. For fluids, it provides two effects: (1) the working pressure becomes the piezometric pressure, and (2) the body force due to gravity can be included in the momentum equations. The Gravity model allows the inclusion of the buoyancy source terms in the momentum equations when the Segregated Flow Model is chosen. When the Ideal Gas model is utilized to define a variable density problem, the buoyancy source term is incorporated in the momentum equation without modeling. The set value for the Gravity was 9.81 m/s^2.

- Gas

  The Gas model permits the simulation of a single gas only.

- Ideal Gas

  The Ideal Gas model utilizes the Ideal Gas equation to express density as a function of pressure and temperature. The Ideal Gas model permits dependency on the working pressure if the Ideal Gas is compressible. The dependency on pressure for all simulations was included within the models in this work. Incompressible flow was chosen for each case.

- Segregated Flow

  The Segregated Flow model solves the flow equations (one for pressure and one for each velocity component) in a segregated, or uncoupled, manner. The connection between the continuity and momentum equations is accomplished with a predictor-corrector approach. The Segregated Flow solver controls two additional solvers; namely Velocity and Pressure solvers. For each of these solvers, under-relaxation factor is provided to control the solution update.

  Under-relaxation factors are available to dampen and suppress steep oscillations in the flow solution that result from numerical errors. Too small under-relaxation factors will significantly slow down convergence, sometimes misleading the user to assume that the solution is converged when in reality, it is not. A rule of thumb is to always use under-relaxation factors as high as possible without causing in oscillations or divergence. In STAR-CCM+, a high under-relaxation factor advances the solution quicker than a low under-relaxation factor; however, this often results in convergence of the simulations.

- Segregated Fluid Temperature

  The Segregated Fluid Temperature model solves the total energy equation with temperature as the independent variable. Enthalpy is calculated from temperature based on the equation of state. Any simulations that do not involve combustion can embrace this model.

- Turbulent

  The Turbulent solver defines the non-laminar flow field and permitting necessary selection of turbulence modeling for the simulation.

- k-ε Turbulence

  A k-ε turbulence model, a two-equation model, of which transport equations are solved for the turbulent kinetic energy and its dissipation rate. Various forms of the K-Epsilon model have been in use for several decades, and it has become the most widely used model for industrial applications. The k-ε turbulence model is used in RANS codes to solve the unknown relationships between the Reynolds stresses due to random turbulent fluctuations and the mean flow field quantities. STAR-CCM+ has a choice of eight different K-Epsilon turbulence models:

  - Standard K-Epsilon
  - Standard Two-Layer K-Epsilon
  - Standard Low-Reynolds number
  - Realizable K-Epsilon
  - Realizable Two-Layer K-Epsilon
  - Abe-Kondoh-Nagano low-Reynolds number
  - Elliptic Blending K-Epsilon
  - V2F low-Reynolds number

- Realizable Two-Layer k-ε

  The Realizable Two-Layer k-ε model is a combination of the Realizable k-ε model with the two-layer approach. The model gets the added flexibility of an all y+ wall treatment with similar coefficients. The Realizable k-ε model comprises a new transport equation for the turbulent dissipation rate, ε. A critical coefficient of the model, C_μ, is not assumed constant but it is expressed as a function of mean flow and turbulence properties. The two-layer approach permits the k-ε model to be applied in the viscous sublayer. In the two-layer approach, the calculation is segregated into two layers. The turbulent dissipation rate and the turbulent viscosity are identified as functions of wall distance in the near-wall layer. The turbulent dissipation rate values in the layer next to the wall are integrated smoothly with the values computed from solving the transport equation far from the wall. The turbulent kinetic energy equation is solved in the entire flow.

- Reynolds Averaged Navier Stokes (RANS)

  RANS is the turbulence modeling method which was used within the simulations.

- Two-layer All-y+ Wall Treatment

  In STAR-CCM+, the all y+ wall treatment is a near wall modeling assumptions for use with each turbulence model. The all y+ wall treatment is a hybrid model of which it tries to emulate the high y+ wall treatment for coarse meshes and the low y+ wall treatment for fine meshes. The high y+ wall treatment is basically an empirical wall-

function approach (where the near-wall cell centroid falls within the logarithmi region of the boundary layer) while the low y+ wall treatment is suitable only for low-Reynolds number turbulence models in which the viscous sublayer is properly resolved, i.e. the mesh is fine enough to resolve the viscous sublayer.

Two-Layer All Wall Treatment is a formulation that is similar to the All y+ Wall Treatment; however, it has a wall boundary condition that is consistent with the two-layer formulation. This wall treatment is suggested in most simulations.

VII.1.5. Simulation Set And Test Matrix

For preliminary investigation, four cases were simulated. Case 1 was the case of all four risers were subjected to uniform inlet boundary conditions of 5 m/s and inlet temperature of 120 ^{o}C (ΔT = 95 ^{o}C assuming 25 ^{o}C room temperature). Case 3 has the similar set-up as Case 1 except the inlet velocity was reduced to 2.25 m/s. Case 2 was the case of which only one riser was used (Riser ④) with inlet boundary conditions of 5 m/s and inlet temperature of 120 ^{o}C (ΔT = 95 ^{o}C), also by assuming 25 ^{o}C of the room temperature. Case 4 has the same arrangement with Case 2 but the inlet velocity was decreased to 2.25 m/s.

VII.1.6. Simulation Results

Seven cross-sectional planes (three vertical and four horizontal) of interest were chosen for the CFD simulations. Six of these planes (V-T-A, V-T-B, V-T-C, H-T-A, H-T-B, and H-T-C) were selected for the placement of insertion rods for thermocouple racks (discussed in the instrumentation section) after considering many factors, including feasibility of installation, space constraints introduced by the experimental test facility, strategic locations for turbulence mixing explanations, etc. These six planes were also being selected for the velocity measurements using PIV.

As mentioned earlier, for computations, the air flow is assumed to be an ideal gas, having a steady flow with three-dimensional Reynolds Averaged Navier-Stokes (3D-RANS). Turbulent computations are executed by enabling the realizable two-layer k-ε model with two-layer all y+ wall treatment. 4,000 numbers of iterations are being used for normalized residuals of the continuity, three-component of momentum (x, y and z), energy, turbulent kinetic energy, and turbulent dissipation rate for convergence. Convergence to less than 10^{-3} from the original values was achieved despite the diffusive nature of polyhedral meshes (Figure 68 to Figure 71). However, since the primary objective of the simulation is to identify the general flow behavior, the convergence criterion was deemed acceptable. Pressure outlet boundary condition is applied to the twin exhaust outlets. The non-slip wall boundary condition is assigned to the internal surface of the upper/hot plenum as well as for each riser.

It was observed in Case 1 and Case 3 (one riser cases) that the velocity and temperature profiles were symmetric which implied even flow distribution across the upper plenum and the two exhaust pipes. For Case 2 and Case 4 (four riser cases), the flow was asymmetric and it exited the upper plenum via the nearest outlet, i.e. the inlet of the right chimney, due to the fact that only Riser ④ was in operation. Flow recirculation occurred near the inlet of the chimney(s) for all cases. Hence, it was imperative to place velocity, temperature and visualization (boroscope) ports near the inlet of each exhaust pipe in order to investigate this behavior experimentally. The flow of the heated air from the inside of the upper plenum followed the 45^{o}, 90^{o}, 45^{o} curvatures of the two exhaust pipes for Case 1 and Case 3. Boundary layer detachment which caused flow separation from the exhaust pipe walls was observed near the first 45^{o} curvature. This flow separation has resulted in a localized low velocity region with recirculation flows. Therefore, it was sensible to place measurement ports to measure velocity and temperature together with visualization ports (boroscope) near these locations for experiments. The results of the CFD simulations for all cases (velocity vectors and temperature distribution at seven cross-sectional planes) are presented in Figure 72 to Figure 87.

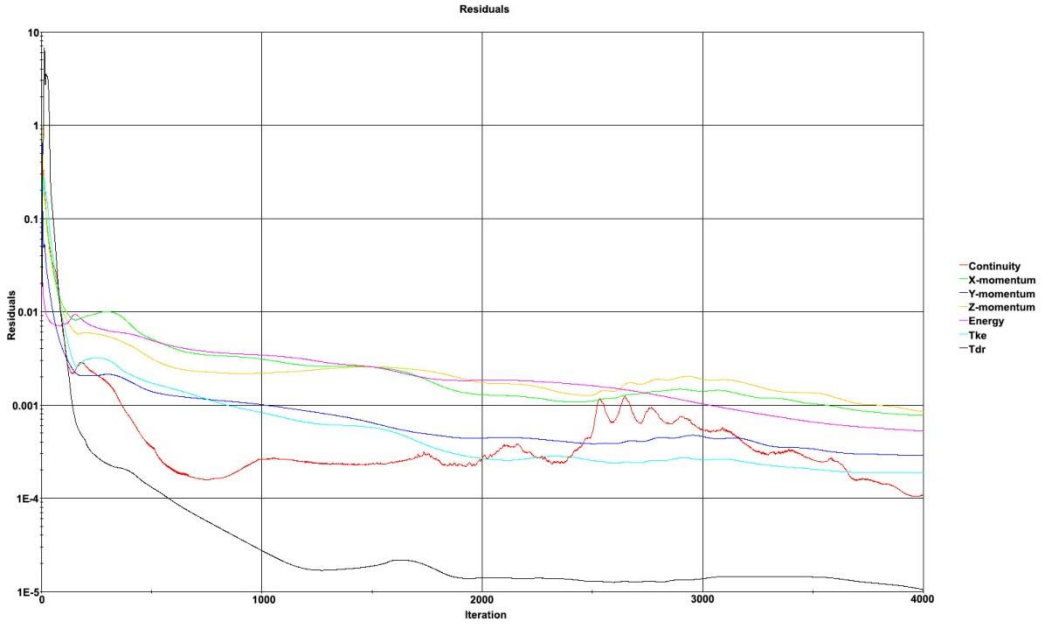

Figure 68. Residual for Case 1.

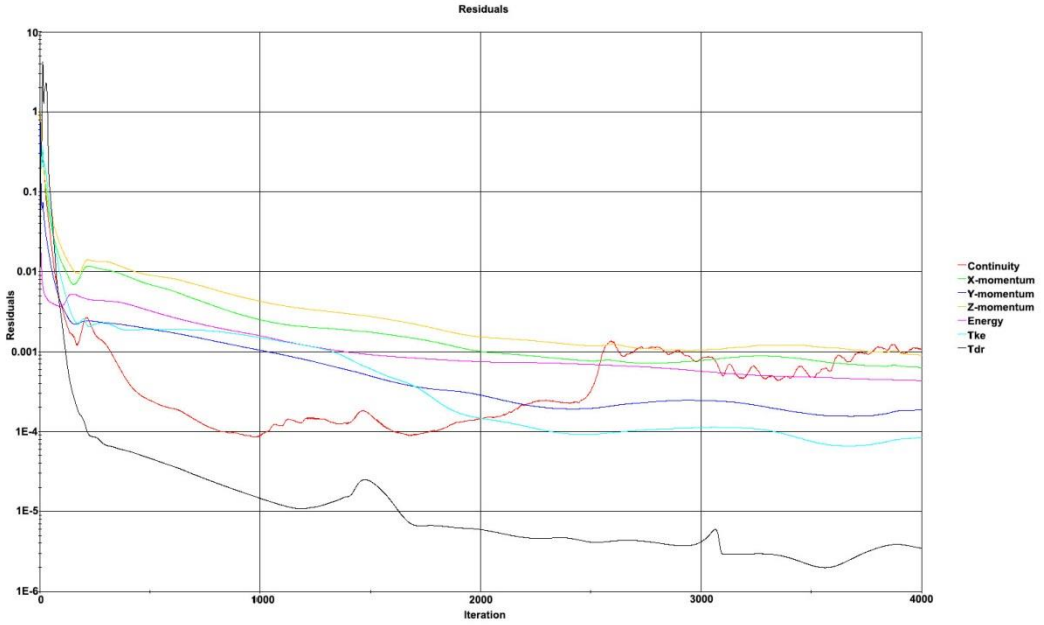

Figure 69. Residual for Case 2.

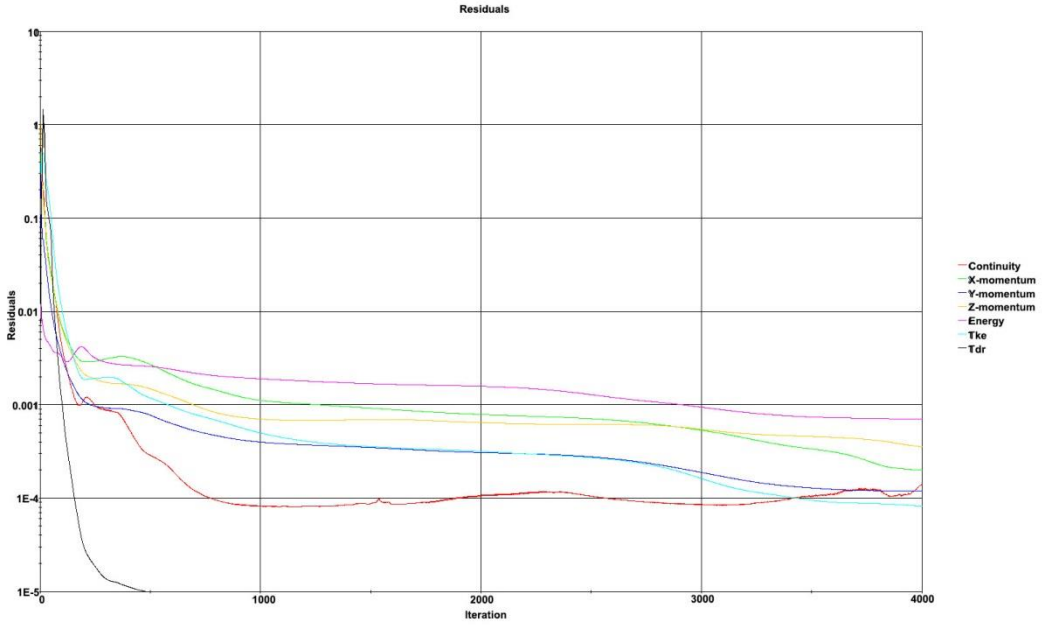

Figure 70. Residual for Case 3.

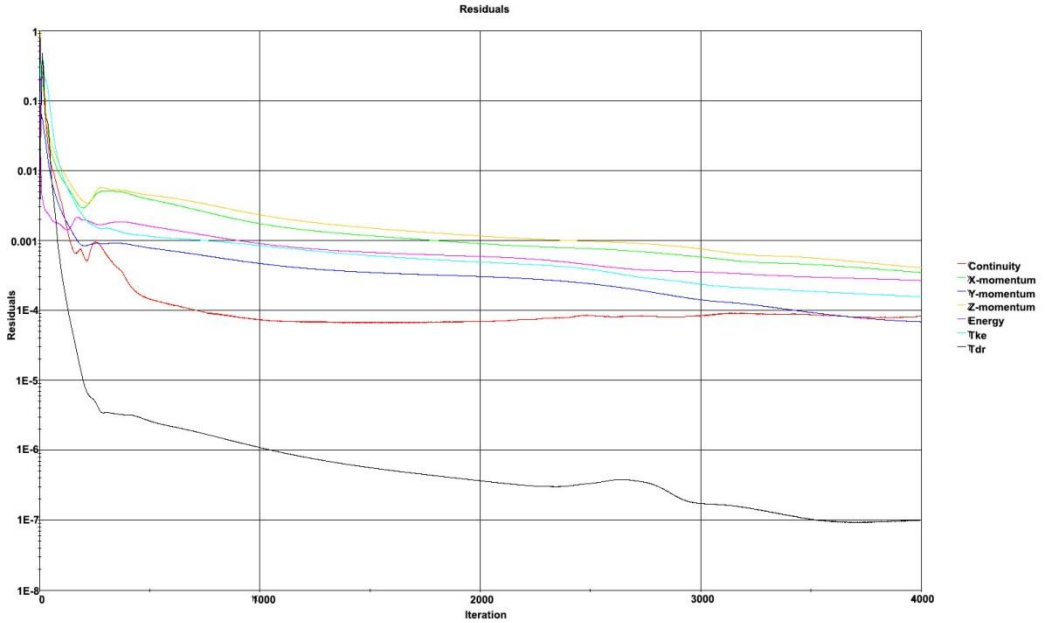

Figure 71. Residual for Case 4.

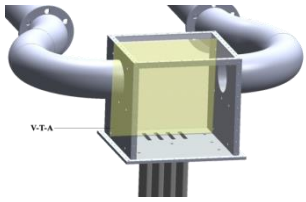

V-T-A Plane

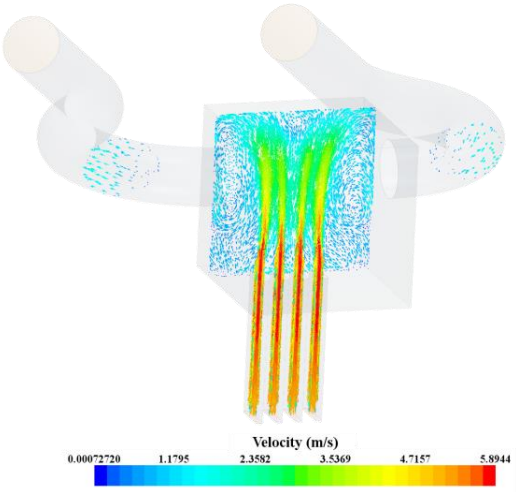

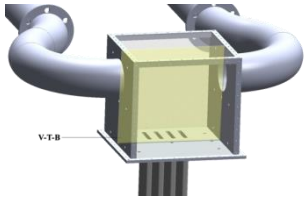

V-T-B Plane

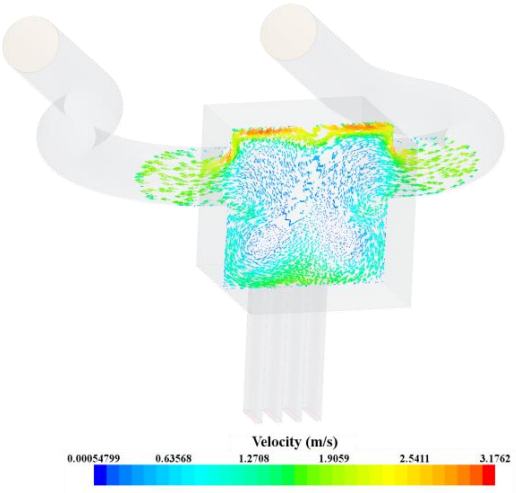

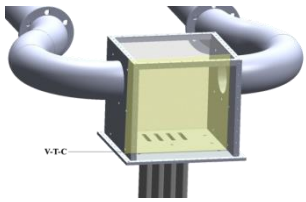

V-T-C Plane

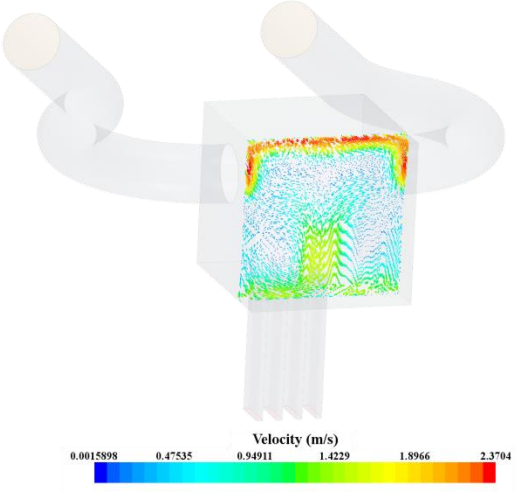

Figure 72. Three vertical planes for Case 1 (velocity vectors).

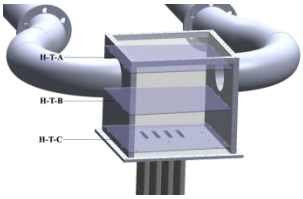

H-T-A, H-T-B, H-T-C Planes

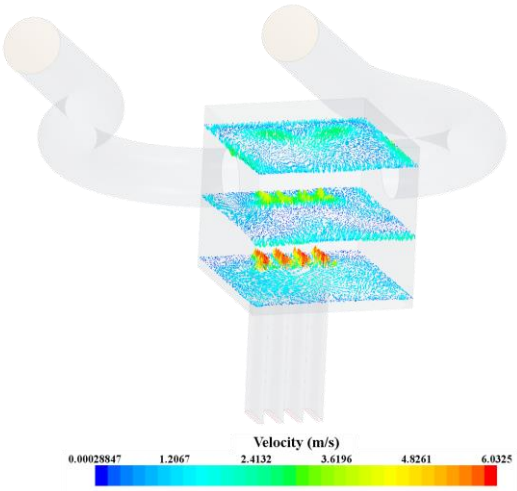

Horiozontal midplane

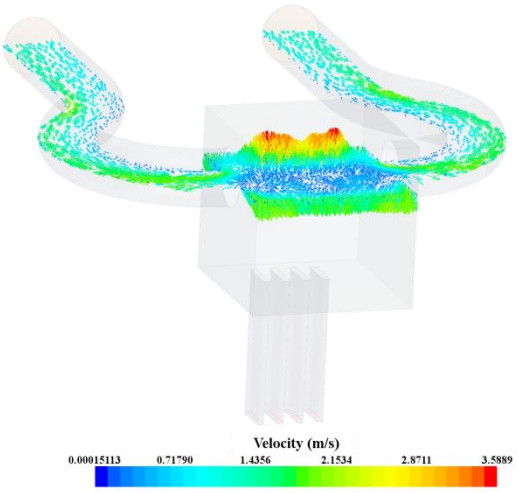

Figure 73. Four horizontal planes for Case 1 (velocity vectors).

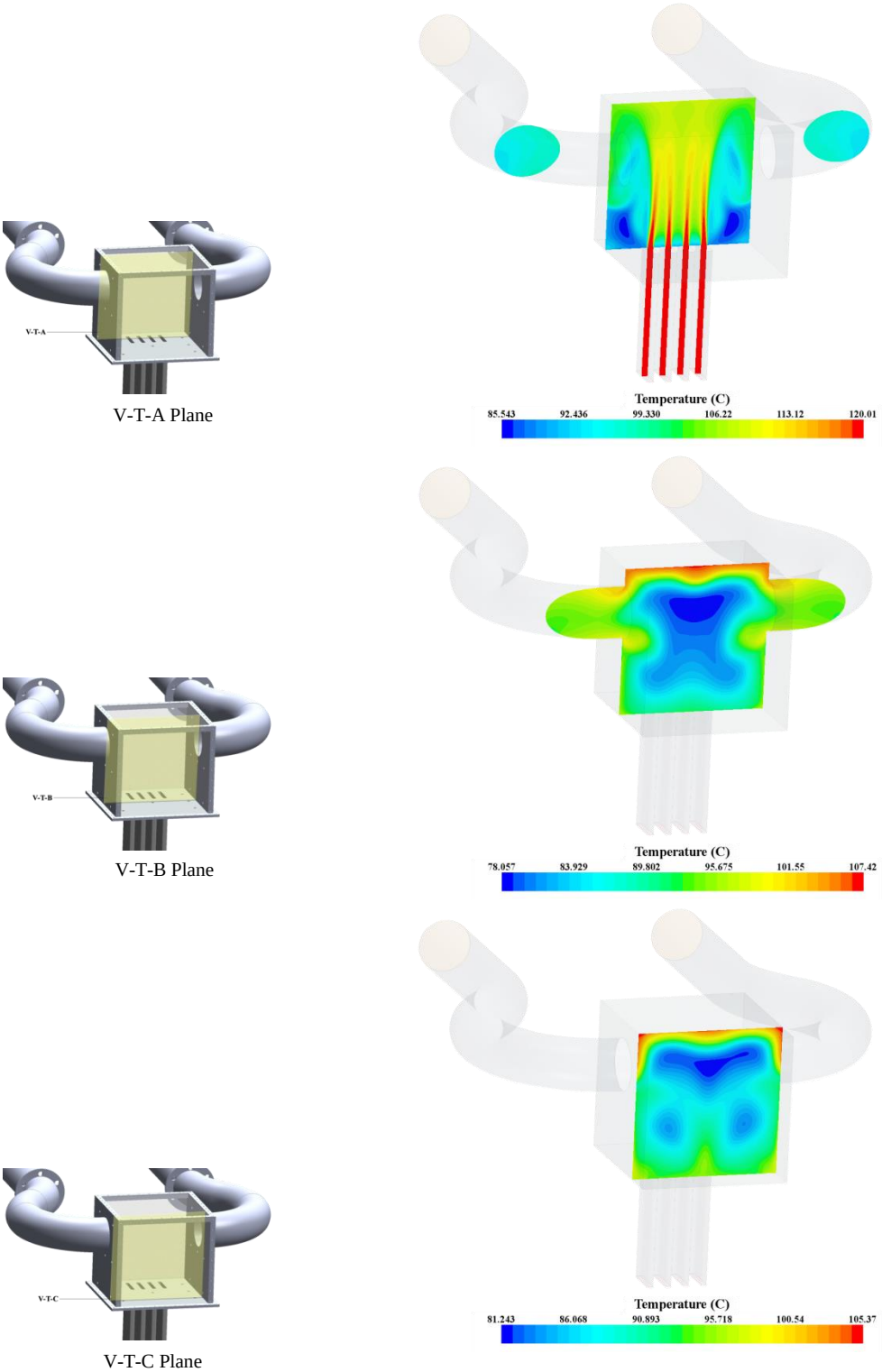

Figure 74. Three vertical planes for Case 1 (temperature distributions).

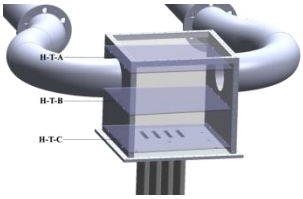

H-T-A, H-T-B, H-T-C Planes

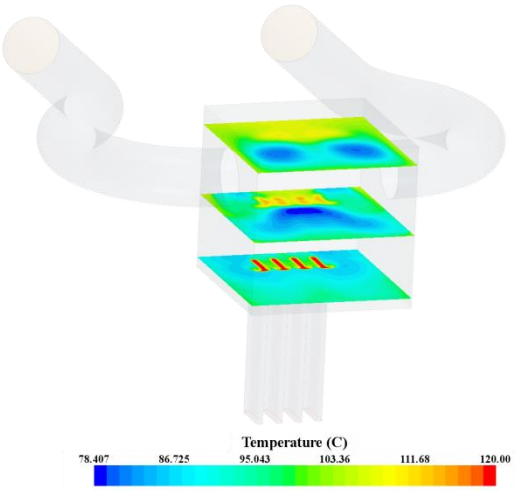

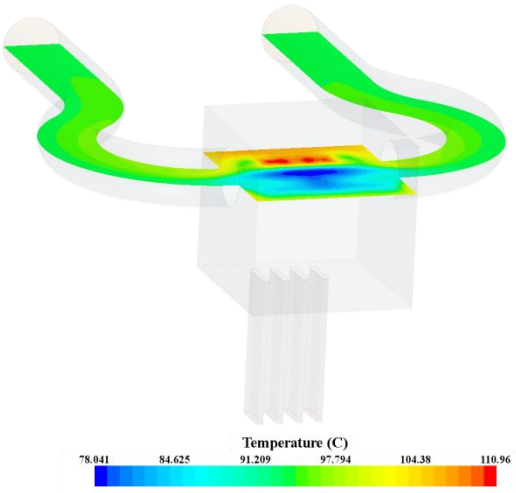

Horiozontal midplane

Figure 75. Four horizontal planes for Case 1 (temperature distributions).

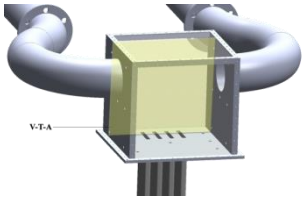

V-T-A Plane

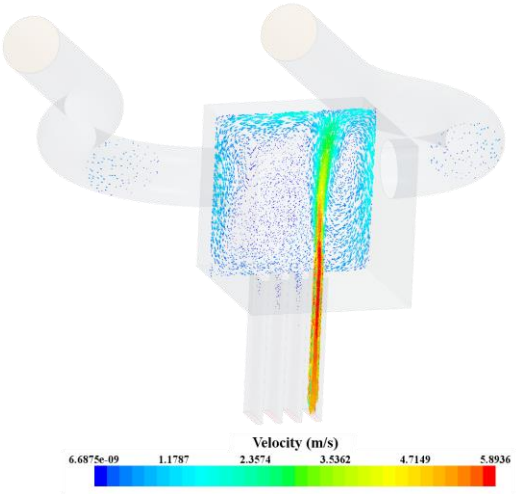

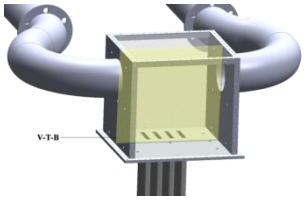

V-T-B Plane

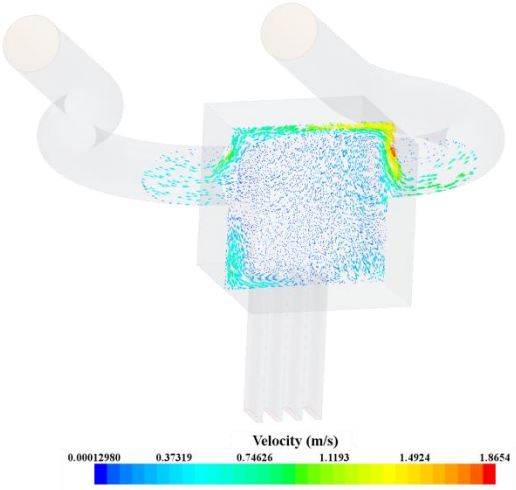

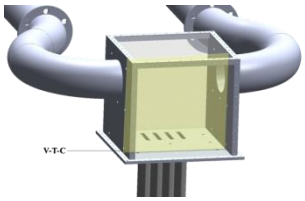

V-T-C Plane

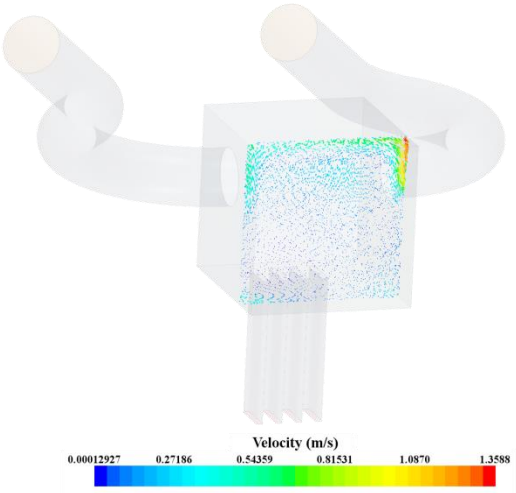

Figure 76. Three vertical planes for Case 2 (velocity vectors).

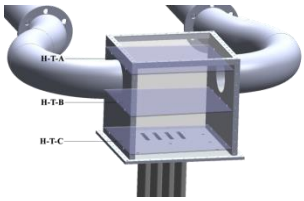

H-T-A, H-T-B, H-T-C Planes

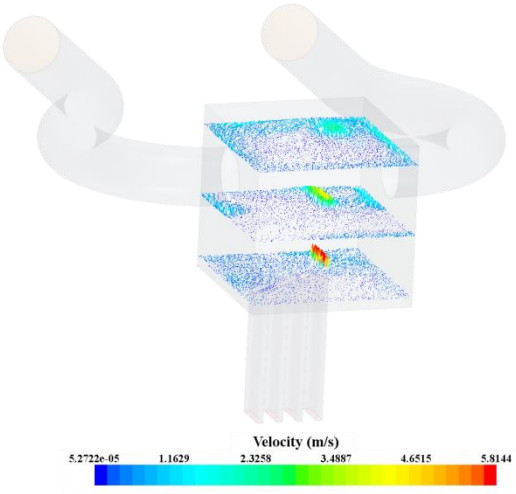

Horiozontal midplane

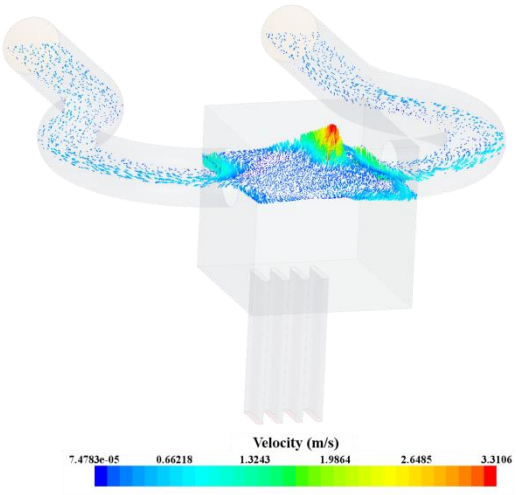

Figure 77. Four horizontal planes for Case 2 (velocity vectors).

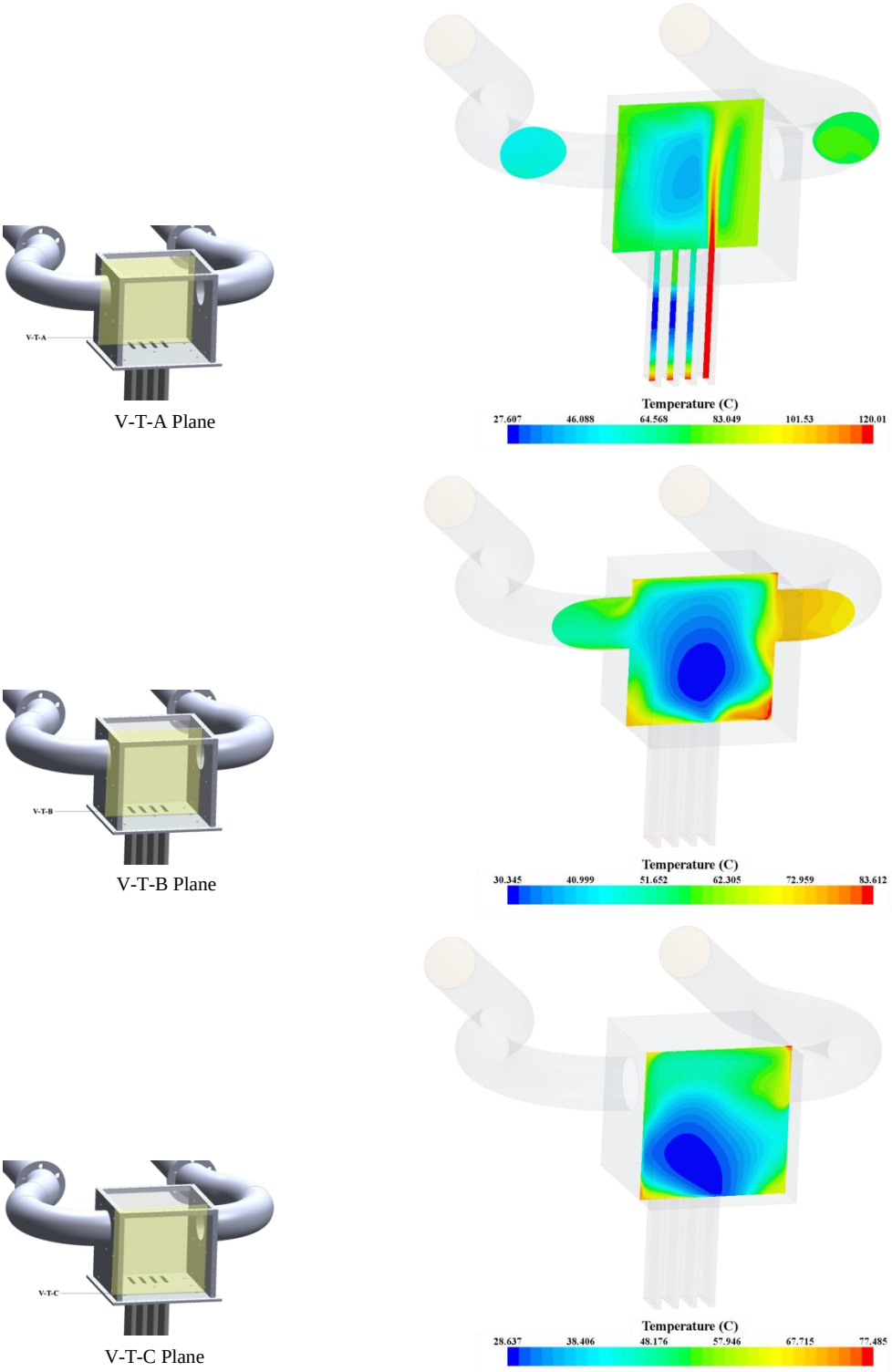

Figure 78. Three vertical planes for Case 2 (temperature distributions).

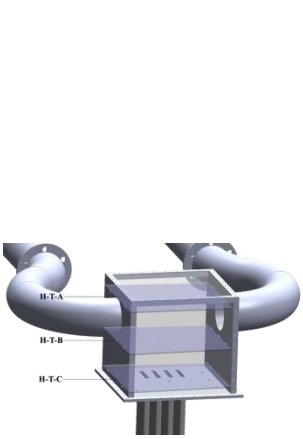

H-T-A, H-T-B, H-T-C Planes

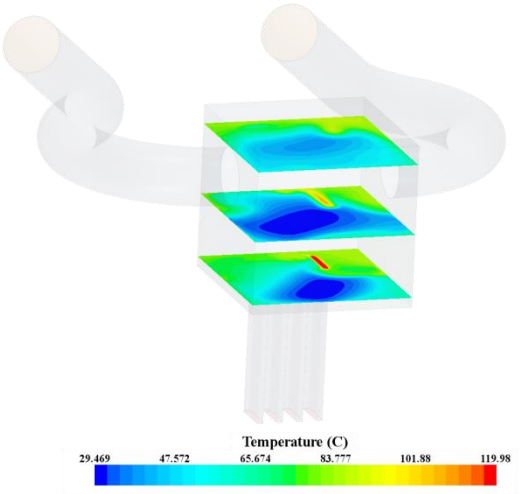

Horiozontal midplane

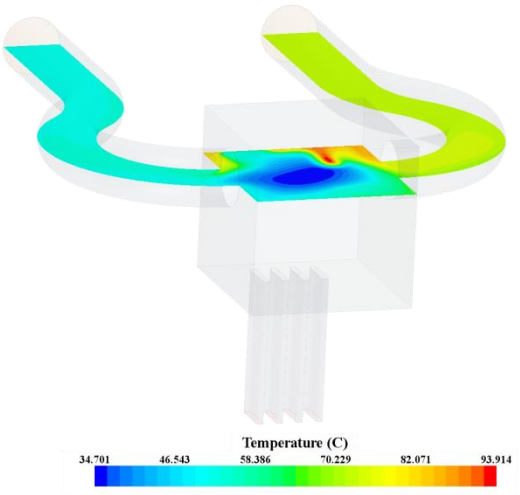

Figure 79. Four horizontal planes for Case 2 (temperature distributions).

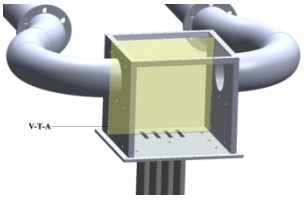

V-T-A Plane

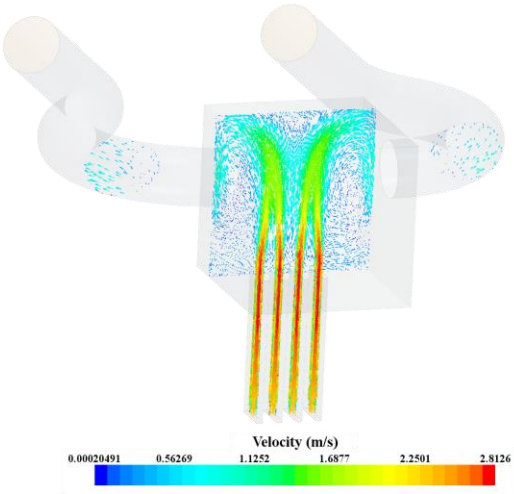

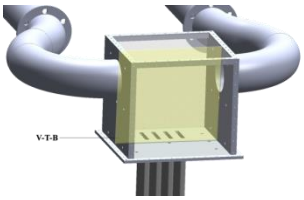

V-T-B Plane

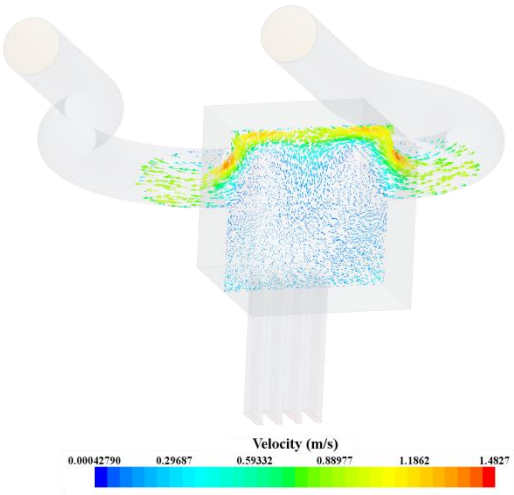

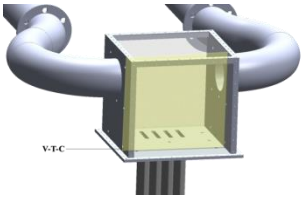

V-T-C Plane

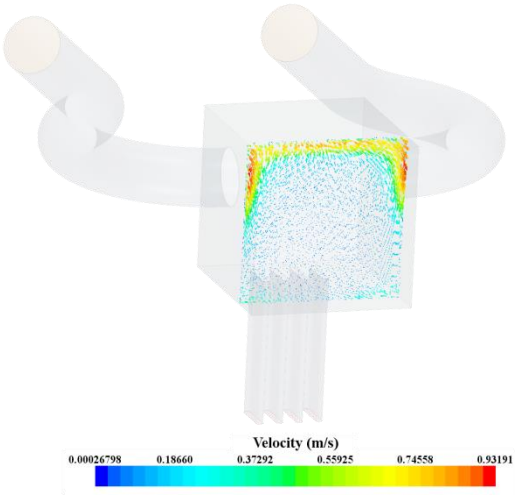

Figure 80. Three vertical planes for Case 3 (velocity vectors).

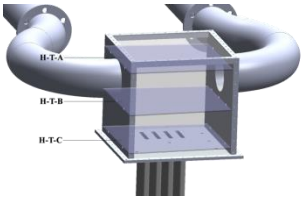

H-T-A, H-T-B, H-T-C Planes

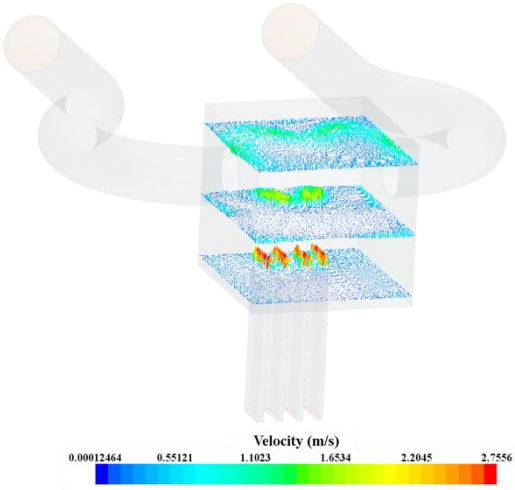

Horiozontal midplane

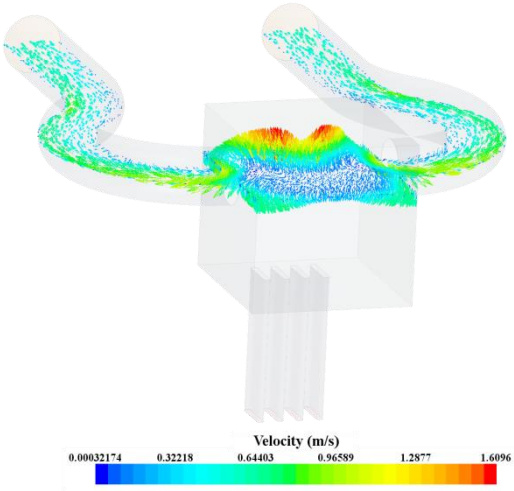

Figure 81. Four horizontal planes for Case 3 (velocity vectors).

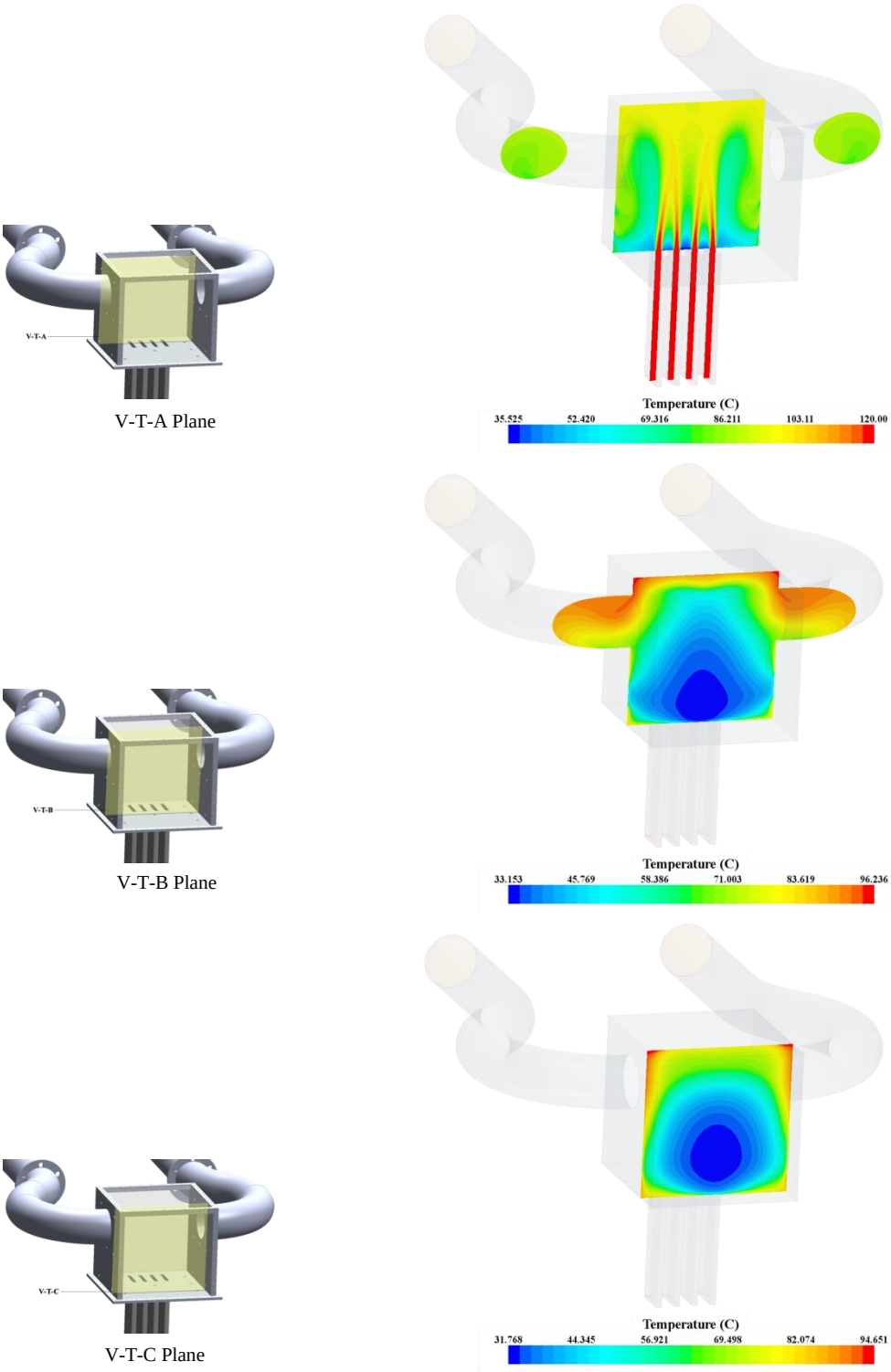

Figure 82. Three vertical planes for Case 3 (temperature distributions).

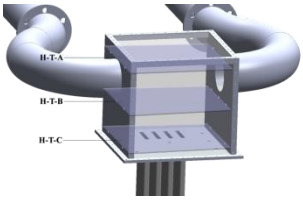

H-T-A, H-T-B, H-T-C Planes

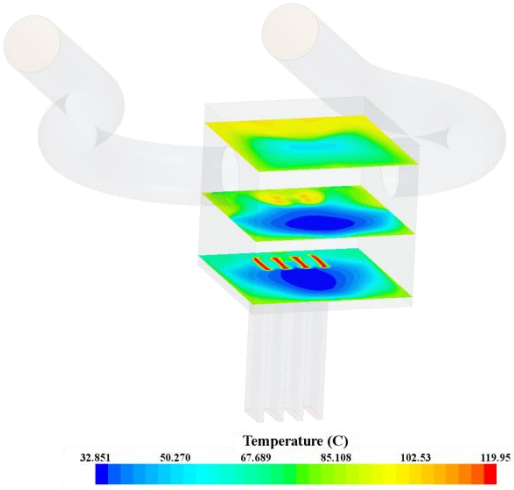

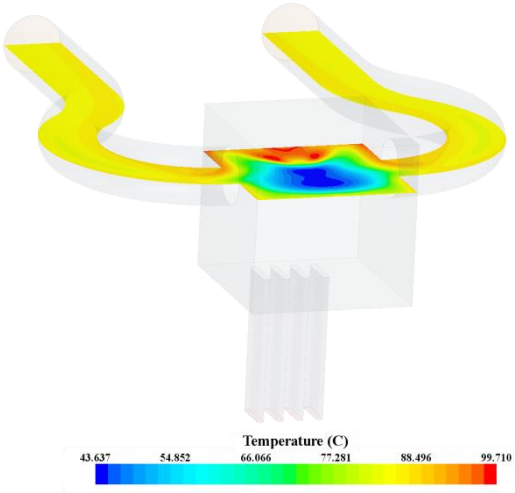

Horiozontal midplane

Figure 83. Four horizontal planes for Case 3 (temperature distributions).

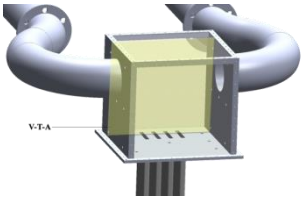

V-T-A Plane

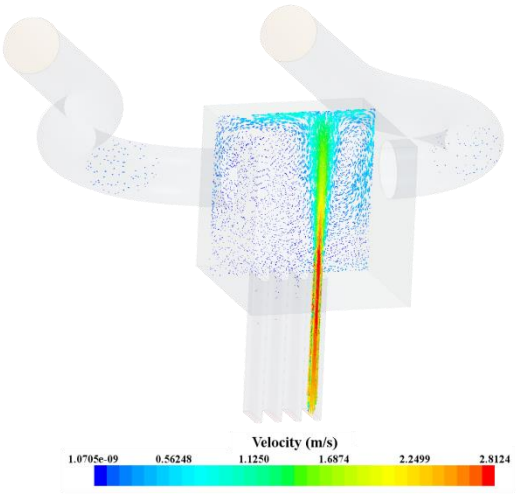

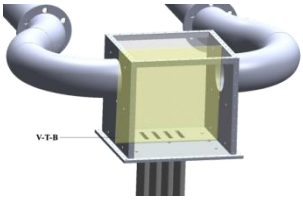

V-T-B Plane

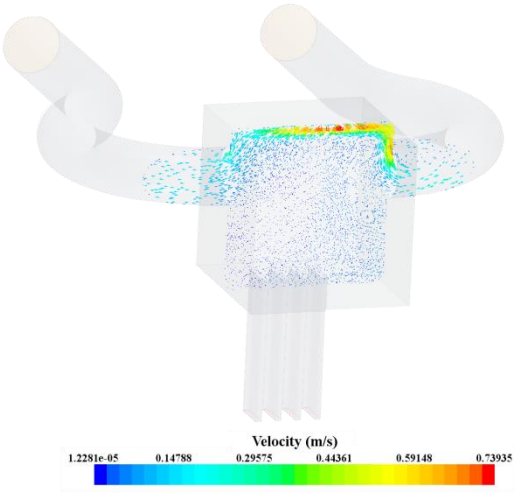

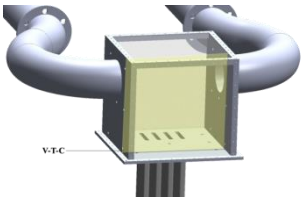

V-T-C Plane

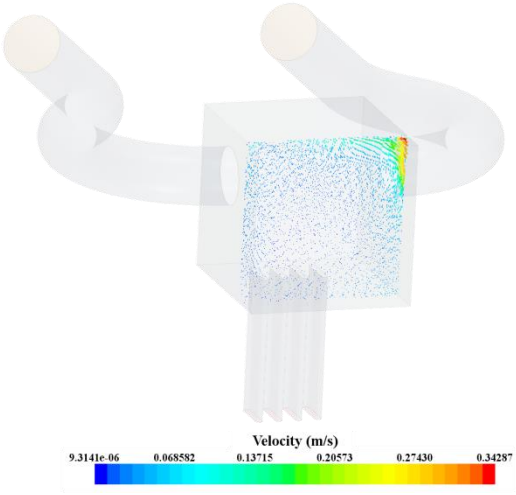

Figure 84. Three vertical planes for Case 4 (velocity vectors).

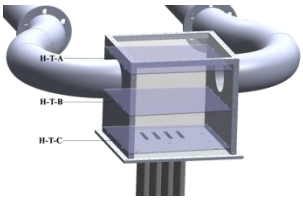

H-T-A, H-T-B, H-T-C Planes

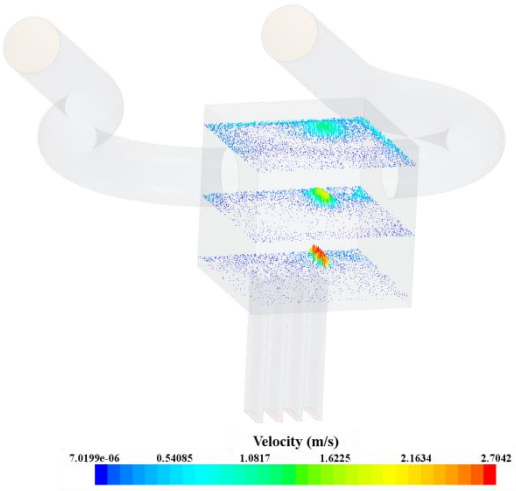

Horiozontal midplane

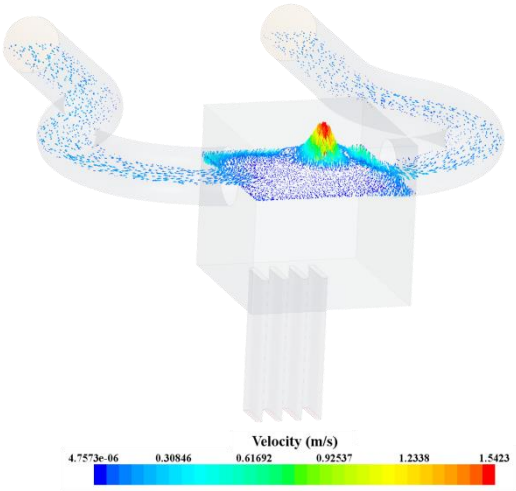

Figure 85. Four horizontal planes for Case 4 (velocity vectors).

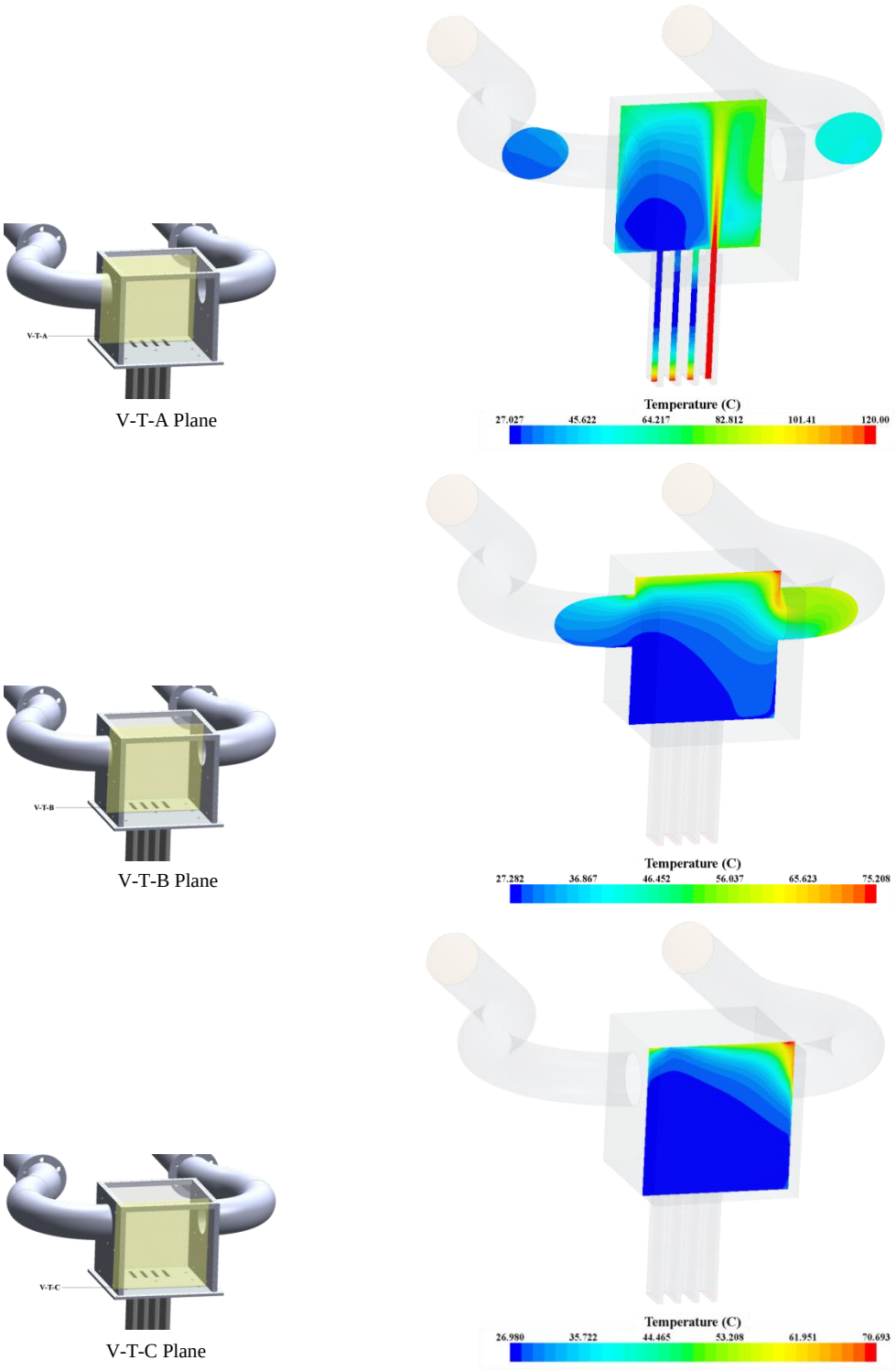

Figure 86. Three vertical planes for Case 4 (temperature distributions).

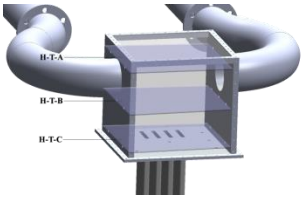

H-T-A, H-T-B, H-T-C Planes

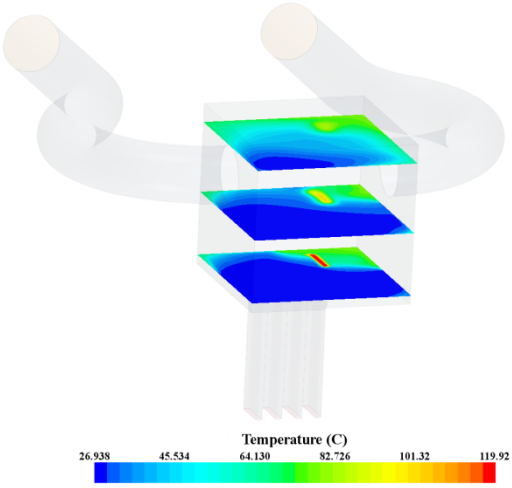

Horiozontal midplane

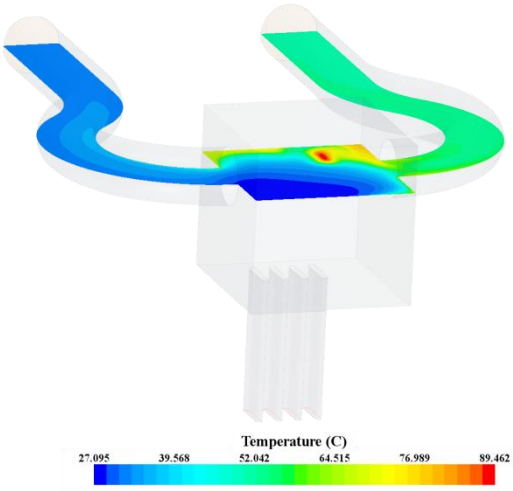

Figure 87. Four horizontal planes for Case 4 (temperature distributions).

VII.2. Instrumentations

The results from STARCCM+ CFD simulations in the earlier section were useful to assist not only on prediction of the general air flow in the TAMU Air-Cooled RCCS scaled-model but also to determine the optimal configuration of the flow measurement sensors ports (temperature and pressure) at the risers, the upper/hot plenum, and the twin exhaust pipes (Table 13).

Table 13. Measurement sensor ports for ⅛ scale TAMU Air-Cooled RCCS (Sulaiman et al, 2014 and 2015).

Part	Temperature	Pressure	Light
Exhaust pipes (2 units)	x10 (share)	x10 (share)	x6
Upper/Hot Plenum (1 unit)	x18	x3	-
Riser (4 units)	x12	x12	x12

A total of 12 instrumentation ports (for each temperature and pressure) were fixed at the inlet, in the middle, and at the outlet of each riser (1/8” female NPT threaded through type fitted with 1/8” male NPT, 1/16” OD Omegalok compression fittings). These ports would enable the spatial profile measurements of temperature for each riser at varying

elevation. 12 units of boroscope ports were also installed (3/8” female NPT threaded through type fitted with 1/8” male NPT, 1/16” OD Omegalok compression fittings). Seven instrumentation ports for temperature and one instrumentation port for pressure were fitted at each of the plenum side face (perpendicular to the inlet of the exhaust pipes) and the bottom face. These ports were 1/4” female NPT threaded through type fitted with steel Yor-Lok tube fitting (straight adapter for 5/16" tube OD x 1/4” male NPT). These ports were intentionally located at the bottom, middle, and upper sections of the upper plenum to allow the measurements of each riser’s jet flow temperature spatial profile utilizing custom-made vertical and horizontal rod insertions with mounted fine thermocouple wires. Ten instrumentation ports with similar specifications as the risers (for either temperature or pressure) were installed at strategic locations of the exhaust pipes. These ports were intended to capture temperature and velocity of the air flow, in particular the flow behavior at the inlet of each exhaust pipe (90^{o} curvature) of which flow separation was observed to occur in the STAR-CCM+ simulations. Ten boroscopes ports were installed 8” apart from the temperature and pressure ports (Figure 88).

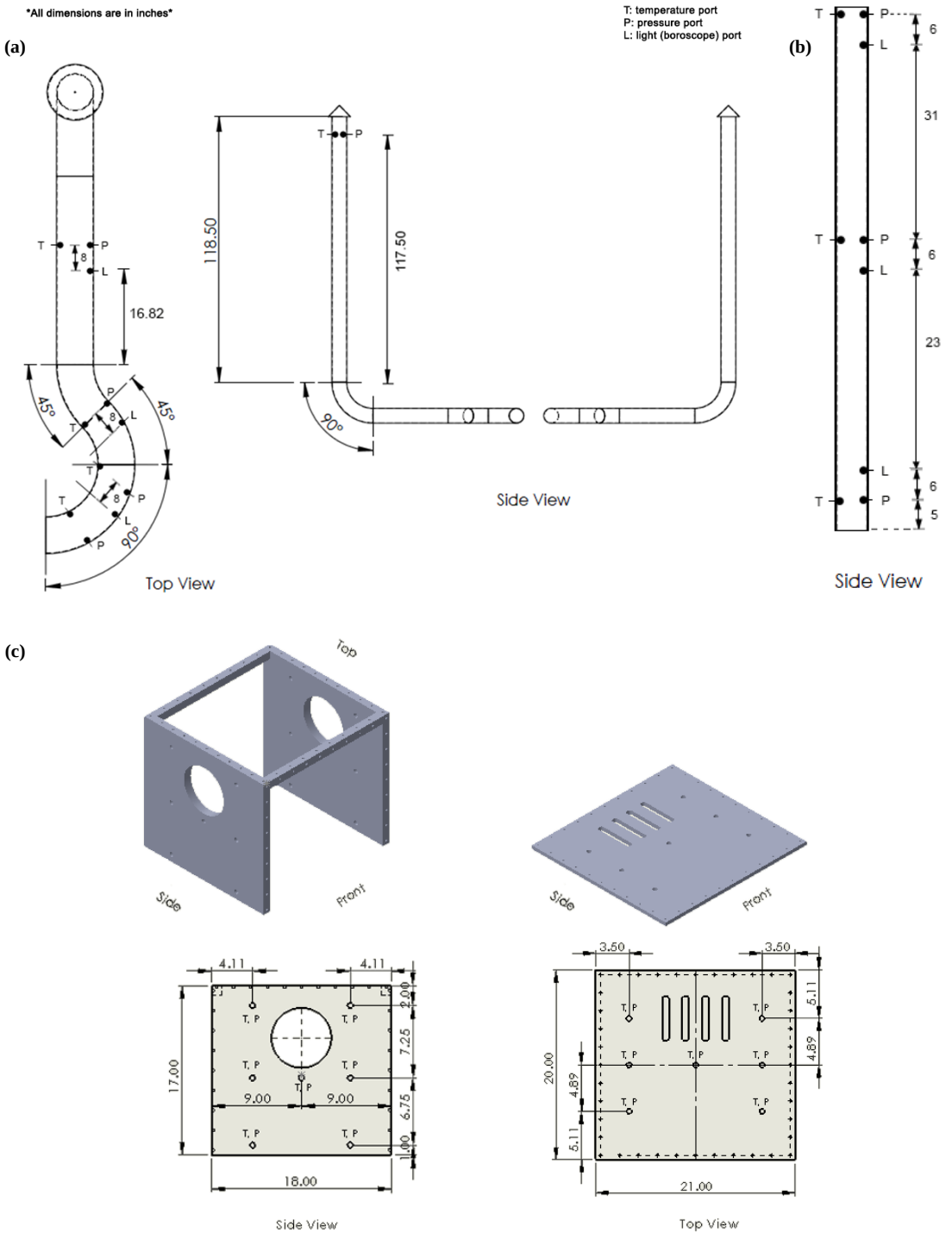

Figure 88. Positions of the measurement ports for the TAMU Air-Cooled RCCS. (a) The exhaust pipes, (b) The risers, (c) The upper plenum (Sulaiman et al., 2014 and 2015).

VII.2.1. Thermocouples Labeling Convention

A labeling convention was established for each instrument to facilitate quick identification during experiment and data acquisition. The label convention followed equipment – instrument – column – row (E-I-C-R) format. For each component, a designated letter was used for labeling; i.e. R for riser, E for exhaust, V for vertical insertion and H for horizontal insertion. T and P were reserved for thermocouple and pressure transducer under instrument. Column and row refer to alphabet and number based on specific view of equipment (Figure 89 to Figure 92).

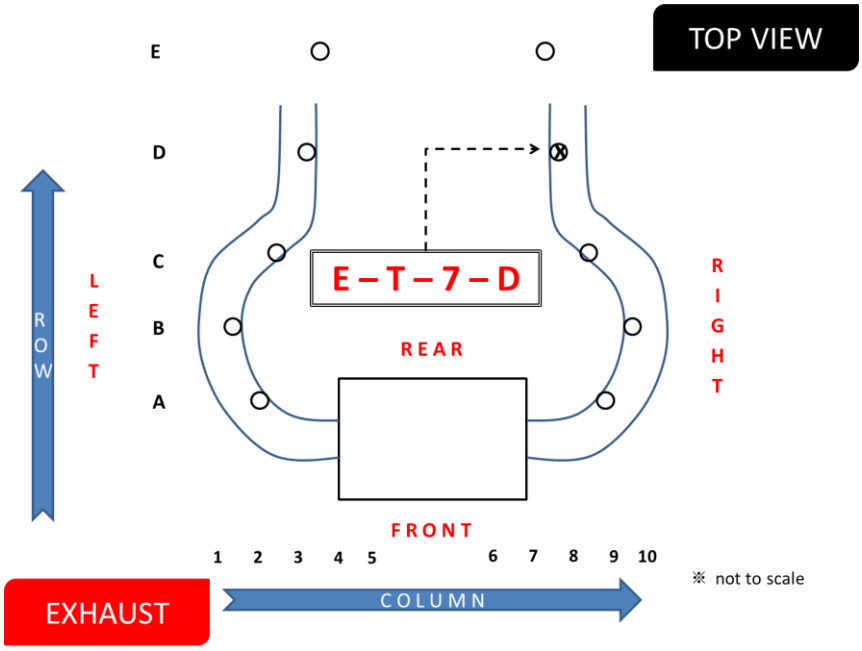

Figure 89. Example of label convention of thermocouple installed at location x (E-T-7-D). Top view of the exhaust pipes was used for labelling reference.

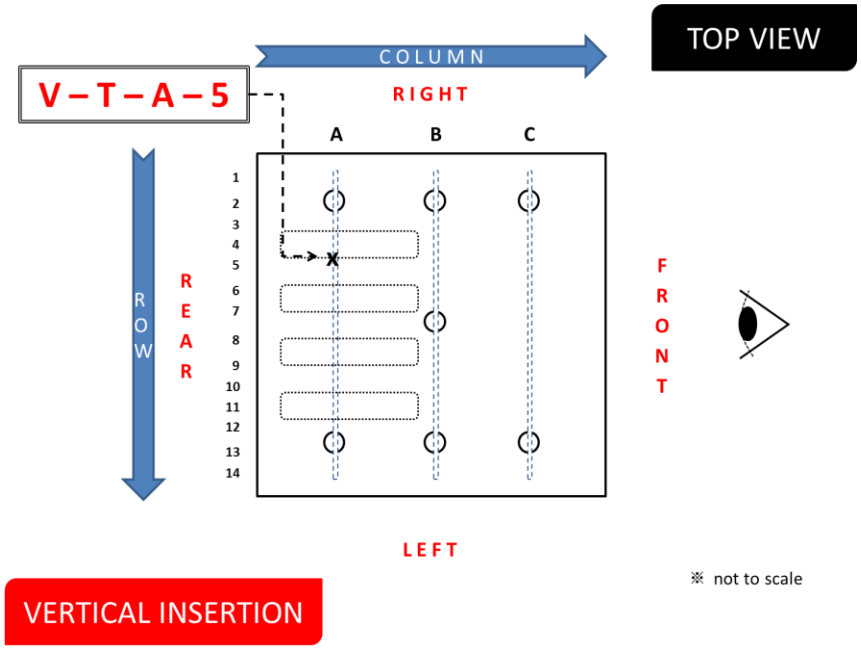

Figure 90. Example of label convention of thermocouple installed at location x (V-T-A-5). Top view of the upper plenum was used for labelling reference.

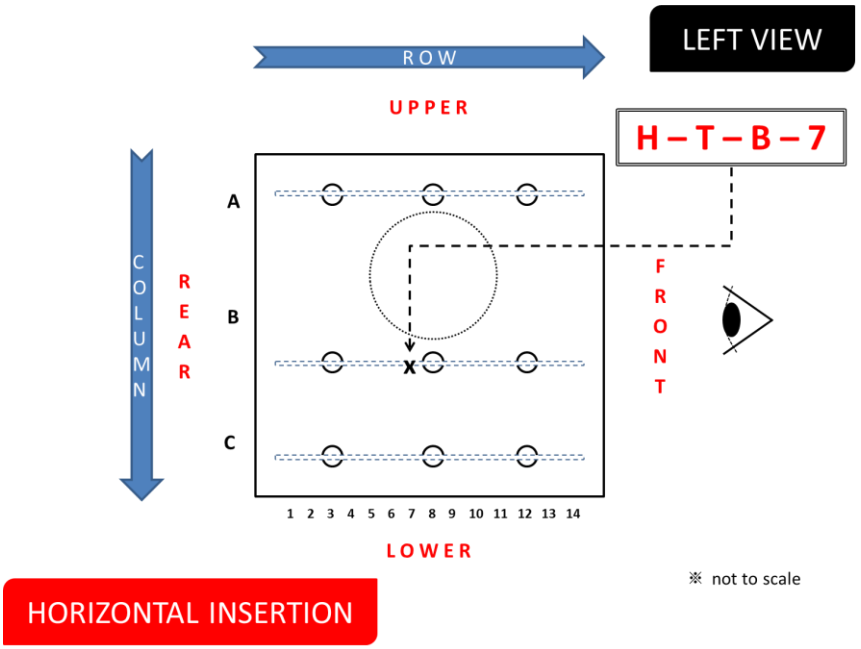

Figure 91. Example of label convention of thermocouple installed at location x (H-T-B-7). Top view of the upper plenum was used for labelling reference.

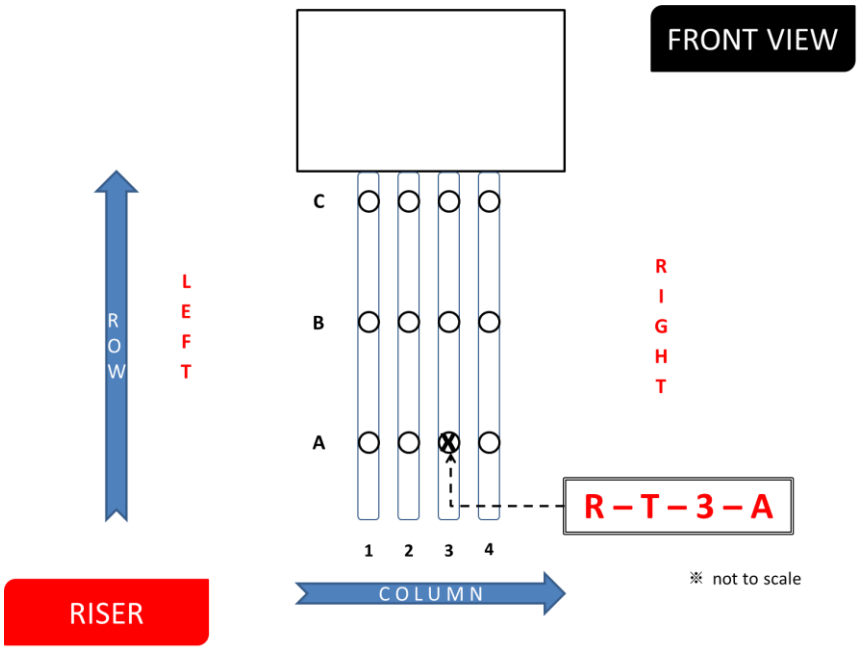

Figure 92. Example of label convention of thermocouple installed at location x (R-T-3-A). Top view of the risers was used for labelling reference**.**

VII.2.2. Thermocouple Racks

A total of 84 units of Omega fine wire insulated thermocouples wires (copper-constantan, -267 ℃-260 ℃, greater of 0.5 ℃ or 0.4% accuracy) with special limit error (SLE) were used inside the upper plenum. Thermocouple wire junctions were made using an Omega TL-Weld welding machine. This 120 V machine has an output range between 0 to 60 joules and capable to weld thermocouple wire up to 1.1 mm diameter. The thermocouple wire junctions were mounted on the 6 units of 0.028” diameter, 15” length of multipurpose 304/304L stainless steel tube crossbars (Figure 93) using J.B. weld at 1” intervals. 12 units of 3’ precision miniature stainless steel tubing (0.238” OD, 0.218” ID,

0.01” wall) were used as horizontal and vertical insertion racks (Figure 93). Six units of these tubes were inserted from the bottom plate of the upper plenum through 0.25” NPT female (threaded through type) with steel Yor-Lok tube fitting (straight adapter for 5/16" tube OD x 0.25” NPT male), i.e. vertical insertion rack (Figure 94 and Figure 96), whereas the remaining six units were inserted from the right side of the upper plenum with the same fitting for the holes, i.e. horizontal insertion rack (Figure 95 and Figure 96). 80/20 frames were used for the construction of the horizontal and vertical insertion maneuvering systems.

Adhesive scales were attached to the 80/20 frames and serve as a guide during the movement of the insertion systems during experiments and also provides indication of insertion rod depth. These scales were carefully calibrated with the insertion crossbars to assure accurate displacements inside the upper plenum. All the thermocouple wires were calibrated using two-point reference temperature (ice bath at 0 $^{\circ}$C and boiling water at 100 $^{\circ}$C). A rugged handheld and fast response Fluke 52 II dual input digital thermometer ± (0.05% of reading + 0.3 $^{\circ}$C, type-J, K, T, E) was utilized to verify the freezing and boiling temperatures. 12 units of 8” quick disconnect thermocouple probe with miniature connectors (copper-constantan, T-type, exposed junction, -267 $^{\circ}$C -260 $^{\circ}$C, greater of 0.5 $^{\circ}$C or 0.4% accuracy, 0.062” diameter stainless steel shealth) were used for the four risers at 5”, 40” and 77” from the risers’ bottom support plate (Figure 88). These thermocouple probe tips were inserted horizontally into the centroid of the cross-sections of each riser; therefore the temperatures in the lower, middle, and upper portion of the risers could be monitored. All the thermocouple wires and probes were connected to the 12 x 8 Omega

bezel strips mounting for quick and easy change-over of thermocouples. The bezel strip mounting was connected to the data acquisition system.

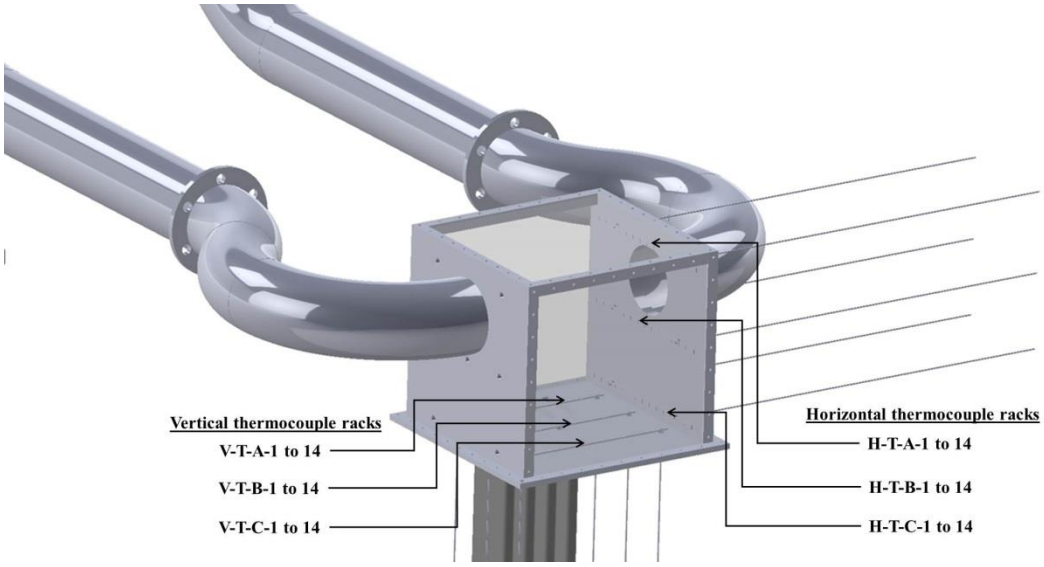

Figure 93. Positions of the fine thermocouple wires mounted on the crossbars inside the upper plenum.

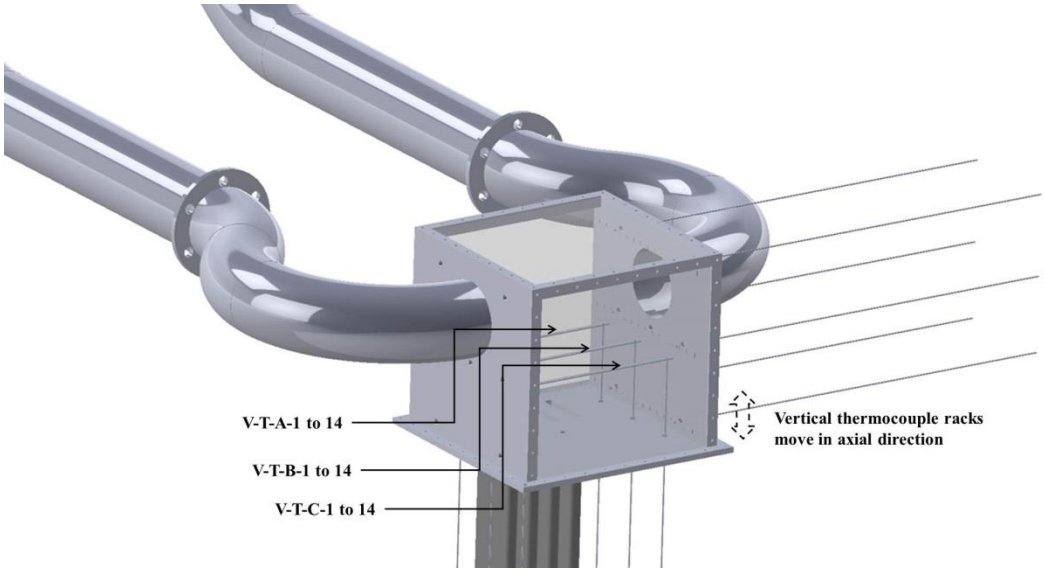

Figure 94. Movement of the vertical thermocouple racks inside the upper plenum.

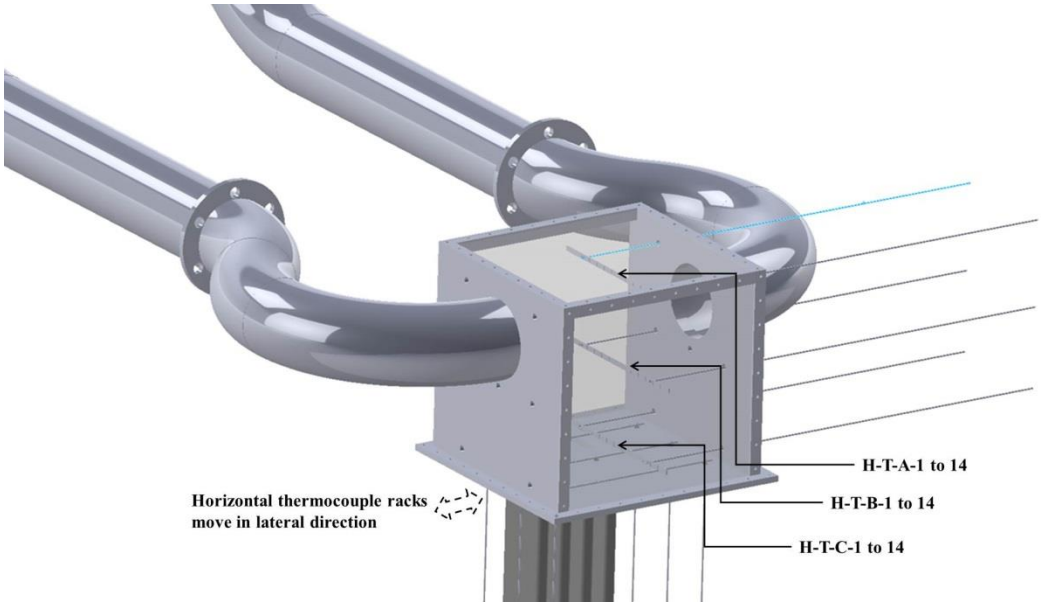

Figure 95. Movement of the horizontal thermocouple racks inside the upper plenum.

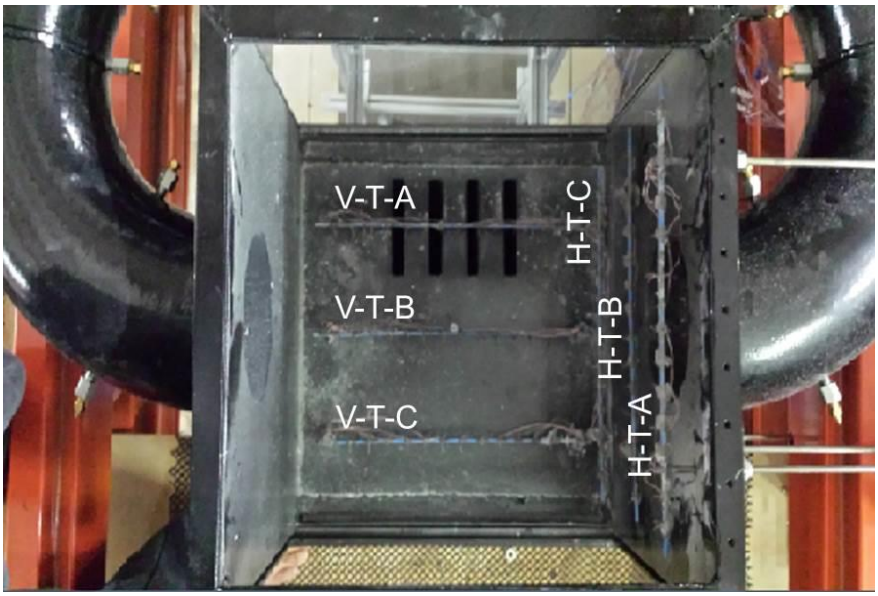

Figure 96. Actual arrangement of vertical and horizontal thermocouple racks inside the upper plenum.

VII.2.3. Data Acquisition System

A portable, high performance, nine-slot chassis NI PXIe-1078 was used for data acquisition (Figure 97). It comprised three main components; namely chassis, controller, and peripheral modules. Three NI PXIe-4353 thermocouple input module (each has 32-channels, 24-bit analog-to-digital, high-speed (90 S/s/ch) and high-resolution (1 S/s/ch) modes) provided integrated data acquisition and signal conditioning for temperature measurements (Figure 98). The NI PIXe 1078 controller slot provided control through a workstation that was installed in the 2nd floor of the experimental facility. Table 14 summarizes the instrumentation of the experimental test facility.

Table 14. Summary of instrumentation of ⅛ scale TAMU Air-Cooled RCCS.

Measurement	Location	Quantity	Instrument
Flow velocity	Heater inlet	x4	Amprobe hot wire anemometer
	Portable	x1	VelociCalc 9545-A air flow meter
		x1	Fluke 52 II digital thermometer
Temperature (TC)	Risers	x12	Omega type-T
	Upper plenum	x84	Omega type-T
	Chimney	x4	Omega type-T
Data acquisition	Throughout	x1	NI DAQ

Figure 97. NI PXIe-4353 chassis.

Figure 98. NI PXIe-4330 temperature module.

VII.2.4. Piping and Instrumentation Diagram

Figure 99 depicts the overall piping and instrumentation diagram (P&ID) for the TAMU Air-Cooled RCCS experimental test facility. The ambient air was first drawn into two GMB 2360 Thermo Andersen Instruments (0-110 V, 50/60 Hz compatible) (Figure 100) and two TE5005 TISCH Environmental air blowers (0-110V, 50/60 Hz compatible) (Figure 100). These 8 amps blowers capable of delivering maximum flow rate of 60 CFM, and were regulated by variable transformers (or variacs) manufactured by Stacy Energy Products Company (0-120 V input voltage, 140 V maximum voltage, 50 Hz, 6-12 amps) (Figure 101). Digital multimeters produced by Commercial Electric (MAS830B) were connected to these variable transformers (Figure 102). This connection was essential for voltage vs. velocity calibration curve since the analog dial reading from the variable transformers was hard to quantify. The air from the outlet of the air blowers was then channeled to the FT-400 in-line, open coil heaters fabricated by Tutco-Farnam Custom Products (Figure 103). These heaters were designed to accommodate high flow rates with

minimal pressure drop. The heaters have a maximum flow rate and pressure of 500 SCFM and 3 psig, respectively and the maximum power is 10 kW (cycle rate setting) with maximum outlet temperature of 482^{o}C (900 ^{o}F). The heaters would heat the air at the required temperature. The heating power was regulated by Tutco-Farnam power controllers that supply load to the heaters open coils. Tutco-Farnam 7550 series process controllers (range: 0-1093 ^{o}C with 1 ^{o}C resolution) (Figure 104) were wired between the heaters and building main power supply, on two separate circuits of 240 VAC and 480 VAC. Heater protection was provided by an independent set of electronics (PID units wired to the high limit thermocouple, type-K) which physically turned off the safety relay if the preset temperature was exceeded. The heated air would be channeled to the risers via associated pipings. The heated air from each riser would be collected and mixed inside the hot/upper plenum and exited via two exhaust pipes or chimneys. The twin chimneys that linked to the hot/upper plenum were 3.23 m in elevation, and consisted of two 0.1254 cm (6") diameter ducts that allowed different vent path configurations. The air was then released to the atmosphere inside the laboratory. Note that the experimental test facility was located inside the laboratory building; therefore the ambient air was governed by the temperature inside the building and not influenced by the building's outside temperature.

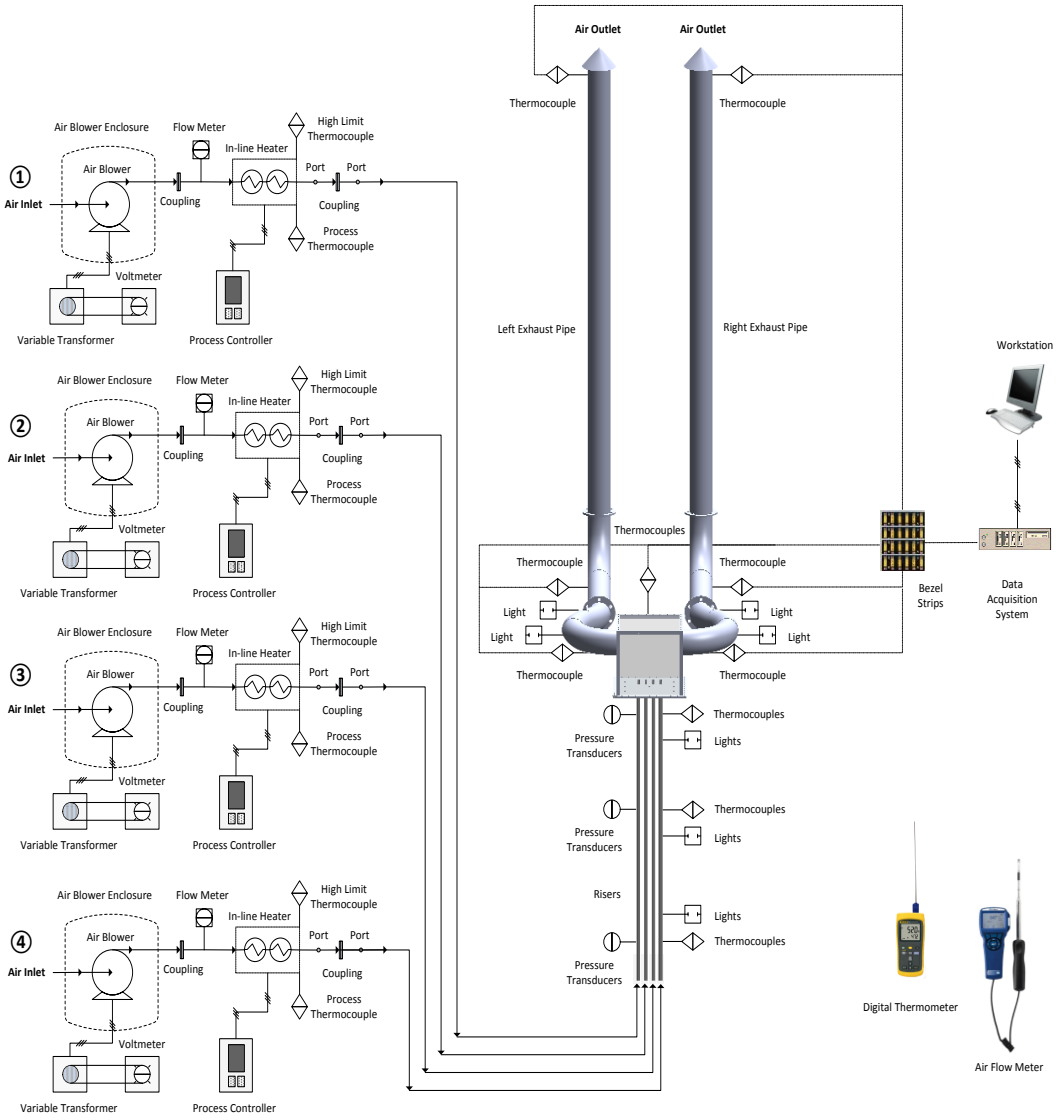

Figure 99. The overall piping and instrumentation diagram of the experimental test facility.

(a) (b)

Figure 100. (a) Tisch Environmental 5005 blower, (b) Thermo Andersen Instrument GBM2360 blower.

Figure 101. Stacy Electric Products Company 3NP1010 variable auto-transformer or variac.

Figure 102. Commercial Electric MAS830B digital multimeter.

Figure 103. Tutco-Farnam FT-400 in-line heater.

Figure 104. Tutco-Farnam process heater controller.

CHAPTER VIII

STAGE 5: EXPERIMENTAL TEST FACILITY SHAKEDOWN AND CHARACTERIZATION [*]

The experimental test facility shakedown was carried out to ensure that all instruments and equipment were functioning properly and safely, experimental data was recorded correctly and also to examine the general behavior of the experimental facility prior to commencing the experimental activities. The experimental test facility characterization was performed to observe the trend and general behavior of the experimental test facility, which fulfilled the expectations before starting the experimental activities based on selected cases. Several parameters of interest were monitored to confirm the ability of the experimental test facility to furnish reliable and repeatable data sets without any major modifications during the experiments. The experimental test facility shakedown and characterization was focused primarily of the measurement of inlet boundary conditions by the following sequences:

- Velocity profile for each riser
- Velocity-to-voltage calibration curve (analog-to-digital) for each variable auto-transformer

[*] Part of the data reported in this chapter is reprinted with permission from "Design considerations and experimental observations for the TAMU air-cooled reactor cavity cooling system for the VHTR" by Sulaiman, S. A., Dominguez-Ontiveros, E. E., Alhashimi, T., Budd, J. L., Matos, M. D., & Hassan, Y. A., 2015. *AIP Conference Proceedings*, 1659, 030002. http://dx.doi.org/10.1063/1.4916850-. Copyright [2015] by AIP Publishing LLC.

- Heater settings for selected cases
- Temperature start-up curves for selected cases
- Inlet temperature profiles for steady state cases

VIII.1. Velocity Profile for Each Riser

The TSI VelociCalc 9545-A (0-30 m/s, -10-60 °C, ±3% of the reading or ± 0.015 m/s accuracy) air velocity meter was used to measure air velocity profile from the outlet of each riser or the inlet of the upper plenum (Figure 105). The VelociCalc probe was placed at every ½" interval points started from the front side towards the rear side along each riser and the instantaneous velocity of the riser was recorded (Figure 106). All risers were in operation during the measurements; either at 2.25 m/s or 5 m/s. Top and rear windows of the upper plenum were intentionally put in close position throughout the measurement process in order to avoid any external influence from the surrounding. Only the front window was open for the access of the air flow meter. Velocity profile for each riser demonstrated slightly higher velocity distribution towards the rear side of the upper plenum (Figure 107 to Figure 110). This trending was more prominent at the higher velocity, i.e. 5 m/s. This is likely explained due to the probe partially restricting the inlet flow, which according to mass conservation, would increase the riser inlet velocities the more the probe was covering the inlet.

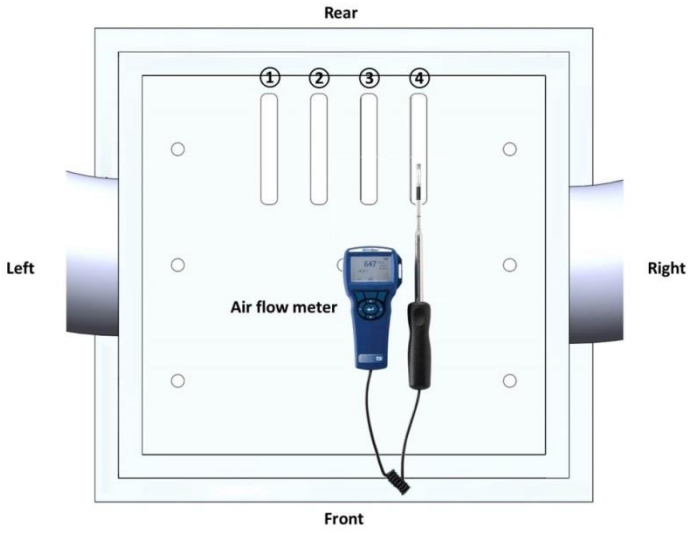

Figure 105. Plan view of the upper plenum showing the position of the air flow meter during measurements.

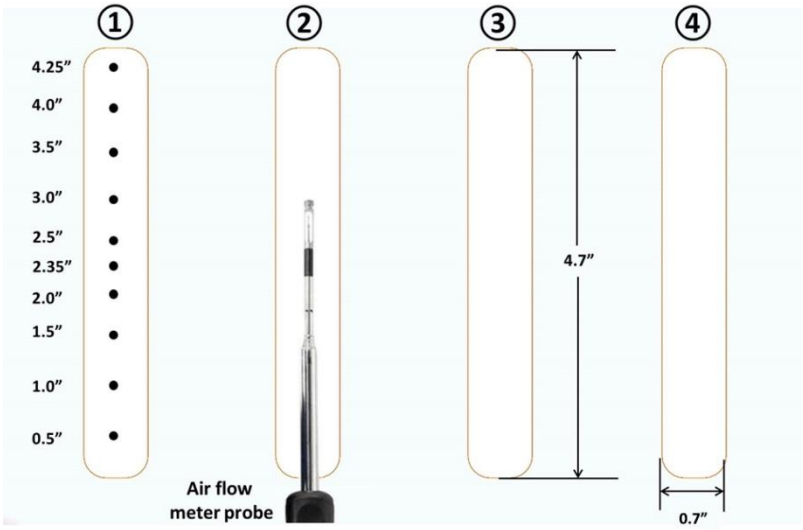

Figure 106. Measurement interval for the velocity profile.

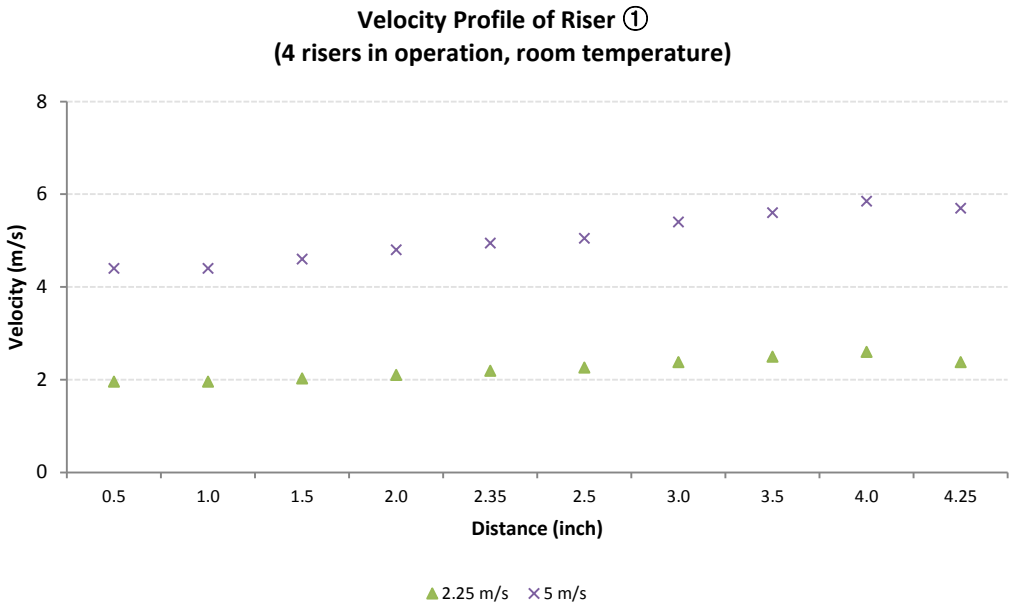

Figure 107. Velocity profile of Riser ①.

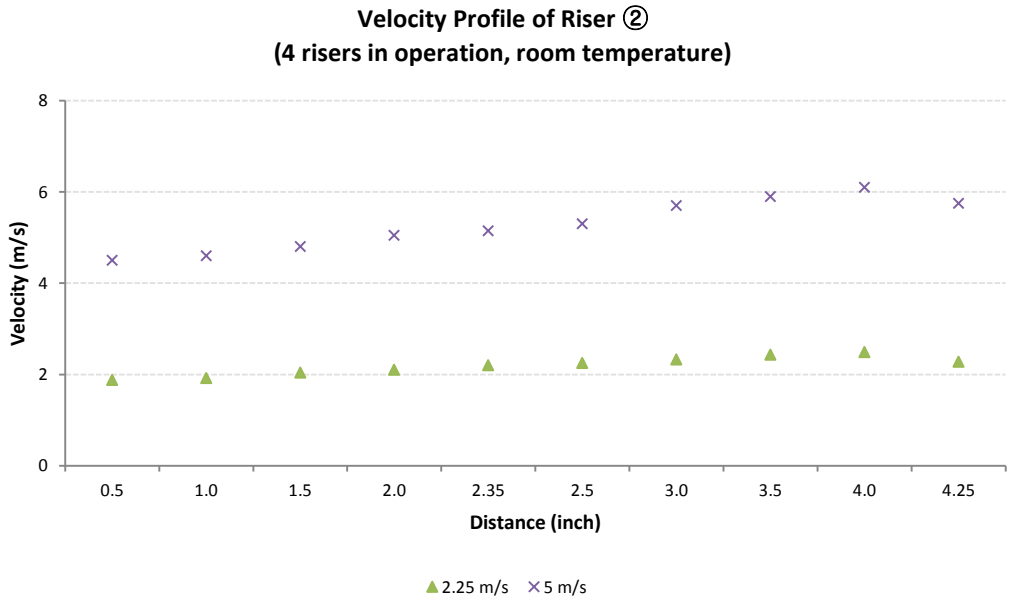

Figure 108. Velocity profile of Riser ②.

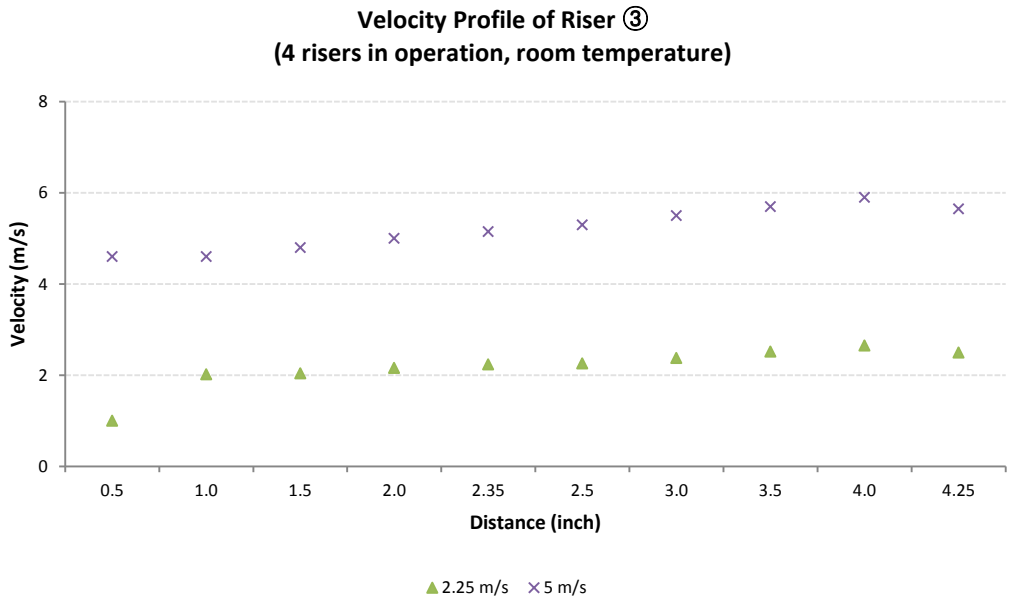

Figure 109. Velocity profile of Riser ③.

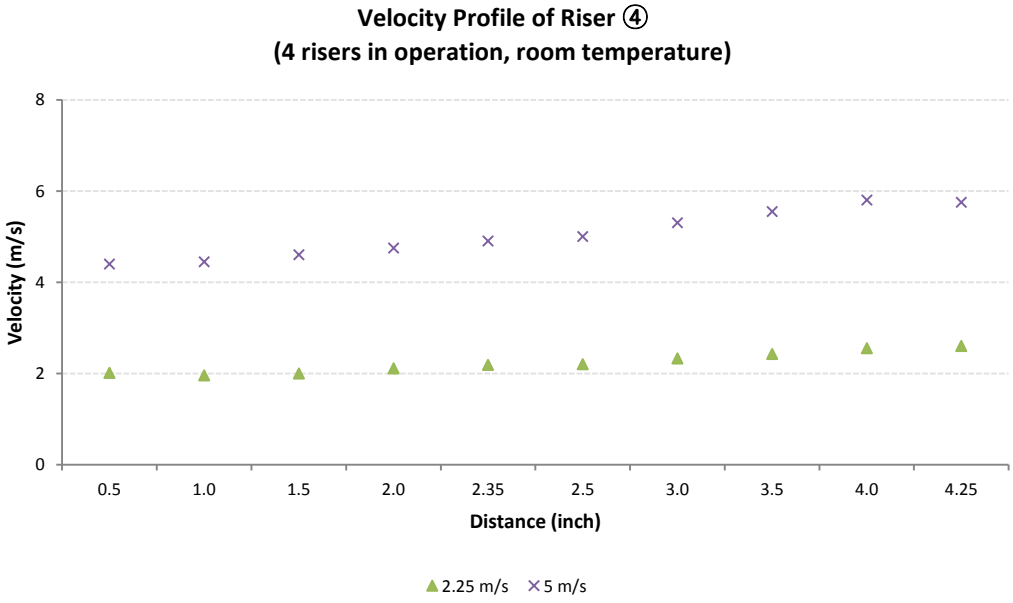

Figure 110. Velocity profile of Riser ④.

VIII.2. Velocity Calibration Curve (Analog-to-Digital) for Each Variable Auto-Transformer

Each variable auto-transformer was equipped with a Commercial Electric MAS830B digital multimeter for digital voltmeter reading. The installation of the digital multimeter was necessary due to ambiguity to provide precise and consistent value by analog dial reading of each variable auto-transformer. In fact, the provision of digital multimeter assisted the production of velocity vs. voltage curve for each riser (Figure 111 to Figure 114). The generation of these plots was very important step since these plots would be the primary reference for velocity setting and adjustment in every experiment. Only center-point velocity (at 2.35") was used in the plots. The plots demonstrated linear relationship between velocity and voltage for 2 m/s and above. The setting of each variable auto-transformer was checked periodically after several experiments.

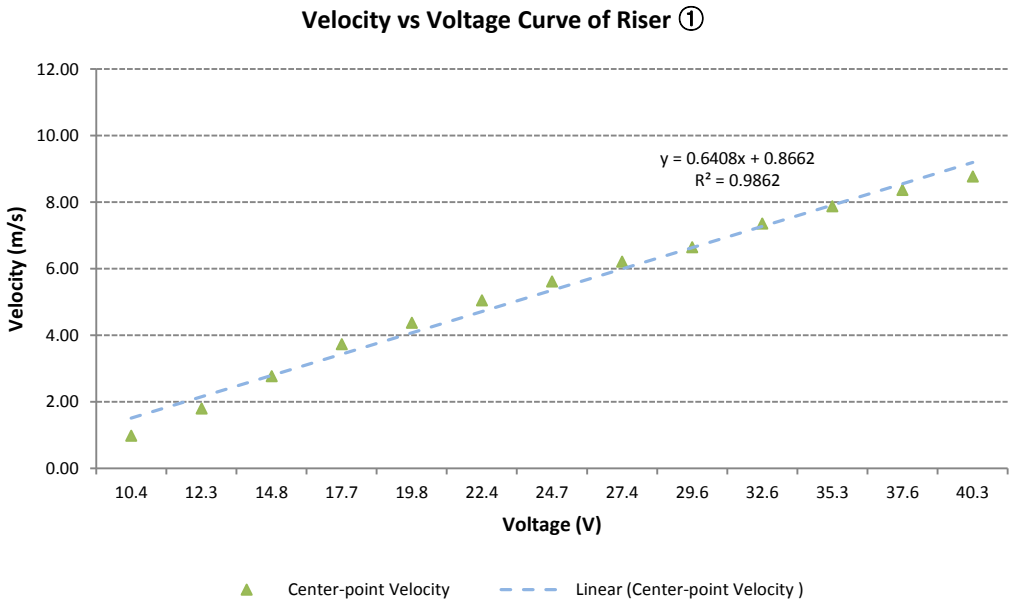

Figure 111. Velocity vs. voltage calibration of Riser ①.

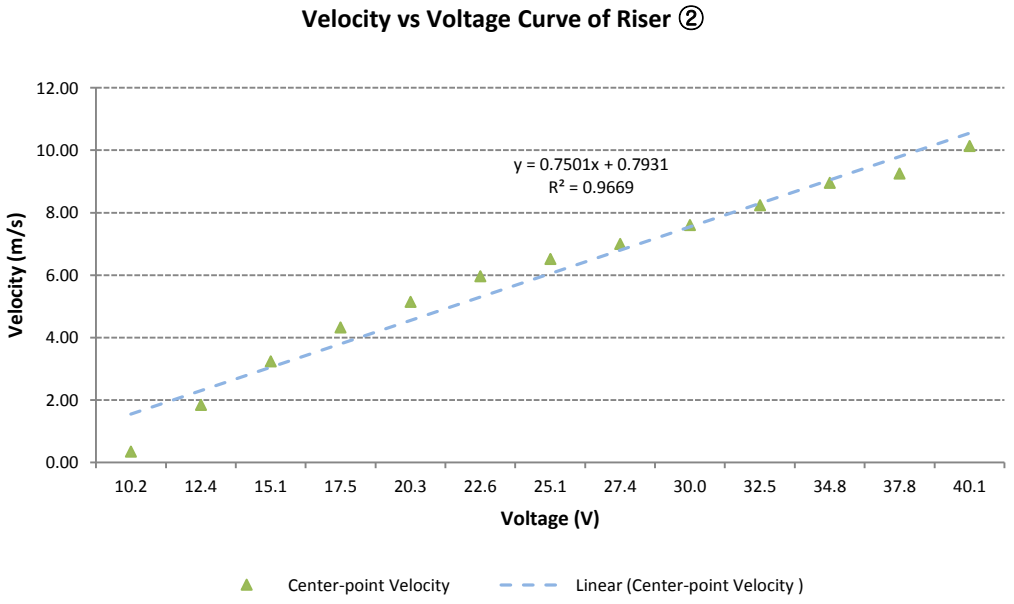

Figure 112. Velocity vs. voltage calibration of Riser ②.

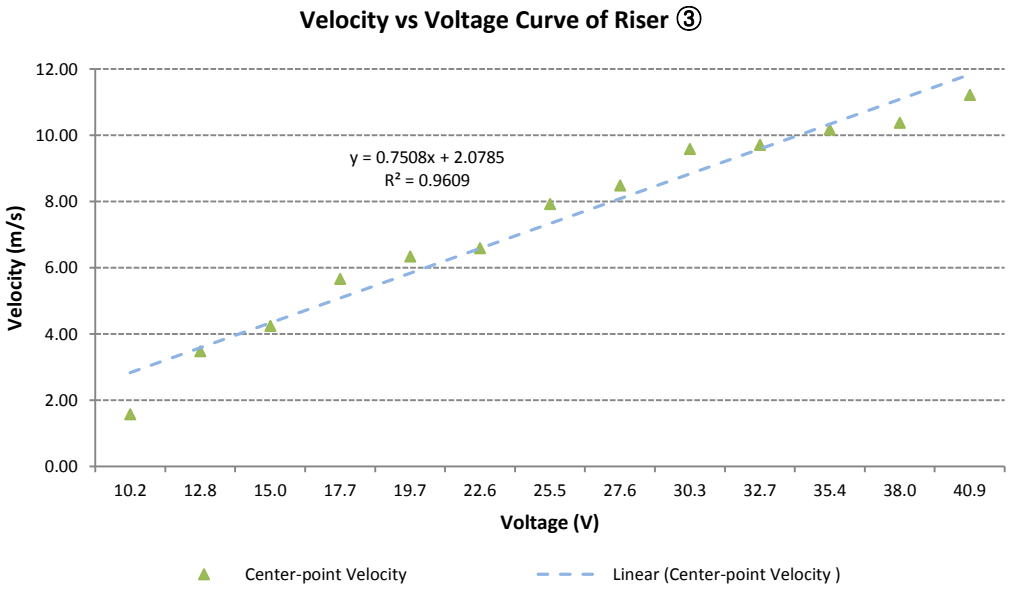

Figure 113. Velocity vs. voltage calibration of Riser ③.

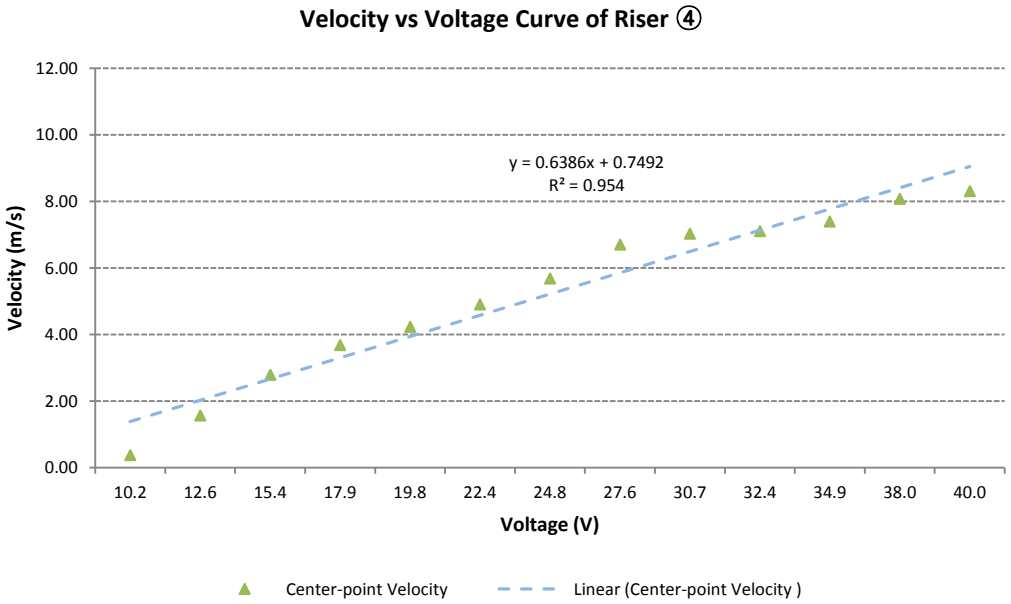

Figure 114. Velocity vs. voltage calibration of Riser ④.

VIII.3. Heater Settings for Selected Cases

Heater settings were very essential in order to ensure stable and constant heat generation for the inlet temperature boundary condition. The control scheme adopted by the heater process controller was based on the standard proportional, integral, and derivative (PID) with anti-reset windup. The first mode of control, P (Proportional) referred to the basic control scheme. The concept was the controller would compute the percentage of heat needed by the system and attuned the average power input to the heater to balance the system. The time proportioning was obtained by rationing the amount of time the heater was turned on to the amount of time the heater was turned off. The second mode, I (Integral) or regularly termed 'Automatic Reset Mode' was responsible to compute the difference between the current process temperature and the desired set point and mathematically rectified the system to compensate for the droop caused by the proportional mode. Droop was defined as the difference between the set point and the control point in a proportional system. Anti-reset windup was a special feature incorporated in the software to eliminate large errors when the system automatically adjusting the droop prior to nearing the system stability. The third mode, D (derivative) or frequently referred to 'Rate' was used to eliminate overshoots as the temperature was stabilizing and it was responsible to control the temperature rate of change when huge temperature fluctuations occurred.

Table 15. Nomenclature for the heater set-up mode.

Parameter	Description	Setting Range
PS	Process Setpoint	32 to 1999 F 0 to 1093 ^{o}C
HI	High Alarm Setpoint	32 to 1999 F 0 to 1093 ^{o}C
LO	Low Alarm Setpoint	32 to 1999 F 0 to 1093 ^{o}C
dL	Deviation Limit	0 to 199 F 0 to 111 ^{o}C
AC	Access Code	0 to 9999
Cr	Cycle Rate	1 to 19 seconds
Pb	Proportional Band	0 to 199 F 0 to 111 ^{o}C
rE	Reset	0 to 199 seconds
rA	Rate	0 to 199 seconds
CA	Calibration	± 99 F ± 55 ^{o}C
At	Auto Tune	ON/OFF
Fb	Filter Band	0 to 25 F/ ^{o}C
FP	Filter Period	0 to 10.0 seconds
tU	Temperature Units	Celcius or Fahrenheit
Hd	Heater Delay	0 to 199 seconds
AS	Auto Start	NO/YES

Under the set-up mode of the heater controller, the in-line heater parameters could be adjusted (Table 15). PS was the process set point for the heater system and it was the target temperature for the three mode PID algorithm. Different values were used for each case as indicated in Table 16 to Table 19. HI was the High Temperature Alarm Setpoint and 400^{o}C was set for all the experiments. HI would be activated if the Process Temperature was exceeding this set point. LO was the Low Temperature Alarm Setpoint and 38^{o}C was used throughout all cases. LO would be activated if the Process Temperature fallen below this setpoint. dL, the Deviation Limit was set at 28^{o}C and it would shut-off the Solid State Relay (SSR) output if the Process Temperature reached the set point plus this setting. AC stands for Access Code and this parameter was turned off in all the experiments.

Cr stood for the Cycle Rate of the heater system and 1 second was employed for all experiments. Cr role was to set the rate at which the heater power output would turned on and off since the controller was the standard proportional time base unit. Pb was defined for Proportional Band which was used to indicate the range over which the controller would proportion. The Pb was set at 70^{o}C for all the controllers except for the controller for Heater ③ since during the experimental test facility characterization, it was found that by setting the Pb at 110^{o}C, the temperature fluctuation experienced in the beginning of the experiments would be eliminated. rE stood for the integration time for the second mode in the three mode control. 115^{o}C was employed in all controllers except Heater ③ controller (119^{o}C) due to similar reasoning used for the different Pb set-up. rA was the Rate function for the heating mode which assigned the Differentiation constant for the

third mode of three mode control scheme. Heater ③ controller was set at two while five was used for the other controllers.

CA (the digital calibration for process sensor) provided a direct digital offset to the process temperature was set to zero for all controllers. At (Auto Tune) was turned off for all experiments. Fb (Filter Band) was set to $2^{o}C$ for all controllers to produce a more stable display of the average temperature readings. 10^{th} of the seconds was adopted for FP (Filter Period) since this value was the smallest number that provided a stable display. Celcius unit was used for tU (Temperature Unit) throughout the experiments. Hd (heater time delay) was set to zero for all controllers. No AS (Auto Start) was adopted for all experiments. The corresponding digital multimeter settings are provided in Table 20 to Table 23.

Table 16. Case 1 heater controller settings (4 risers, 5 m/s, 120 ºC).

Parameter	Riser ①	Riser ②	Riser ③	Riser ④
PS	168	184	160	200
HI	400	400	400	400
LO	38	3	38	38
dL	28	28	28	28
AC	00	00	00	00
Cr	01	01	01	01
Pb	70	70	110	70
rE	115	115	119	115
rA	05	05	02	05
CA	00	00	00	00
At	OFF	OFF	OFF	OFF
Fb	02	02	02	02
FP	10.0	10.0	10.0	10.0
tU	C	C	C	C
Hd	00	00	00	00
A5	no	no	no	no

Table 17. Case 2 heater controller settings (1 riser, 5 m/s, 120 ºC).

Parameter	Riser ①	Riser ②	Riser ③	Riser ④
PS	-	-	-	214
HI	-	-	-	400
LO	-	-	-	38
dL	-	-	-	28
AC	-	-	-	00
Cr	-	-	-	01
Pb	-	-	-	70
rE	-	-	-	115
rA	-	-	-	05
CA	-	-	-	00
At	-	-	-	OFF
Fb	-	-	-	02
FP	-	-	-	10.0
tU	-	-	-	C
Hd	-	-	-	00
A5	-	-	-	no

Table 18. Case 3 heater controller settings (4 risers, 2.25 m/s, 120 ºC).

Parameter	Riser ①	Riser ②	Riser ③	Riser ④
PS	197	209	179	217
HI	400	400	400	400
LO	38	38	38	38
dL	28	28	28	28
AC	00	00	00	00
Cr	01	01	01	01
Pb	70	70	110	70
rE	115	115	119	115
rA	5	05	02	05
CA	00	00	00	00
At	OFF	OFF	OFF	OFF
Fb	02	02	02	02
FP	10.0	10.0	10.0	1 .0
tU	C	C	C	C
Hd	00	00	00	00
A5	no	no	No	no

Table 19. Case 4 heater controller settings (4 risers, 2.25 m/s, 120 ºC).

Parameter	Riser ①	Riser ②	Riser ③	Riser ④
S	-	-	-	203
HI	-	-	-	400
LO	-	-	-	38
dL	-	-	-	28
AC	-		-	00
Cr	-	-	-	01
Pb	-	-	-	70
rE	-	-	-	115
rA	-	-	-	05
CA	-	-	-	00
At	-	-	-	OFF
Fb	-	-	-	02
FP	-	-	-	10.0
tU	-	-	-	C
Hd	-	-	-	00
A5	-	-	-	no

Table 20. Case 1 digital multimeter settings (4 risers, 5 m/s, 120 ºC).

Parameter	**Riser ①**	**Riser ②**	**Riser ③**	**Riser ④**
Voltage (V)	21.1	20.3	17.5	21.6

Table 21. Case 2 digital multimeter settings (1 riser, 5 m/s, 120 ºC).

Parameter	**Riser ①**	**Riser ②**	**Riser ③**	**Riser ④**
Voltage (V)	-	-	-	21.8

Table 22. Case 3 digital multimeter settings (4 risers, 2.25 m/s, 120 ºC).

Parameter	**Riser ①**	**Riser ②**	**Riser ③**	**Riser ④**
Voltage (V)	13.4	13.5	13.6	12.0

Table 23. Case 4 digital multimeter settings (1 riser, 2.25 m/s, 120 ºC).

Parameter	**Riser ①**	**Riser ②**	**Riser ③**	**Riser ④**
Voltage (V)	-	-	-	23.3

VIII.4. Temperature Start-Up Curves for Selected Cases

Prior to the start-up of the heaters, the upper plenum's glass windows and insulation were reinstalled. The breaker for each heater controller was closed and data to reach to the desired temperature as per Table 16 and Table 19 were keyed-in. The heaters were energized and started to generate heat. The system was allowed to reach steady state after several hours. The temperature start-up data for each case was recorded by the NI Signal Express at 1 hertz and 5 sampling rate (Figure 115 to Figure 120, Figure 123 and Figure 124). The temperature readings of the temperature probes installed near the risers' exit were monitored closely until reaching the steady state.

Heater and digital multimeter settings based on Table 20 and Table 23 were utilized for the final settings of the start-up of the experimental facility for Case 1. Figure 115 shows that all risers were subjected to nearly uniform heat rate initially, until half an hour later, where Riser ①, ②, and ③ rate of increase were slightly above Riser ④. As a result, the heater settings for Riser ①, ②, and ③ were adjusted to the values provided in Table 16 to reach the steady state target temperature of 120^{o}C. The left and right exhaust pipe inlet temperatures were close to each other throughout the heating up process. Similar behavior was exhibited by the left and right exhaust pipe outlet temperatures as well. This trending suggested that the flow inside the upper plenum was symmetric.

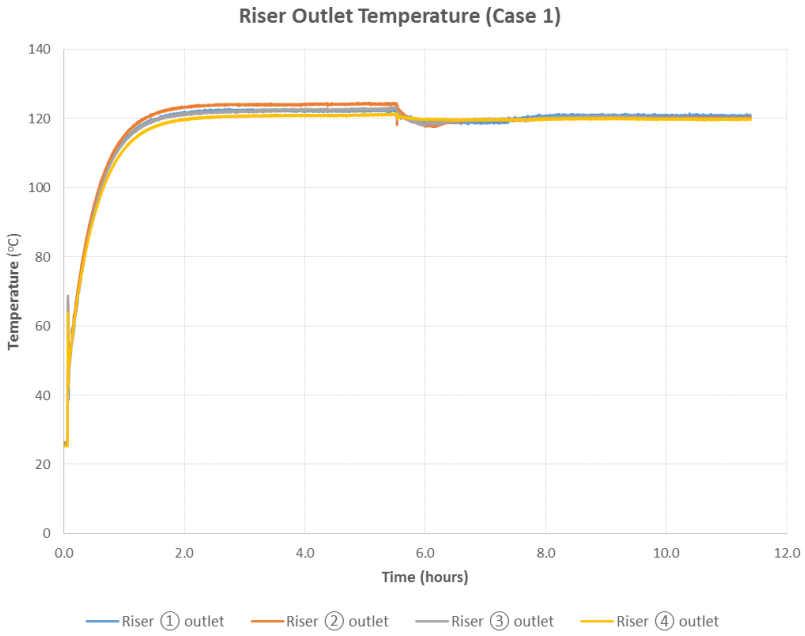

Figure 115. Riser outlet temperature start-up curve (Case 1).

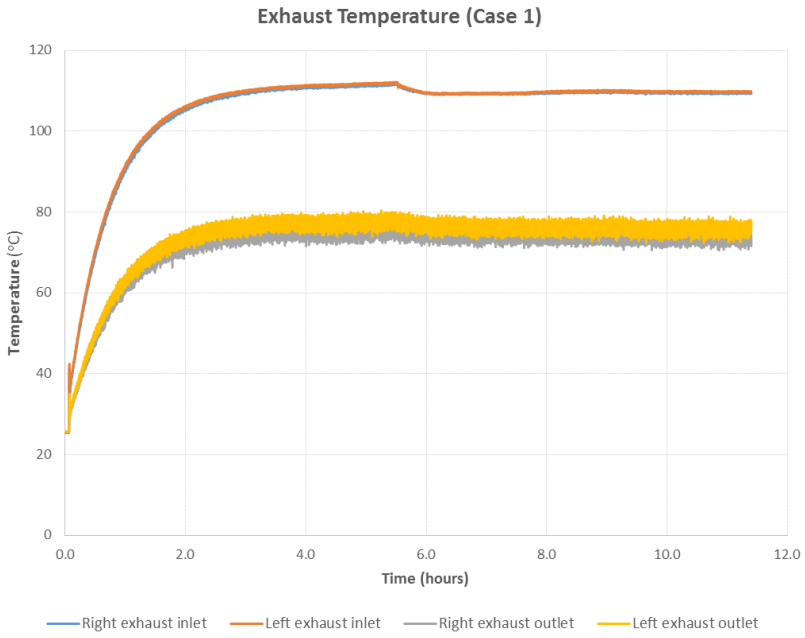

Figure 116. Exhaust temperature start-up curve (Case 1).

For the start-up curves final settings of Case 2, the heaters used settings provided in Table 17 whereas the values in Table 21 were utilized by the digital multimeters. In Case 2, only one riser, namely Riser ④ was active. The neighboring risers were also affected by the heating of Riser ④ of which the nearest riser, i.e. Riser ③ has the next highest temperature followed by Riser ② and lastly Riser ① (Figure 117).

For the first ten minutes, the flow exited the upper plenum via the inlet of the two exhaust pipes. However, after ten minutes, the flow has started to become asymmetric. It was noted that most of the flow exited through the inlet of the left exhaust pipe only which was not the nearest exit and more importantly in opposite direction. This was indicated by the rise and fall of the left and right exhaust outlet temperatures, respectively (Figure 118). This trending indicated the flow inclination towards one direction, i.e. preferential flow and of course this event could trigger the flow reversal phenomenon.

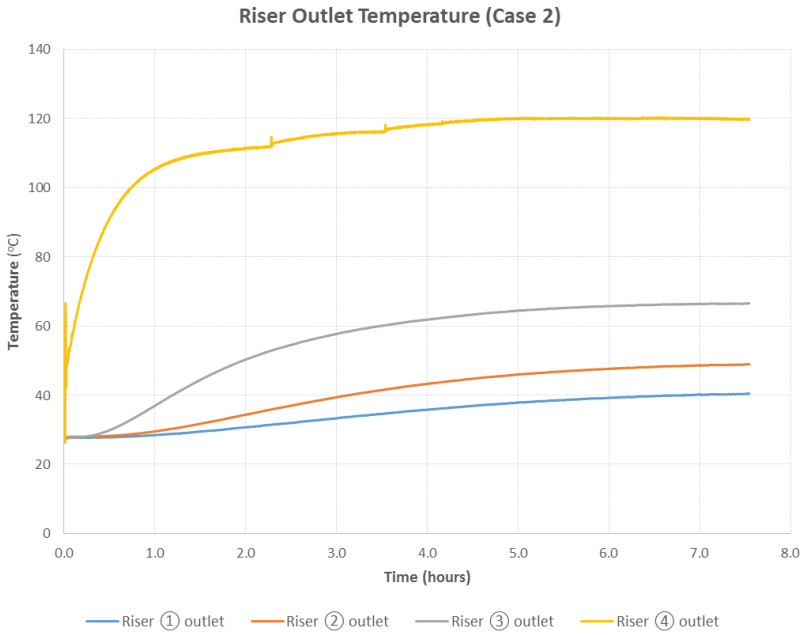

Figure 117. Riser outlet temperature start-up curve (Case 2).

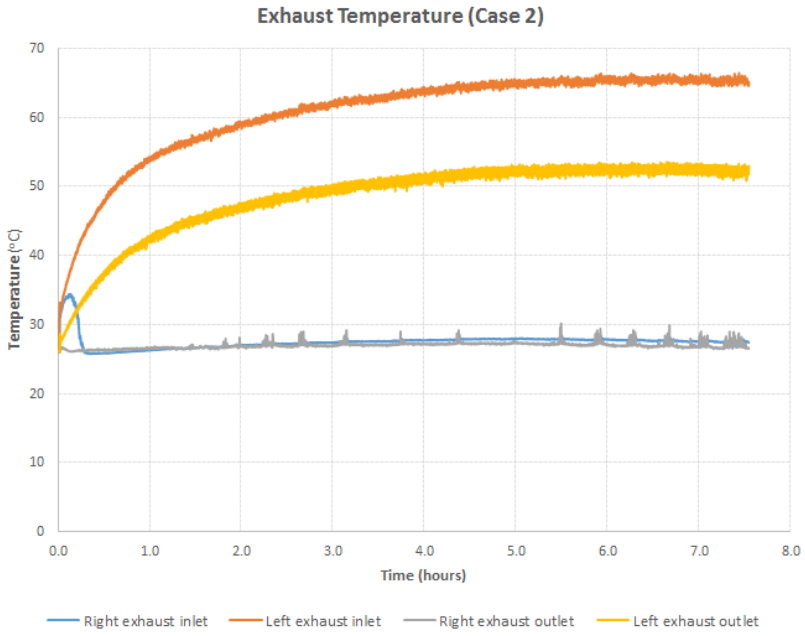

Figure 118. Exhaust temperature start-up curve (Case 2).

For Case 3, the settings of the heaters and digital multimeters were based on Table 18 and Table 22 in order to achieve 120°C steady state temperature and 2.25 m/s velocity at the inlets of the upper plenum. Prior to finalization of the start-up settings, the heater PS value for Riser ① was lower than the other risers. Therefore, the PS value for Riser ① was adjusted twice in between three to five hours after the initial start-up (Figure 119) so that the desired steady state temperature could be achieved.

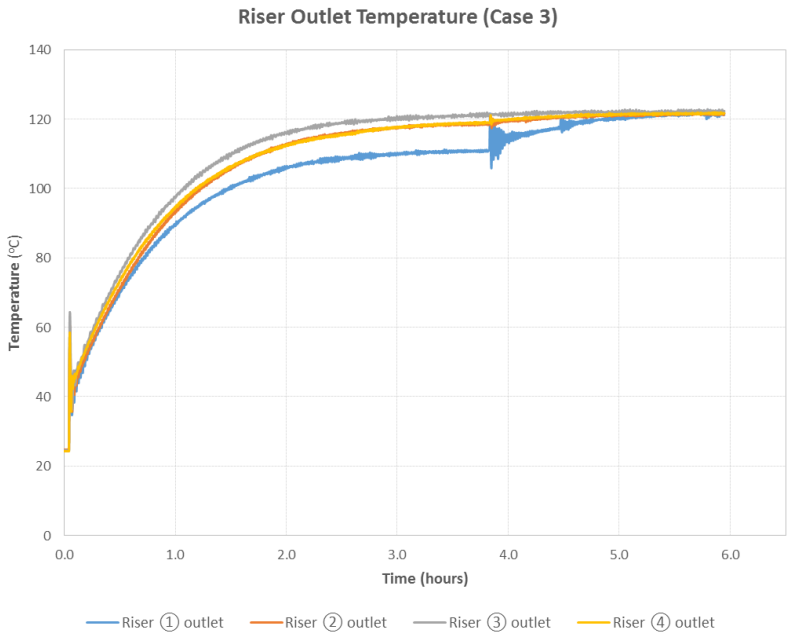

Figure 119. Riser outlet temperature start-up curve (Case 3).

Within the first two hours after the start-up, both the left and right exhaust inlet temperatures were close to each other, respectively. Similar trend was exhibited by the left and right exhaust outlet temperatures as well. Just after passing two hours, both the right

exhaust inlet and outlet temperatures plummeted to the value of room temperature, respectively (Figure 120).

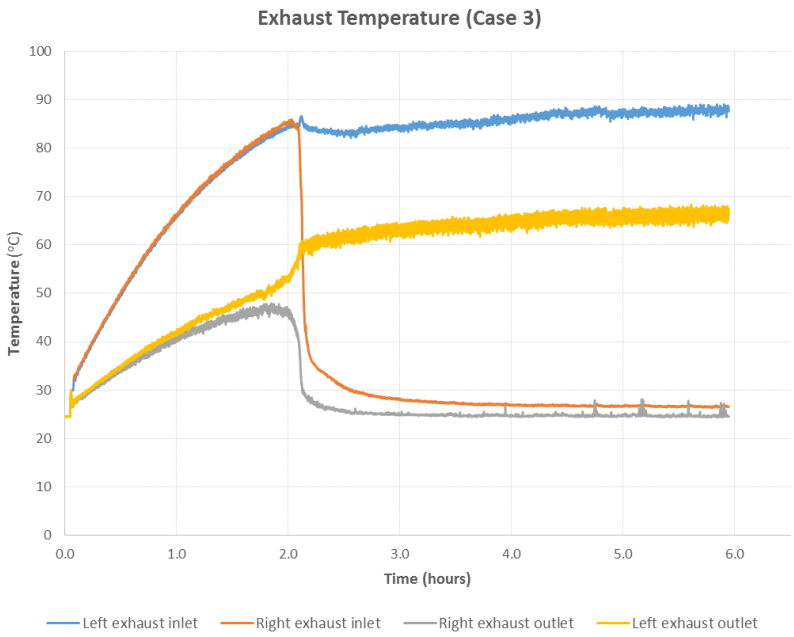

Figure 120. Exhaust temperature start-up curve (Case 3).

This flow reversal phenomenon deserved more detailed analysis than other cases. Observation of temperature differences at various points demonstrated the behavior of the system pre and post occurrence. Figure 121 shows the locations and definitions of various temperature differences. It was observed that ΔT_{out} has started to rise from the beginning at the start-up. The rate of increase was gradual prior to reach two hours. At this time, the value of ΔT_{in} was negligible. Both ΔT_{left} and ΔT_{right} were increased during this time as

well. Just before reaching two hours, ΔT_{left} has started to decrease while ΔT_{right} was still increasing. After two hours, the slopes of both ΔT_{out} and ΔT_{in} were at the maximum, respectively; ΔT_{right} reached its peak value, and ΔT_{left} continued to decrease (Figure 122).

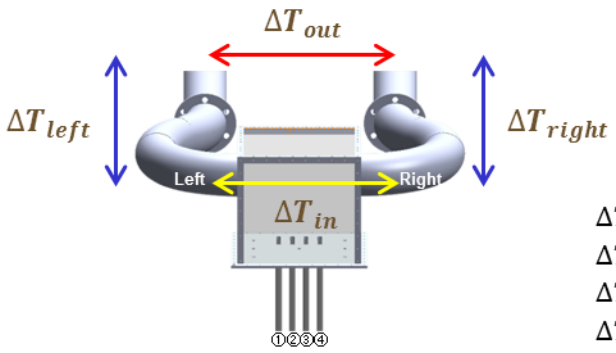

Figure 121. Temperature differences schematic for Case 3.

ΔT_{right} plummeted sharply at the onset of flow reversal. ΔT_{left} also continued to drop. Both ΔT_{left} and ΔT_{out} continued to rise, respectively; however, the rate of increase was more gradual.

Table 19 and Table 23 furnished the heater and the digital multimeter settings for Case 4. The trending for the riser outlet and exhaust temperatures was very similar to Case 2 (Figure 123 and Figure 124). However, it was noticed that it took less than ten minutes for the flow to become preferential flow and therefore led to flow reversal.

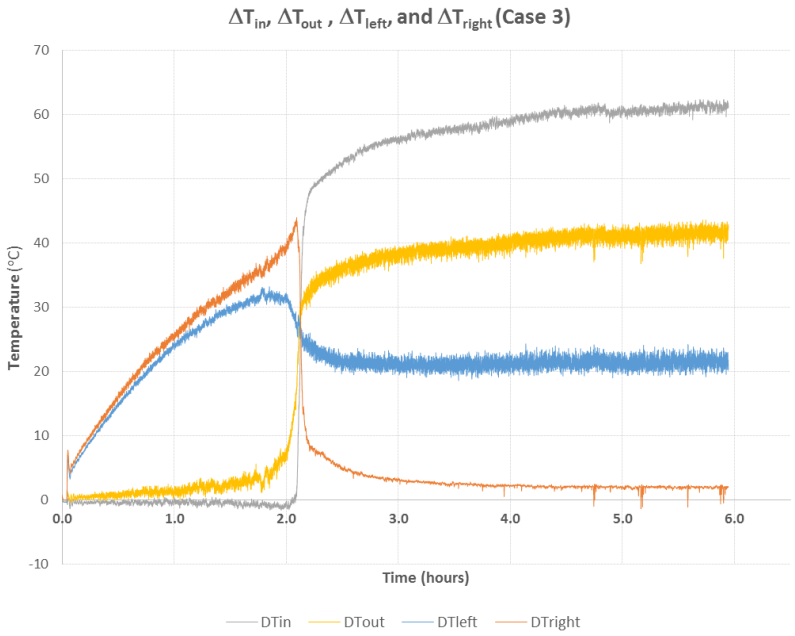

Figure 122. Temperature difference curves for Case 3.

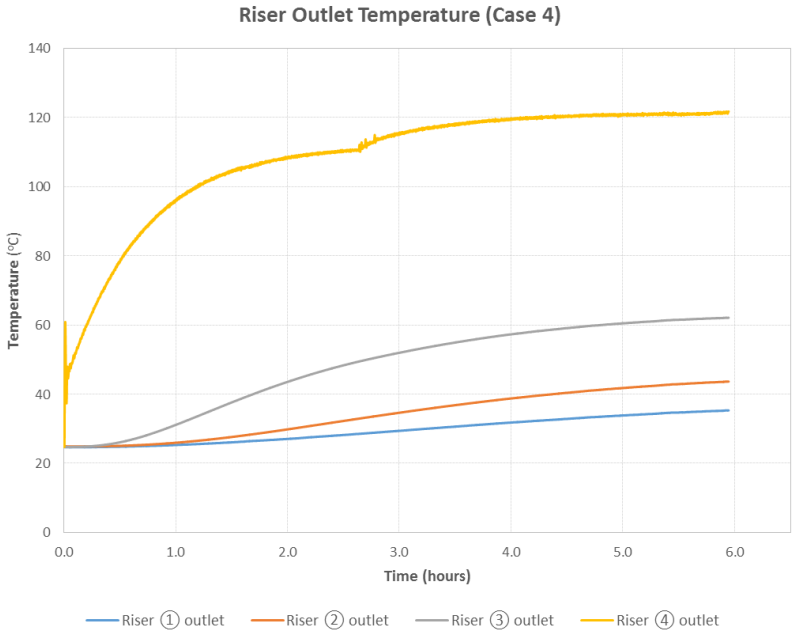

Figure 123. Riser outlet temperature start-up curve (Case 4).

For each case, several runs were conducted to verify the repeatability of the system to reproduce the same start-up curves prior to the actual experiments. Checking and verification on the pipe joints, flanges, connections, instrumentation ports were also carried out in parallel to ensure everything was sealed and plugged.

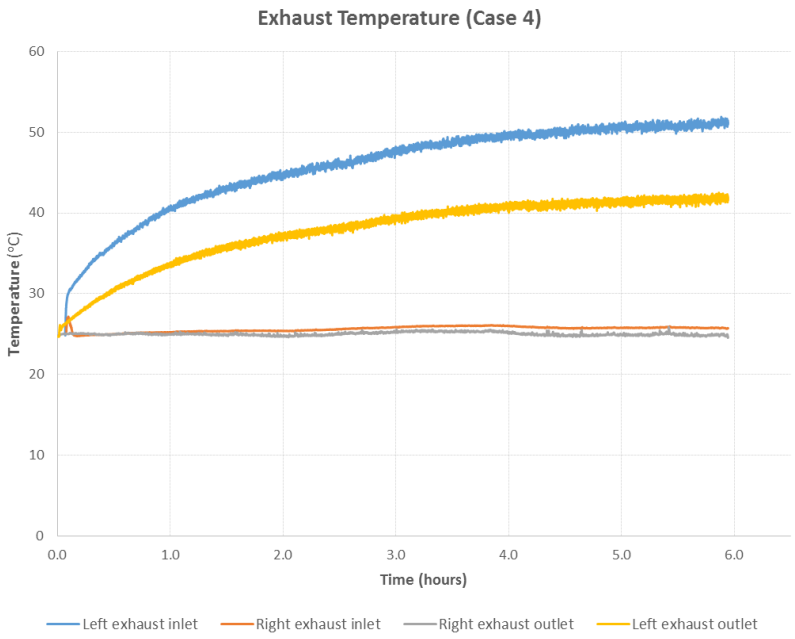

Figure 124. Exhaust temperature start-up curve (Case 4).

CHAPTER IX

STAGE 6: DEVELOPMENT OF TEST MATRIX AND EXPERIMENTAL RESEARCH ACTIVITIES [*]

IX.1. Experimental Matrix

Four selected cases at steady state temperature and velocity were identified for the experimental matrix (Table 24).

Table 24. Experimental matrix for temperature and velocity measurements at steady state condition.

Case	Riser	Inlet Velocity (m/s)	Inlet Temperature (°C)
1	All	5	120
2	Riser ④	5	120
3	All	2.25	120
4	Riser ④	2.25	120

[*] Part of the data reported in this chapter is reprinted with permission from "Design considerations and experimental observations for the TAMU air-cooled reactor cavity cooling system for the VHTR" by Sulaiman, S. A., Dominguez-Ontiveros, E. E., Alhashimi, T., Budd, J. L., Matos, M. D., & Hassan, Y. A., 2015. *AIP Conference Proceedings*, 1659, 030002. http://dx.doi.org/10.1063/1.4916850-. Copyright [2015] by AIP Publishing LLC.

In addition to the above cases, four more cases at the adiabatic conditions were carried out for the velocity measurements (Table 25).

Table 25. Additional experimental matrix for velocity measurements at adiabatic condition.

Case	Riser	Inlet Velocity (m/s)	Inlet Temperature (°C)
1a	All	5	Room temperature (~25)
2a	Riser ④	5	Room temperature (~25)
3a	All	2.25	Room temperature (~25)
4a	Riser ④	2.25	Room temperature (~25)

IX.2. Experimental Procedures

IX.2.1. Temperature Measurements

The generic procedure described in this section was applicable to the steady state temperature profile measurements in the upper plenum for the four risers. It was also applicable to certain extent (with slight modifications) on any experiments involving any number of risers. Ambient temperature measurement was carried out prior to perform any experiments using Fluke 52 II dual input digital thermometer (± 0.05% of reading + 0.3 ^{o}C accuracy; type-J, K, T, E) at two different locations on the 2nd floor of the experimental

facility. Visual observation was made to ensure that both thermocouple racks were at their initial position. The insulation and all glass windows of the upper plenum were removed for the visual inspection of 84 units of fine thermocouple wires inside the upper plenum. Temperature probes in the risers and the exhaust pipes were inspected to ensure their condition and functionality. Confirmation of the connection of all miniature thermocouple connectors mounted on the bezel strips was executed. The DAQ system and the workstation in the 2nd floor were turned on and the NI Signal Express was used to check each thermocouple reading. Each blower was started and the flow rate was controlled by each variable transformer or variac.

The TSI VelociCalc 9545-A (0-30 m/s, -10-60 ^{o}C, ±3 % of the reading or ± 0.015 m/s accuracy) air velocity meter was used to measure air velocity from the outlet of each riser or the inlet of the upper plenum. The VelociCalc probe was placed in the middle of the riser and the variac was regulated to obtain the required velocity. Each variac was equipped with a voltmeter to provide digital reading for data acquisition since the analog dial reading of the variac could lead to ambiguity. After obtaining the velocity data in the middle of the first riser, measurement of velocity spatial profile of that riser was carried out at 0.5" interval. The mean velocity of the first riser was computed and the process was repeated for remaining risers. The upper plenum's insulation and glass windows were reinstalled prior to the start-up of the heaters. The breaker for each heater controller was closed and data for reach desired temperature was key-in. The heaters were energized and started to generate heat. The system was allowed to reach steady state after several hours and the start-up temperature data was recorded. The temperature readings of the

temperature probes installed near the risers' exit were monitored closely until reaching the steady state.

Once the steady state was reached, measurement using the vertical rack thermocouples was initiated. The vertical insertion system was used to move the vertical thermocouple racks in axial direction (Figure 94). The temperature data was taken from 1" to 17" at 0.5" interval. The vertical thermocouple rack was withdrawn to its original position at 1" prior to proceed to the horizontal temperature racks measurement. Similarly, the horizontal insertion system was utilized to move the horizontal thermocouple rack in lateral direction (Fig. 5-6-4). Data for temperature from 1" to 16.5" at the interval of 0.5" was captured by the NI Signal Express. Observations on alignment of the three levels of horizontal thermocouple racks, i.e. H-T-As, H-T-Bs, and H-T-Cs, at 5", 10", and 15" were carried out at the window provided by the upper plenum's top insulation. The horizontal thermocouple rack was retracted to its initial position after obtaining all required temperature measurements. All the heaters were turned off and their breakers were moved to open position. The blowers were remained in operation to cool down the experimental facility for an extended period of time. The post-experiment measurement of velocity spatial profile for each riser was performed at the room temperature in order to ensure consistency and reliability of the pre-experiment inlet velocity boundary conditions data.

IX.2.2. Velocity Measurements

Prior to describing the procedure of steady state velocity measurement using PIV technique, a brief description of equipment that formed the system was described in the following paragraphs.

Beamtech Vlite-200 was a compact, dual-cavity laser designed for particle image velocimetry (PIV) application that provided a transmission of green (532 nm) light pulse (Table 26). Two water-proof 1064 nm laser heads (695 mm x 198 mm x 115 mm) with a beam delivery arm were mounted on a single base plate (Figure 125). The optical layout for the laser head is portrayed in Figure 126.

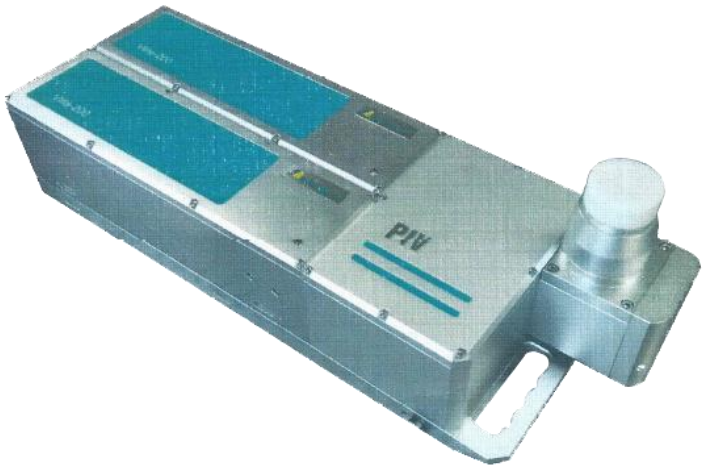

Figure 125. Beamtech Vlite-200 laser head (light arm is not shown) (Beamtech Optronics Co. Ltd., 2013).

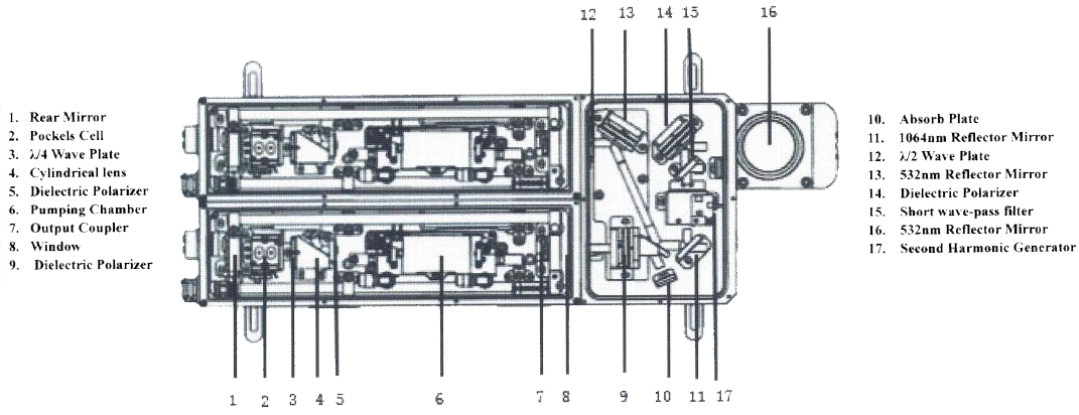

Figure 126. Outline of Beamtech Vlite-200 laser head (Beamtech Optronics Co. Ltd., 2013).

Power supply for the Vlite-200 was required to control the laser and signal for the laser operation. A closed loop cooling water was in place to absorb the heat generated by the two pumping chambers inside the laser head. The pump circulated cool distilled water from the 7-liter stainless steel reservoir through a polypropylene colophony filter prior to enter the laser head. Removal of contaminants, i.e. ions, dirt, and deposits that could potentially reduce the output power were carried out by the filter. The heated distilled water was sent back to the air-to-water heat exchanger by passing through the flow sensor. The flow sensor would send a signal to the power supply to shutdown the laser should the water flow rate decrease to dangerous levels. Temperature controller and an internal valve were used to stabilize the cooling water temperature and adjustment of the flow rate for maintaining constant temperature (Figure 127).

Table 26. Laser descriptions and specifications for the PIV experiments (Beamtech Optronics Co. Ltd., 2013).

Description	Specification
Model	Vlite-200
Wavelength (nm)	532
Repetition Rate (Hz)	0-15
Pulse Energy (mJ)	200
Energy Stability (1)	≤ 2%
Pulse Duration (ns) (2)	< 8
Beam Diameter (mm)	7
Beam Divergence (mrad) (3)	< 3
Pointing Stability (μrad)	< 50
Spectral Purity	≥ 99.8%
Near Field Beam Profile	Flat-top, Uniform
Jitter (ns) (4)	± 0.5

(1) 100% pulse-to-pulse energy stability measured over 1 hour
(2) Full width half maximum (FWHM)
(3) Full angle at $1/e^2$ of the peak
(4) With respect to external trigger

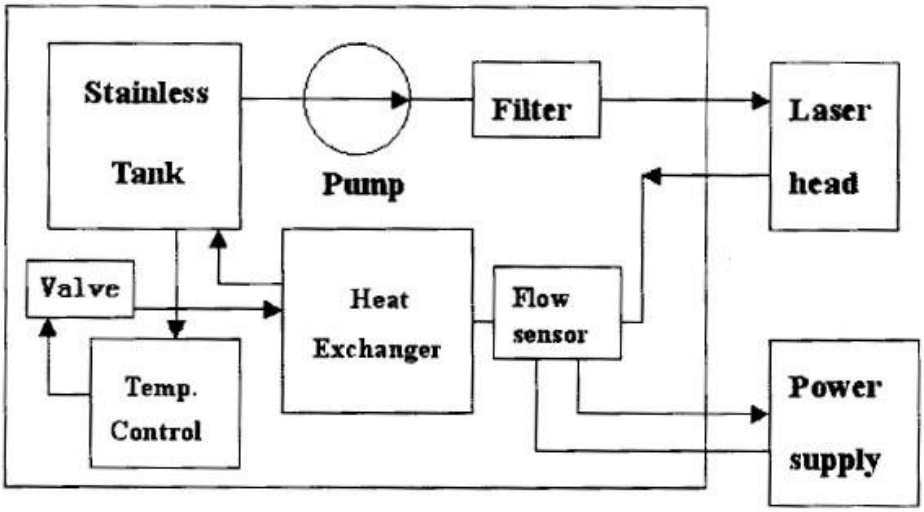

Figure 127. Closed loop cooling water system for Beamtech Vlite-200 laser head (Beamtech Optronics Co. Ltd., 2013).

Figure 128. Beamtech Vlite-200 power supply and cooling system (Beamtech Optronics Co. Ltd., 2013).

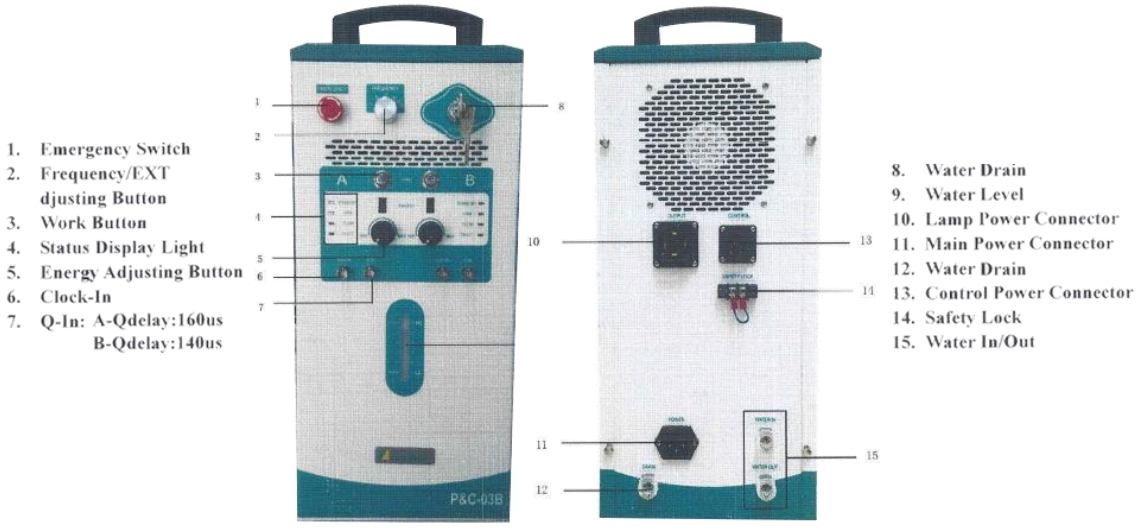

Figure 129. Beamtech Vlite-200 power supply panel (Beamtech Optronics Co. Ltd., 2013).

Power supply and cooling unit came as one unit (Figure 128 and Figure 129). A beam delivering arm was attached in between the laser head and optics for the laser sheet (Figure 130). The optics for laser sheet was fixed to the z-direction of the BiSlide positioning system (Figure 131).

Figure 130. The beam delivering arm for Beamtech Vlite-200 laser.

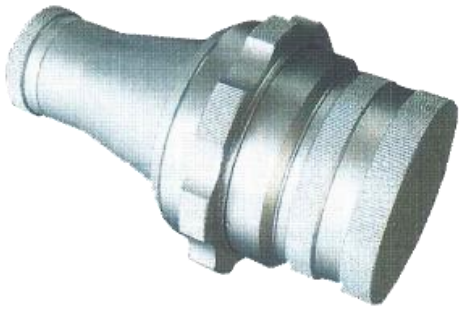

Figure 131. Beamtech Vlite-200 laser optics (Beamtech Optronics Co. Ltd., 2013).

Figure 132. Simran SIM-2000 **s**tep-up/down transformers with fuse protection.

Figure 133. Quantum Composers 9618+ pulse generator (Quantum Composers, Inc., 2012).

A Simtran SIM-2000 step up/down transformer (2000 W maximum capacity, 50/60 Hz compatible, 22 lbs weight, 13”x9”x7” dimensions, fused protected, converts 110/120 V to 220/240 V or converts 220/240 V to 110/120 V) was connected for the laser (Figure 132). A Quantum Composers 9618+ digital delay pulse generator (8 independent channel outputs, 10 ns resolution, 2-20 V output range, 10 ns and 0.0001 X (width and delay) accuracy, < 500 ps jitter) was used to control the delay periods and pulse outputs of the laser and the high speed camera (Figure 133).

Figure 134. Tektronix TDS 210 digital real-time oscilloscope (Tektronix, Inc., 2012).

Tektronix TDS 210 digital real-time oscilloscope (60 MHz bandwidth with selectable 20 MHz bandwidth limit, 1 GS/s sample rate, 2500 point record length for each channel, high-resolution, high-contrast LCD display) was used to monitor signal from the camera and also being utilized to set up the time delay between two laser pulses, $\Delta t_{PIV} = 500\ \mu s$ (Figure 134). The laser head, the beam delivering arm, the laser power supply and cooling system, the pulse generator and the oscilloscope were put together in a movable cart made from 80/20 frames (Figure 135).

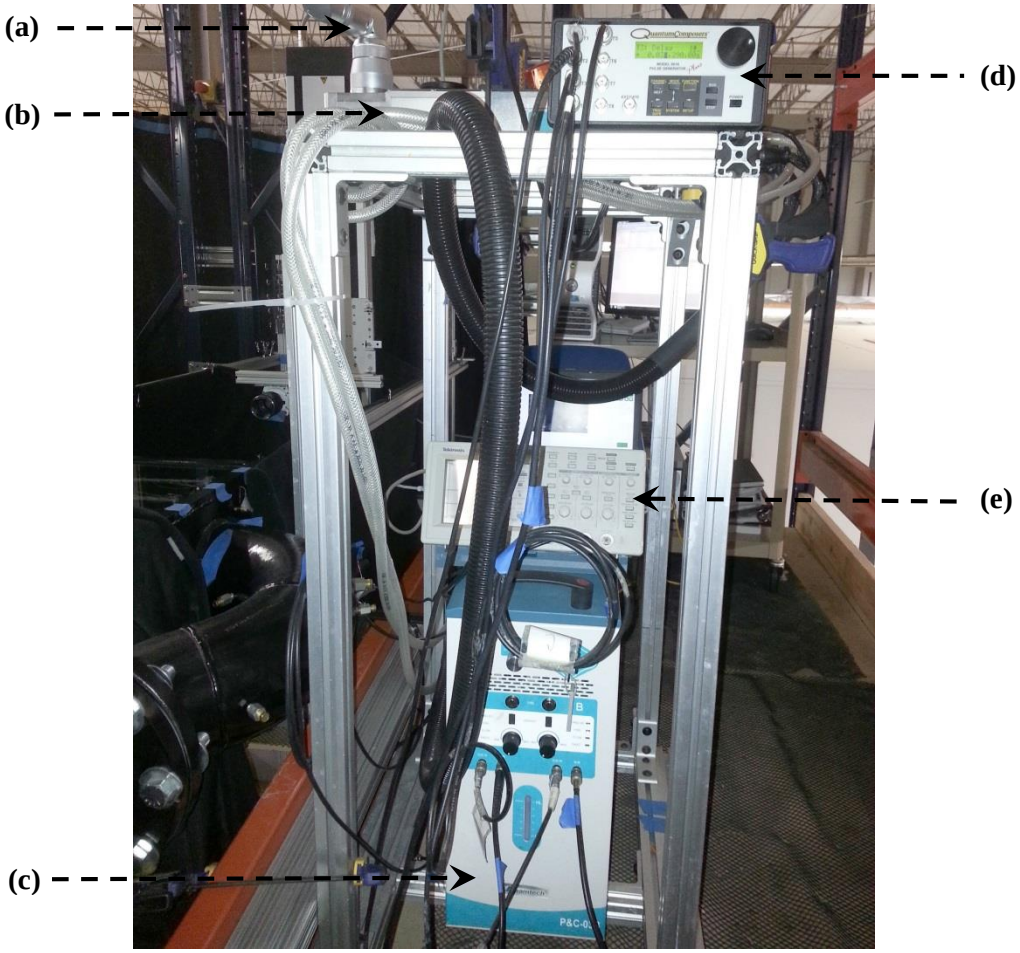

Figure 135. A cart made of 80/20 aluminum frames for mounting of: (a) the beam delivering arm, (b) the laser head, (c) the laser power supply and cooling system, (d) the pulse generator, and (e) the oscilloscope.

Figure 136. Vision Research Phantom Miro 310 high-speed digital camera (Vision Research, Inc., 2012).

Vision Research Phantom Miro 310 digital high-speed camera was used for the experiment (Figure 136). Maximum image resolution of 1280 x 800 pixels, sample rate of 30 Hz and 300 images were adopted during the experiments. The specifications of the high-speed camera are provided in Table 27. The lens was Carl Zeiss (f/2-f/22 50 mm) macro lens. The high-speed camera was mounted on the plate attached to the 80/20 frame. The 80/20 was attached to the traverse system movable plate (Figure 137).

For generation of seed particles in the PIV experiment, TSI Six-Jet Atomizer Model 9306 was utilized to generate oil droplets (Figure 138 and Figure 139). This equipment has several important features, including capability to introduce particles into a pressurized system, a built-in pressure regulator and pressure gauge, a self-contained air dilution system, and selection of one to six particle-generating atomizer jets. Therefore, a wide array of control over the particle concentration and over the particle output (TSI, I.,

2014). Carbonell Extra Virgin Olive Oil was used as a seed material since it was readily available and cheap (Figure 140).

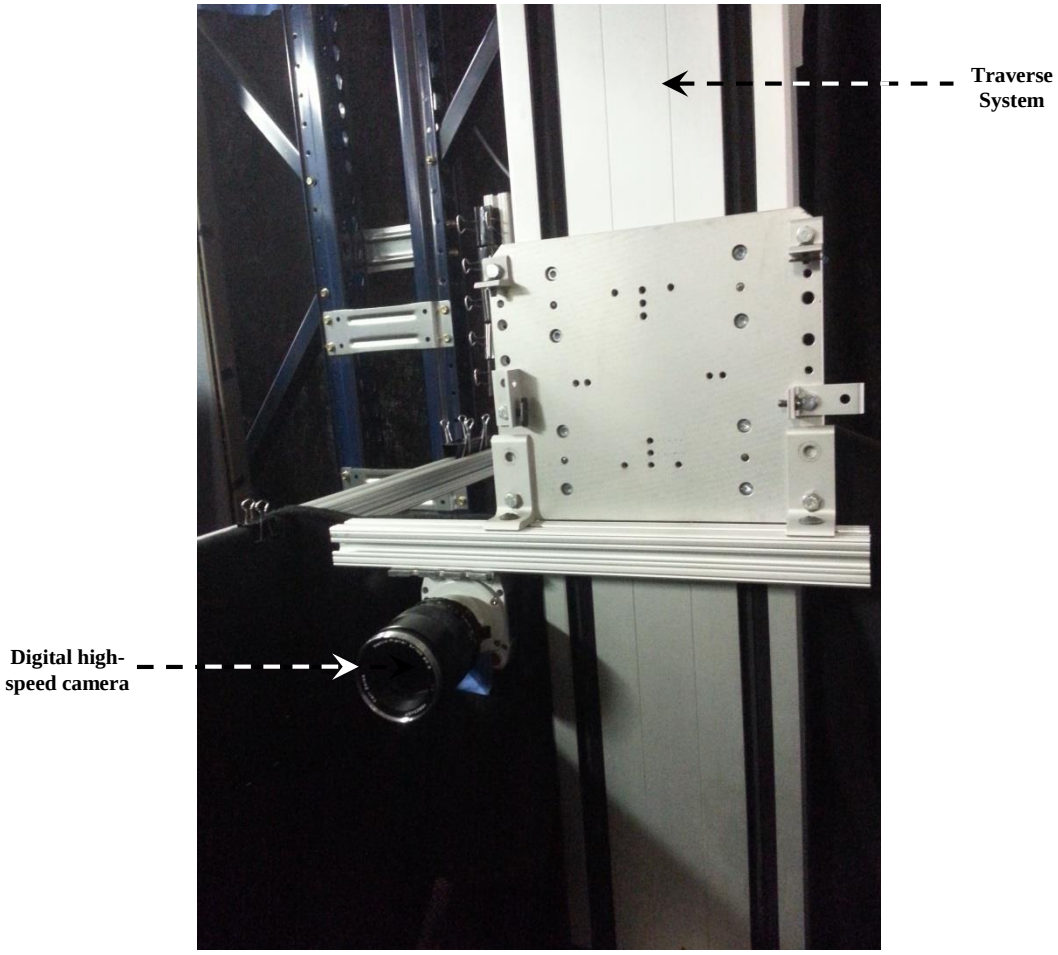

Figure 137. Mounting of the high speed digital camera to the right side of the traverse system.

Table 27. High-speed digital camera specifications for the PIV experiments (Vision Research, Inc., 2012).

Description	Specification
Model	Phantom Miro 310
Maximum Resolution	1280 x 800
Maximum Frame Rate at Maximum Resolution	3200 fps
Throughput (Gpx/s)	3.2 Gpx/s
Sensor Size	25.6 mm x 16.0 mm
Pixel Pitch	20 μm
Minimum Exposure	1 μs
ISO (12232 SAT Method)	13,000 T Mono 3900 T Color

The olive oil was inserted inside the reservoir of the atomizer. All six atomizers were used in the experiment at regulated pressure of 6 psi. A clean source of compressed air at 40 psi was connected to the atomizer at the inlet fitting on the pressure regulator. The pressurized air created a high-velocity jet via a 0.015" diameter orifice. The olive oil was drawn from the reservoir due to the negative pressure established by the jet. The olive oil was made into droplets by the compressed air jet. Large droplets are bombarded onto the spherical impactor and returned to the reservoir. Small droplets formed an aerosol and exited through the outlet of the atomizer (Figure 141). The olive oil droplets travelled

through the hoses between the atomizer and the bottom of the risers (Figure 142). The oil droplets entered to the risers via R-T-C instrumentation ports. Generic properties of the olive oil droplets generated by the atomizer are furnished in Table 28. The mean size particle was determined by the in-situ measurement as described in Appendix B.

Table 28. Typical properties of the olive oil seed material generated by the atomizer (TSI, Inc., 2014).

Description	**Specification**
Seed Material	Olive Oil
Density (kg/m^3)	0.913 g/cm^3
Refractive Index	1.47
Vapor Pressure	Very Low
Mean Particle Size (μm)	0.745 (range: 0.5 – 1.2)
Particle Output Concentration (particles/cc)	4.0×10^6

Figure 138. TSI six-jet atomizer (TSI, Inc., 2014).

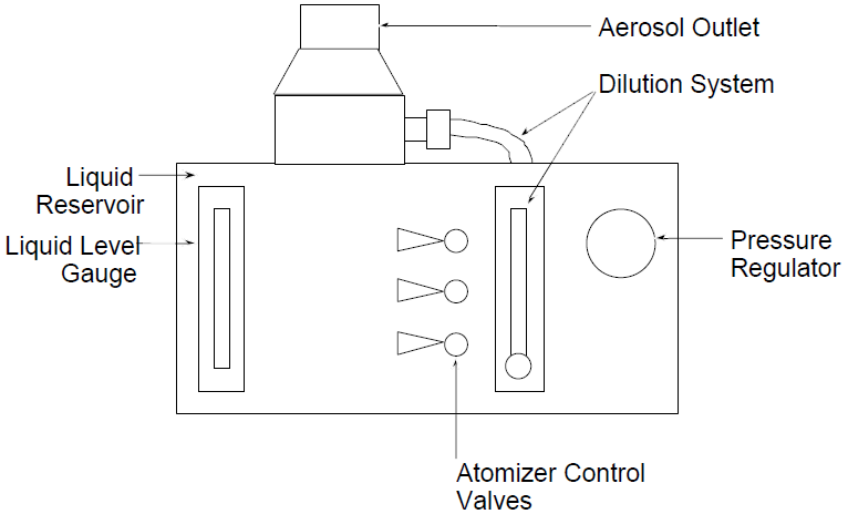

Figure 139. TSI **s**ix-jet atomizers outline drawing (TSI, Inc., 2014).

Figure 140. Olive oil as a seed material.

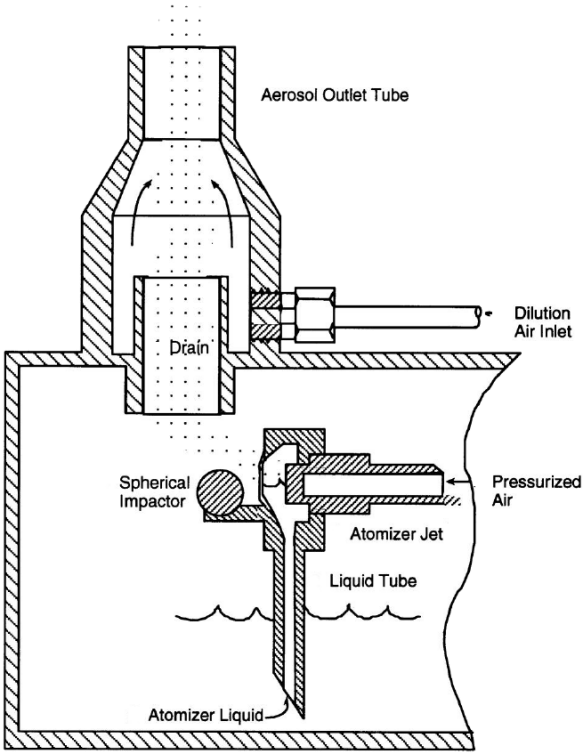

Figure 141. Schematic of TSI six-jet atomizer internal assemblies (TSI, Inc., 2014).

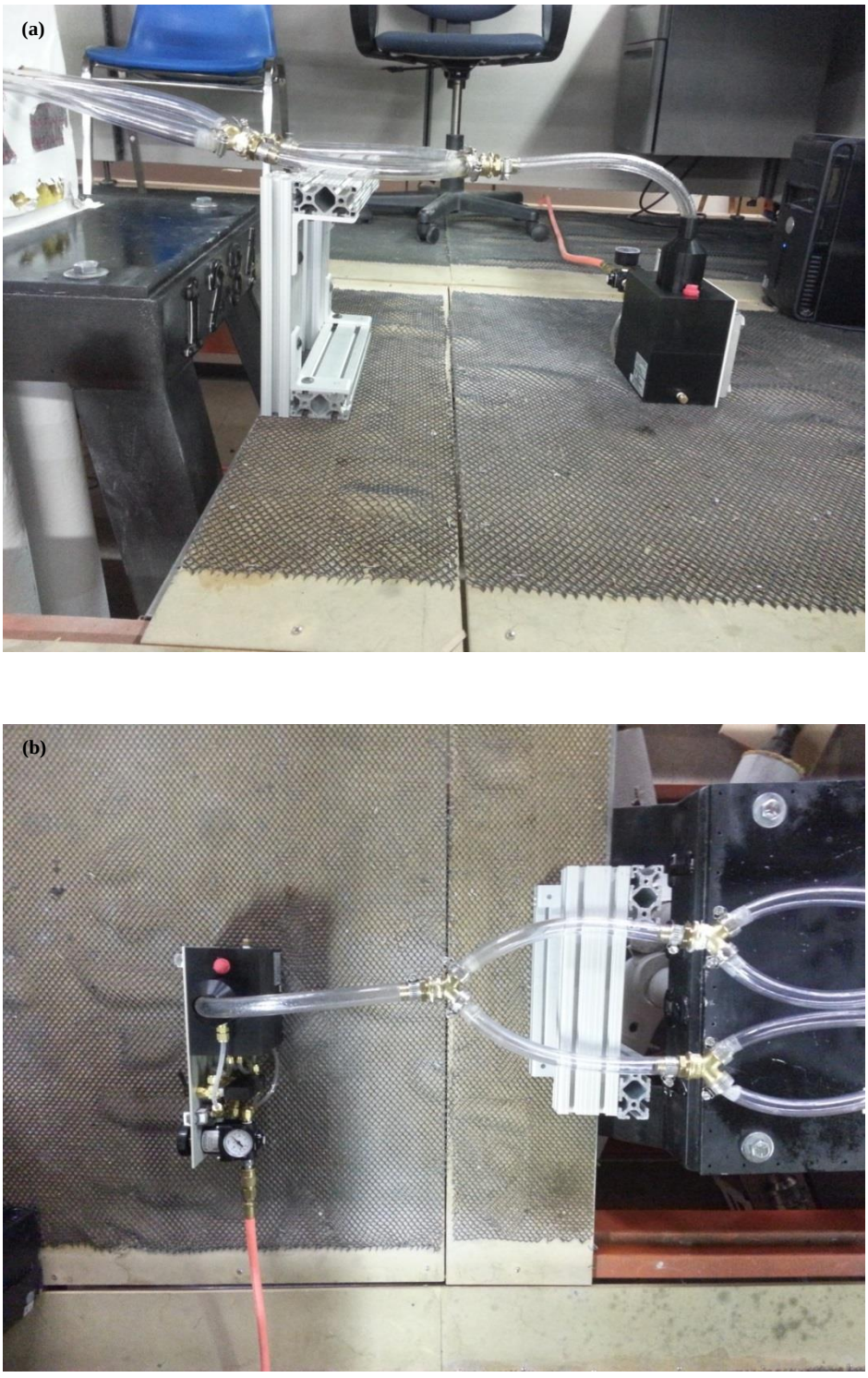

Figure 142. PIV seeding system from two different views. (a) Side view, and (b) Top view.

Dantec Dynamics 3D traversing system was used for precise movement of the high speed camera (Figure 143). Its features include rigid construction with step-motor driven high precision lead screws integrated in all traverse direction, electrical limit switches in all units, high resolution, and improved bearings with high load capacity (Table 29). Dantec Dynamics BSA Flow Software was used to control the movement of the traverse system.

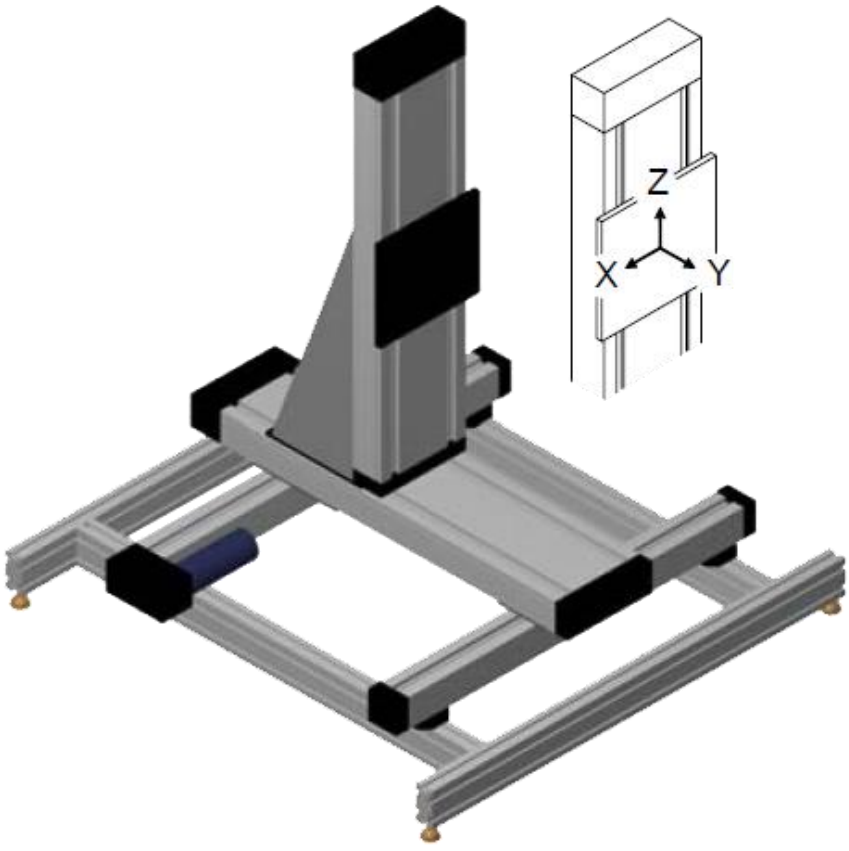

Figure 143. Dantec Dynamics 3D traverse system (Dantec Dynamics, Inc., 2012).

Table 29. Dantec Dynamics 3D traverse system specifications (Dantec Dynamics, Inc., 2012).

Description		**3D Traversing Mechanism**
Range	X (mm)	110 – 2710
	Y (mm)	110 – 2710
	Z (mm)	110 – 2710
Speed (mm/sec)		Up to 25
Resolution (μm)		6.25
Dimensions	X (mm)	X + 540
	Y (mm)	Y + 540
	Z (mm)	Z + 720
Maximum Load	Mx (Nm)	175
(Dynamic)	My (Nm)	150
	Mz (Nm)	340
Lift Capacity (kg)		60
Included Parts		▪ Electromagnetic brake built-in the vertical traverse unit ▪ Mounting plate for Dantec Dynamics bench profile or Probe support ▪ Adjustable feet

High accuracy and precise positioning of the laser arm and laser optics were accomplished by installing the three-axis Velmex Inc. Bislide Positioning System in between two teardrop beams above the upper plenum on the second floor (Figure 144 and Figure 147). The maximum travel for each x, y, and z direction was 40'' in linear motion. For x- and y-axis, motor-driven assemblies were adopted since most of the movement for PIV experiments was in these directions (Figure 145). VXM Stepping Motor Controller was used to control the movement in x- and y-direction (Figure 146). For z-axis, since less movement was involved, a manual driven assembly complete with a knob crank with a digital counter position readout was used (Figure 145). A plate was mounted on 4.6" x 3.1" mounting surface carriage of the BiSlide in z-direction. Two perpendicular 80/20 aluminum bars were used to form the base for mounting the beam delivering arm (Figure 147).

Figure 144. Velmex three-axis BiSlide positioning system (Velmex, Inc., 2001).

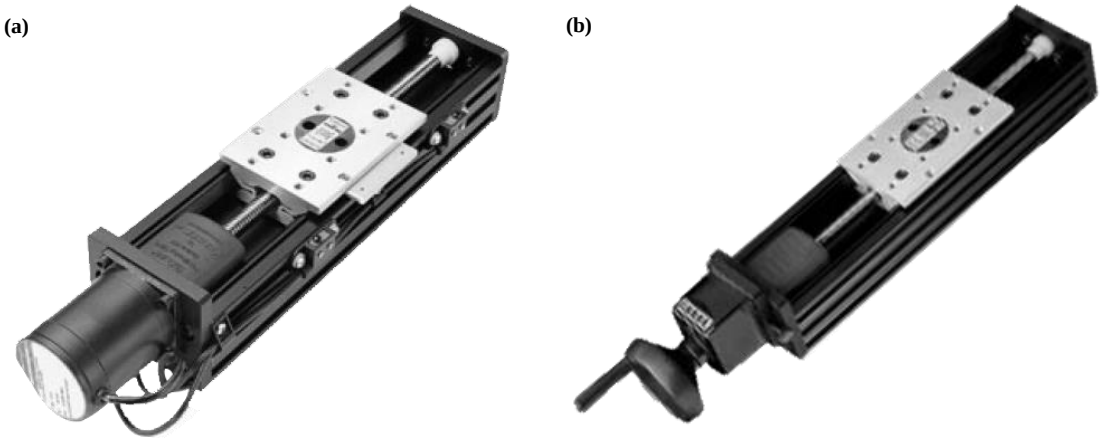

Figure 145. Velmex BiSlide positioning system: (a) Motor driven, and (b) Manual driven (Velmex, Inc., 2001).

Figure 146. Velmex VXM stepping motor controller (Velmex, Inc., 2004).

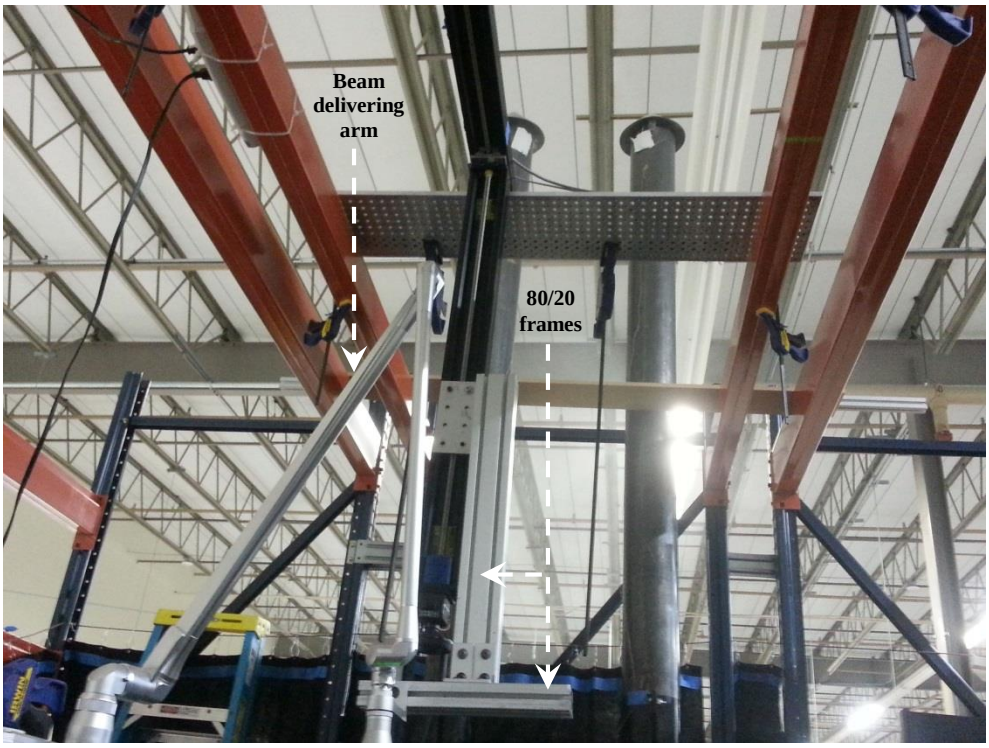

Figure 147. Two 80/20 aluminum frames were used for connection between z-direction BiSlide positioning system and the beam delivering arm.

The generic procedure described herein was applicable to the steady state velocity measurements in the upper plenum for the four risers using PIV technique. It was also applicable to certain extent (with slight modifications) on any experiments involving any number of risers. The Dantec Dynamics 3D traverse system was installed on the second floor of the facility (Figure 143). The traverse system was fixed on the experimental test facility platform. The 3D traverse system was tested for its precise positioning and functionality in x, y, and z-direction. The Vision Research Phantom Miro 310 digital high-speed camera was mounted on the right side of the z-direction the 3D traverse system movable plate (Figure 137). The high-speed camera was tested and aligned with the laser sheet of each measurement plane of interest. The three-axis Velmex, Inc. BiSlide Positioning System was adopted for precise positioning of the laser arm and the laser optics. Multiple test runs were carried on the Bislide system out to ensure smooth movement and no presence of obstructions. The VT-200 laser system was installed including the laser head, the beam delivering arm, the laser power supply and cooling system, the pulse generator and the oscilloscope (Figure 135 and Figure 134). The laser arm and the laser optics were mounted on the two 80/20 aluminum bars attached to the BiSlide system in z-direction (Figure 147). All communication cable connections between the oscilloscope, the pulse generator, and the camera were installed accordingly.

The pulse generator (Figure 133) was utilized to create signals for the high-speed camera and the laser. Both the high-speed camera and the laser were turned on and their signal on oscilloscope were verified and monitored. The oscilloscope (Figure 134) was used together with the pulse generator in setting up time delay between pulses of the laser,

Δt_{PIV}. In most experiments, the Δt_{PIV} was set at 500 μs at a frequency of 30 Hz. The high speed-camera resolution was set 1280 x 800 pixels, sample rate of 30 Hz, and 300 acquired images. In order to have high resolution of seeding particles, four vertical positions were needed to cover each plane, i.e. P1 (lower), P2 (middle lower), P3 (middle upper), and P4 (upper). The three measurement planes were very close to the V-T-A, V-T-B, and V-T-C planes used for the steady state temperature measurements (±1"). The exact placements for the laser sheet on the V-T-A, V-T-B, and V-T-C were impossible due to the obstruction introduced by the thermocouple rack crossbars. The movable curtain structure was constructed around the 3D traverse system, the high-speed camera, and the upper plenum to minimize any outside reflections (Figure 148). A small opening of the curtain on top of the upper plenum was carefully designed to allow the thin light sheet from the laser arm and the laser optics to penetrate (Figure 148). Binder clips were used to attach the curtains and the structures.

The particle seeding system (Figure 142) was connected to the compressed air line at 40 psi. The compressed air pressure was regulated at 6 psi upstream of the TSI Six-Jet Atomizer (Figure 138). The value of the regulated compressed air pressure was selected based on the density and clarity of the seeding particles images. All six atomizers were in operation for any experiments with maximum opening of dilution air valve. For the experiments involving four risers, all four hoses connecting the outlet of the atomizer and R-T-C ports were utilized. Similarly, for one riser experiments, only one riser port was used for connection to the outlet of the atomizer.

Figure 148. Front view of PIV measurement set-up (including movable curtain frames).

The laser arm and the laser optics were moved to the vertical plane close to V-T-A plane by the BiSlide system. The vertical position was clearly marked and labeled. The laser was turned on to produce a thin laser sheet that illuminated the intended vertical plane. The BiSlide system was fine-tuned to obtain a fairly homogenous laser light sheet. The high-speed camera was moved to the P1 position using the 3D traverse system and its lens was refocused to yield clear and sharp video images. The measurements were taken

three times per vertical position. Then the high-speed camera was shifted to the P2 position using the 3D traverse system and the same measurement procedure for P1 position was carried out. Similar steps were performed until P4 position. Then the laser arm and the laser optics were moved to the vertical plane close to V-T-B position. The same procedures used for the vertical plane close to V-T-A plane were applied to the vertical planes close to V-T-B and V-T-C. The overall PIV measurement set-up is depicted in Figure 149 and Figure 150.

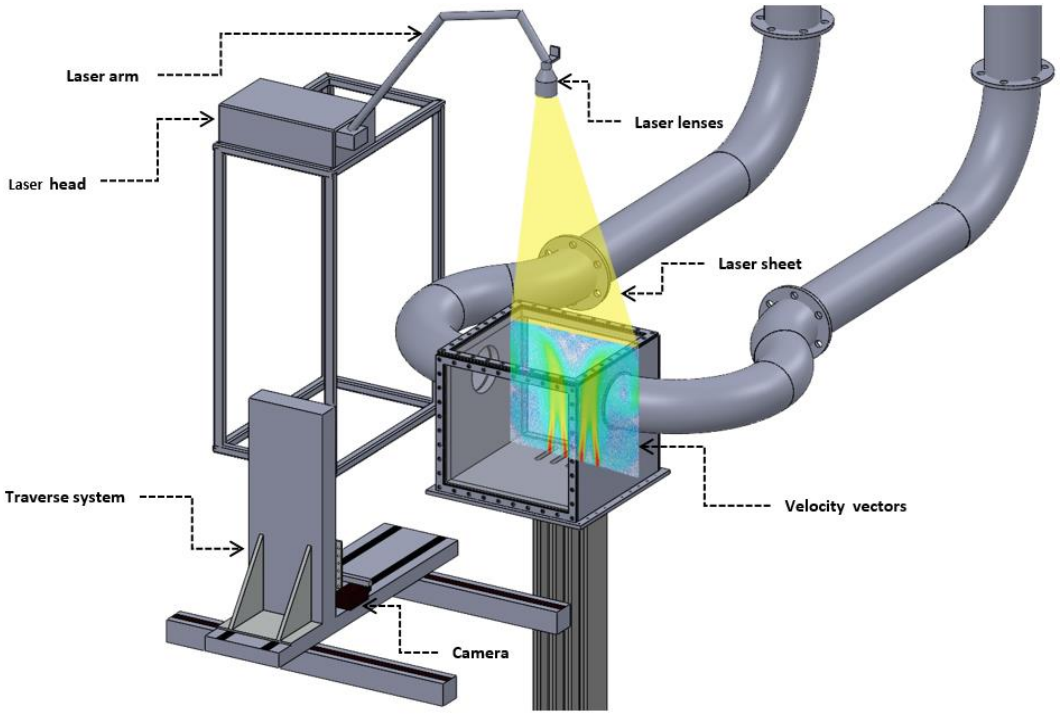

Figure 149. Schematic of PIV overall set-up.

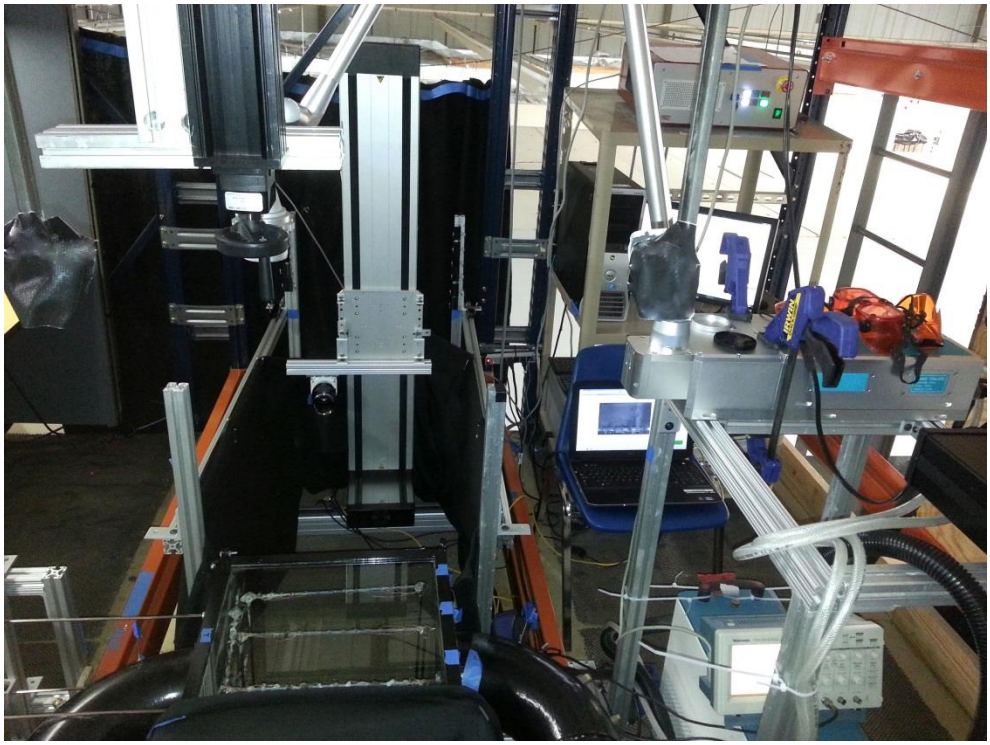

Figure 150. PIV measurement overall set-up.

CHAPTER X

STAGE 7: EXPERIMENTAL DATA ANALYSIS AND DISCUSSIONS [*]

X.1. Post Processing of Experimental Data

The post-processing of temperature and velocity experimental data are presented in this section.

X.1.1. Post-Processing of Temperature Measurements Data

Measured temperature data recorded by the NI Signal Express 2013 was extracted for the calculation of averaged values. A Matlab R2014a script was developed to calculate the mean temperature, $\langle T \rangle$ and the root-mean square (rms) fluctuating temperature, T' values of 900 samples at each measuring point. The equation used to compute $\langle T \rangle$ is defined below:

$$\langle T \rangle = \frac{\sum_{i=1}^{N} T_i(\vec{R})}{N} \tag{X-1}$$

[*] Part of the data reported in this chapter is reprinted with permission from "Design considerations and experimental observations for the TAMU air-cooled reactor cavity cooling system for the VHTR" by Sulaiman, S. A., Dominguez-Ontiveros, E. E., Alhashimi, T., Budd, J. L., Matos, M. D., & Hassan, Y. A., 2015. *AIP Conference Proceedings*, 1659, 030002. http://dx.doi.org/10.1063/1.4916850-. Copyright [2015] by AIP Publishing LLC.

where $\langle T \rangle$ is the mean temperature, T_i is the instantaneous temperature at the measurement point, $\vec{R}$ is the point in 3-D Cartesian coordinates (X, Y, Z), and N is the total number of samples.

The corresponding instantaneous fluctuating temperature at a point is computed as the following:

$$T_i'(X,Y,Z) = T_i(X,Y,Z) - \langle T(X,Y,Z) \rangle \tag{X-2}$$

The root-mean square (rms) fluctuating temperature, $\langle T' \rangle$ is calculated as follows:

$$\langle T'(X,Y,Z) \rangle = \sqrt{\frac{1}{N}\sum_{i=1}^{N}[T_i'(X,Y,Z)]^2} \tag{X-3}$$

From the output files of the Matlab script, rendering of 3-D volumetric temperature plots were carried out. Plots for $\langle T \rangle$ and $\langle T' \rangle$ were generated using Tecplot 360 EX 2014 R1 for each heated case, i.e. Case 1, Case 2, Case 3, and Case 4. The summary of the temperature measurements is depicted in Figure 151.

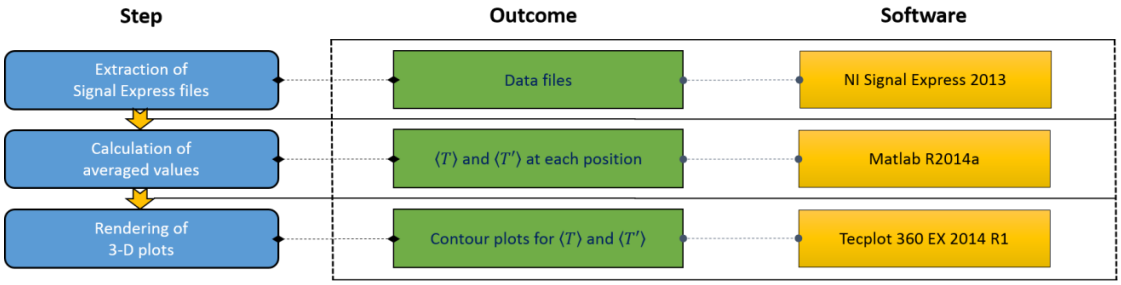

Figure 151. Flow of post-processing for the thermocouple rack temperature measurements.

X.1.2. Post Processing of Velocity Measurements Data

Measured PIV cinema files recorded by the Vision Research Phantom Miro 310 digital high-speed camera were first converted to bitmap files by using Phantom PCC 2.1 software. Next, Image J and Total Commander softwares were utilized to convert those bitmap files to 8-bit grayscale bitmap files. This step was necessary in order to optimize the processing speed of images in PIVlab, a Matlab-based software for the computation of velocity vectors. Afterwards, removal of static background and noise was achieved by utilizing the in-house PTV-TAMU v2.1.0 software (Estrada-Perez, 2004). This step was performed by deducting the original image with its group frame average value. Since the images were grouped as odd or even numbers to take into account differing intensities between each consecutive frame, two distinct average images were computed. Next, the separation odd and even number images were carried out by the Total Commander software. The Total Commander software was again utilized to combine the processed images. Finally, these processed images were loaded into the PIVlab software (Thielicke

and Stamhuis, 2014) for the velocity vectors computation. The specifications of the analyses setting in the PIVlab are furnished in Table 30.

The computed velocity vectors in the PIVlab were saved as data files. A Matlab R2014a script was written to compute averaged values for mean and fluctuating velocities (including Reynolds stresses), in both the streamwise and spanwise directions for each position of each plane, respectively.

Velocity statistics from PIV measurements (by ensemble averaging the number of images) were calculated as follows:

$$\langle \Psi \rangle = \frac{\sum_{i=1}^{N} A_i(\vec{\psi})}{N} \tag{X-4}$$

where Ψ is the quantity being averaged, $\vec{\psi}$ is the position vector in Cartesian coordinate (X, Y, Z), and N is the total number of realizations. The above equation is the two-dimensional average of vector fields in X and Z directions. Y–direction is referring to the third point (fixed dedicated points) to enable 3-D plotting of respective plane of velocity measurements.

In other words, the velocity fields are essentially a two-dimensional array in Cartesian coordinate systems with a component each in X -axis and Z-axis directions where each array element contains a measured vector. Each vector in time has implanted in it the information of two-velocity components, denoted by U and V. The statistics

presented make reference to (X, Y, Z), which represent the position of each vector in the array (Figure 152).

Table 30. The specifications used in the analyses settings of PIV Lab for PIV processing.

Description	Specification
PIV algorithm	Fast Fourier Transform (FFT) window deformation
Pass 1	Interrogation Area [pix]: 64; Step [pix]: 32
Pass 2	Interrogation Area [pix]: 32; Step [pix]: 16
Pass 3	Interrogation Area [pix]: 16; Step [pix]: 8
Window Deformation Interpolator	Linear
Sub-Pixel Estimator	Gauss 2x3-point

As such, velocity fluctuating component in streamwise direction for each instantaneous velocity field is given by

$$U_i'(X, Y, Z) = U_i(X, Y, Z) - \langle U(X, Y, Z) \rangle, \quad \text{(X-5)}$$

where U_i' is the instantaneous fluctuating streamwise velocity component, U_i is the instantaneous streamwise velocity component, and $\langle U \rangle$ is the mean streamwise velocity component.

Similarly, velocity fluctuating component in the spanwise direction for each instantaneous velocity field is defined as follows:

$$V_i'(X,Y,Z) = V_i(X,Y,Z) - \langle V(X,Y,Z) \rangle \qquad \text{(X-6)}$$

where V_i' is the fluctuating spanwise velocity component, V_i is the instantaneous spanwise velocity component, and $\langle V \rangle$ is the mean spanwise velocity component.

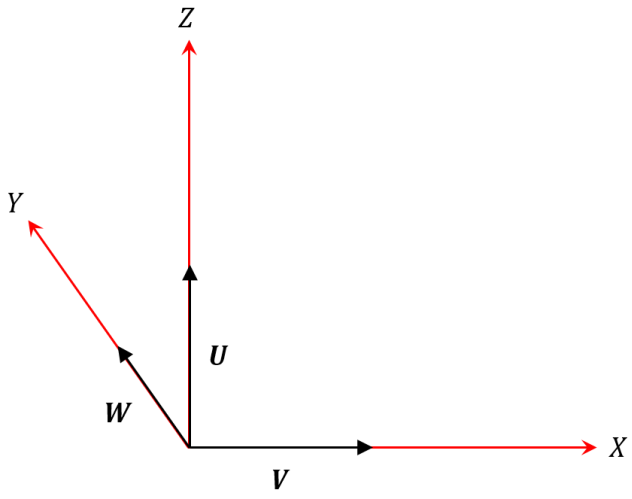

Figure 152. 3-D Cartesian coordinate and velocity convention. ***U*** is a velocity in streamwise direction (Z-coordinate), ***V*** is a velocity in spanwise direction (X-coordinate), and ***W*** is velocity in normal direction (Y-coordinate) (not available in 2-D PIV measurements).

The root-mean-square (rms) quantities of the fluctuating components (both streamwise and spanwise directions, respectively) are computed as the following:

$$\langle U'(X,Y,Z)\rangle = \sqrt{\frac{1}{N}\sum_{i=1}^{N}[U_i'(X,Y,Z)]^2} \tag{X-7}$$

$$\langle V'(X,Y,Z)\rangle = \sqrt{\frac{1}{N}\sum_{i=1}^{N}[V_i'(X,Y,Z)]^2} \tag{X-8}$$

Turbulence intensities (streamwise and spanwise directions) are defined below:

$$TI_U = \frac{\langle U'(X,Y,Z)\rangle}{\langle U\rangle_{max}} = \frac{\sqrt{\frac{1}{N}\sum_{i=1}^{N}[U_i'(X,Y,Z)]^2}}{\langle U\rangle_{max}} \tag{X-9}$$

$$TI_V = \frac{\langle V'(X,Y,Z)\rangle}{\langle U\rangle_{max}} = \frac{\sqrt{\frac{1}{N}\sum_{i=1}^{N}[V_i'(X,Y,Z)]^2}}{\langle U\rangle_{max}} \tag{X-10}$$

The Reynolds stress distributions are an essential part of the turbulence flow characterization and modeling. Since the 2-D PIV measurement technique can furnish two components of the velocity vector, only four components out of nine components of the

Reynolds stress tensors can be determined. Out of these four components, the most prominent component is $\langle U' \rangle \langle V' \rangle$ and it can be computed by the product of the instantaneous velocity fluctuations as the following:

$$\langle U'(X,Y,Z) \cdot V'(X,Y,Z) \rangle = \frac{1}{N} \sum_{i=1}^{N} \{[U_i'(X,Y,Z)][V_i'(X,Y,Z)]\} \qquad \text{(X-11)}$$

Another Matlab code was generated to consolidate and stack the four positions of a plane. The stacked locations were determined prior to carry out the experiment (during calibration of the positions of the camera). Tecplot 360 EX 2014 R1 was utilized for rendering 2-D and 3-D plots. A Matlab script was developed to overlay temperature and velocity plots in Tecplot. The post-processing flow of velocity measurements using PIV is shown in Figure 153.

X.1.3. Relevant dimensionless numbers

Three essential dimensionless numbers were computed in all cases stipulated in the test matrix in order to assist in understanding of the turbulent flow behavior inside the upper plenum (Table 30). The first dimensionless number is Reynolds number, Re (inertia force/viscous force) (Eq. X-12) at the exit of the jet. The densimetric Froude number, Fr (inertia force/buoyancy force) (Eq. X-13) and the Grashof number, Gr (buoyancy force/viscous force) (Eq. X-14) were calculated for the range of the measured temperature

across the volume of the upper plenum. On one hand, in the case of inertia-influenced jet, the Re number must high enough so that the jet are fully turbulent and viscous force are insignificant compared with inertia force. On the other hand, the Gr number should be large enough so that the buoyancy forces are dominant and viscous force will be negligible. The buoyancy effects are determined not just by the density difference but in fact the ratio of buoyancy to inertial forces (the Fr number) (Hossain and Rodi, 1982; Gebhart, Hilder, and Kelleher, 1984). The $Fr = \infty$ for the pure-jet case and $Fr = 0$ for the pure-plume case.

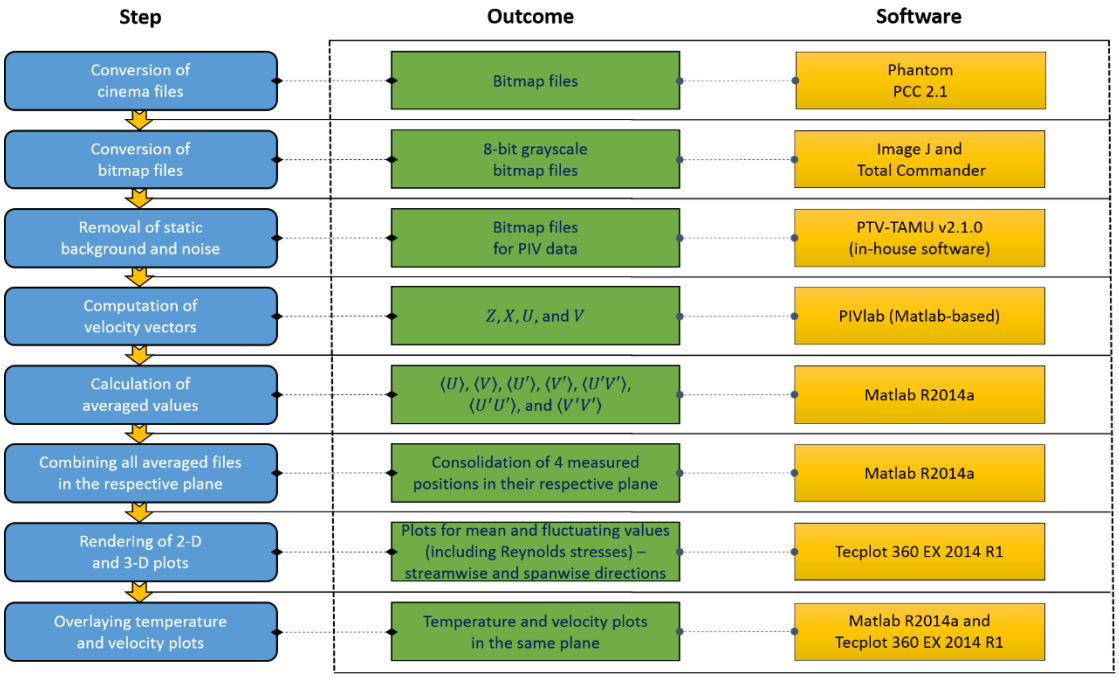

Figure 153. Flow of post-processing for the velocity measurement using PIV.

$$Re = \frac{\rho\, U_o D_H}{\mu} = \frac{U_o D_H}{\nu} = \frac{Inertia\ force}{Viscous\ force} \tag{X-12}$$

where ρ is the density of air, U_o is the riser outlet velocity, D_L is the height of the upper plenum, and ν is the momentum diffusivity/ kinematic viscosity of air.

$$Fr = \frac{M_o U_o}{W_o D_L} = \frac{U_o^2}{D_L g'} = \frac{U_o^2}{D_L \frac{g(\rho_E - \rho_o)}{\rho_o}} = \frac{Inertia\ force}{Buoyancy\ force} \tag{X-13}$$

where M_o is momentum flux, W_o is buoyancy flux, U_o is the riser outlet velocity, D_L is the height of the upper plenum, g' is the reduced gravity, g is the gravity, ρ_E is the density of ambient air , and ρ_o is the density of air at the riser outlet.

$$Gr = \frac{g(\rho_E - \rho_o) D_L^3}{\rho_o \nu^2} = \frac{Buoyancy\ force}{Viscous\ force} \tag{X-14}$$

where g is the gravity, ρ_E is the density of ambient air , ρ_o is the density of air at the riser outlet, D_L is the height of the upper plenum, W_o is buoyancy flux, U_o is the riser outlet velocity, and ν is the momentum diffusivity/ kinematic viscosity of air.

Table 31. Summary of the dimensionless numbers (Re, Fr, and Gr).

Adiabatic Cases

	Case 1a	**Case 2a**	**Case 3a**	**Case 4a**
Re (jet exit)	9,936	9,936	4,471	4,471

Heated Cases

	Case 1		**Case 2**		**Case 3**		**Case 4**	
Temp. Range	107 °C	120 °C	37 °C	120 °C	50 °C	120 °C	28 °C	120 °C
Re (jet exit)	6,134		6,134		2,760		2,760	
Gr range (inside the UP)	5.7×10^7	0	9.0×10^8	0	6.5×10^8	0	1.1×10^9	0
Fr range (inside the UP)	160	∞	21	∞	5	∞	4	∞

X.2. The Cases of One Riser

X.2.1. Case 2a vs. Case 2

Case 2a and Case 2 are cases of which a turbulent jet issues from a rectangular slot (i.e. Riser ④) into a confined and stagnant surrounding of the same fluid, of which the inlet jets are at both room temperature (i.e. 25 ^{o}C) and heated temperature (i.e. 120 ^{o}C). There are fewer pieces of literature focusing on rectangular jets in a confined environment as opposed to those in a free and infinite ambient. In order to gain further insight of the flow characteristics and turbulence mixing of the air-cooled RCCS under this configuration, measurements of a jet issuing from the rectangular slot were performed. The risers outer cross section dimensions were 0.127 m (5") and 0.0254 m (1"). The long (L) and short (D) inner dimensions of the rectangular slot were 0.11938 m (4.7") and 0.01778 m (0.7"). The spacing (S) between the slots was 0.05334 m (2.1") (Figure 154). A mean velocity of 5 m/s was maintained at the exit plane of each slot. The air jet exited into the upper plenum having dimensions of 0.4318 m x 0.4572 m x 0.4318 m (17" x 18" x 17").

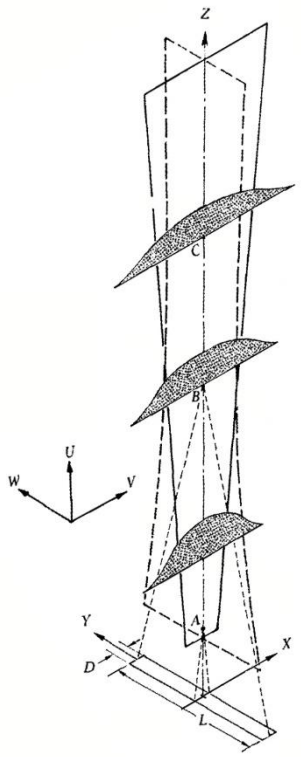

Figure 154. Schematic representation of the flow field of a rectangular free jet.

Gebhart et al. (1984) classified the jet-ambient mechanism according to four major criteria which include jet buoyancy (neutrally buoyant or buoyant [positively or negatively]), orientation of discharge (horizontal, vertical, inclined), ambient motion (quiescent/stagnant or flowing), and ambient stratification (unstratified, linearly stratified, other stratification). Krothapalli, Baganoff, and Karamcheti (1980; 1981) characterized the flow field of the rectangular free jet into three distinct regions (Figure 154). The first region was classified as a potential core region (constant axial velocity); the second region denoted by AB, in which the velocity decays at a rate roughly the same as that of a planar jet, would be represented to as the two-dimensional region or interaction region; and the

third region downstream of B, in which the velocity decays at nearly the same rate as that of an axisymmetric jet, would be referred to as an axisymmetric region or fully developed region. The two-dimensional type region commenced at about the location where the two shear layers in the X, Z plane (containing the short dimension of the nozzle) met. The axisymmetric region originated at a place where the two shear layers in the X, Z plane (containing the long dimension of the nozzle) would meet.

Profiles of the normalized mean streamwise velocity in the X, Z plane for the two cases are shown in Figure 155. The highest velocity in the V-T-A plane, normally near the exit of each jet, was used for the normalization. Spreading of higher normalized mean streamline velocity at the jet exit of Case 2 was found to be slightly greater than Case 2a. This was due to the fact that in Case 2, the jet was considered buoyancy-influenced flow whereas Case 2a it was considered non-buoyant or inertia-influenced flow. The heat from convection flow of the riser caused buoyancy effects arising from density differences between the jet and the ambient inside the upper plenum. The flow field for the general case of "forced plume" can be characterized with three distinct regions which are referred to as: a pure-jet region, a transition region, and a pure-plume, assuming the jets do not interact with any walls or free surfaces region (Hossain and Rodi, 1982).

For a buoyant jet with relatively strong initial momentum, the jet acts like a pure jet. However as the effect of buoyancy becomes greater, after a certain transition region, the flow ultimately behaves like a pure plume. Both the pure jet and the pure plume spread linearly at different rate in uniform environment. In stably stratified environment, the jet initially acts like a buoyant jet similar to the one we found in the uniform environment; however the buoyancy flux reduces continuously and becomes negligible at the point of neutral buoyancy. From this point onwards the buoyancy force is negative so that the flow decelerates and the jet attains a maximum height and then turns downward and spreads sideways (laterally). There was no solid evidence from Case 2 that the jet has transformed completely into the pure plume. From these observations, one might deduce that near the top of the upper plenum, the buoyant jet was inside the zone of established flow and it was in transition to become pure-plume.

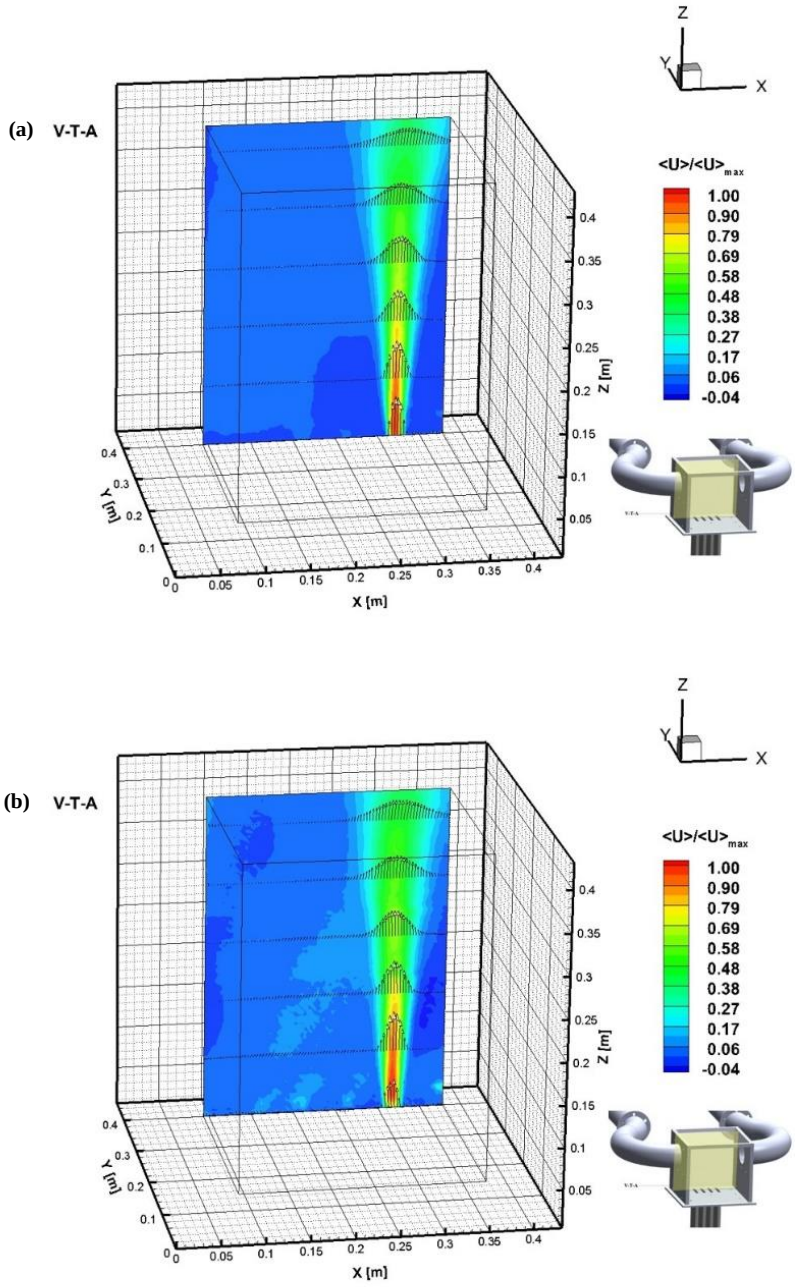

Figure 155. Normalized mean streamwise velocity (V-T-A plane): (a) Case 2a, (b) Case 2.

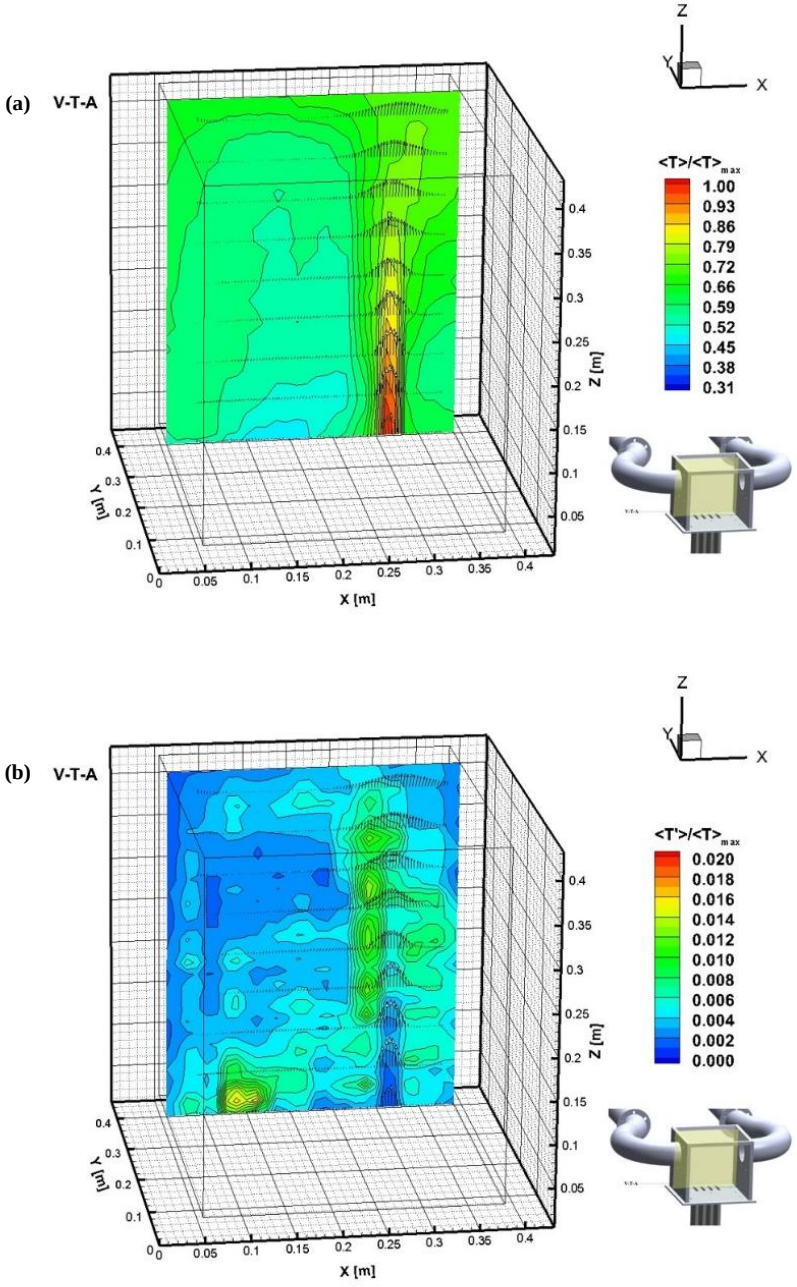

Figure 156. (a) Normalized mean temperature contour with velocity vectors (V-T-A plane for Case 2), (b) Normalized fluctuating temperature with velocity vectors (V-T-A plane for Case 2).

Figure 156 shows the normalized mean temperature contour as the jet travelled downstream along the Z-direction. The highest temperature in the V-T-A plane, normally near the exit of each jet, was used for the normalization. Despite of unavailability of full field velocity data near the top wall in Figure 155 due to obstruction introduced by the upper frame of the upper plenum's front window, it was obvious in Figure 156 that the jet impinged the top wall based on the pattern of the mean temperature contour. The coverage of the measurement plane (V-T-A) for the temperature was in fact larger than the velocity. The presence of the top and side walls in the upper plenum not only changes the boundary conditions inside the upper plenum, but more importantly it changes the jet behavior away from the free jet. For example, the confined environment has the effect of restricting the mechanism of entrainment of ambient fluid as compared with the free surrounding (Chua and Lua, 1998). A huge temperature gradient (> 50% difference) between the outlet of Riser ④ and the other risers was observed. A small temperature gradient (~ 16% difference) between the top and bottom of the upper plenum was recorded. Thermal stratification layers were established at this steady state condition. There was also a presence of small induced jets at the exit of each non-active risers, i.e. Riser ② to ④, due to slightly negative pressure in the upper plenum (Figure 155). The temperature fluctuation was less for the jet in the pure jet region since the temperature was homogenously mixed near the jet exit.

Presence of higher fluctuating temperature at the interface boundary between the moving jet flow and stagnant flow inside the upper plenum was observed in Figure 156. This was caused by high momentum and energy transfer at the interface boundary as the

moving jet flow shearing the stagnant flow. Higher fluctuations occurred on the left hand side of the jet as compared with the right hand side due to an increase in macroscopic diffusion of fluid momentum transfer, which was a result of the presence of the wall that redirected the momentum transfer towards the right side of the jet. Localized high temperature fluctuation at the outlet of Riser ① might be due to the influence of the small-induced jets.

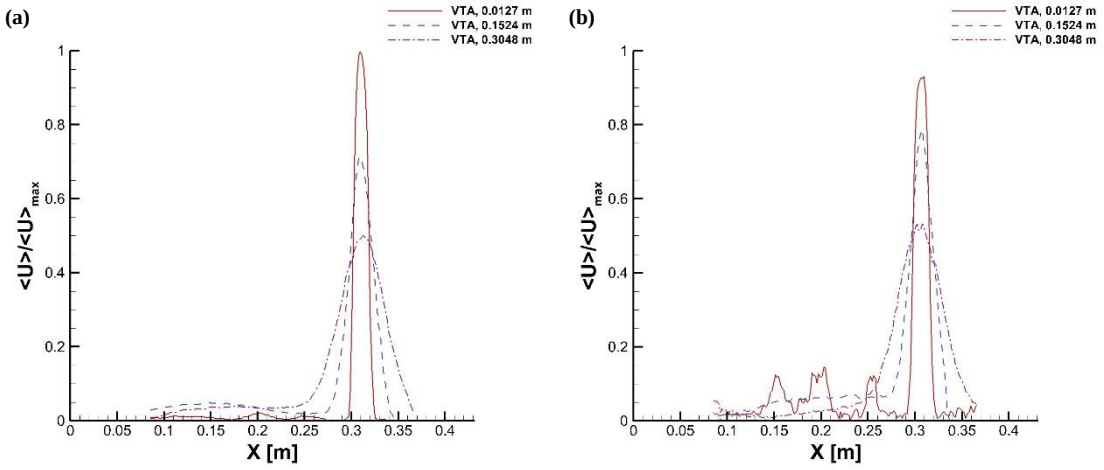

Figure 157. Cross-sectional of normalized mean streamwise velocity (V-T-A plane): (a) Case 2a, (b) Case 2**.**

In most of reported literatures for jet flows, it was indicated that mean and fluctuating velocities in streamwise direction had more prominent influence in the flow characteristics than their counterparts in spanwise direction. Therefore, it was sensible to pay close attention on the jet behavior for V-T-A plane. Figure 157 depicts the cross-section of normalized mean streamwise velocity at three different Z-axis elevations;

namely 0.0127 m (0.5”), 0.1524 m (6”), and 0.3048 m (12”). The first elevation provided the information near the jet exit, the second elevation specified the data in between the bottom part of the plenum and the outlets of the flow, and the third position furnished the condition in between the left and right outlets (i.e. left and right chimney inlets).

In general, the pattern and shape at each elevation for the two cases were almost identical. In both cases, the exit velocity profiles were top-hat distributions. The normalized mean streamwise velocity magnitude was at its peak near the jet exit (at the lowest cross-sectional elevation). The trajectory of the jet as it travelled further downstream demonstrated that its magnitude started to decay and spread as evidence from Figure 157. In fact, the presence of negative pressure inside the plenum was initiated at the adiabatic condition but the magnitude was very little. The presence of heat and buoyancy forces, combined with the increase in negative pressure inside the upper plenum, amplified the induced jet magnitudes to approximately 15% higher than the induced jet magnitudes at the adiabatic condition.

The turbulence intensities played a vital role in transferring fluid momentum between the adjacent fluid layers; hence, they augment flow mixing. For Case 2a, the highest streamwise turbulence intensity was recorded at the lower elevation (~ 26%) (Figure 158). As the jet began to spread downstream, the interface boundary also expanded, causing widening fluctuation points in X-axis direction while simultaneously lowering the magnitude of the jet centerline. Since the mean streamwise velocity was homogeneous near the jet centerline, for Case 2, similar observations were documented. However, the high fluctuation points included the points above the active and the non-

active risers (small-induced jets). The highest streamwise turbulence intensity for this case was ~29%. In general, magnitude of turbulence intensity at the same elevation was higher for the heated case than the adiabatic case, notably at the lowest elevation, particularly near the points directly above the active and the non-active risers (small-induced jets).

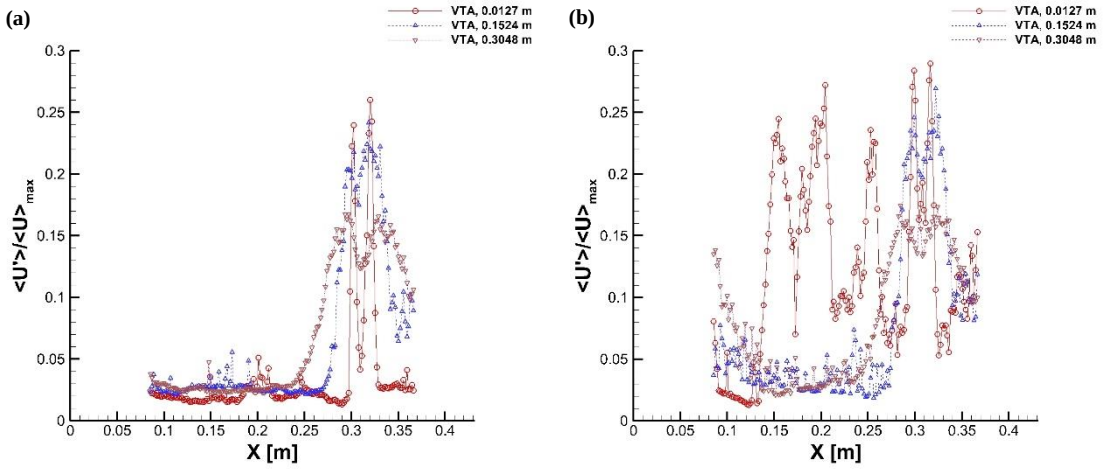

Figure 158. Left: Cross-sectional at different Z-elevation of streamwise turbulence intensity (V-T-A plane): (a) Case 2a, (b) Case 2.

For Case 2, at 0.0127 m elevation, the jet flow was still within the zone of flow establishment of which its characteristics were governed by the jet discharge conditions and initial momentum. Velocity and temperature profile underwent transition from their early discharge formation via a turbulent shear layer formed nearby the jet periphery. The turbulent shear layer grows inward and the degree of undisturbed profile became smaller as the mixing of ambient progressed. The ambient condition has little influence of the

momentum jet behavior. At 0.1524 m and 0.3048 m, the jet flow characteristics were strongly determined by its initial and attained momentum, by its buoyancy, and by ambient stratifications and flow conditions (Gebhart et al., 1984). In other words, the early discharge condition had less influence in this zone of established flow. The velocity profile near the jet origin can be described as either "top-hat" or nearly Gaussian depending on circumstances.

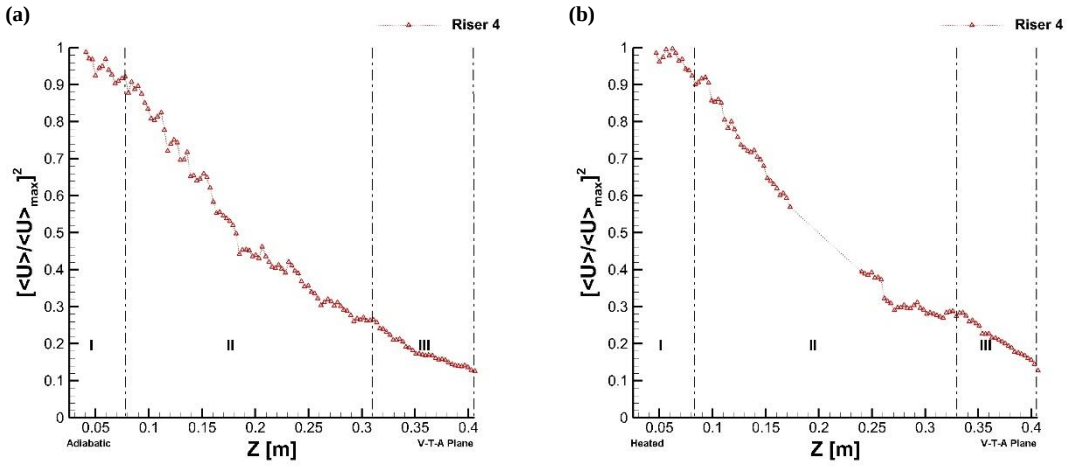

Figure 159. Decay of the mean streamwise velocity along the center-line of the jet (V-T-A plane): (a) Case 2a, (b) Case 2.

Figure 159 shows the measured decay of the square of the mean streamwise velocity along the centerline. Krothapalli et al. (1981) indicated that for an incompressible rectangular jet issued into a quiet surrounding at ambient conditions, power law decay for the two-dimensional-type region and the axisymmetric-type region were Z^{-1} and Z^{-2},

respectively. Chua and Lua (1998) in their investigation of air issuing from a rectangular nozzle of aspect ratio 6 into a confined chamber, deduced that the decay rate for the two-dimensional-type region was better represented by $Z^{-1/2}$ rather than Z^{-1}. For Case 2a and Case 2, three regions have been classified based on decay rate. Decay rates in Region I for Case 2a and Case 2 were not constant as opposed to the previous findings for a rectangular free jet. The rectangular jet exit was very close to the rear wall of the upper plenum apart of the two side walls. This confined configuration affected the initial velocity reading for a buoyant jet with relatively strong initial momentum in the pure jet region. At 5 m/s, Region I decay rate for the adiabatic case was higher than the heated case. Region II has the fastest decay rate amongst the two other regions due to the steepest slope in both cases. Region II was located inside the interaction region, where the buoyant effects became stronger prior to the jet transition to the pure plume. In Case 2, the square of the mean streamwise velocity plummeted at Z = 0.17 m, which might be a result of the stacking of two different positions of P1 and P2, respectively. However, more detailed investigation of the flow field is required to comprehend the origin of such behavior.

The streamwise and spanwise turbulence intensities of two components of velocity on the centerline of the jet are shown in Figure 160. From Figure 157, the exit profiles for both Case 2a and Case 2 were top-hat distributions. The magnitude of both turbulence intensities varied monotonically with Z until they reached a value of about 17% at Z = 0.17 m for Case 2a and Z = 0.18 m for Case 2. They then decreased and increased several times in downstream direction. Such a behavior, for Z less than 0.22 m, was typical for a jet with turbulent boundary layers at the nozzle exit in a pure jet region prior to entering

the transition or interaction region. The variation of streamwise turbulence intensity with Z has been observed to depend upon the state of the boundary layers near the jet exit (Hill, Jenkins, and Gilbert, 1976; Bradshaw, 1966). The variation of spanwise turbulence intensity along the centerline, as depicted in Figure 160, also exhibited characteristics similar to the streamwise turbulence intensity. The magnitude of streamwise turbulence intensity was greater than the spanwise turbulence intensity as found in other free shear layer flows for Case 2. However, for Case 2, in the transition region, notably in between Z = 0.27 m and Z = 0.30 m, the spanwise turbulence intensity values were slightly above the streamwise turbulence intensity most probably due to buoyancy effects. The increased and decreased behavior of both streamwise and spanwise turbulence intensities might also be contributed from the confined ambient environment condition.

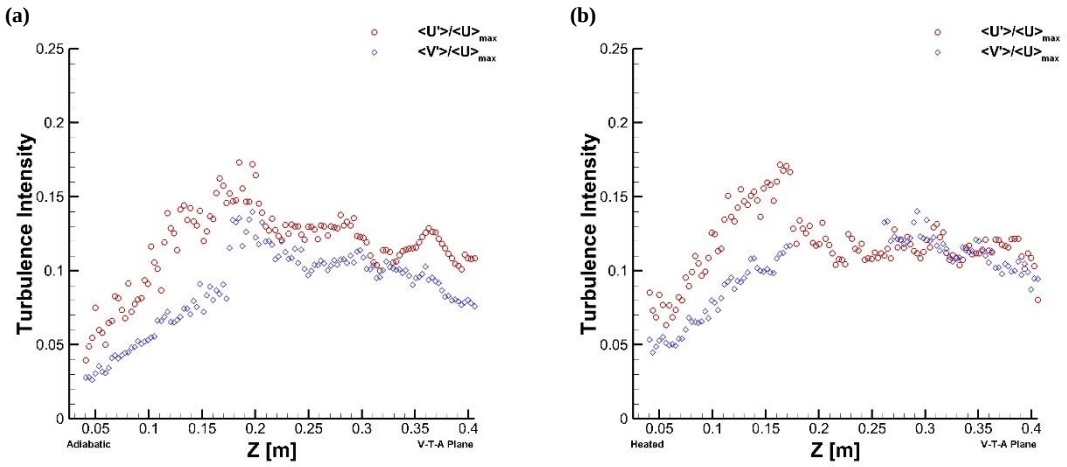

Figure 160. Variation for turbulent intensities along the center-line of the jet (V-T-A plane): (a) Case 2a, (b) Case 2.

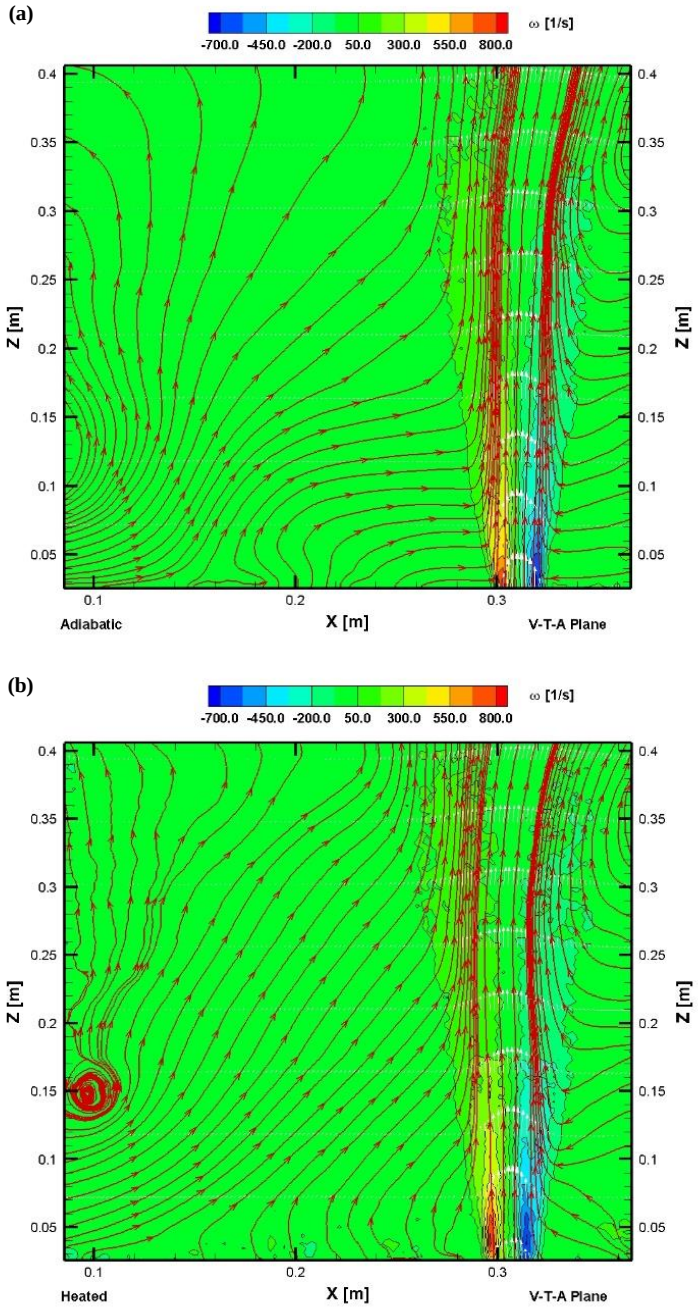

Figure 161. Vorticity contour with streamtraces (V-T-A plane): (a) Case 2a, (b) Case 2.

The vorticity contour plots with streamtraces for V-T-A plane for both Case 2a and Case 2 are shown in Figure 161. In both cases, the streamtraces on both sides of the jet were observed to shift toward the jet, which indicated the jet entrainment process through its shear layer. Vortex structures with opposite directions were observed in the outer regions of the jet. The opposite directions of the vortices were indicated by positive and negative values in Figure 161. In the center region of the jet, vortex structures have scarcely been recognized. The magnitudes of these from Case 2a and Case 2 were comparable with each other. A medium size counter clockwise vortex was generated at X = 0.1 and Z = 0.15 m for Case 2. The presence of the vortices in the outer regions of the jets validated the entrainment of ambient fluid as shown by the shifted streamtraces toward the jet. Case 2 underwent flow reversal and will be discussed in great length in the later subsection.

X.2.2. Case 4a vs. Case 4

Case 4a and Case 4 were similar to Case 2a and Case 2; however, with slight modification of the boundary condition. The upper plenum inlet velocity from Riser ④ (or Riser ④ discharge velocity) was changed from 5 m/s in Case 2a and Case 2 to 2.25 m/s for Case 4a and Case 4. The inlet temperature was unchanged; room temperature for Case 4a and 120^{o}C for Case 4.

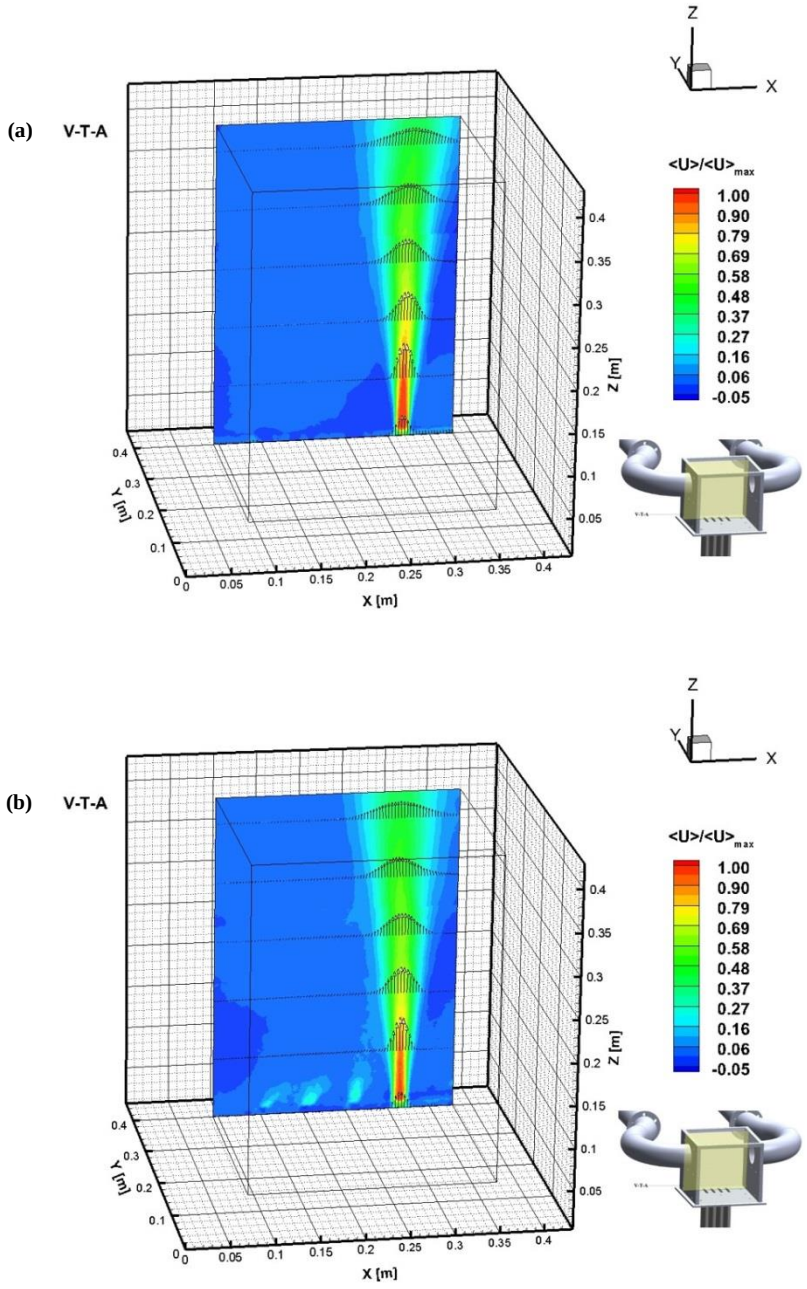

Figure 162. Normalized mean streamwise velocity (V-T-A plane): (a) Case 4a, (b) Case 4.

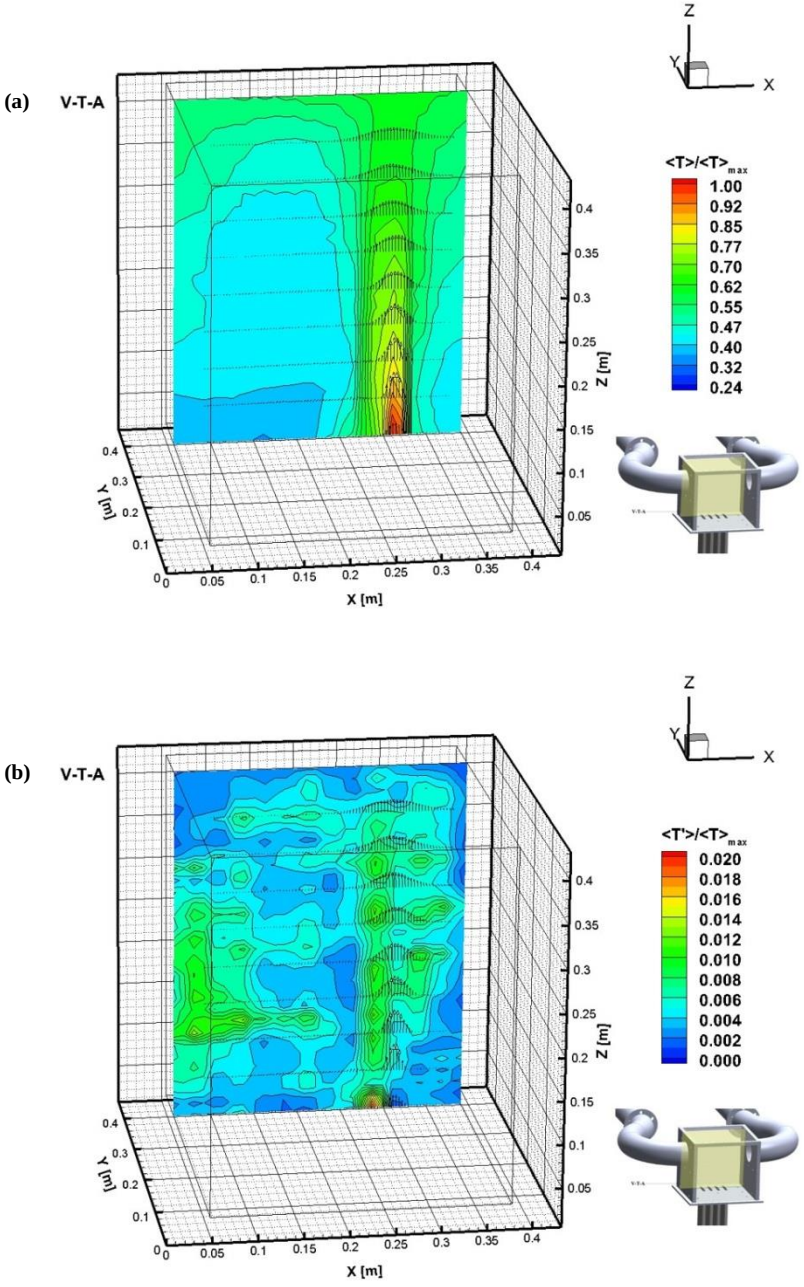

Figure 163. (a) Normalized mean temperature contour with velocity vectors (V-T-A plane for Case 4), (b) Normalized fluctuating temperature with velocity vectors (V-T-A plane for Case 4).

The normalized mean streamwise velocity profiles in the X, Z plane, for Case 4a and Case 4 are depicted in Figure 162. Similar patterns and trends of the normalized mean streamwise velocity profiles were observed with Case 2a and Case 2. The presence of small-induced jets at the exit of each non-active risers, i.e. Riser ② to 4, was due to slightly negative pressure in the upper plenum, which was more noticeable in the mean temperature contour of Case 4 than Case 2. There was no manifestation of the small-induced jets from the adiabatic case, Case 4a.

There was an indication of the buoyant jet impinging on the upper plenum's top wall based on the profiles of the normalized mean temperature distribution (Figure 163). Huge growth of colder regions above the non-active risers was observed. The area between the jet and the upper plenum's right wall was at the same temperature with the area above the non-active risers. A medium scale temperature gradient of ~ 20% difference between the regions close to the top and bottom of the upper plenum was noted. This temperature gradient was 4% greater than Case 2. The existence of thermal stratification layers in the upper plenum was pronounced on left and right hand sides of the jet boundaries. A similar explanation in Case 2 was adopted for the higher fluctuating temperature at the boundary interface between the moving jet flow and stagnant flow inside the upper plenum. High temperature fluctuation was recorded at the elevation near the inlet of the left chimney, most probably contributed by the presence of wall jets of the cold incoming air from the right chimney during the flow reversal. The flow reversal will be discussed in detail in the following sections.

The cross-section of normalized mean streamwise velocity profiles at three different elevations for Case 4a and Case 4 are illustrated in Figure 164. Under the adiabatic condition, where there was no presence of any heat source and no heat transfer, the induced jet from the non-active risers was insignificant. This implied that the pressure inside the upper plenum was similar to the outside ambient pressure. On one hand, at 5 m/s (i.e. Case 2a), the magnitude of the induced jet has reached to as high as 2% of the highest mean streamwise magnitude whereas at 2.25 m/s (i.e. Case 4a), the induced jet was totally negligible. On the other hand, at the heated condition with 2.5 m/s inlet velocity, the induced jet magnitude went more than 21% of the highest mean streamwise magnitude for Case 4 and only 14% for Case 2. This entailed that the negative pressure of Case 4 was greater than Case 2. For Case 4, at all elevations, similar rationalizations given for Case 2 were applicable.

Comparable fluctuating patterns and trends of the cross-section at different elevations of streamwise turbulence intensity were observed between Case 4a and Case 2a as well as Case 4 and Case 2 (Figure 165). However, it was noticed that at 0.0127 m and 0.1524 m, the rms intensity distribution was more evenly distributed and less scattered, particularly above the non-active risers locations, for Case 4a than Case 2a. This was due the absence of the induced jet of the non-active risers at the adiabatic condition. The corresponding magnitudes of the streamwise turbulence intensity were intensified at the heated condition for 0.0127 m and 0.1524 m elevations, with less scattered distribution at 0 0.0127 m for Case 4 compared with Case 2. For Case 4a and Case 4, the peak

streamwise turbulence intensity was about 26% and 28%, which were comparable to Case 2a and Case 2, respectively.

The measured decay of the square of the mean streamwise velocity along the centerline is shown in Figure 166. A similar approach in Case 2a and Case 2 was adopted for the analysis of Case 4a and Case 4 of which three regions have been classified based on decay rate. As observed in Case 2a and Case 2, the decay rate for Region I for Case 4a and Case 4 was not constant, as opposed to the previous findings for a rectangular free jet. At 2.25 m/s, Region I decay rate at the adiabatic condition was less than the heated condition, which was opposite of 5 m/s case. This entailed that the momentum jet at 5 m/s was relatively stronger than the momentum jet at 2.25 m/s; therefore influence of buoyancy forces was faster for 2.25 m/s case. Region II has the highest decay rate since it was within the interaction region where the buoyant effects became more pronounced prior to the jet transition to the pure plume. At Region III, both inertia-dominated and buoyant-dominated jets have lost most of their kinetic energy; therefore, the decay rate was the lowest compared with the other regions.

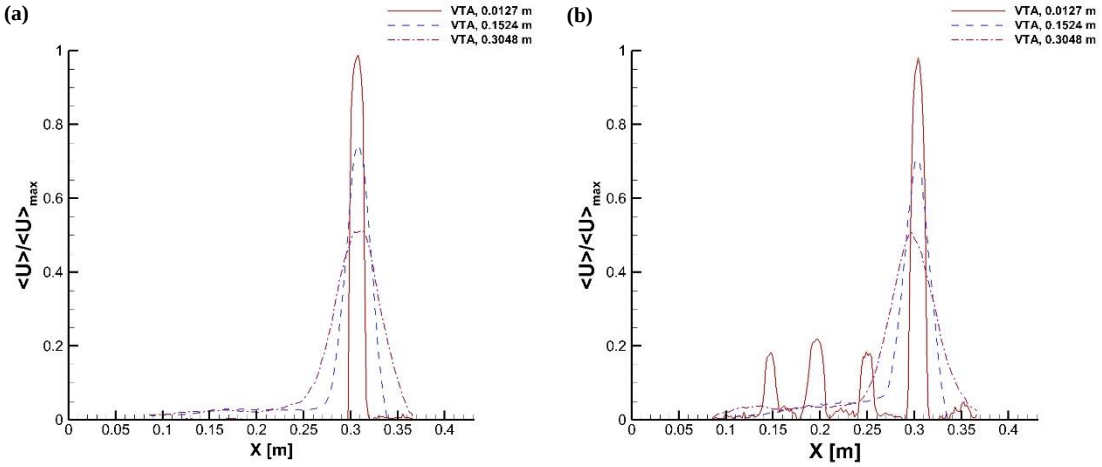

Figure 164. Cross-sectional of normalized mean streamwise velocity (V-T-A plane): (a) Case 4a, (b) Case 4.

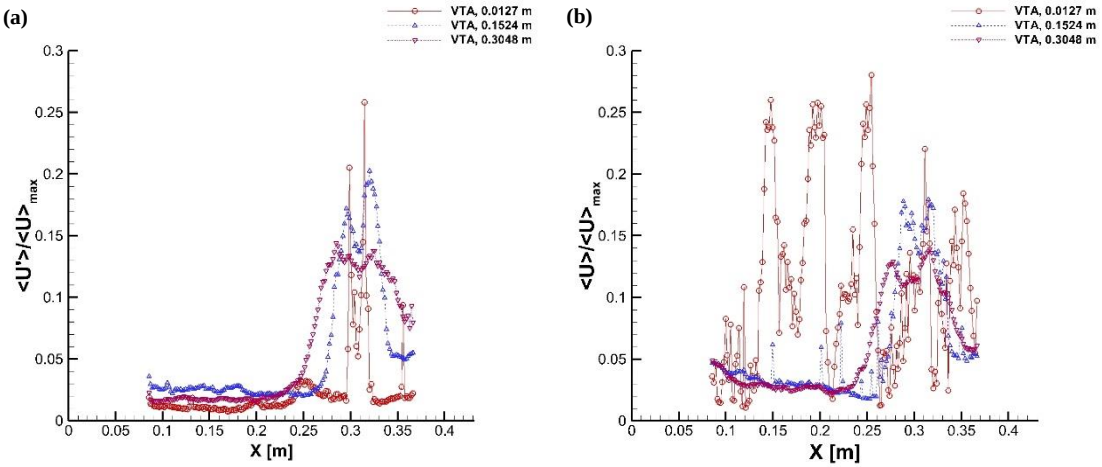

Figure 165. Cross-sectional at different Z-elevation of streamwise turbulence intensity (V-T-A plane): (a) Case 4a, (b) Case 4.

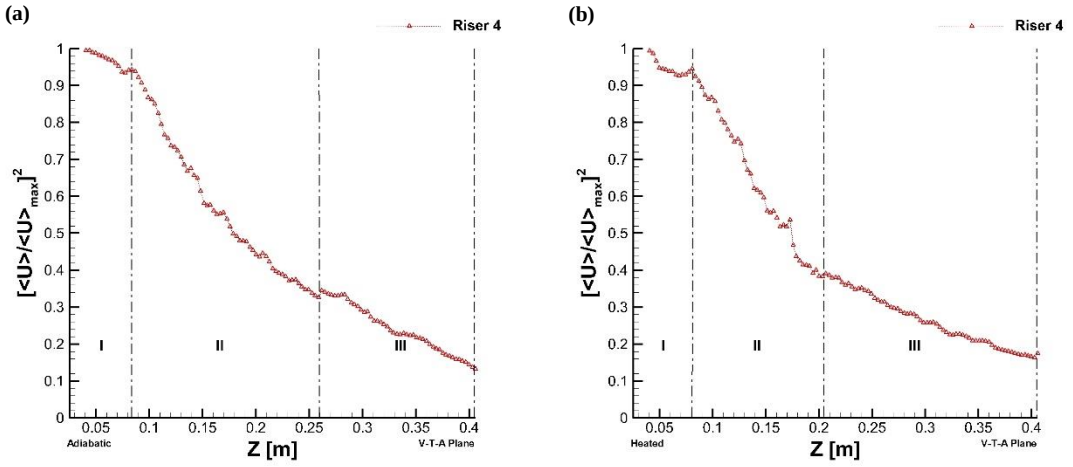

Figure 166. Decay of the mean streamwise velocity along the centerline of the jet (V-T-A plane): (a) Case 4a, (b) Case 4.

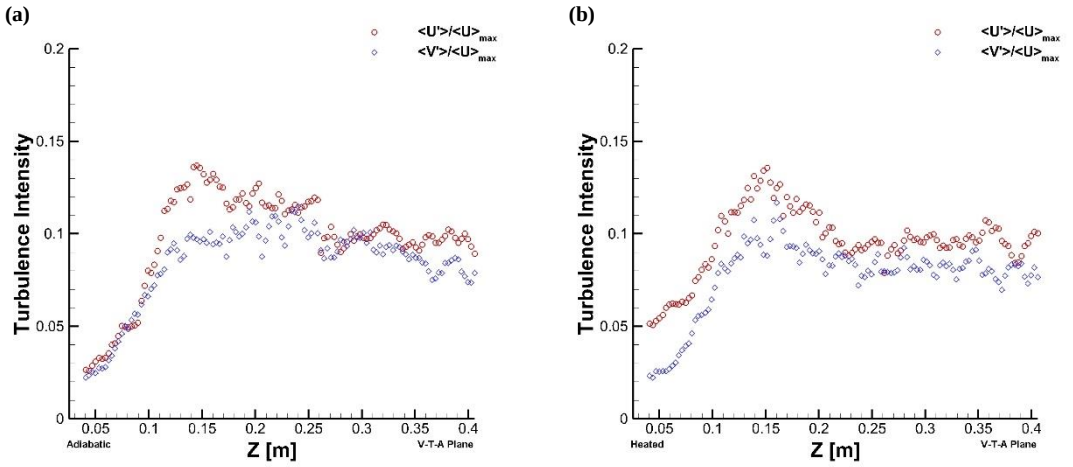

Figure 167. Variation for turbulent intensities along the centerline of the jet (V-T-A plane): (a) Case 4a, (b) Case 4.

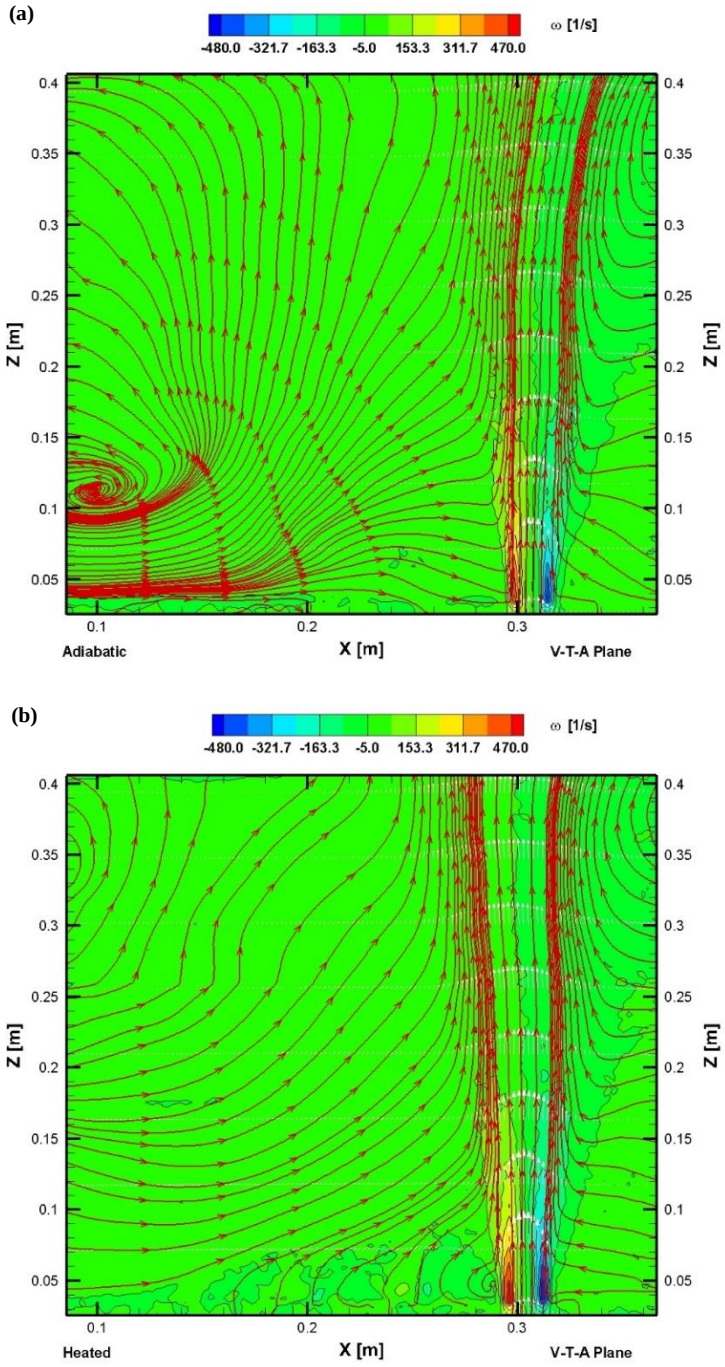

Figure 168. Vorticity contour with streamtraces (V-T-A plane): (a) Case 4a, (b) Case 4.

The streamwise and spanwise turbulence intensities of two components of velocity on the centerline of the jet are shown in Figure 167. The magnitude of both turbulence intensities varied monotonically with Z until they reached a value of about 14% at Z = 0.14 m for Case 4a and Z = 0.15 m for Case 4. They then decreased and increased several times in downstream direction. As mentioned previously, for Z less than 0.17 m and 0.23 m for Case 4a and Case 4, this manner was predictable for a jet with turbulent boundary layers at the jet exit. The variation of spanwise turbulence intensity along the centerline, as illustrated in Figure 167, also displayed attributes similar to the streamwise turbulence intensity. The magnitude of streamwise turbulence intensity was greater than the spanwise turbulence intensity as found in other free shear layer flows for Case 4a and Case 4. The confined ambient conditions substantially affect the rise and fall behaviors of both streamwise and spanwise turbulence intensities.

The vorticity contour plots with streamtraces at the V-T-A plane for both Case 4a and Case 4 are presented in Figure 168. As seen in Case 2a and Case 2, the streamtraces on both sides of the jet were observed to shift toward the jet, which indicated the jet entrainment process through its shear layer. Vortex structures with opposite directions were observed in the outer regions of the jet. The opposite directions of the vortices were indicated by positive and negative values in Figure 161. In the center region of the jet, vortex structures have scarcely been recognized. Unlike Case 2a and Case 2, the magnitude of the vorticity was lower in the adiabatic case than the heated case. As mentioned previously, the presence of the vortices in the outer regions of the jets substantiated the entrainment of ambient fluid as shown by the shifted streamtraces toward

the jet. The range of magnitude in 5 m/s cases was greater than 2.25 m/s cases at the adiabatic and the heated conditions. A medium size counter clockwise vortex was generated with its center at X = 0.1 and Z = 0.11 m for Case 4a. It was found that another counter clockwise vortex was also formed at the V-T-C plane at X = 0.28 m and Z = 0.14 m. Another interesting flow behavior was, in spite of the non-availability of the induced jet from the non-active risers at low velocity and adiabatic condition, the inertia-dominated flow was still energetic and capable of forming a vortex at one of its corners. It was obvious from Case 2 that the induced jets played some role in forming the vortex centered at X = 0.1 m and Z = 0.11 m on V-T-A plane. Further detailed investigations are required to comprehend this behavior.

X.3. The Cases of Four Risers

X.3.1. Case 1a vs. Case 1

Case 1a and Case 1 are cases of which turbulent jets issuing from multiple rectangular slots; namely Riser ①, Riser ②, Riser ③, and Riser ④ into a confined and quiescent surrounding of the same fluid at room (i.e. 25 ^{o}C) and heated temperature (i.e. 120 ^{o}C). As mentioned previously, there were scarce references concentrating on multiple rectangular jets investigations, either inertia-dominated or buoyant-dominated jets, in a stratified and confined environment as opposed to uniform, free and infinite surrounding. Temperature and velocity measurements were carried out inside the upper plenum to

further understanding on the flow characteristics, turbulence mixing, and mechanism of flow instability that can lead to deterioration of cooling performance. The same test experimental facility with similar dimensions was utilized as per one riser cases, i.e. Case 2a, Case 2, Case 4a, and Case 4. For Case 1a and Case 1, a mean velocity of 5 m/s was imposed at the exit plane of each slot.

Previous investigations on twin parallel rectangular jets as well as multiple jets provided means to comprehend the fluid mechanical structure of the flow. In a multiple jet configurations, mutual influence of the adjacent jets towards each other is of paramount importance and therefore necessitates vivid understanding of the multiple jet interactions. A schematic of the flow field of the multiple rectangular free jet is illustrated in Figure 169. The generic mean streamwise velocity profiles for X, Z plane is provided in the schematic.

Since the experiments imposed a uniform inlet velocity at four parallel rectangular jets, or equivalently "double" twin parallel rectangular jets, it was sensible to adopt previous findings from the twin parallel rectangular jets investigations as guidelines for the flow characterizations. Adopting the same convention utilized in the twin parallel jets investigations, the flow field for both inertia-dominated and buoyant-dominated jets issuing from the rectangular nozzles could be characterized by three distinct regions; namely the converging region, merging region, and combined region. A sub-atmospheric pressure region existed in between the adjacent jets which caused the jets to deflect with one another. These converging jets would approach the plane of symmetry with increasing downstream distance Z (Figure 169) from the rectangular nozzle exits.

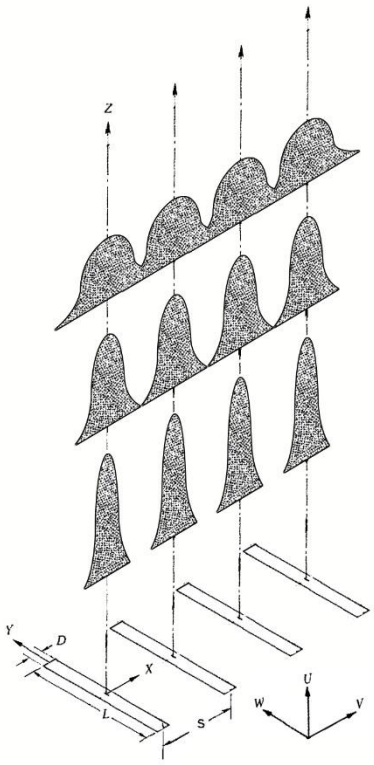

Figure 169. Schematic representation of the flow field of a multiple rectangular free jet.

In these experiments, there were three symmetry lines; the first one was situated in between the jets of Riser ① and Riser ②, the second one was lying in between the jets of Riser ② and Riser ③, and the third one was placed in between the jets of Riser ③ and Riser ④. At the end of the converging region, these jets merged at merging points, or MPs. The merging point was a point on the symmetry axis where the streamwise mean velocity was zero. At this stagnation point, the streamwise mean velocity direction was balanced in the sense that it has negative value upstream the MP and positive value downstream of the MP. The mean streamwise velocity then grew from zero at the MP to

its peak velocity on the symmetry axis. The point at which the mean streamwise velocity was maximum was identified as combined point, or CP. Beyond the CP, the jets behaviors were similar to a single jet of which self-similarity conditions were achieved.

In these experiments, three MPs were obtained at the respective symmetry lines. They were labelled as $MP_{1,2}$ (merging point of the jets from Riser ① and Riser ②), $MP_{2,3}$ (merging point of the jets from Riser ② and Riser ③), and $MP_{3,4}$ (merging point of the jets from Riser ③ and Riser ④). Two combined points were identified and they were marked as $CP_{1,2}$ (combined point of the jets from Riser ① and Riser ②) and $CP_{3,4}$ (combined point of the jets from Riser ③ and Riser ④). The approximate location of the MPs and the CPs were determined from the normalized mean streamwise velocity contour with velocity vectors in Figure 170 and tabulated in Table 32.

From Table 32, it was discovered that the locations of the MPs were non-uniform for Case 1a and quasi-uniform for Case 1. At the exit plane, top-hat profiles with essentially identical magnitudes for Case 1a and uneven magnitudes for Case 1 were attained with very little secondary flow between the jets, as evidenced in Figure 170 and Figure 171. Significant merging of the jets seemed to occur as early as $Z \cong 0.006$ m for Case 1a. The complete merging of all the jets was accomplished at $Z \cong 0.033$ m and $Z \cong 0.017$ m for Case 1a and Case 1. It was observed that the jets from Riser ① and Riser ② would combine together at certain CPs and the same behavior demonstrated by the jets from Riser ③ and Riser ④. This was logical since the configuration of the nearest exit for the jets from Riser ① and Riser ② was the inlet of the left chimney whereas the right chimney inlet was the closest for the jets originated from Riser ③ and Riser ④.

Table 32. Location ($\boldsymbol{Z}$-elevation) of the MPs and CPs for Case 1a and Case 1**.**

	$\boldsymbol{Z}$**-elevation (m)**	
Point	**Case 1a**	**Case 1**
$MP_{1,2}$	~ 0.033	~ 0.017
$MP_{2,3}$	~ 0.015	~ 0.014
$MP_{3,4}$	~ 0.006	~ 0.014
$CP_{1,2}$	~ 0.173	~ 0.218
$CP_{3,4}$	~ 0.183	~ 0.224

The tabulation of the MPs and CPs for the heated conditions revealed a degree of uniformity. The equivalent degree of uniformity was displayed by the CPs of the adiabatic case; nonetheless, some degree of non-uniformity exhibited by the MPs of Case 1a. This suggested that different domains in the upper domain have different merging regions which translated into different turbulence mixing conditions at adiabatic conditions. It appeared that the uniformity of the MPs and CPs of Case 1 indicated a positive relationship with the presence of buoyancy forces in the system, i.e. the buoyancy forces tended to even out or balance the distribution of the MPs and CPs of the system.

At 0.0127 m and 0.1524 m, both streamwise and spanwise rms intensities recorded higher values at the heated condition than the adiabatic condition, respectively. This was

expected due to considerable turbulence kinetic energy production from buoyancy forces on the transition of momentum-dominated pure jets to buoyancy-dominated pure plume. Further downstream in the streamwise direction, the buoyant flux has reduced significantly and finally reached zero at the point of neutral buoyancy prior to impinging the upper plenum top wall. The flow would be decelerated once it hit the point of neutral buoyancy, and the buoyancy force would be negative, turned downwards and spread sideways. Based on Figure 171 and Figure 172, there was a strong indication that the combined buoyant jets have maintained their acceleration and impinged the top wall of the upper plenum; therefore the points of neutral buoyancy were not reached for Case 1. At 0.3048 m, both streamwise and spanwise rms intensities registered comparable values at the heated and adiabatic conditions, respectively (Figure 170-Figure 171 and Figure 173-Figure 174).

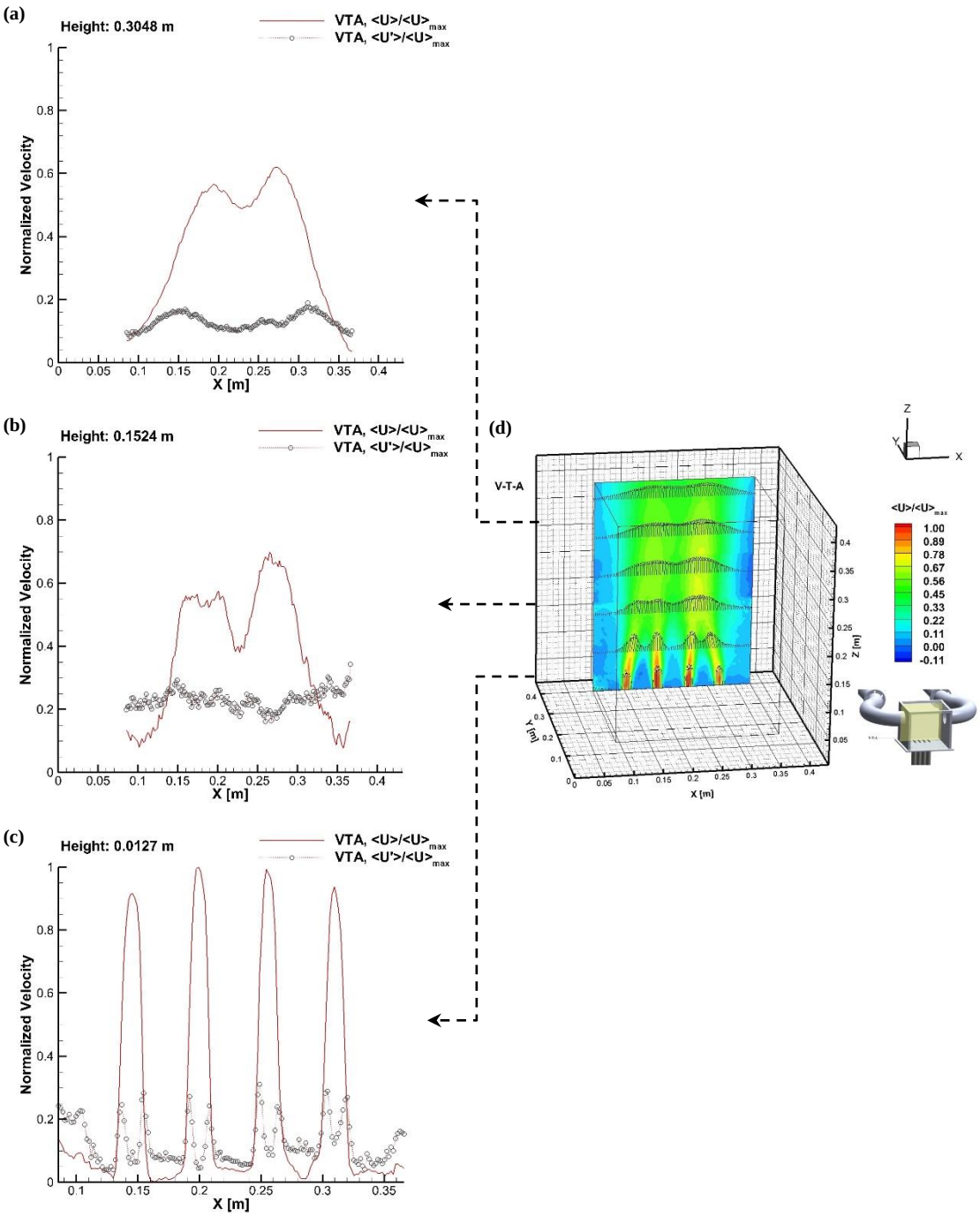

Figure 170. Case 1a V-T-A plane: (a)-(c) Cross-sectional of normalized mean streamwise velocity and streamwise turbulence intensity, (d) Normalized mean streamwise velocity contour with velocity vectors.

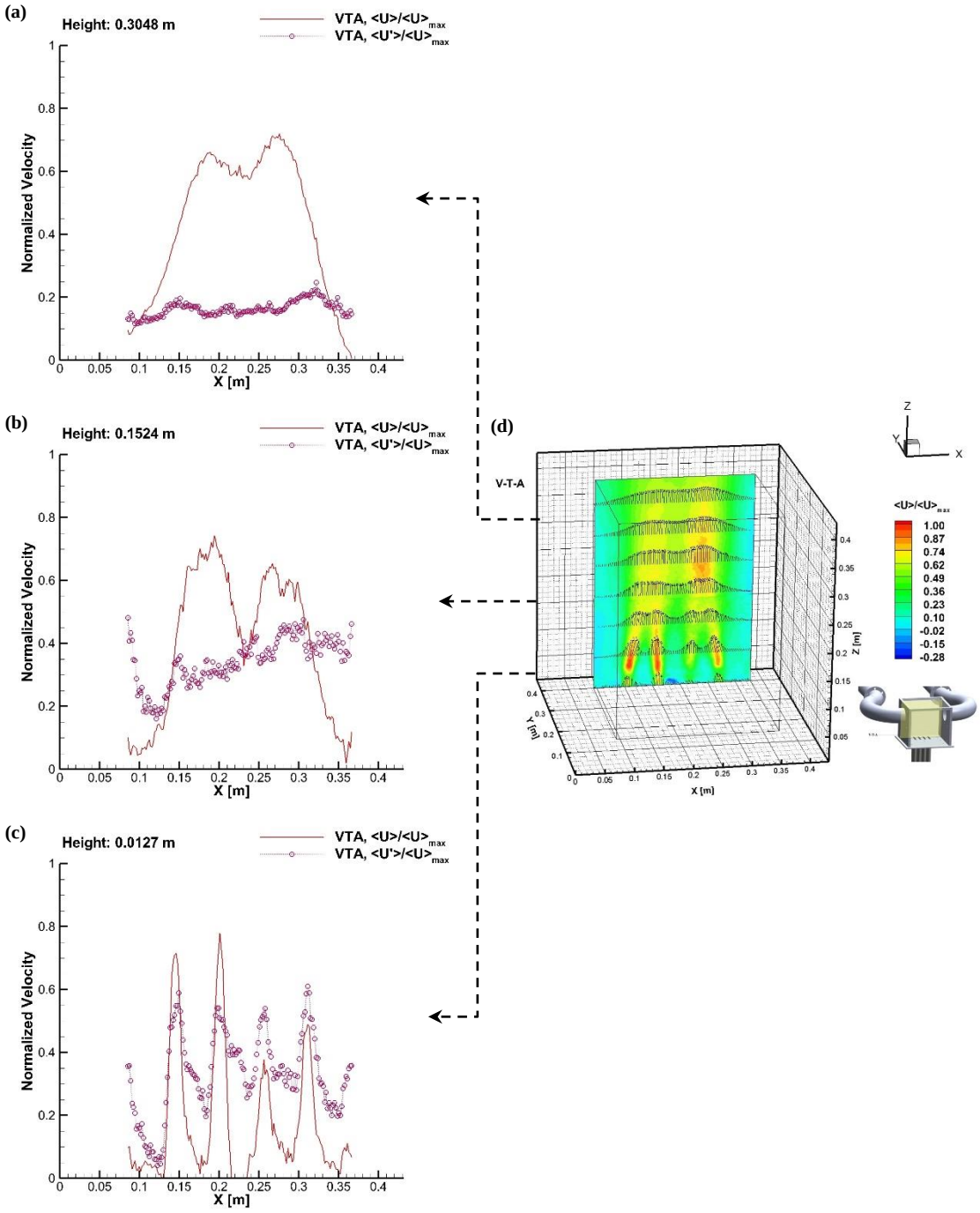

Figure 171. Case 1 V-T-A plane: (a)-(c) Cross-sectional of normalized mean streamwise velocity and streamwise turbulence intensity, (d) Normalized mean streamwise velocity contour with velocity vectors.

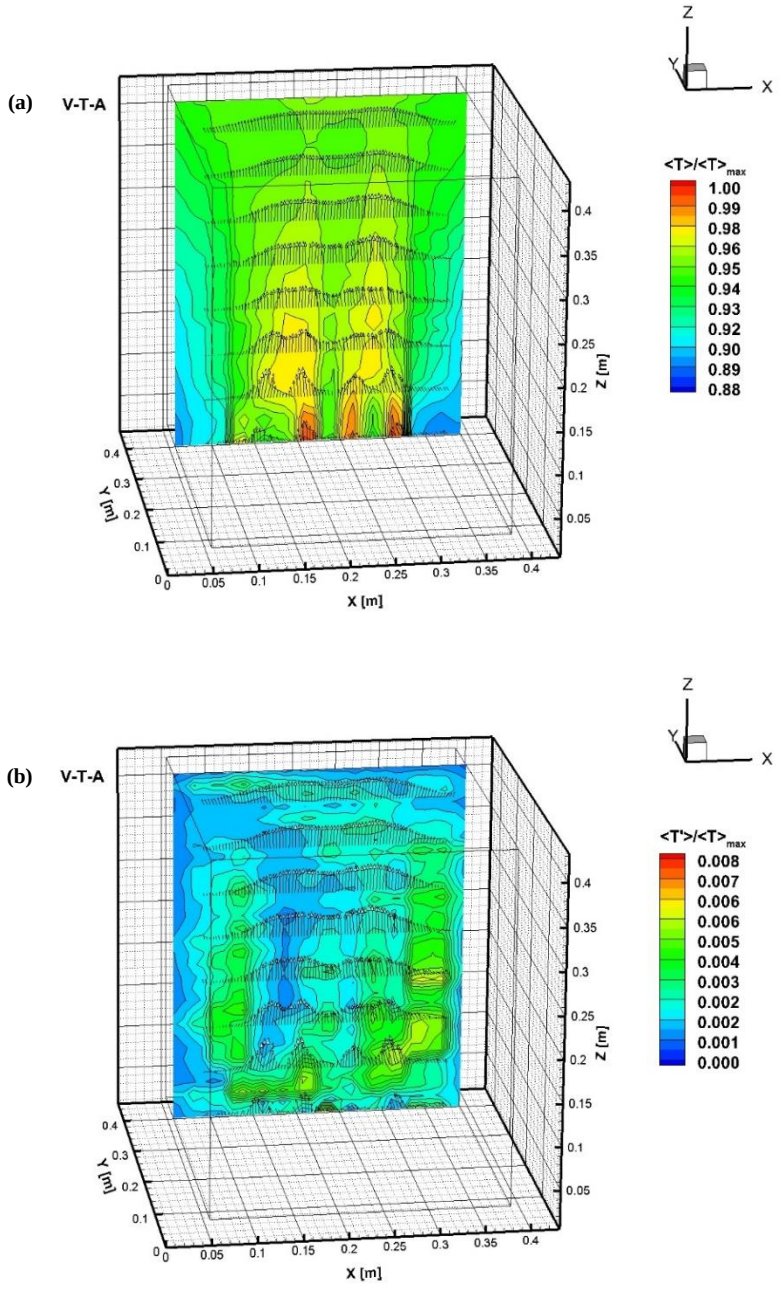

Figure 172. Case 1 V-T-A plane: (a) Normalized mean temperature contour with velocity vectors, (b) Normalized fluctuating temperature contour with velocity vectors.

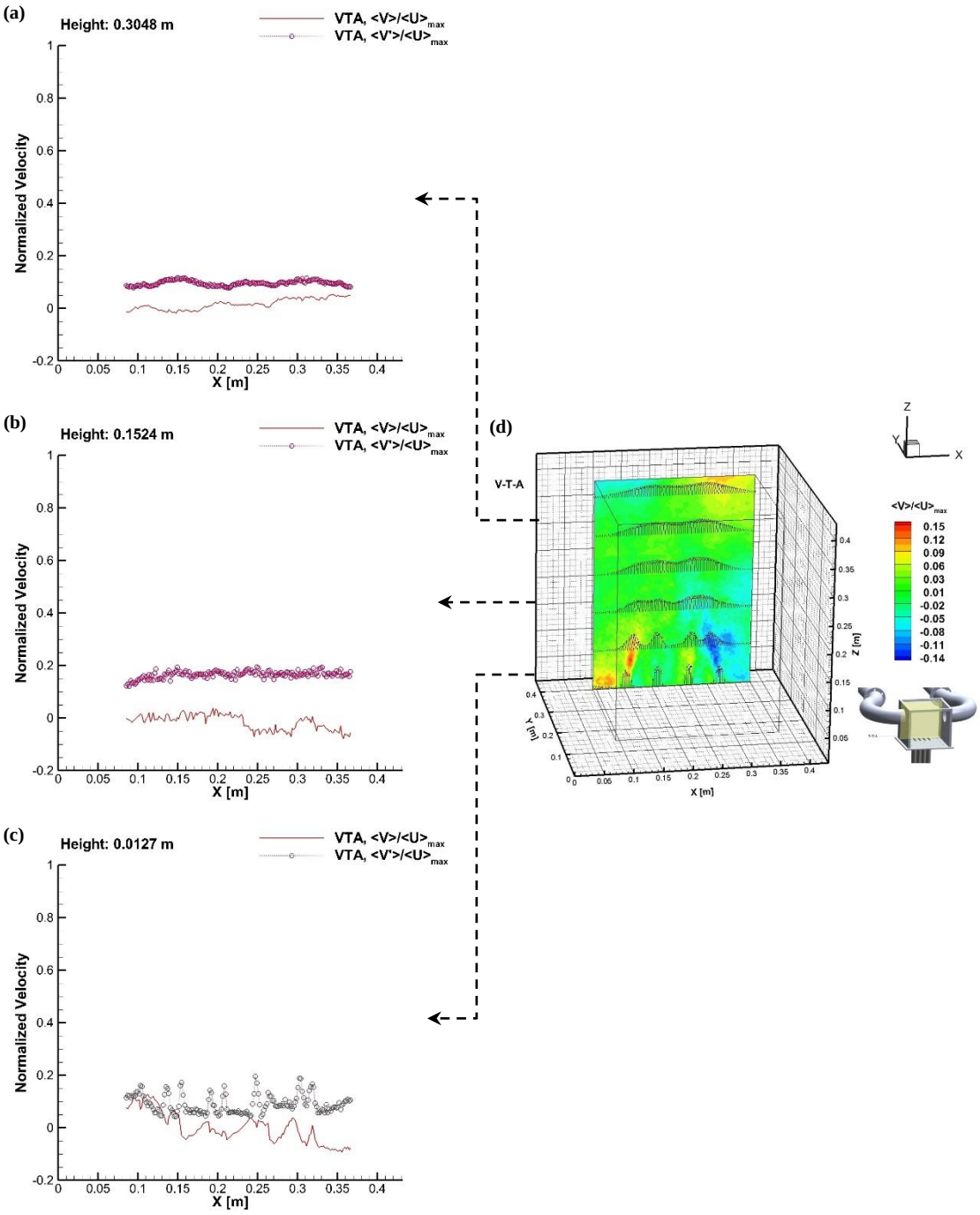

Figure 173. Case 1a V-T-A plane: (a)-(c) Cross-sectional of normalized mean spanwise velocity and spanwise turbulence intensity, (d) Normalized mean spanwise velocity contour with velocity vectors.

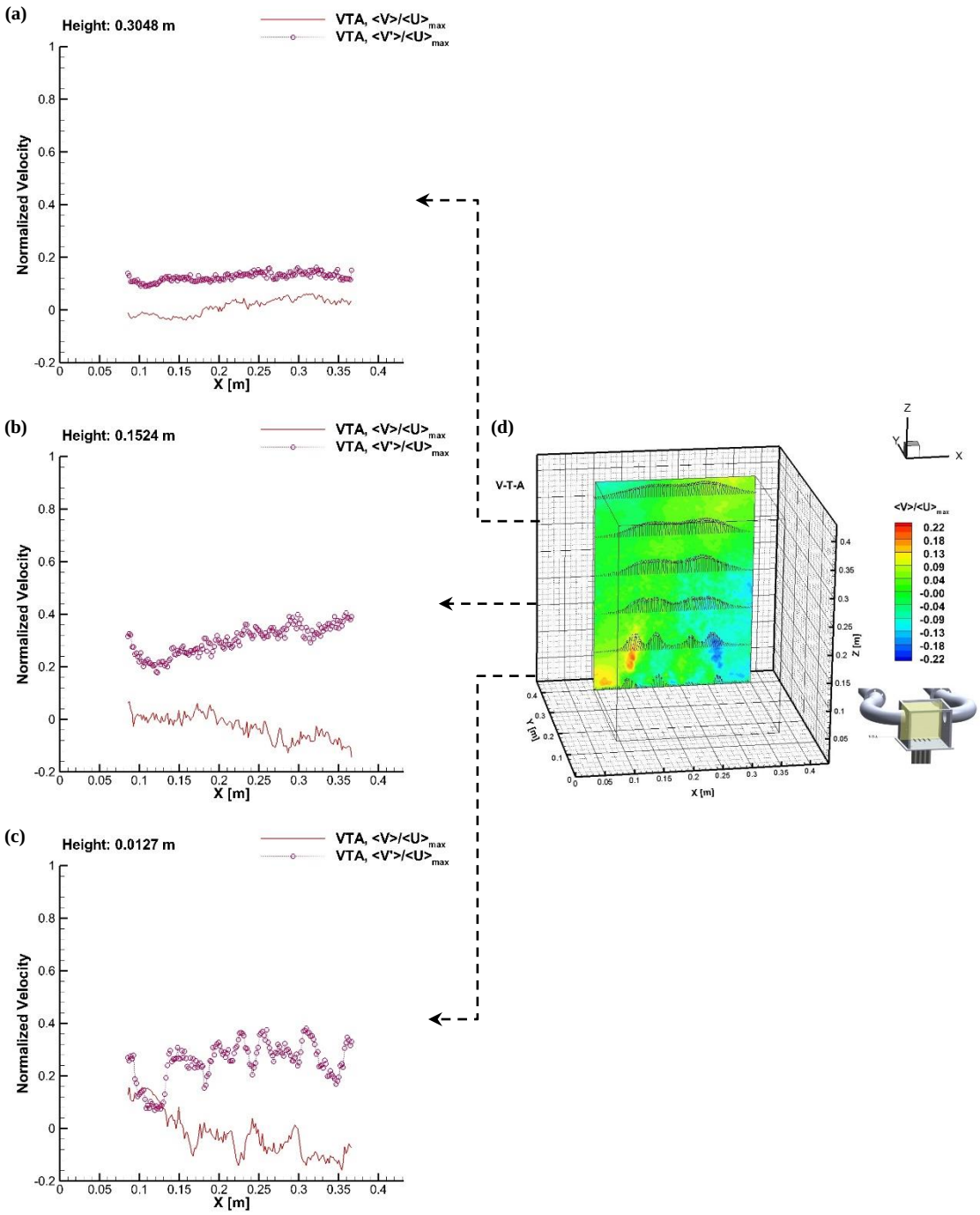

Figure 174. Case 1 V-T-A plane: (a)-(c) Cross-sectional of normalized mean spanwise velocity and spanwise turbulence intensity, (d) Normalized mean spanwise velocity contour with velocity vectors.

The normalized mean and fluctuating temperature contours with velocity vectors for Case 1 are portrayed in Figure 172. A fairly symmetric normalized mean temperature distribution was observed. The highest temperature was recorded near the jets' exit. A fairly low temperature region at the left and right hand corner of V-T-A plane was due to entrainment of the ambient fluid. High temperature fluctuations were registered for regions in between the upper plenum's left wall and the jet of Riser ①, the upper plenum's right wall and the jet of Riser ④ and slightly above the jets exit. Higher fluctuation pattern near the jets interface boundary with quiescent ambient was similar to the single jet cases.

Figure 175 and Figure 176 present the cross-section of the normalized Reynolds stress distribution and the normalized Reynolds stress contour with velocity vectors for Case 1a and Case 1. In turbulent flow, Reynolds stress or turbulent shear stress is an important diffusional mechanism for transport of fluid momentum toward the boundary. The sum of Reynolds stress (caused by fluid momentum macroscopic diffusion) and the viscous shear stress (caused in part by fluid momentum molecular diffusion and by attractive forces between molecules at the shear plane) is equal to the total shear stress across the shear plane. The Reynolds stress distribution at 0.0127 m has less scattered distribution as compared with its distribution at 0.1524 m for the adiabatic case. Similar behavior was shown at the said elevations for the heated case. The magnitudes of the Reynolds stress at 0.0127 m and 0.1524 m were higher for the heated case than the adiabatic case. At 0.3048 m, the magnitudes of the adiabatic case were comparable to the heated case; however, the distribution of the turbulent shear stress has a highly scattered pattern at the heated condition as compared with the adiabatic condition.

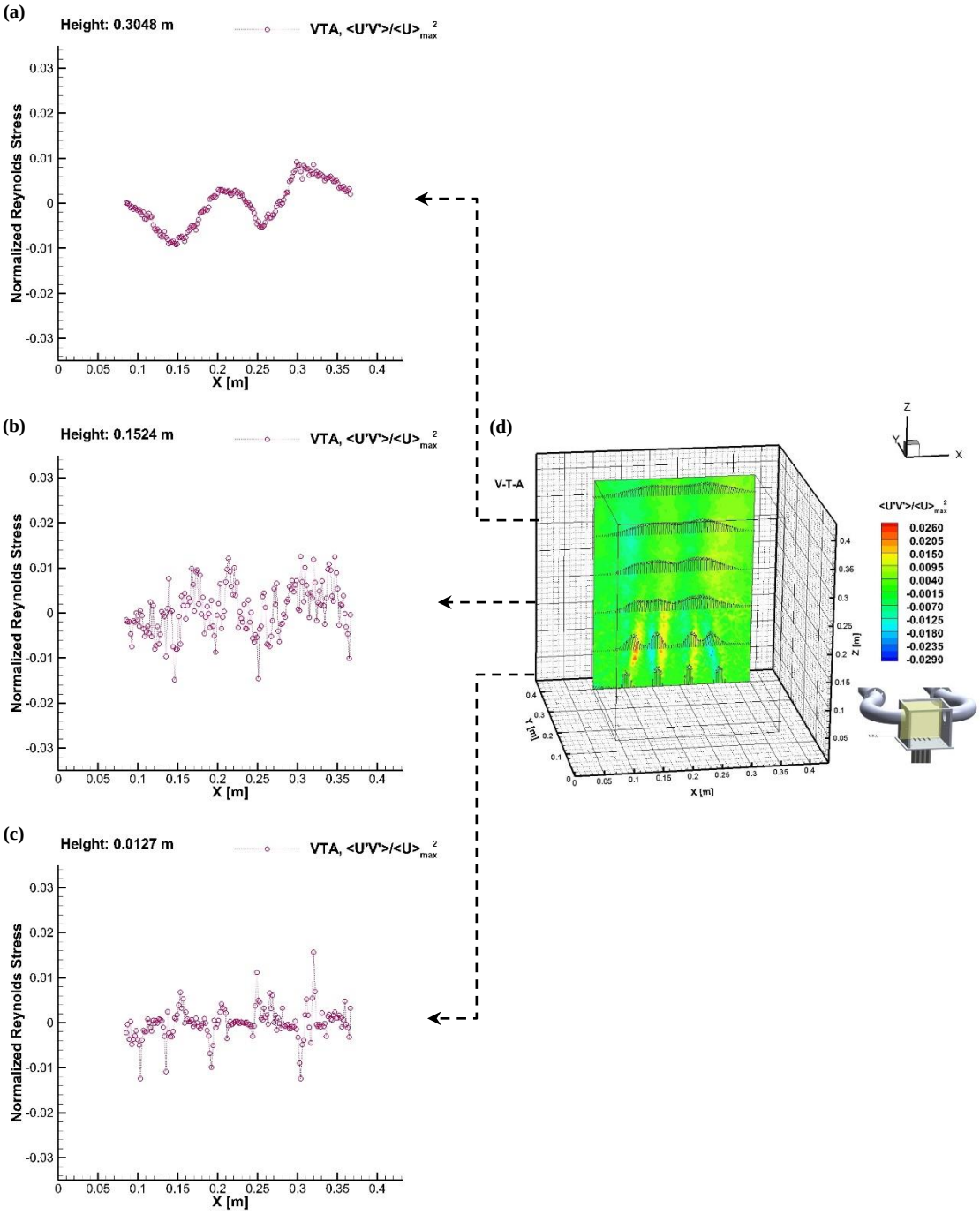

Figure 175. Case 1a V-T-A plane: (a)-(c) Cross-sectional of normalized Reynolds stress distribution, (d) Normalized Reynolds stress contour with velocity vectors.

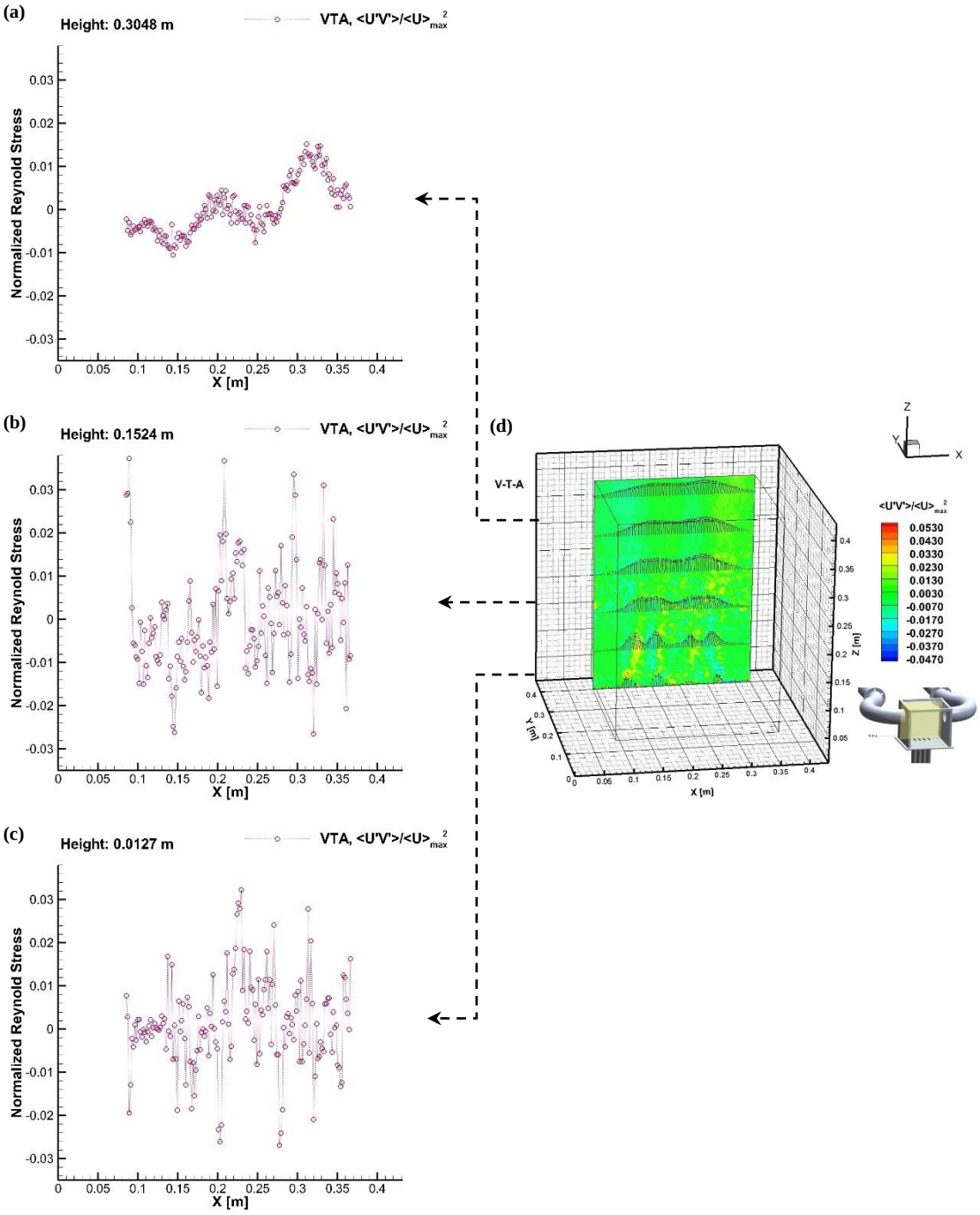

Figure 176. Case 1 V-T-A plane: (a)-(c) Cross-sectional of normalized Reynolds stress distribution, (d) Normalized Reynolds stress contour with velocity vectors.

The measured decay of the square of the mean streamwise velocity along the centerline for Case 1a and Case 1 are illustrated in Figure 177. The jets issued from Riser ② and Riser ③ ("the inner jets") and from Riser ① and Riser ④ ("the outer jets") exhibited nearly similar trend at both adiabatic and heated conditions. For Case 1a and Case 1, the velocity decay showed similar trending as the one riser cases of which the decay rate could be segregated into three regions based its decay behavior. However, unlike the one riser cases where Region II has the highest decay rate, Region I has the steepest slope and therefore it has the fastest velocity decay rate for both Case 1a and Case 1. In fact, Region II for Case 1a has the slowest velocity decay rate. In general, the magnitudes of the decay velocity were greater for the inner jets than the outer jets. The distribution of the velocity decay was higher and highly scattered in the heated case compared with the adiabatic case.

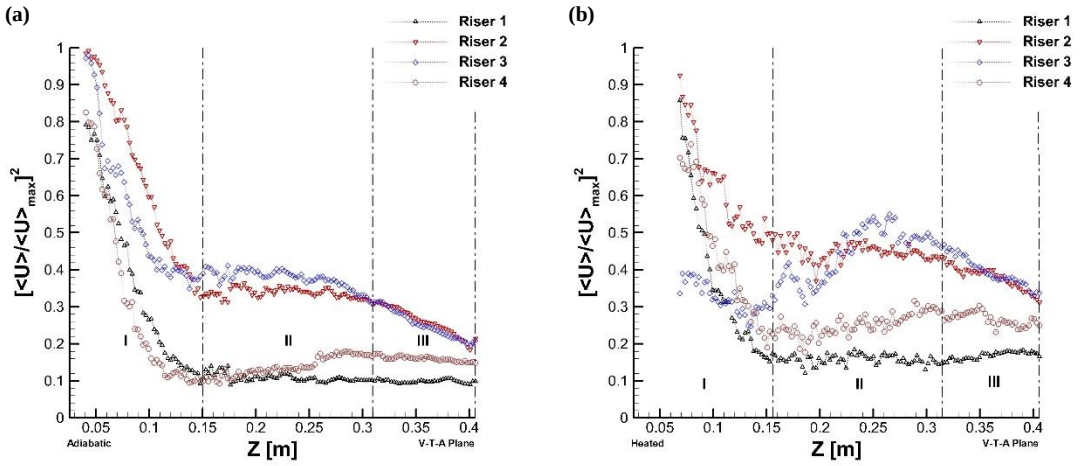

Figure 177. Decay of the mean streamwise velocity along the centerline of the jet (V-T-A plane): (a) Case 1a, (b) Case 1.

At the heated condition, the jets exhibited three regions decay rate characteristics as well; however, Riser ③ and Riser ④ demonstrated some anomalies from the trend of the adiabatic condition in Region II. It was observed that the both Riser ③ and Riser ④ have positive slopes which indicated the build-up of the mean streamwise velocity. In fact, Riser ④ has a positive slope at Region II for Case 1a and Case 1. It was anticipated that the non-uniformity of the inlet boundary condition and irregularities of the risers' geometry and outlet configurations might have somehow contributed to the problem. Further investigation is needed to verify this behavior. Buoyancy forces has played a significant part in altering the decay pattern and distribution to be more scattered as seen in Figure 177 for Case 1.

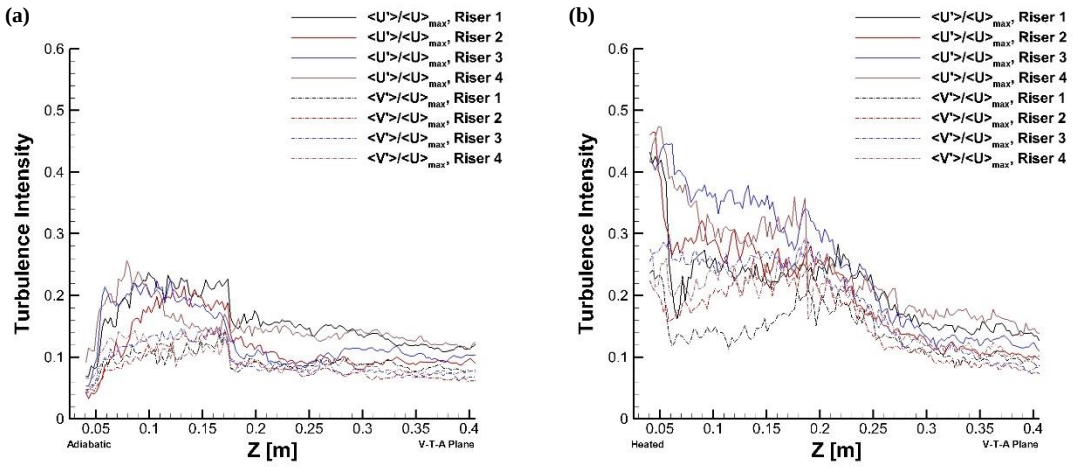

Figure 178. Variation for turbulent intensities along the centerline of each jet (V-T-A plane): (a) Case 1a, (b) Case 1.

The streamwise and spanwise turbulence intensities of two components of velocity along the centerline of each jet are shown in Figure 178. The highest recorded streamwise turbulence intensities were up to 26% at $Z = 0.079$ m (Riser ④) for Case 1a and up to 47% at $Z = 0.048$ m (Riser ④) for Case 1. Variation of the streamwise turbulence intensity was fairly high at $Z \lesssim 0.17$ m and $Z \lesssim 0.19$ m for Case 1a and Case 1. The magnitude of the streamwise turbulence intensity started to decrease downstream of said locations. From Figure 178, the corresponding spanwise turbulence intensity magnitude at each point for each riser's jet was found to be less than its streamwise counterpart at corresponding locations in the X, Z plane. From these observations, one might deduce that the presence of buoyancy forces contributed to the rise of the streamwise turbulence intensity.

X.3.2. Case 3a vs. Case 3

Case 3a and Case 3 were similar to Case 2a and Case 2 but in these experiments, each jet exit velocity was replaced by 2.25 m/s instead of 5 m/s. The other boundary condition remained unchanged.

From Table 33, it was learned that the positions of the MPs were non-uniform for Case 3a and quasi-uniform for Case 3. At the exit plane, top-hat profiles with almost equal magnitudes for Case 1a and uneven magnitudes for Case 1 were achieved with very small recirculating flow between the jets, as depicted in Figure 179 and Figure 180. Substantial merging of the jets seemed to occur as early as $Z \cong 0.010$ m for both Case 3a and Case 3,

respectively. The complete merging of all the jets was accomplished at $Z \cong$ 0.028 m and $Z \cong$ 0.014 m for Case 3a and Case 3. It appeared that the jets' combining preference in Case 3a and Case 3 was similar to Case 1a and Case 1 despite the difference of the upper plenum's inlet velocity.

Table 33. Location (***Z***-elevation) of the MPs and CPs for Case 3a and Case 3**.**

	***Z*-elevation (m)**	
Point	**Case 3a**	**Case 3**
$MP_{1,2}$	~ 0.050	~ 0.011
$MP_{2,3}$	~ 0.010	~ 0.010
$MP_{3,4}$	~ 0.028	~ 0.014
$CP_{1,2}$	~ 0.215	~ 0.246
$CP_{3,4}$	~ 0.162	~ 0.241

On one hand, the tabulation of the MPs and CPs for the heated condition presented some degree of consistency. On the other hand, the adiabatic condition revealed a lack of orderliness for its MPs and CPs. This suggested that different domains in the upper plenum

have different merging regions which implied different turbulence mixing conditions at adiabatic conditions. It appeared that the consistency of the MPs and CPs of Case 3 has positive relationship with the presence of buoyancy forces in the system. Similar behaviors were observed for Case 1a. It was strongly believed that the geometry of the system as well as the confined ambient environment have contributed to the lack of uniformity of the MPs and CPs at the adiabatic condition.

As seen in Case 1a and Case 1, at 0.0127 m and 0.1524 m respectively, it was documented that both streamwise and spanwise rms intensities had higher values at the heated condition than the adiabatic condition. Similar explanation for Case 1a and Case 1 was applicable for Case 3a and Case 3. By referring to Figure 180 and Figure 181, it was believed that the combined buoyant jets maintained their acceleration and impinged the top wall of the upper plenum; therefore the points of neutral buoyancy were absent for Case 3. Again, at 0.3048 m, both streamwise and spanwise rms intensities registered comparable values at the heated and adiabatic conditions, respectively (Figure 179-Figure 180 and Figure 182-Figure 183).

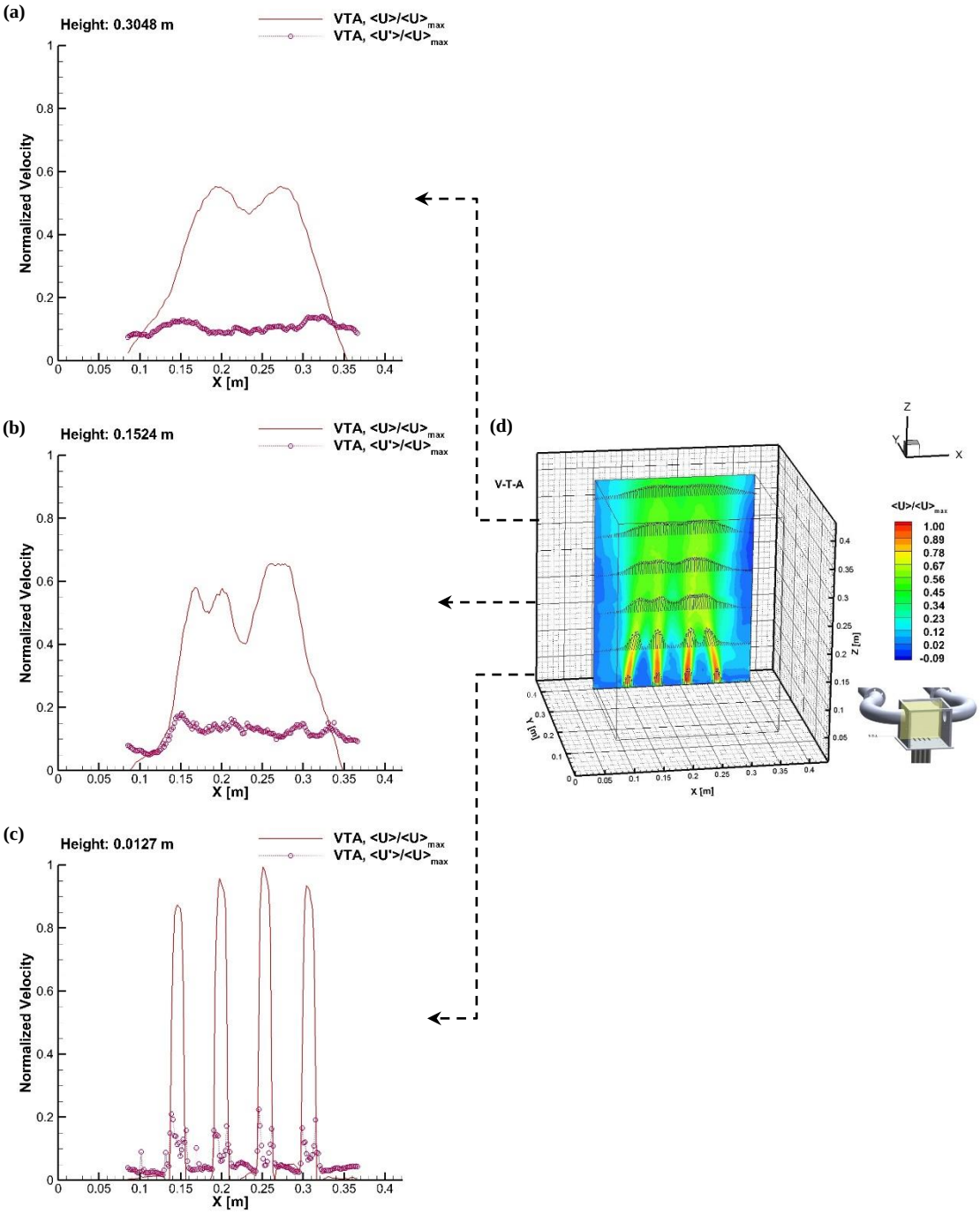

Figure 179. Case 3a V-T-A plane: (a)-(c) Cross-sectional of normalized mean streamwise velocity and streamwise turbulence intensity, (d) Normalized mean streamwise velocity contour with velocity vectors.

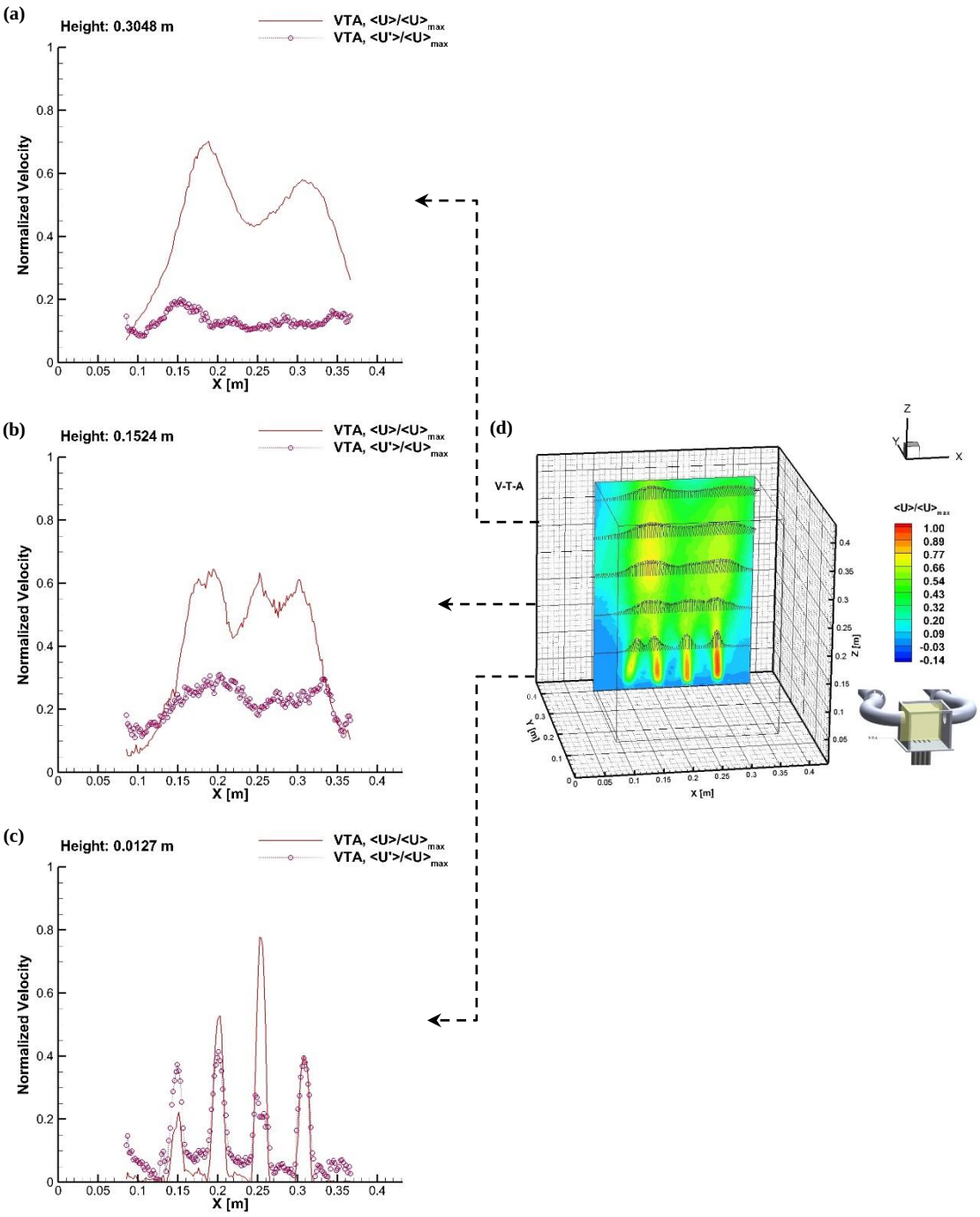

Figure 180. Case 3 V-T-A plane: (a)-(c) Cross-sectional of normalized mean streamwise velocity and streamwise turbulence intensity, (d) Normalized mean streamwise velocity contour with velocity vectors.

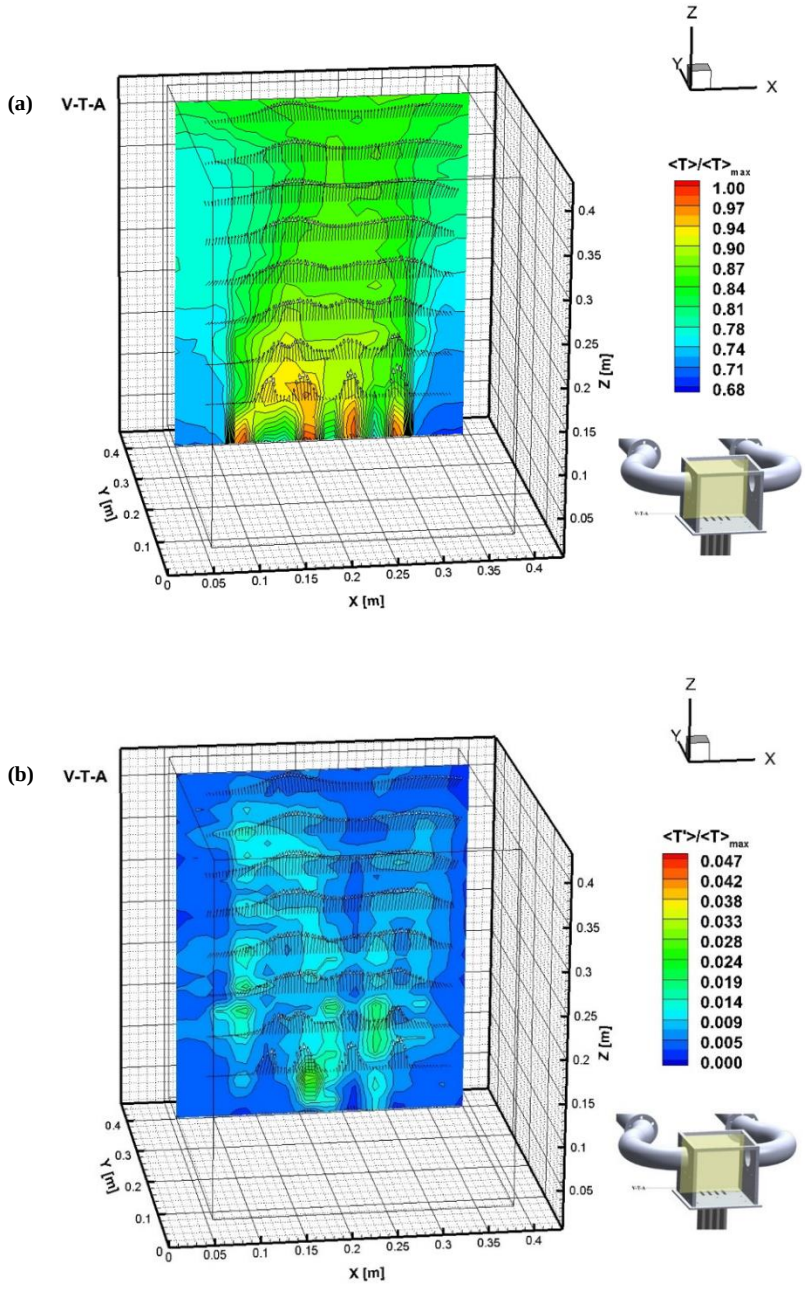

Figure 181. Case 3 V-T-A plane: (a) Normalized mean temperature contour with velocity vectors; (b) Normalized fluctuating temperature contour with velocity vectors.

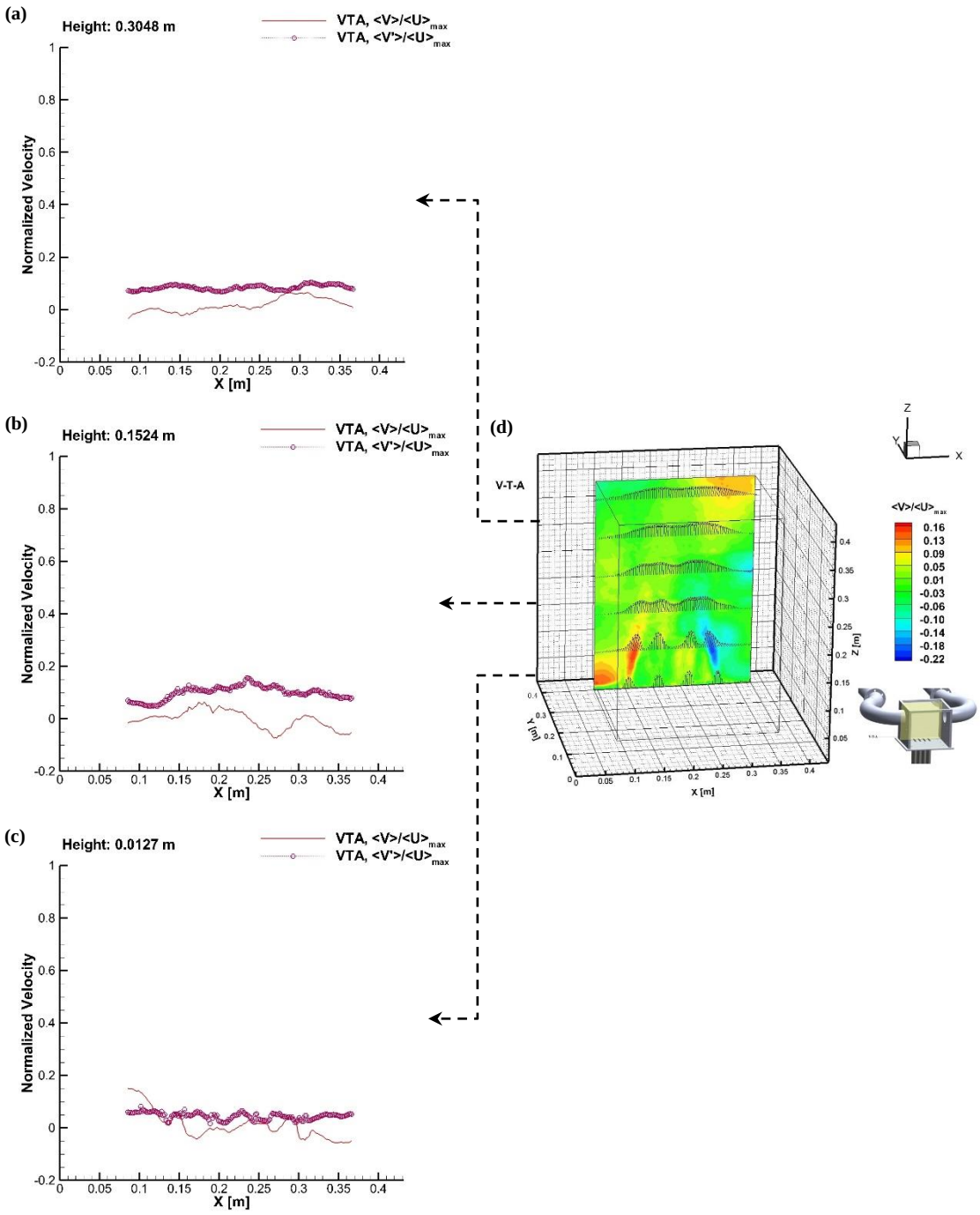

Figure 182. Case 3a V-T-A plane: (a)-(c): Cross-sectional of normalized mean spanwise velocity and spanwise turbulence intensity, (b) Normalized mean spanwise velocity contour with velocity vectors.

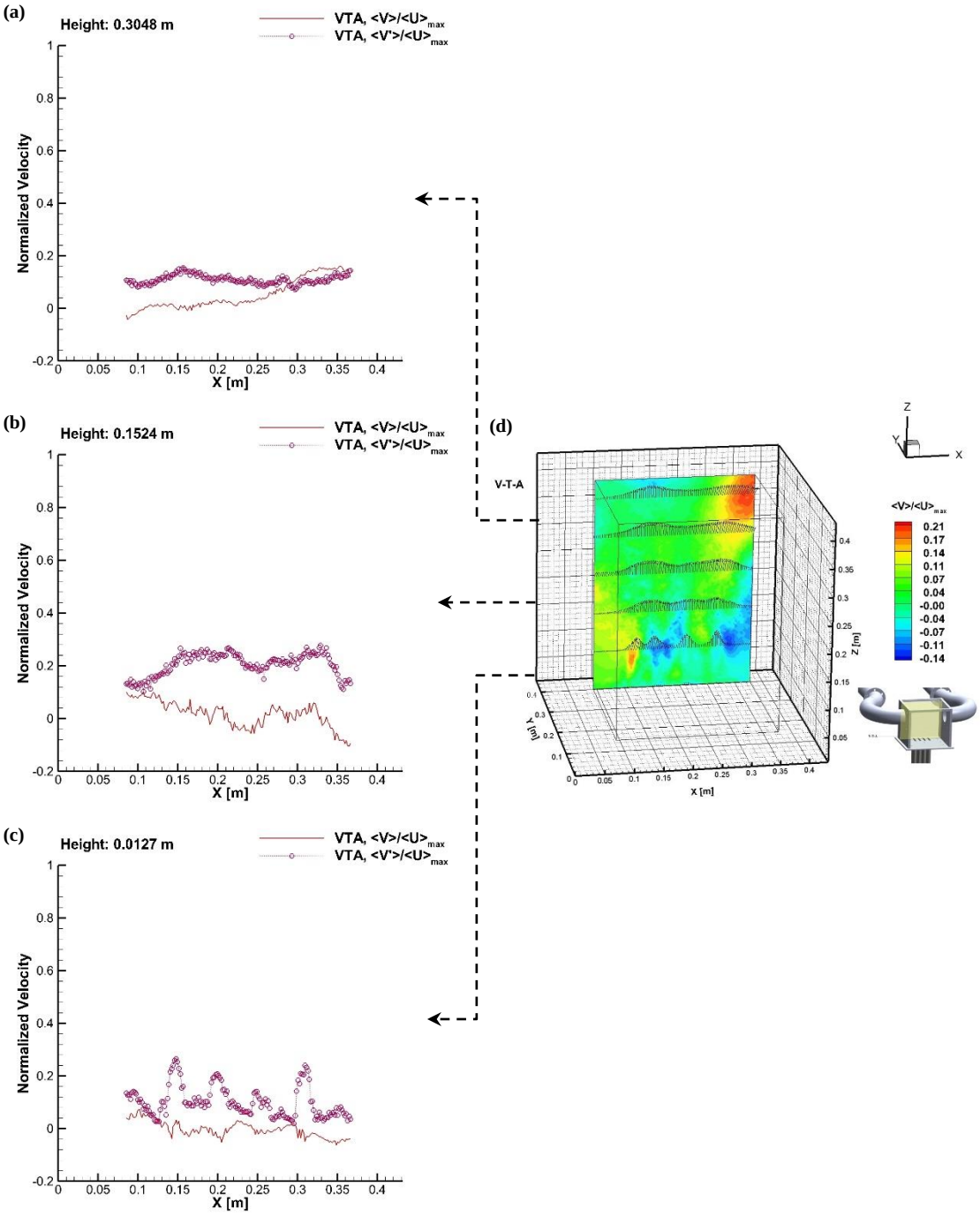

Figure 183. Case 3 V-T-A plane: (a)-(c) Cross-sectional of normalized mean spanwise velocity and spanwise turbulence intensity, (d) Normalized mean spanwise velocity contour with velocity vectors.

The normalized mean and fluctuating temperature contours with velocity vectors for Case 3 are portrayed in Figure 181. An asymmetric normalized mean temperature profile was observed despite symmetrical boundary conditions for each riser. The highest temperature was recorded near the jets exit. A high temperature gradient across the volume of the upper plenum (43-100%) was recorded for Case 3 as compared with Case 1 (88-100%). The normalized mean temperature contour right across the exits of the jets showed uneven temperature distribution which suggested that the jets from Riser ① and Riser ② were slightly hotter than the other two jets. As a result, the jet from Riser ② registered higher fluctuation near its exit. As the jets travelled downstream, their temperature fluctuations have lessened and became more homogeneous. It was observed that the temperature fluctuation diminished near the upper plenum side walls. The pattern of higher fluctuation near the jets interface boundaries with quiescent ambient was also apparent.

Figure 184 and Figure 185 display the cross-section of normalized Reynolds stress distribution and the normalized Reynolds stress contour with velocity vectors for Case 3a and Case 3. In general, for the adiabatic case, the Reynolds stress variation at 0.1524 m was higher than its distribution at 0.0127 m. Identical behavior was exhibited by the heated case at the said elevation. As observed in Case 1a and Case 1, the magnitudes of the Reynolds stress at 0.0127 m and 0.1524 m were higher at the heated condition than the adiabatic condition. At 0.3048 m, the magnitudes of the adiabatic case were similar to the heated case at many points; however, the distribution of the turbulent shear stress was highly scattered at the heated condition as compared with the adiabatic condition.

The measured decay of the square of the mean streamwise velocity along the centerline is shown in Figure 186. As observed in Case 1a and Case 1, the trends and behaviors of the inner jets (the jets issued from Riser ② and Riser ③) and the outer jets (the jets issued from Riser ① and Riser ④) were comparable at both the heated and the adiabatic conditions, respectively. It was interesting to pay attention to the pattern of decrease and increase of the decay velocity rate in Region II at the heated condition, particularly for the jets from Riser ②, Riser ③, and Riser ④. This pattern implied that the buoyant jets have high interaction and turbulence mixing in this region. The magnitudes of the decay velocity were greater for the inner jets than the outer jets. The distribution of the velocity decay was higher and highly scattered in the heated case compared with the adiabatic case.

The streamwise and spanwise turbulence intensities of two components of velocity along the centerline of each jet are shown in Figure 187. The highest recorded streamwise turbulence intensities were 18% at $Z = 0.083$ m (Riser ①) for Case 3a and 52% at $Z = 0.047$ m (Riser ①) for Case 3. Variation of the streamwise turbulence intensity has started to become more stable passing the maximum CP at $Z \gtrsim 0.215$ m and 0.07 m $Z \gtrsim 0.246$ m for Case 3a and Case 3. The corresponding spanwise turbulence intensity magnitude at each point for each riser's jet was found to be mostly less than its streamwise counterpart at corresponding locations in the X, Z plane as portrayed in Figure 187. Again, the buoyancy forces affected the rise and fall of the streamwise turbulence intensity.

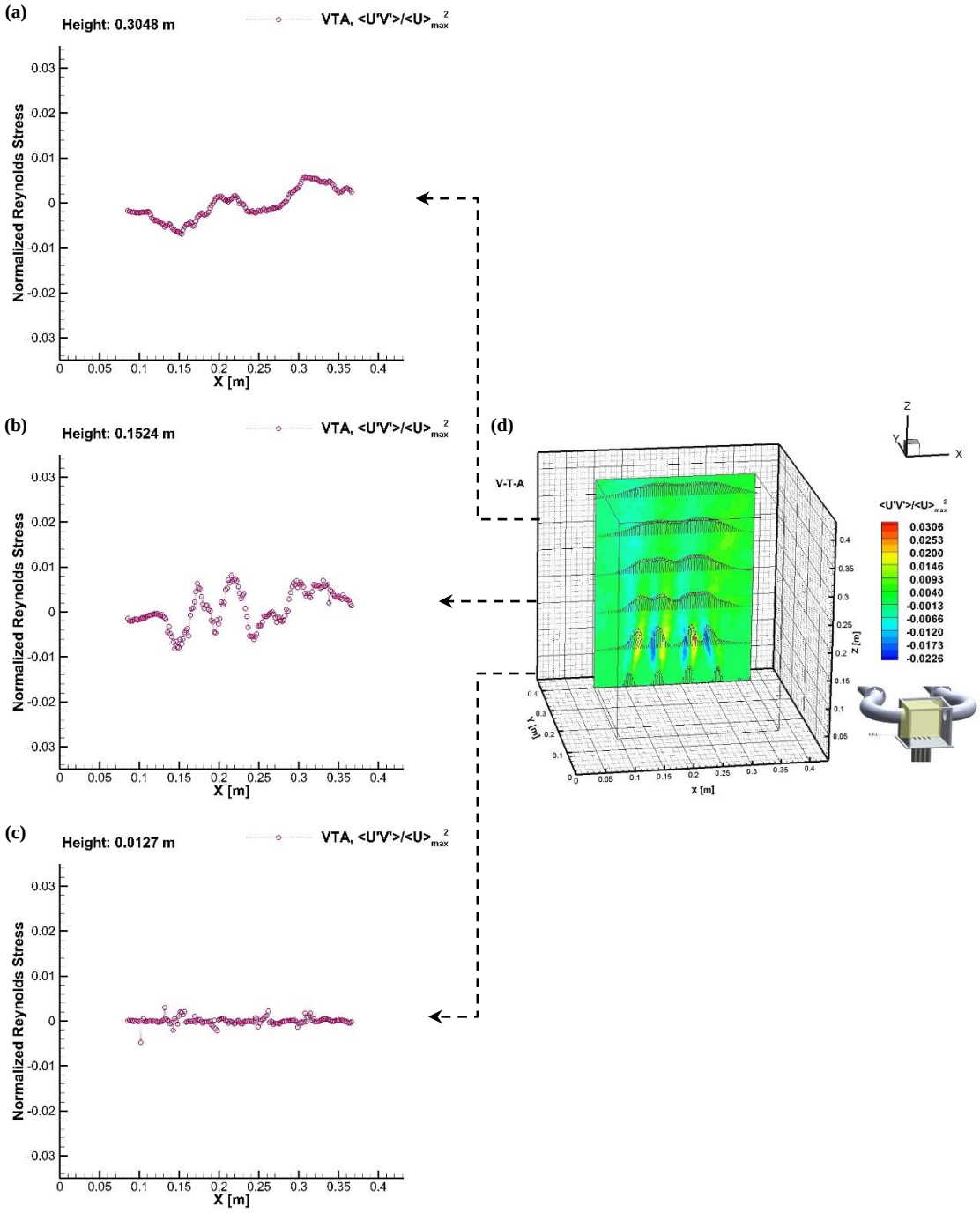

Figure 184. Case 3a V-T-A plane: (a)-(c) Cross-sectional of normalized Reynolds stress distribution, (d) Normalized Reynolds stress contour with velocity vectors.

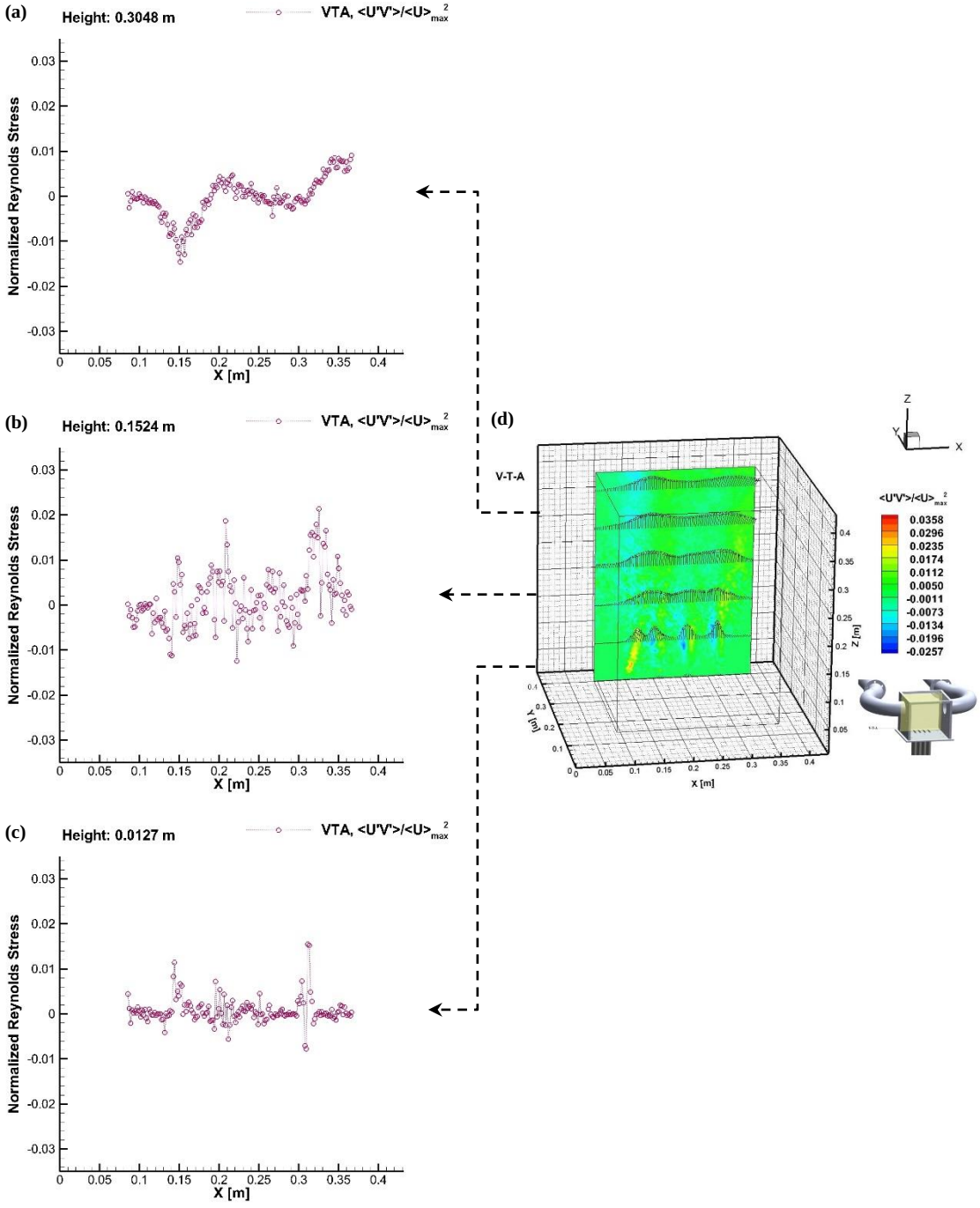

Figure 185. Case 3 V-T-A plane: (a)-(c) Cross-sectional of normalized Reynolds stress distribution, (d) Normalized Reynolds stress contour with velocity vectors.

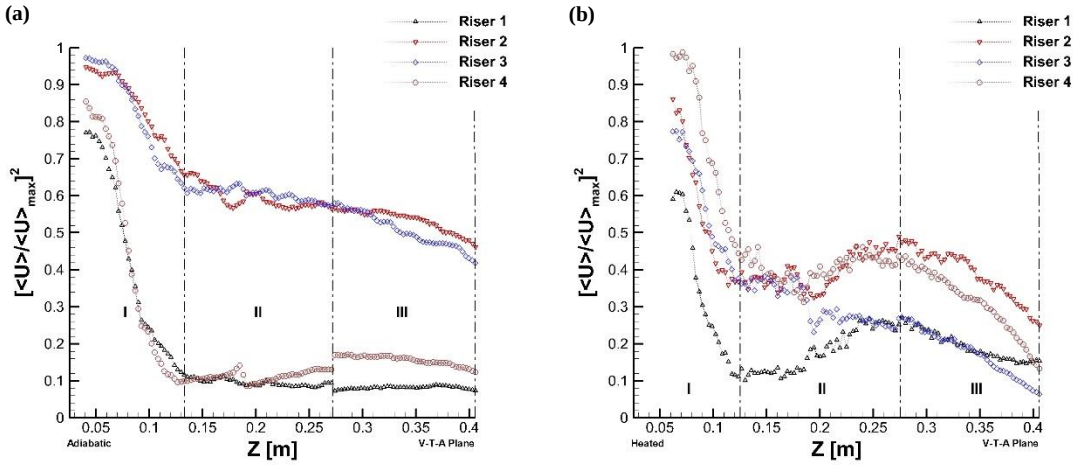

Figure 186. Decay of the mean streamwise velocity along the centerline of each jet (V-T-A plane): (a) Case 3a, (b) Case 3.

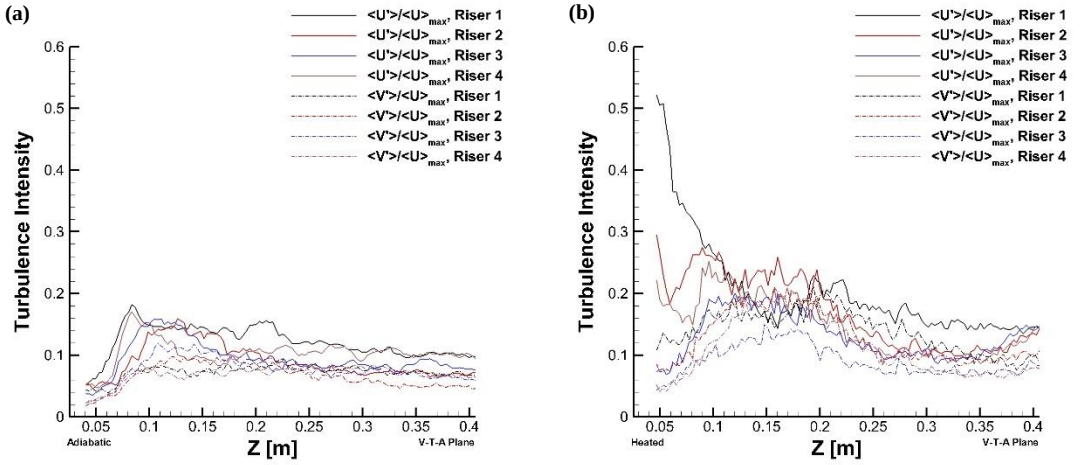

Figure 187. Variation for turbulent intensities along the centerline of each jet (V-T-A plane): (a) Case 3a, (b) Case 3.

X.4. Thermal Stratification and Flow Reversal

It was discovered during the steady state experiments for Case 2, Case 3, and Case 4 that the flow inside the upper plenum was asymmetric and its direction was from left to right. As such, it was prudent to investigate the behaviors of temperature and velocity at V-T-B plane rather than V-T-A plane. In addition, information from V-T-C plane could be utilized to have a complete picture of the flow vectors and magnitudes during the event. The normalized mean streamwise velocity and streamwise turbulence intensity, at different Z-elevations of V-T-B plane are furnished in Figure 188. The corresponding normalized mean spanwise velocity and spanwise turbulence intensity at several height of V-T-B plane are shown in Figure 188 as well. It was found that the magnitudes of mean streamwise and spanwise velocities were approximately comparable with each other at 0.0127 m. At 0.1524 m and 0.3048 m, there was a substantial reduction of the magnitudes of mean streamwise and spanwise velocities due to the presence of the incoming cold air from the right chimney. The values of the mean streamwise velocity were very much less in V-T-B plane in comparison with their counterparts in V-T-A plane.

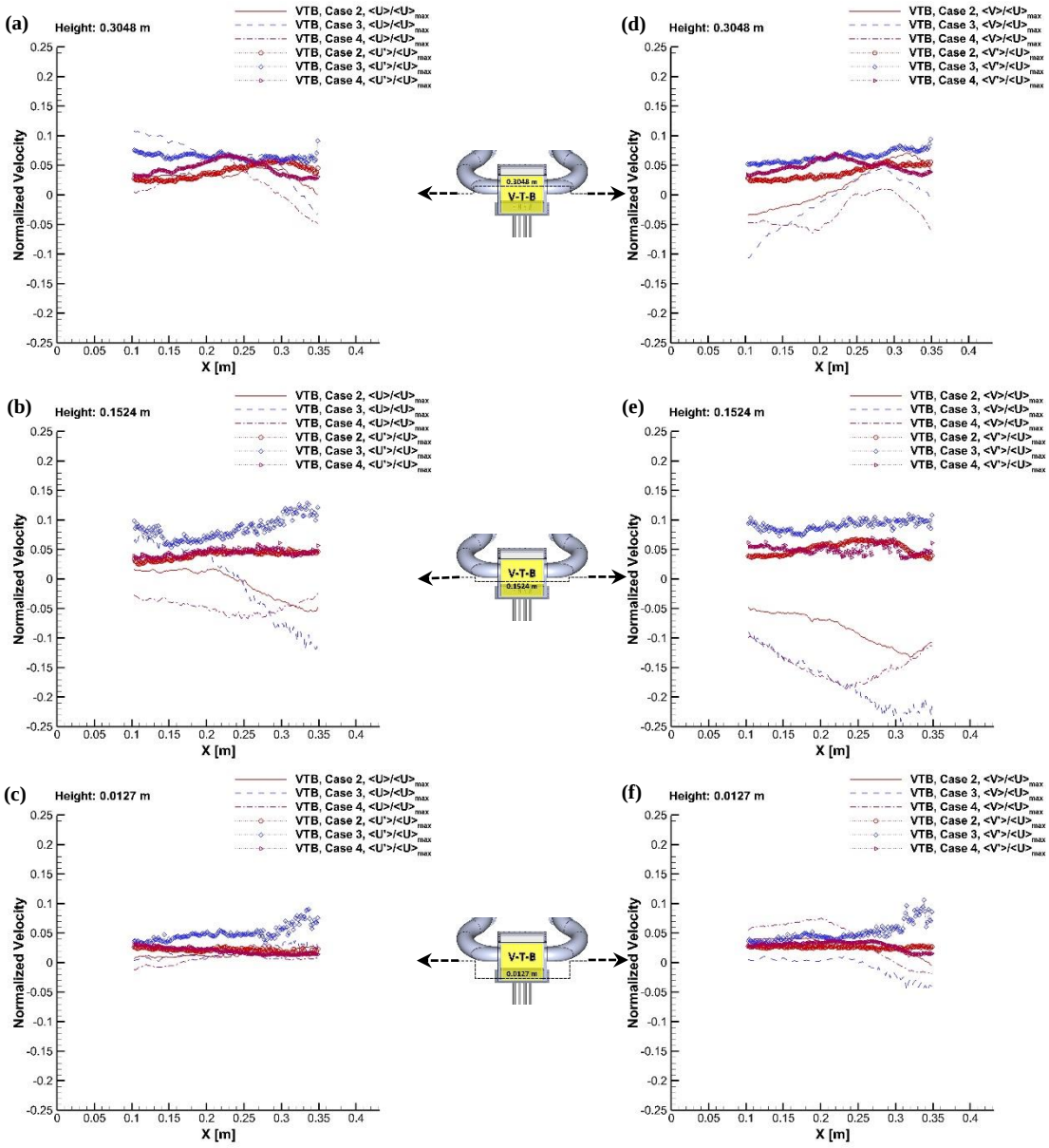

Figure 188. (a)-(c) Normalized mean streamwise velocity and turbulence intensity at different elevations (V-T-B plane); (d)-(f) Normalized mean spanwise velocity turbulence intensity at different elevations (V-T-B Plane).

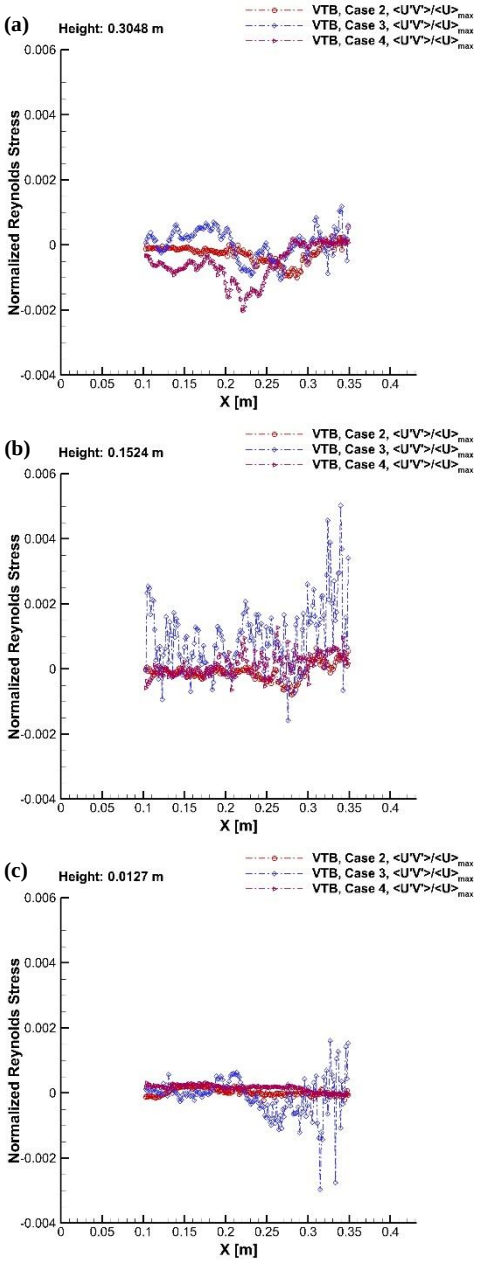

Figure 189. Cross-sectional of normalized Reynolds stress distribution (V-T-B plane).

It was witnessed that the magnitudes of streamwise and spanwise turbulence intensities for Case 3 were more significant than Case 2 and Case 4 at the elevations under study. This was envisaged since Case 3 involved a total of four active risers whereas only a single riser (i.e. Riser ④) was in operation for Case 2 and Case 4. The range of streamwise and spanwise rms intensities were 3.2-12.8% and 3.2-11.0% for Case 3 and less than 7% for Case 2 and Case 4 at all elevations. Case 3 demonstrated more chaotic and highly scattered Reynolds stress distribution at all elevations since more exchange of fluid momentum occurred at interface boundaries for the four jets (Figure 189). For all the cases, the rms intensities recorded high values at 0.1524 m. It was noted that high Reynolds stress fluctuations were recorded at 0.1524 m as well. Fluctuations near the right side of the plenum were noticeable at 0.0127 m and 0.1524 m and more even Reynolds stress distribution at 0.3048 m.

The normalized mean and fluctuating temperature contours with streamtraces and with streamtraces for V-T-B plane of Case 2, Case 3, and Case 4 are shown in Figure 190. The black lines represented the streamtraces computed by Tecplot 360 which assisted to identify the primary flow structure within each velocity field. It was obvious that for all the cases, the flow direction was from right to left across the upper plenum. A sizeable clockwise vortex was formed at the location right above the inlet of right exhaust pipe. Another counterclockwise vortex was established at the lower left hand corner of the upper plenum below the inlet of left exhaust pipe for Case 4. For Case 3, a few small counterclockwise vortices existed near the bottom wall of the upper plenum.

The mean temperature contour signified the presence of incoming cold air gushed into the upper plenum, which originated from the right exhaust pipe. The incoming cold air played a vital role in establishing high temperature gradient across the volume of the upper plenum which finally led to the formation of a stably thermal stratification layer. High temperature fluctuations existed near the inlet of the right exhaust pipe and along the direction of the incoming cold air flow (Figure 190). The incoming cold air has resulted in relatively low value regions for the mean streamwise and spanwise velocity. The incoming cold air swept away all the oil particle droplets which made velocity measurement using PIV impractical (Figure 191).

High turbulence intensities were documented near the inlet of the right chimney for Case 2 (higher jet velocity, 5 m/s) whereas Case 4 (lower jet velocity, 2.25 m/s) has high turbulence intensities on the opposite side, i.e. the inlet of left chimney (Figure 192). Case 3 has high turbulence intensities on the both inlets of the chimneys due to the presence of four jets. Figure 190 and Figure 192 reveal a close agreement in high fluctuation regions for the temperature and velocity.

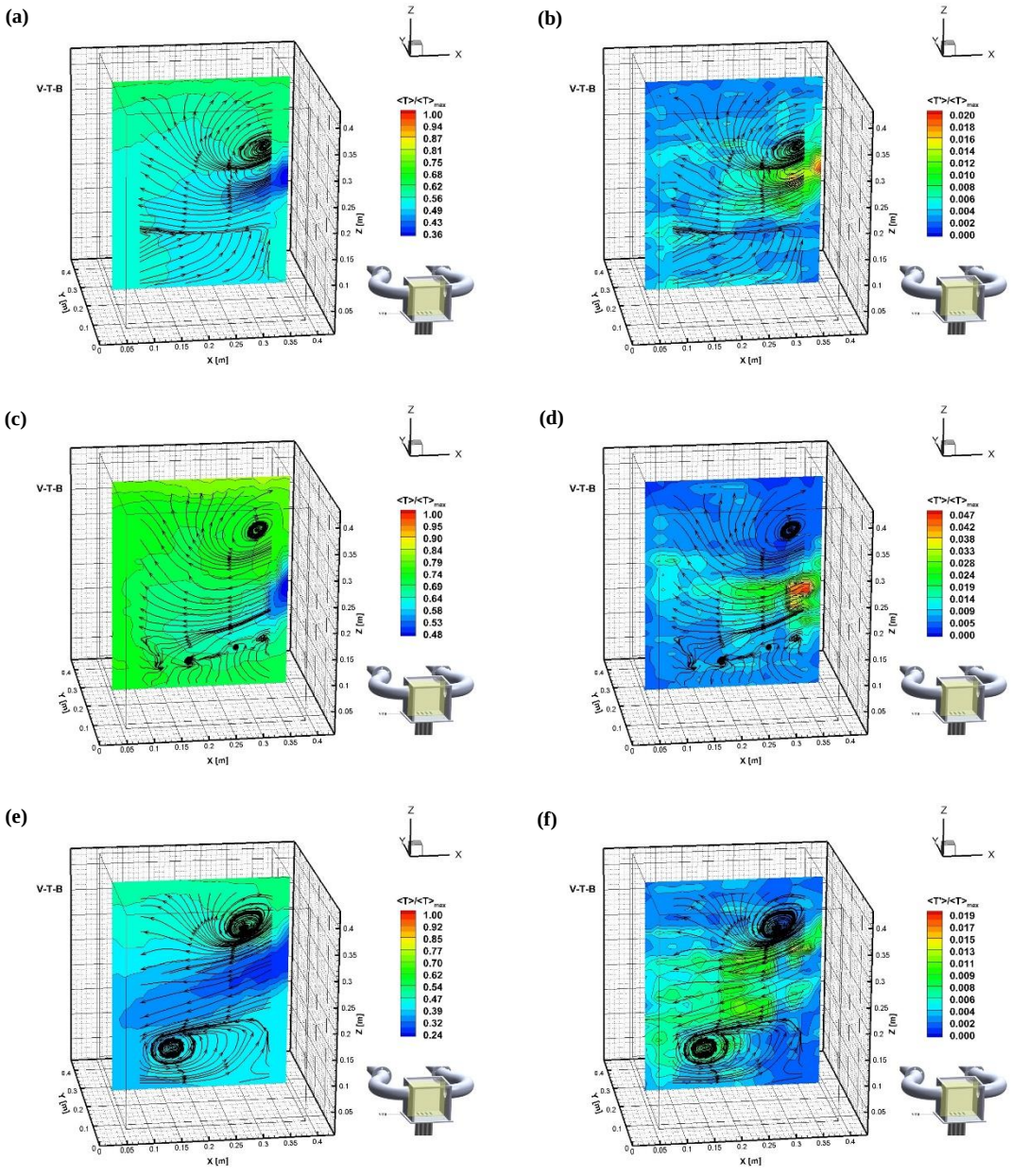

Figure 190. (Left) Normalized mean temperature contour with streamtraces (V-T-B plane); (Right) Normalized fluctuating temperature contour with streamtraces (V-T-B plane): (a) & (b) Case 2, (c) & (d) Case 3, (e) & (f) Case 4.

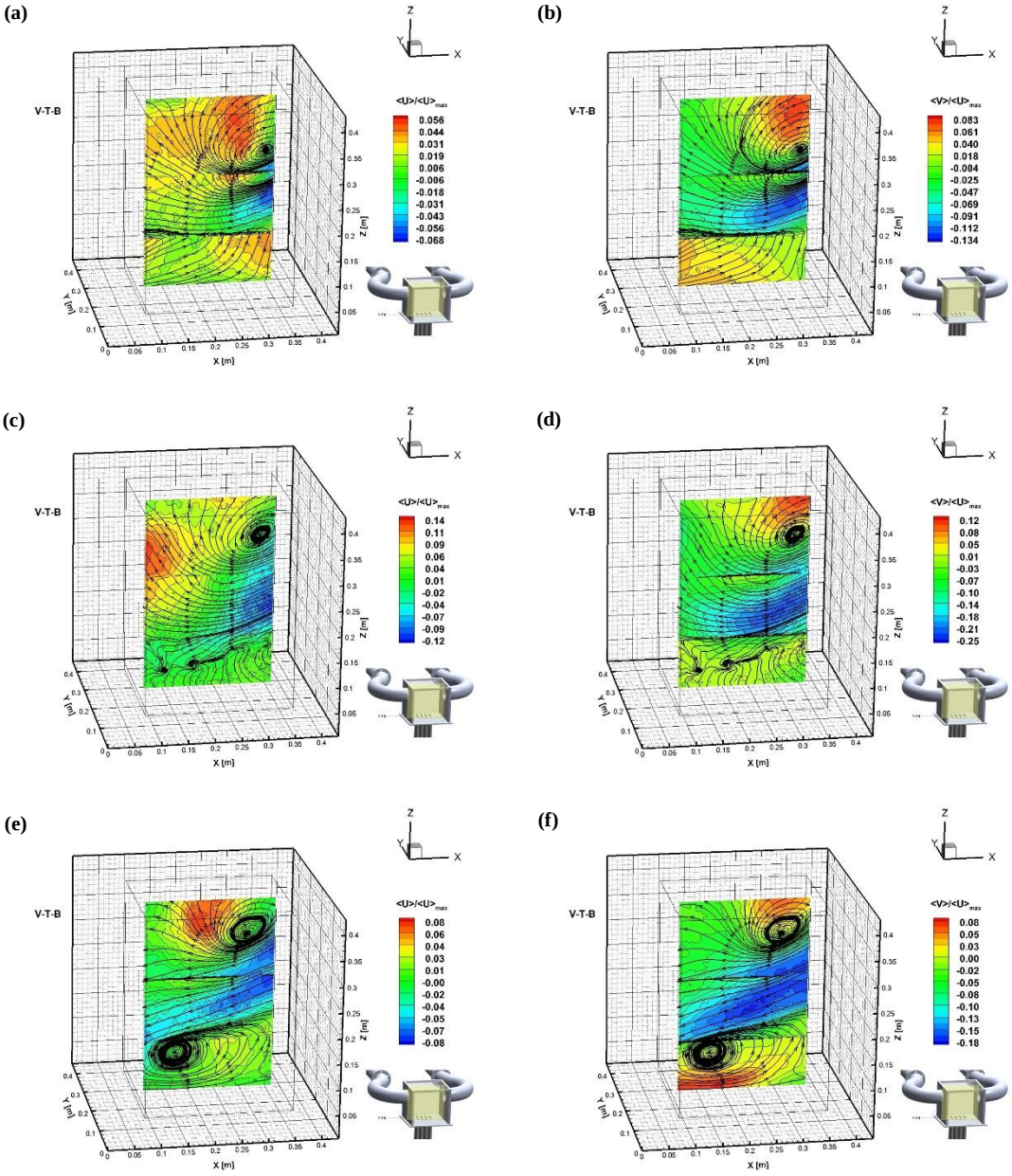

Figure 191. (Left) Normalized mean streamwise velocity contour with streamtraces (V-T-B plane); (Right) Normalized mean spanwise velocity contour with streamtraces (V-T-B plane): (a) & (b) Case 2, (c) & (d) Case 3, (e) & (f) Case 4.

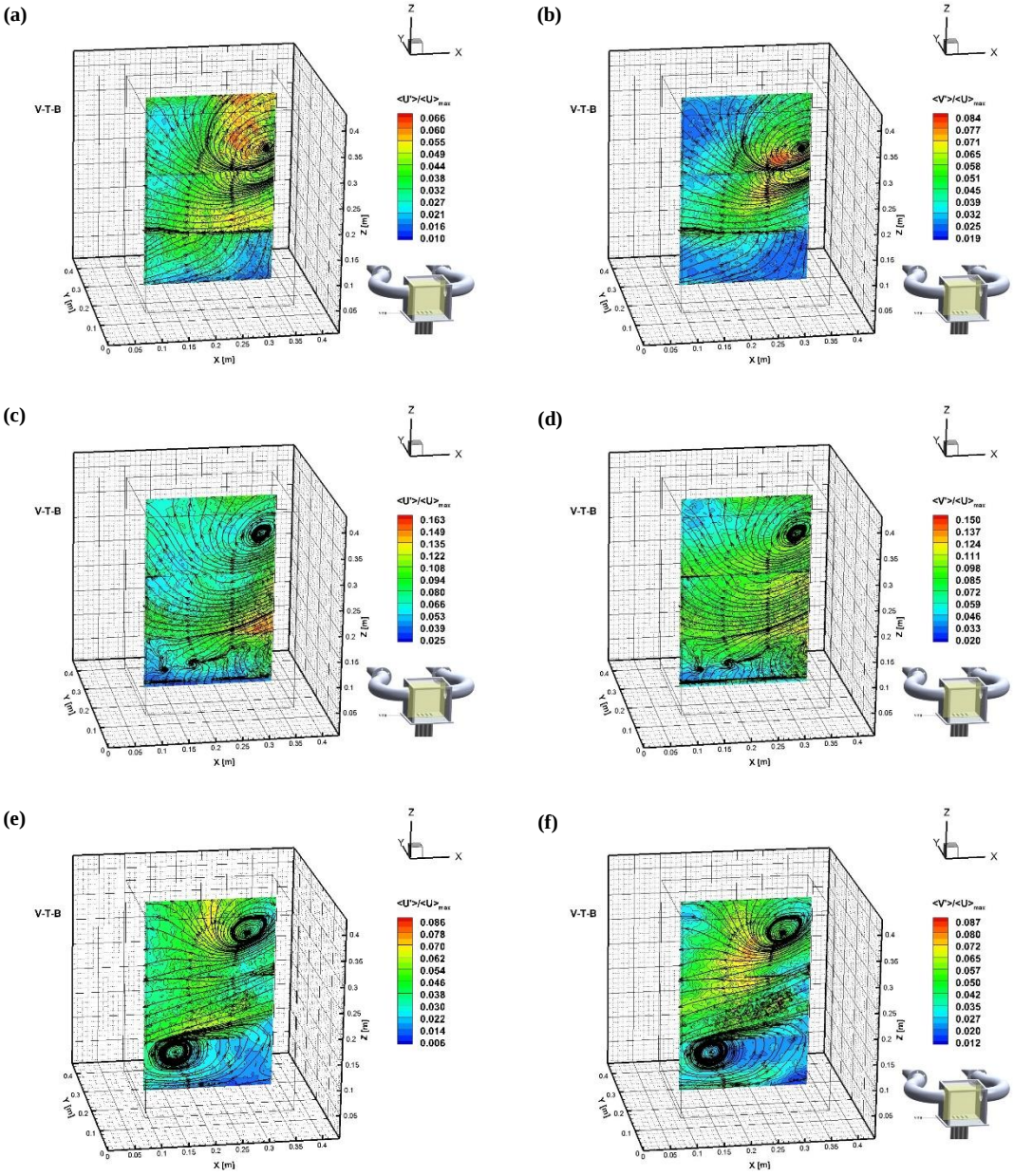

Figure 192. (Left) Streamwise turbulence intensity contour with streamtraces (V-T-B plane); (Right) Spanwise turbulence intensity contour with streamtraces (V-T-B plane): (a) & (b) Case 2, (c) & (d) Case 3, (e) & (f) Case 4.

The normalized mean streamwise velocity and streamwise turbulence intensity at different Z-elevations of V-T-C plane are illustrated in Figure 193. The corresponding normalized mean spanwise velocity and spanwise turbulence intensity at several heights of V-T-C plane are shown in Figure 193 as well. At 0.3048 m, the magnitudes of mean streamwise and spanwise velocities were low on the right side of the upper plenum compared with the left side. In general, the velocity gradients for the mean streamwise and spanwise velocities at 0.0127 m were less than the ones at the higher elevations. As demonstrated by V-T-B plane, the values of the mean streamwise velocity were very much less in V-T-C plane in comparison with their counterparts in V-T-A plane.

From Figure 193, it was substantiated that the magnitudes of streamwise and spanwise turbulence intensities for Case 3 were greater than Case 2 and Case 4 at the elevations under study. Similar reasoning given for V-T-B was applicable for V-T-C (four active risers vs one active riser). High turbulence intensities values recorded at 0.1524 m for all cases. Case 3 had higher turbulence intensity values compared with the other cases at all elevations. On one hand, the range of streamwise turbulence intensity for Case 3 was 5.1-9.8% whereas 1.9-2.6% and 1.6-3.9% for Case 2 and Case 4 at all elevations. On the other hand, Case 3 documented 3.7-9.9% for the range of spanwise turbulence intensity at all elevations while Case 2 and Case 4 recorded 2.0-4.6% and 1.8-4.3%, respectively. As observed in V-T-B plane, Case 3 exhibited more hectic and highly scattered Reynolds stress distributions at all elevations (Figure 194). More orderly distributions of the Reynolds stress were sighted at 0.0127 m.

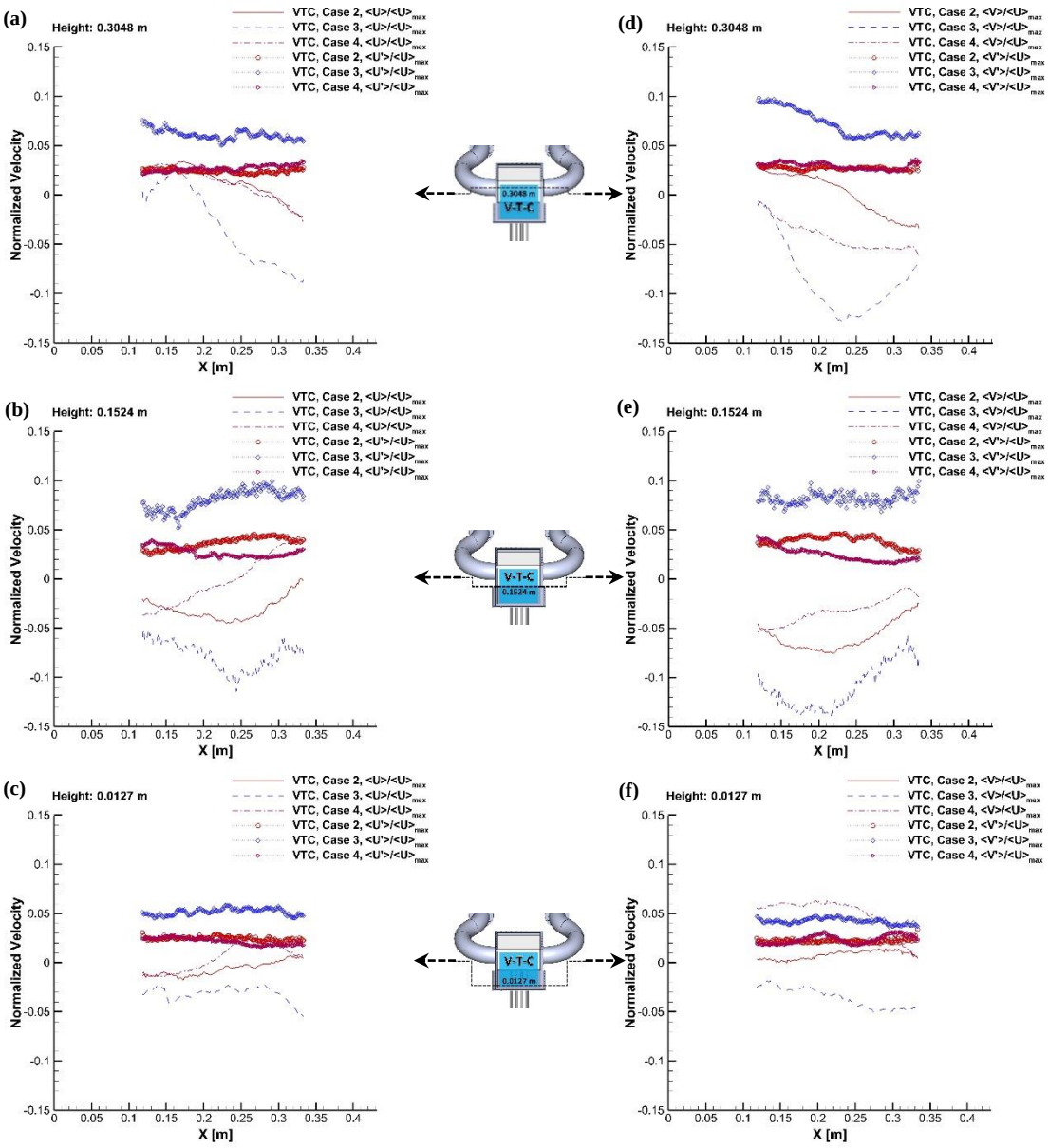

Figure 193. (a)-(c) Normalized mean streamwise velocity and streamwise turbulence intensity at different elevations (V-T-C plane); (d) to (f) Normalized mean spanwise velocity and spanwise turbulence intensity at different elevations (V-T-C Plane).

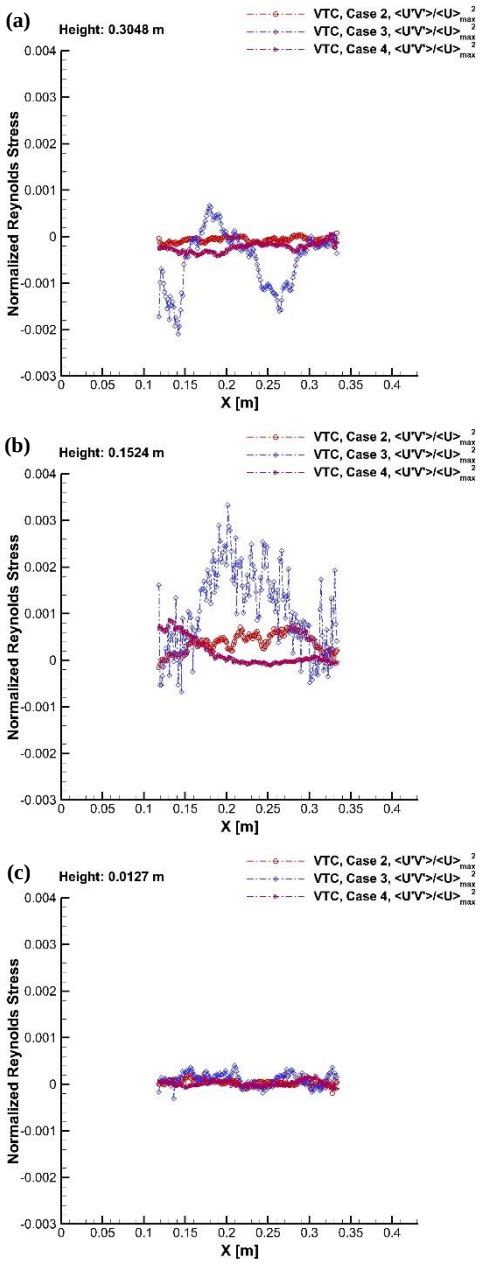

Figure 194. Cross-sectional of normalized Reynolds stress distribution (V-T-C plane).

The normalized mean and fluctuating temperature contours with streamtraces for V-T-C plane of Case 2, Case 3, and Case 4 are portrayed in Figure 195. The black lines represented the streamtraces calculated by Tecplot 360 which assisted in exhibiting the essential features of the flow. It was apparent from the plots that the direction of the flow direction in the upper plenum was from right to left for all cases. Clockwise and counterclockwise vortices were formed near the top and bottom wall of the upper plenum for Case 2 and Case 4. No vortical structure was present for Case 3. Vortical structures at 2.25 m/s (Case 4) were more pronounced than at 5 m/s (Case 2).

The presence of incoming cold air which gushed into the upper plenum was still noticeable in V-T-C plane based on the pattern of the mean temperature contour for all cases. A stably thermal stratification layer were also existed in V-T-C plane. Case 2, Case 3, and Case 4 have 9%, 6% and 10% temperature gradient between near the top and bottom walls of the upper plenum. There existed 10% and 17% temperature gradient between near the left and right walls for the upper plenum for Case 2 and Case 3. High temperature fluctuations along the incoming cold air direction, i.e. from the inlet of the right chimney to the bottom of the left chimney inlet, were observed for Case 2 and Case 3. For Case 3, high temperature fluctuations detected in between the two vortices and near the vicinity of the counterclockwise vortex located right in the middle of the lower half of the upper plenum. High turbulence intensities were documented near the inlet of the left and right chimney inlets (Figure 197). A firm agreement existed between the temperature and velocity contours on the regions of low velocities (Figure 195 and Figure 196) as well as on the regions of high fluctuations (Figure 195 and Figure 197).

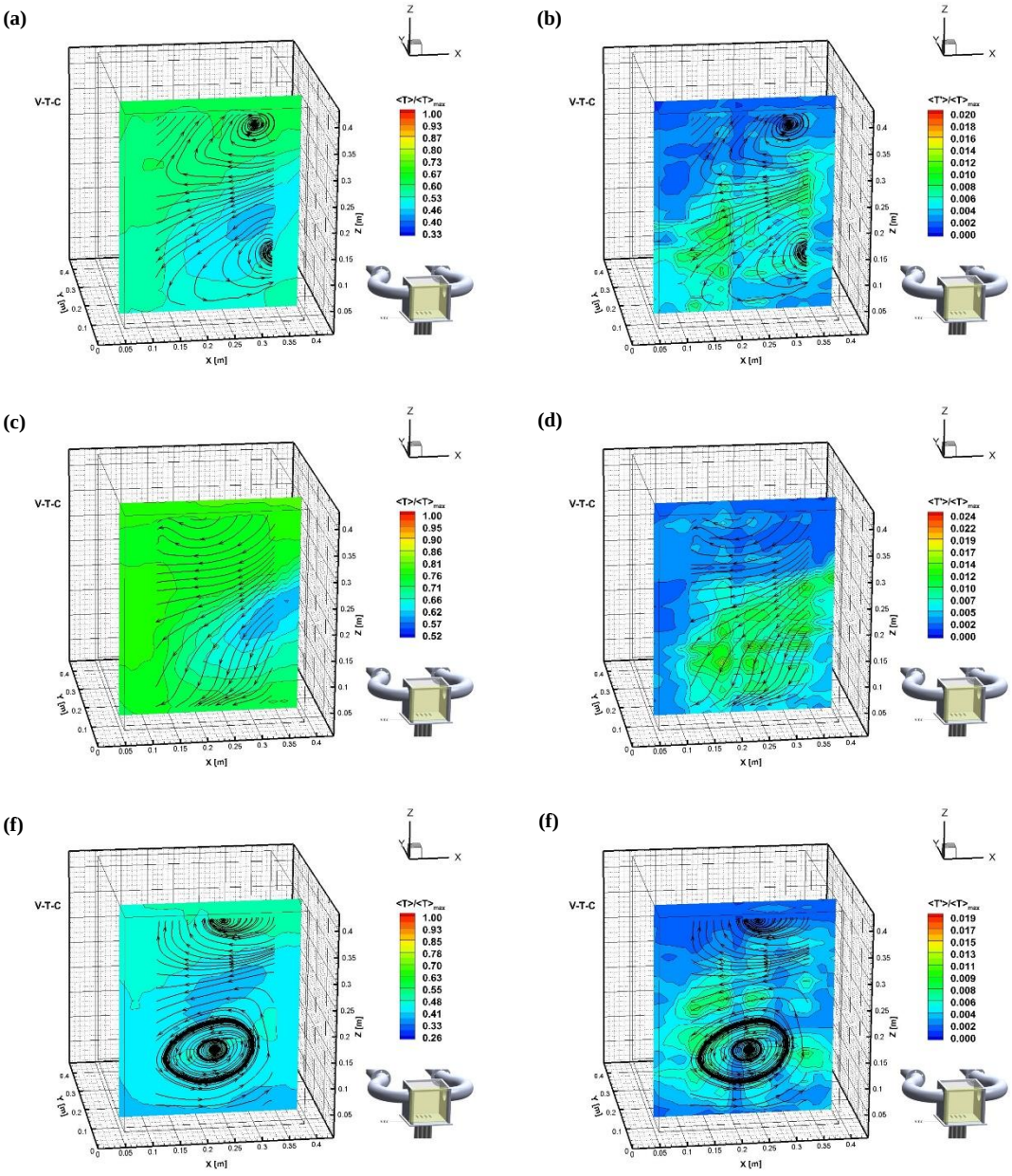

Figure 195. (Left) Normalized mean temperature contour with streamtraces (V-T-C plane); (Right) Normalized fluctuating temperature contour with streamtraces (V-T-C plane); (a) & (b) Case 2, (c) & (d) Case 3, (e) & (f) Case 4.

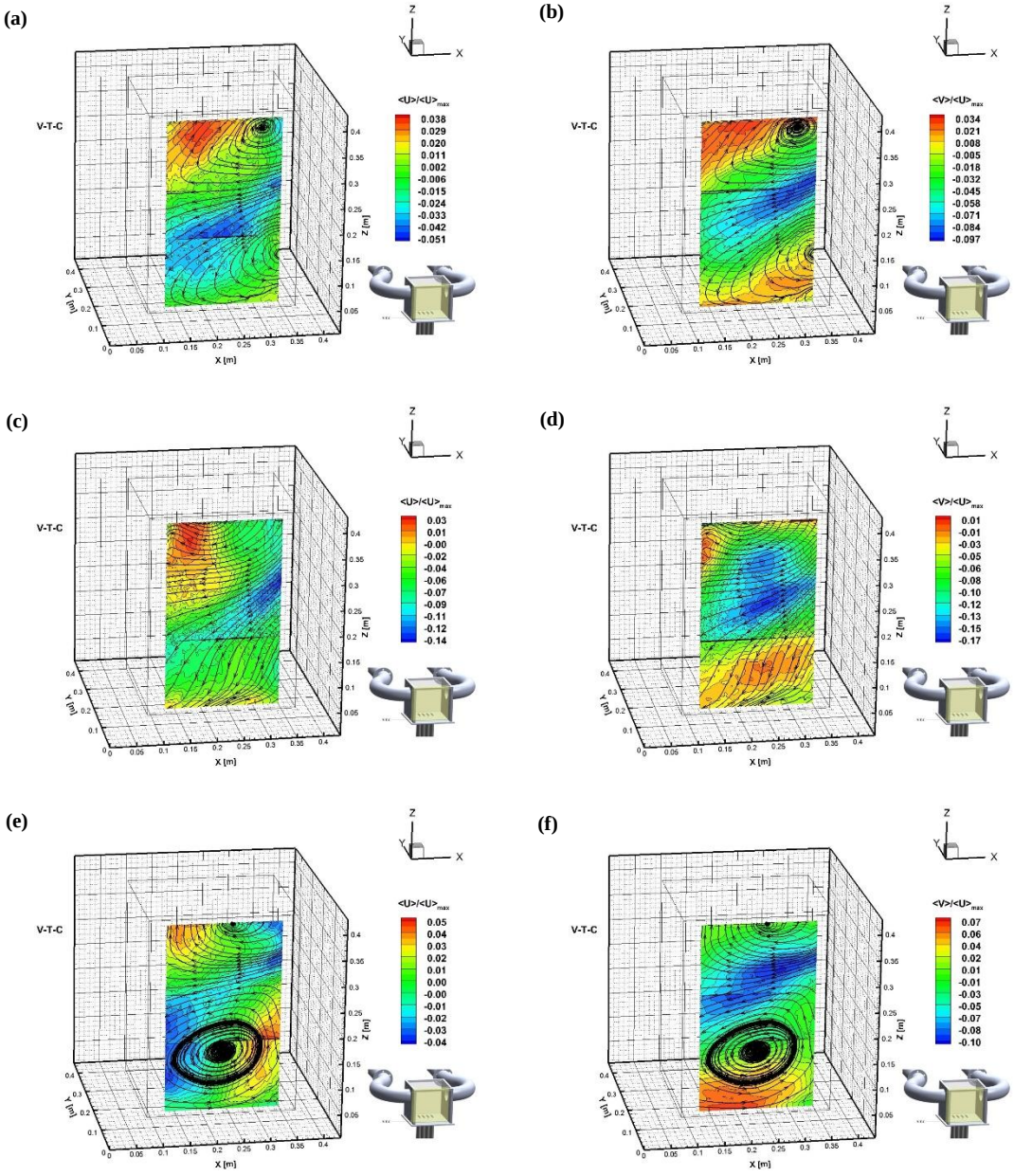

Figure 196. (Left) Normalized mean streamwise velocity contour with streamtraces (V-T-C plane); (Right) Normalized mean spanwise velocity contour with streamtraces (V-T-C plane): (a) & (b): Case 2, (c) & (d) Case 3, (e) & (f) Case 4.

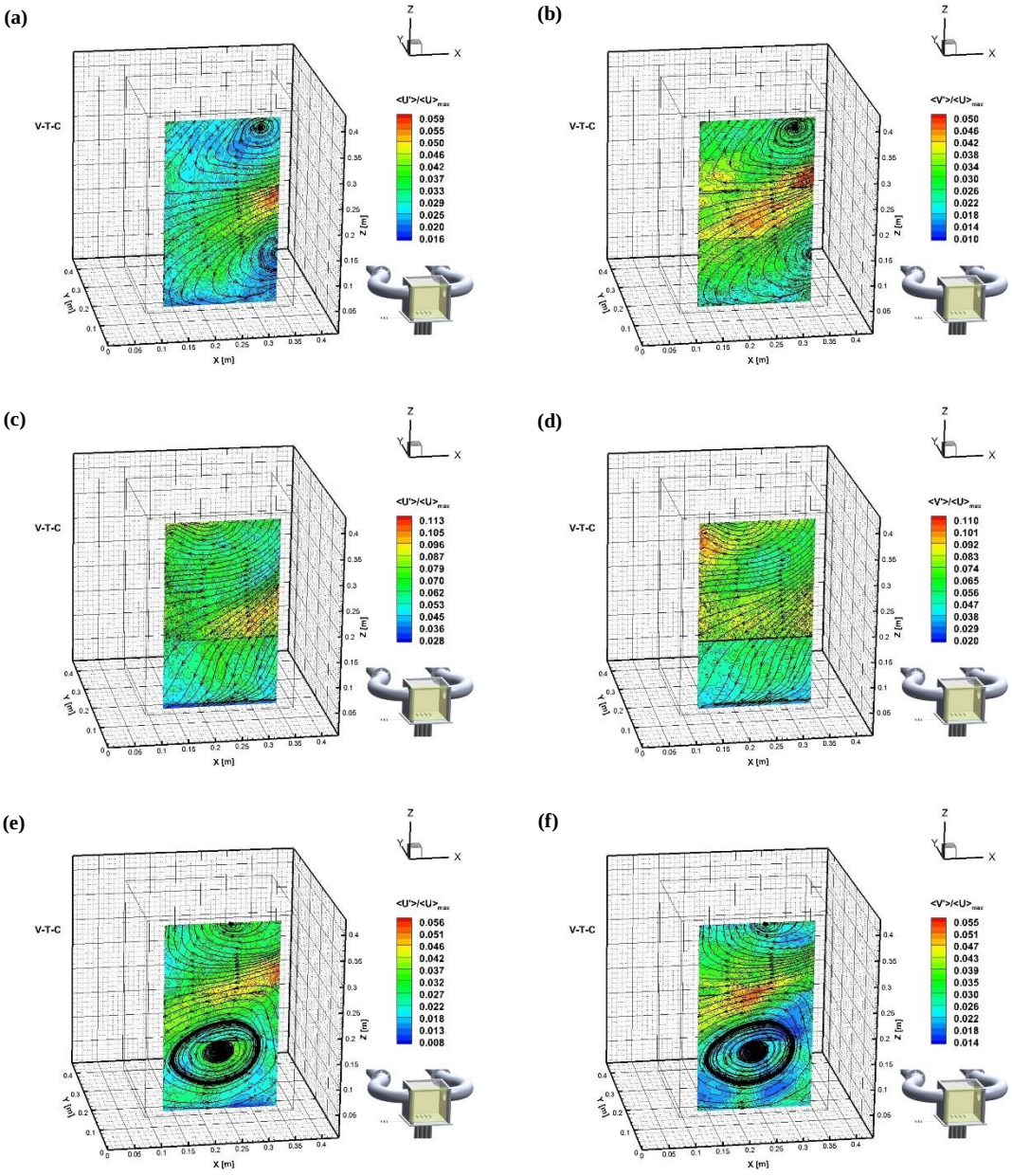

Figure 197. (Left) Streamwise turbulence intensity contour with streamtraces (V-T-C plane); (Right) Spanwise turbulence intensity contour with streamtraces (V-T-C plane): (a) & (b) Case 2, (c) & (d) Case 3, (e) & (f) Case 4.

X.5. Conceptual Flow Reversal Progression

A very small flow perturbation, i.e. triggered by the pressure difference between the inlet and outlet of the chimneys, or by change in any boundary conditions (velocity, temperature, pressure), can result in a flow reversal due to flow instabilities generated by relatively weak driving force of the buoyancy effects. On one hand, the heated air inside the upper plenum will have a significant portion of it exiting towards the chimney which has lower pressure, i.e. preferential flow. On the other hand, the higher pressure chimney will thus experience flow stagnation inside the chimney due to cross flow between cold air from outside of the chimney and a little portion of the heated air from the inside of the upper plenum. As time passes by, the cold air from outside of the higher pressure chimney will accumulate and start to overcome the resistance from the hot air from the inside of the upper plenum. As such, the flow is now in "negative" direction or flow reversal.

By nature, the difference in density will maintain the flow in negative or reverse direction. Flow reversal may lead to thermal stratification layers inside the upper plenum. Under a stably thermal stratification environment, buoyancy forces are diminished by the rise of the potential energy of the system which damping the turbulence. The dampening of turbulence implies reduction in turbulence kinetic energy and consequently less turbulence mixing is anticipated to occur inside the upper plenum. More importantly, natural circulation driven flow may be inhibited by the establishment of stratified layers inside the upper plenum, which in turn reduces the overall effectiveness of decay and residual heat removal, both at steady state and transient conditions, respectively.

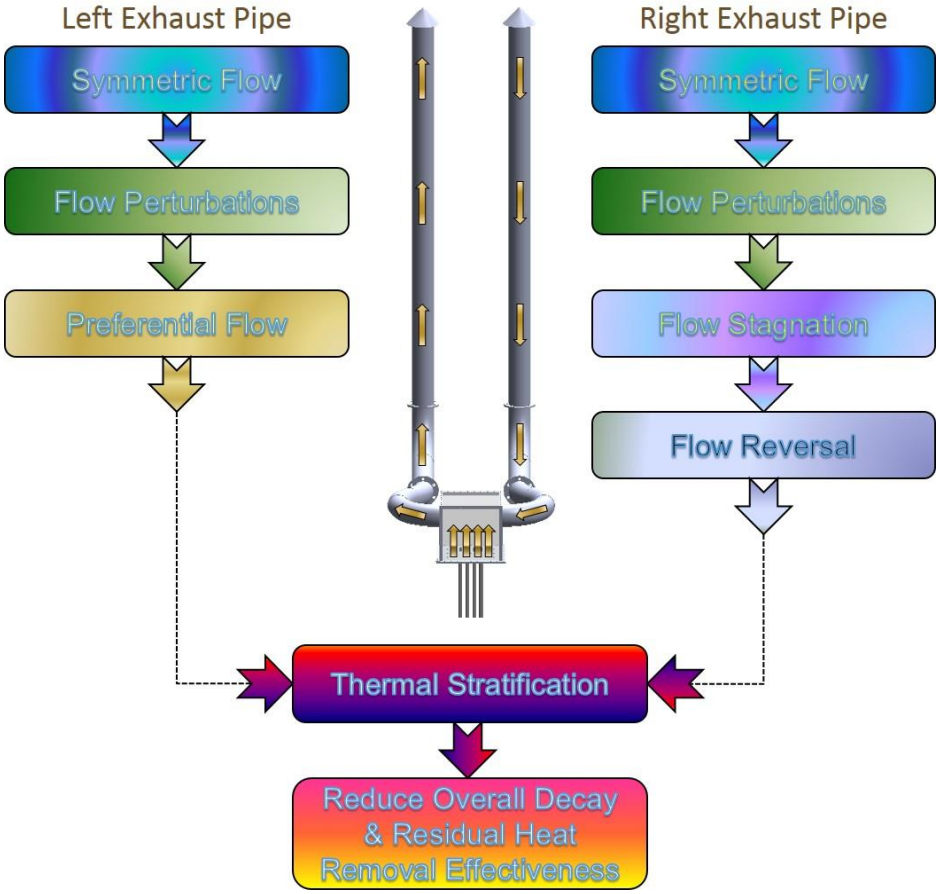

Figure 198. Conceptual flow reversal progression.

From the preliminary CFD simulations, it was observed that the flow of the heated air from the inside of the upper plenum followed the 45º, 90º, 45º curvature of the two exhaust pipes. Flow separation of the heated air was observed near the first 45º curvature. This flow separation has resulted a localized low velocity region with recirculation flows. This phenomenon was compounded with the presence of buoyancy effects due to the heating. As such, geometry and shape of the chimneys are envisaged to contribute to the

flow instability to some degrees that ultimately leads to the flow reversal. A summary of a conceptual flow reversal progression is presented in Figure 198.

X.6. POD Analysis

Since the reverse flow cases have a very significant impact to the air-cooled RCCS cooling performance, it is prudent to investigate the evolution of turbulent coherent structures within the flow fields at the adiabatic and heated conditions using the Snapshots POD method. In this dissertation, only two positions in V-T-A and V-T-B planes; namely V-T-A P1 and V-T-B P1 were chosen to illustrate the application of the mentioned POD method. Rough approximation of the turbulent length scales were obtained for a random instantaneous snapshot reconstructed using the optimal POD modes.

As mentioned in the mathematical background of the POD, the number of ensemble members deemed adequate for a description of the process, N_t must be sufficiently high in order to obtain accurate computation of the eigenfunctions and validity of the POD statistical data. The number of snapshots selected to reconstruct the vorticity or the velocity fields will determine the temporal resolution of the POD analysis. The velocity data obtained in all experiments were acquired at 30 fps for 10 seconds, i.e. 300 images or 150 pair of images using the laser as illumination source (repetition rate: 15 Hz maximum). Therefore, the maximum number of snapshots corresponding to the full POD eignenmodes was 150 modes. Ideally, a high repetition laser and a high frame rate of digital camera (in the order of kilohertz, kHz) should be adopted for better temporal

resolution of the POD applications. Nevertheless, the POD analyses obtained in the current investigations would provide some insights on the low-dimensional model of the actual velocity or vorticity fields which represent most of the characteristics of the coherent structures.

X.6.1. Energies of the POD Modes

The energy content of different POD eigenmodes was obtained for the V-T-A P1, V-T-B P1, and V-T-C P1 of Case 3a and Case 3, respectively (Figure 199). This energy content of each eigenmode was depicted by its corresponding eigenvalue, using the fluctuating part of the velocity as an input for the POD modes computation.

The energy distributions of all eigenmodes (150 modes) and the cumulative sum of the energy with respect to the mode number of the dataset for Case 3a and Case 3 at the respective positions were illustrated in Figure 199. The first POD mode value for the adiabatic case was bigger than the heated case at V-T-A P1 and V-T-C P1 (6.84% > 2.84% and 16.90% > 13.00%) (Table 34). However, at V-T-B P1, the trend was reversed, of which the first POD mode value for the adiabatic case was lower than the heated case (13.27% < 15.42%). This higher value of the first POD mode suggested that the large-scale structures of the flow could be better represented for V-T-A P1 and V-T-C P1 at the adiabatic condition whereas for V-T-B P1, the heated condition was more appealing.

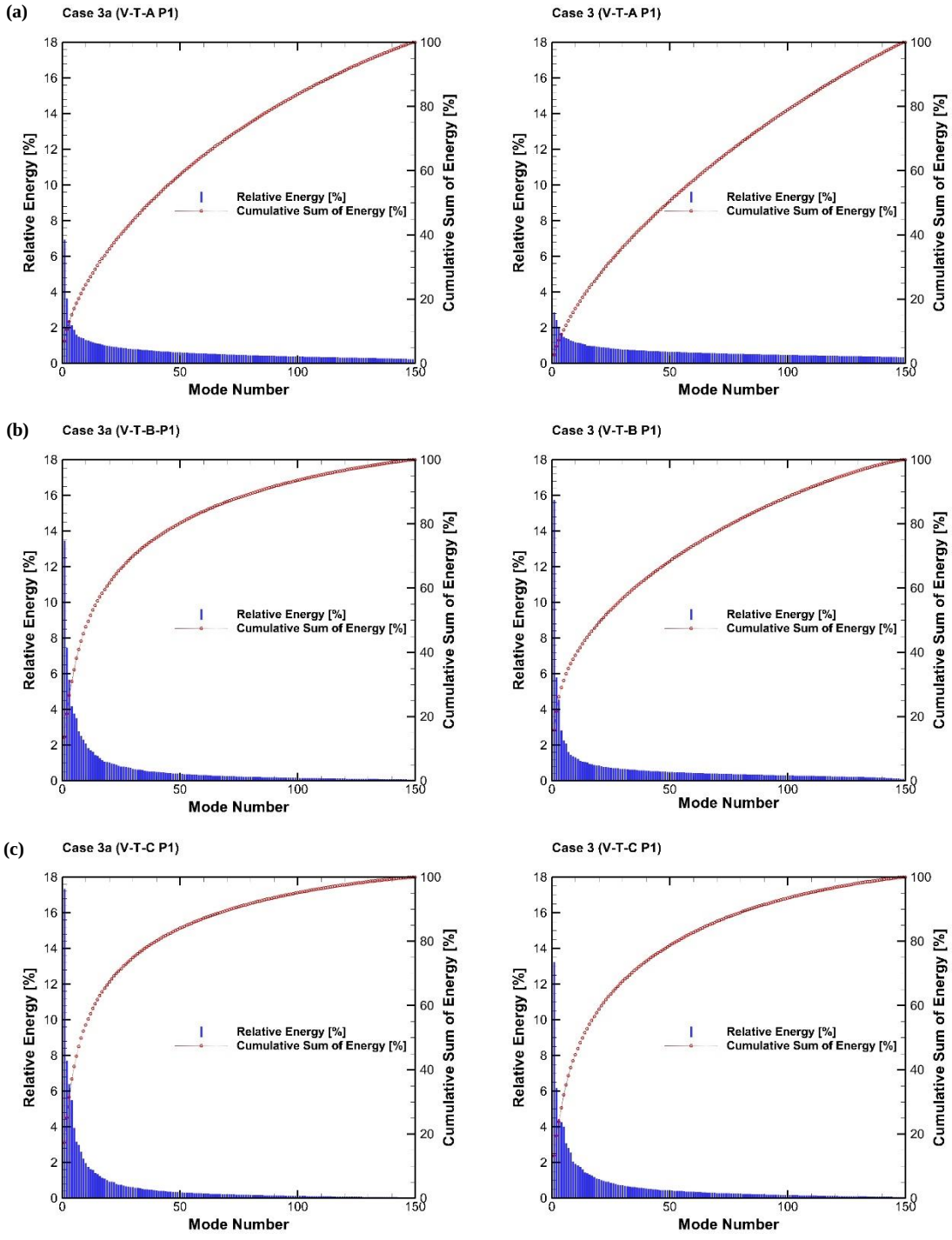

Figure 199. The energies of POD modes for Case 3a (left) and Case 3a (right) at: (a) V-T-A P1, (b) V-T-B P1, and (c) V-T-C P1.

Table 34. The cumulative sum of energy content for the first and seventy-fifth POD modes for Case 3a and Case 3 at the respective positions.

Case	Position	Cumulative Sum of Energy Content (%)	
		First POD mode	First 75 POD modes
Case 3a	V-T-A P1	6.84	72.67
	V-T-B P1	13.27	88.25
	V-T-C P1	16.90	90.76
Case 3	V-T-A P1	2.84	65.83
	V-T-B P1	15.42	79.59
	V-T-C P1	13.00	87.63

From the results of Case 3a and Case 3, it was evident that most of the flow energy was stored in the first few POD eigenmodes. It was noted that less kinetic energy was stored in the same number of eigenmodes as the jet inlet temperature was increased (Table 34). For instance, the first seventy five modes of the adiabatic case at V-T-A P1 contained 72.67% of the total kinetic energy of the field while the same number of modes only contained 65.83% of the total kinetic energy in the field for the heated case. This implied that the flow field could be better represented with a lower number of POD eigenmodes at the adiabatic or a low value of the jet inlet temperature since less intensity of turbulence mixing occurs at low temperature.

Table 35. The relative energy (R.E.) content for the 149 POD-mode for Case 3a and Case 3 at the respective positions.

Case	Position	149th POD-mode
Case 3a	V-T-A P1	0.25
	V-T-B P1	0.08
	V-T-C P1	0.06
Case 3	V-T-A P1	0.36
	V-T-B P1	0.12
	V-T-C P1	0.08

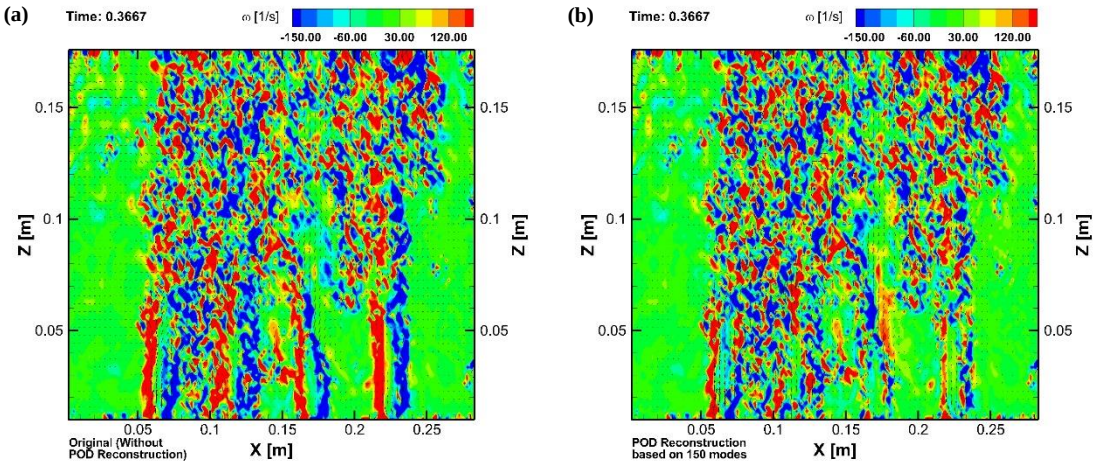

Figure 200. The velocity vector plots and contour plots of vorticity for the V-T-A P1 of Case 3 (for a random instantaneous file): (a) The actual/original plot without the POD modes reconstruction, (b) The POD modes reconstruction plot with 150 modes.

Since the experimental dataset only captured 150 modes, an investigation was carried out to determine the difference between the reconstruction of the vorticity field

using full POD modes and the actual field without any POD reconstruction. In the snapshot method, the last POD mode, e.g. 150th POD-mode in this investigation, was set to equal zero. For the 149th POD-mode, the V-T-A P1 position indicated a highest value bigger than zero as compared with the other two positions (i.e. V-T-B P1 and V-T-C P1) at both adiabatic and heated cases (Table 35). As a result, the V-T-A P1 of Case 3 was selected amongst other positions for the comparison since it recorded the highest value from zero. The corresponding velocity vector plots and contour plots of vorticity for the V-T-A P1 of Case 3 (a random instantaneous file) are illustrated in Figure 200. It was clear that most of the characteristics of the actual field was preserved in the full reconstruction of POD modes' field and only a minor difference was observed. For that reason, it is wise to deduce that the full reconstruction of the POD modes is representing the actual PIV data with acceptable difference.

X.6.2. POD Temporal Evolution, Frequency and Mode Shapes

The time histories and frequencies of the first five POD mode coefficients through the whole measurement period along with the corresponding POD mode shapes are displayed in Figure 201 and Figure 202. The time histories represent the temporal variation of the POD mode amplitudes. For Case 3a V-T-A P1, the maximum amplitude throughout the measurement period for each of the first five POD mode coefficients was in descending order (from the largest POD mode coefficient, Coeff. 1 to the lowest POD coefficient Coeff. 5) (Table 36). The range of each POD mode coefficient throughout the

measurement period demonstrated the same trend. However, the trend exhibited at the adiabatic condition was not repeated in the heated condition, i.e. Case 3 V-T-A P1 (Figure 202). The extraction of the large-scale coherent structures from the complex flow fields was signified by the peak value of power spectrum at low frequencies for each POD mode coefficient. For Case 3a and Case 3 at the V-T-A P1 position, the first two POD mode coefficients have more pronounced peaks than the other POD mode coefficients.

Table 36. The maximum, minimum, and range of the amplitudes of first five POD mode coefficients at the V-T-A P1 for Case 3a and Case 3.

Case	Parameter	Coeff. 1	Coeff. 2	Coeff. 3	Coeff. 4	Coeff. 5
Case 3a V-T-A P1	Maximum	32.61	24.22	18.24	18.44	16.64
	Minimum	-31.77	-21.83	-18.80	-16.58	-21.04
	Range	64.38	46.05	37.04	35.02	37.68
Case 3 V-T-A P1	Maximum	26.33	25.84	27.06	19.01	18.57
	Minimum	-23.98	-24.61	-23.31	-28.17	-34.58
	Range	50.31	50.46	50.37	47.18	53.15

A closer look at the plots of all five POD mode shapes indicated that the primary flow features captured by these modes were for different parts of the jets. For the adiabatic case (Figure 201), the modal shape of the first POD eigenmode captured the jet issued from Riser ① and Riser ②. The jet issued from Riser ③ was represented by the third mode shape. The fifth mode shape contribution was in illustrating the jet issued from Riser

④. For the heated case (Figure 202), the first mode illustrated the jet issued from Riser ① and Riser ③. The modal shape of mode two not only enhancing the jet flow features of Riser ① and Riser ③ but more importantly features from the jet issued from Riser ② and Riser ④ were visible. The jet issued from Riser ② was elucidated by the fourth mode shape. The seventh mode shape (not shown) exemplified the jet issued from Riser ④.

Table 37. The maximum, minimum, and range of amplitudes of the first five POD mode coefficients at the V-T-B P1 for Case 3a and Case 3.

Case	Parameter	Coeff. 1	Coeff. 2	Coeff. 3	Coeff. 4	Coeff. 5
Case 3a V-T-B P1	Maximum	17.13	17.39	15.93	10.71	11.03
	Minimum	-12.97	-12.70	-11.93	-11.79	-10.13
	Range	30.09	30.09	27.85	22.50	21.16
Case 3 V-T-B P1	Maximum	33.08	19.52	14.08	13.61	16.59
	Minimum	-23.06	-20.27	-14.24	-15.55	-15.63
	Range	56.14	39.79	28.32	29.16	32.22

Figure 203 and Figure 204 display the time histories and frequencies of the POD coefficients of the first five modes along with the mode shapes of the corresponding modes at V-T-B P1 for both Case 3 and Case 3a, respectively. The temporal progression of the POD mode coefficients denotes the changes in the amplitude of the POD mode shapes with time. Unlike the adiabatic case at V-T-A P1, only the range of each POD mode

coefficient throughout the measurement period demonstrated the descending order trend (Table 37). It was notable that the range was higher at the heated condition than the adiabatic condition for every POD mode coefficient. The trend of the peak value of power spectrum at low frequencies for each POD mode coefficient at the V-T-B P1 was similar to the V-T-A P1.

A detailed look at each individual mode shape at the V-T-B P1 for Case 3a and Case 3 revealed the contribution of each mode in different segments of the flow. The mode shapes at the V-T-B P1 demonstrated different patterns from the V-T-A P1 due to the absence of the jets. The modal shape of mode one exhibited large scale structures as compared with the other modes. As the modal characteristics progressed from the first mode to the fifth mode, the large coherent structures started to disintegrate and their sizes become smaller and smaller.

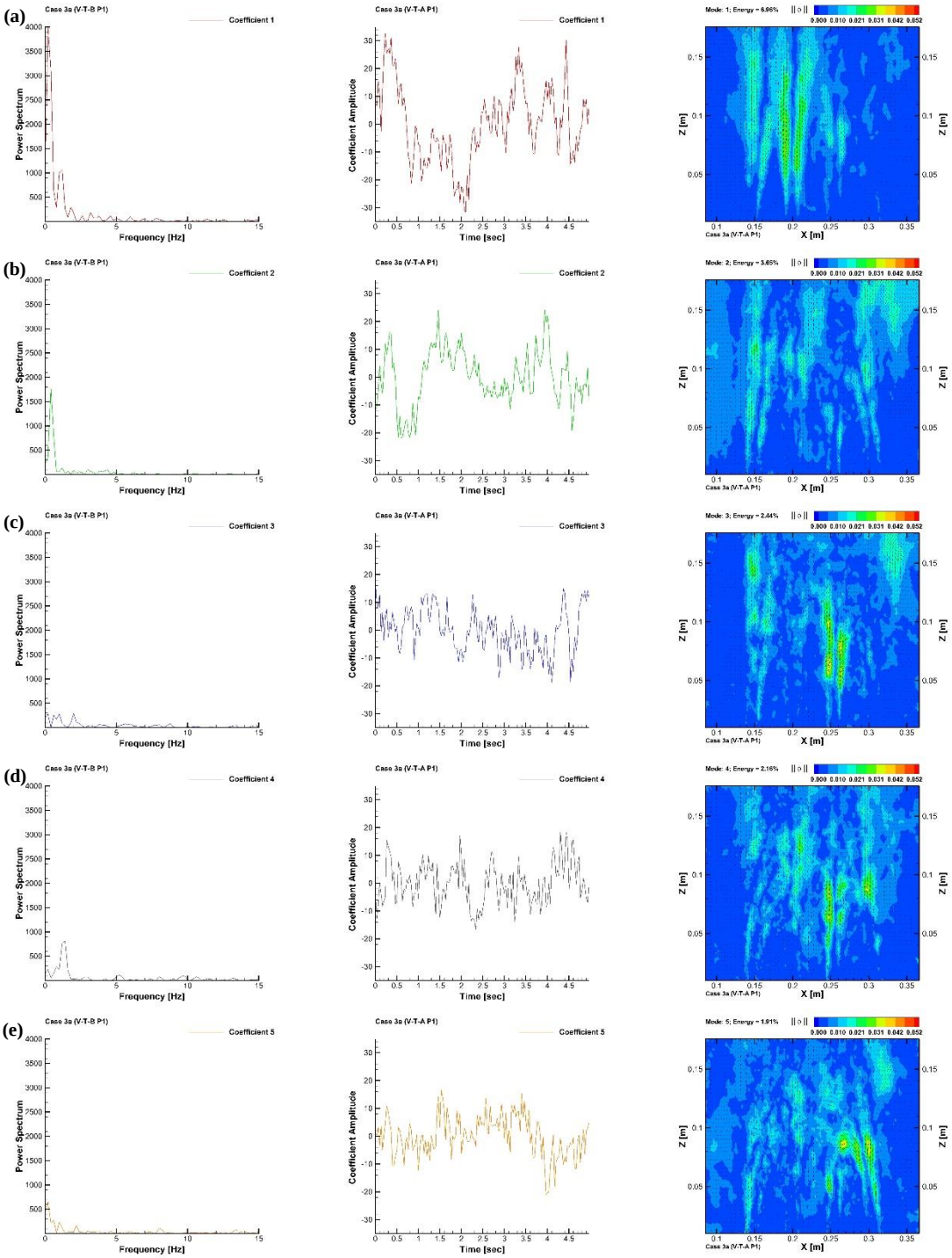

Figure 201. The time histories and frequencies of POD mode coefficients and contour plots of POD modes magnitudes for the V-T-A P1 of Case 3a: (a) 1st mode, (b) 2nd mode, (c) 3rd mode, (d) 4th mode, (e) 5th mode.

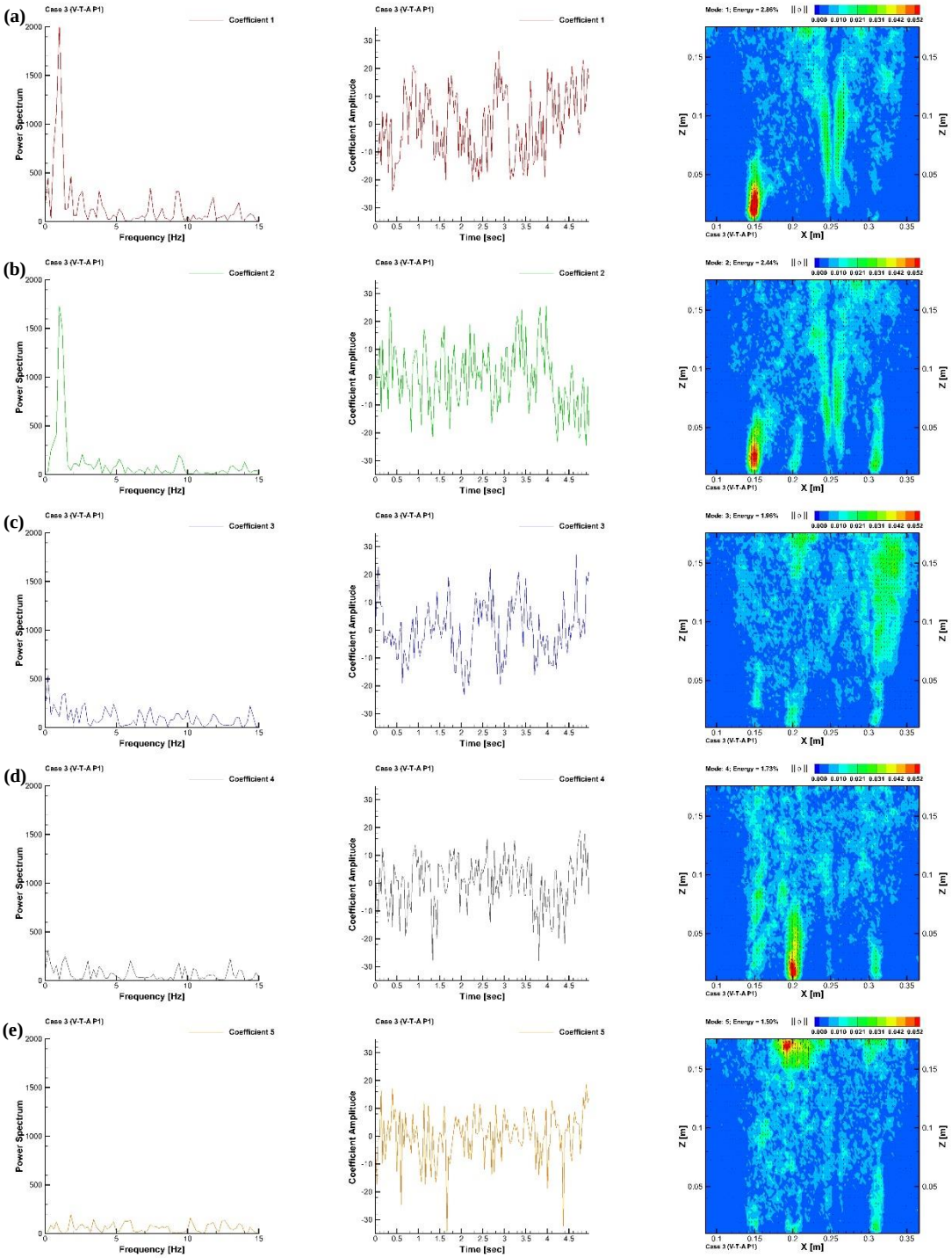

Figure 202. The time histories and frequencies of POD mode coefficients and contour plots of POD modes magnitudes for the V-T-A P1 of Case 3: (a) 1st mode, (b) 2nd mode, (c) 3rd mode, (d) 4th mode, (e) 5th mode.

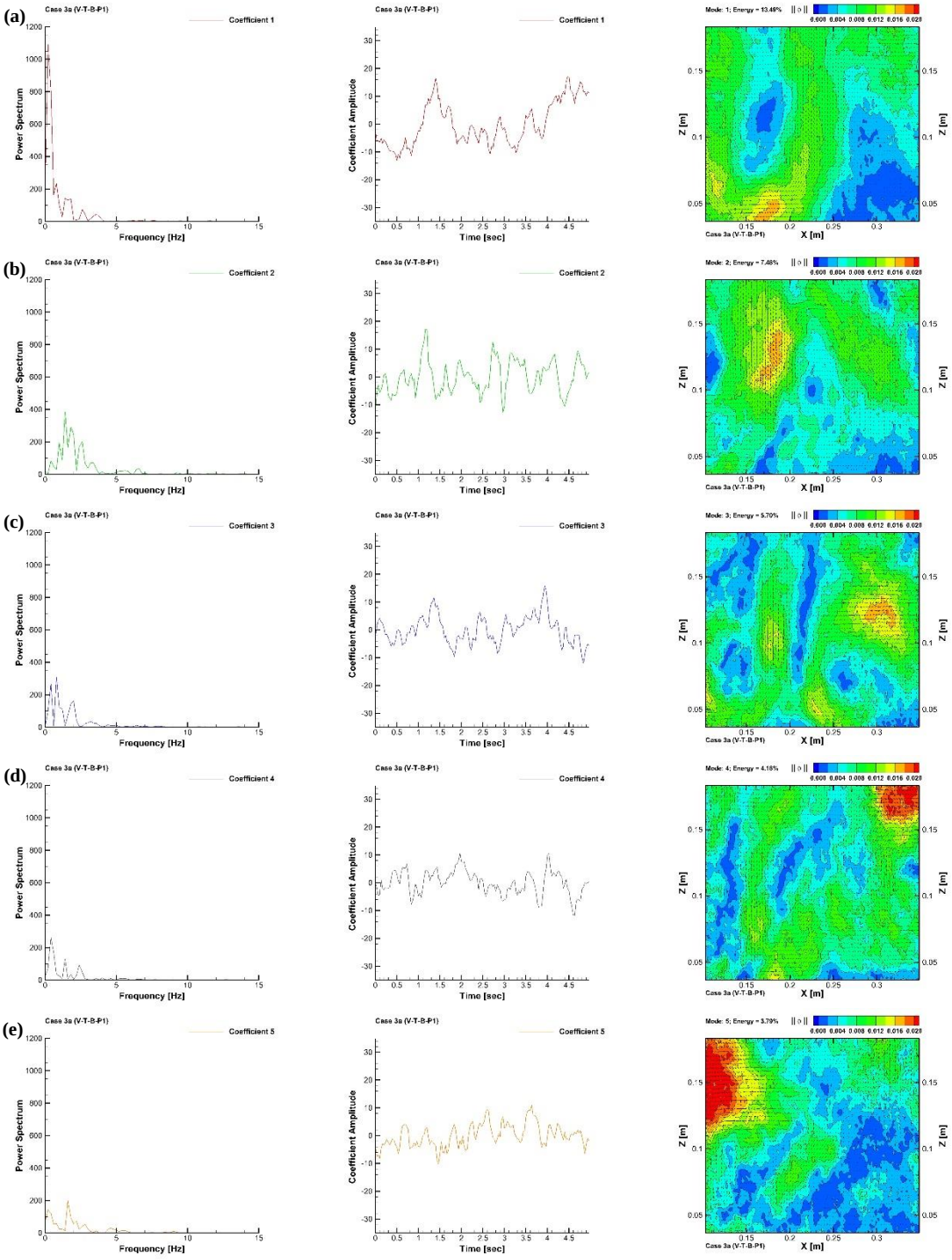

Figure 203. The time histories and frequencies of POD mode coefficients and contour plots of POD modes magnitudes for the V-T-B P1 of Case 3a: (a) 1st mode, (b) 2nd mode, (c) 3rd mode, (d) 4th mode, (e) 5th mode.

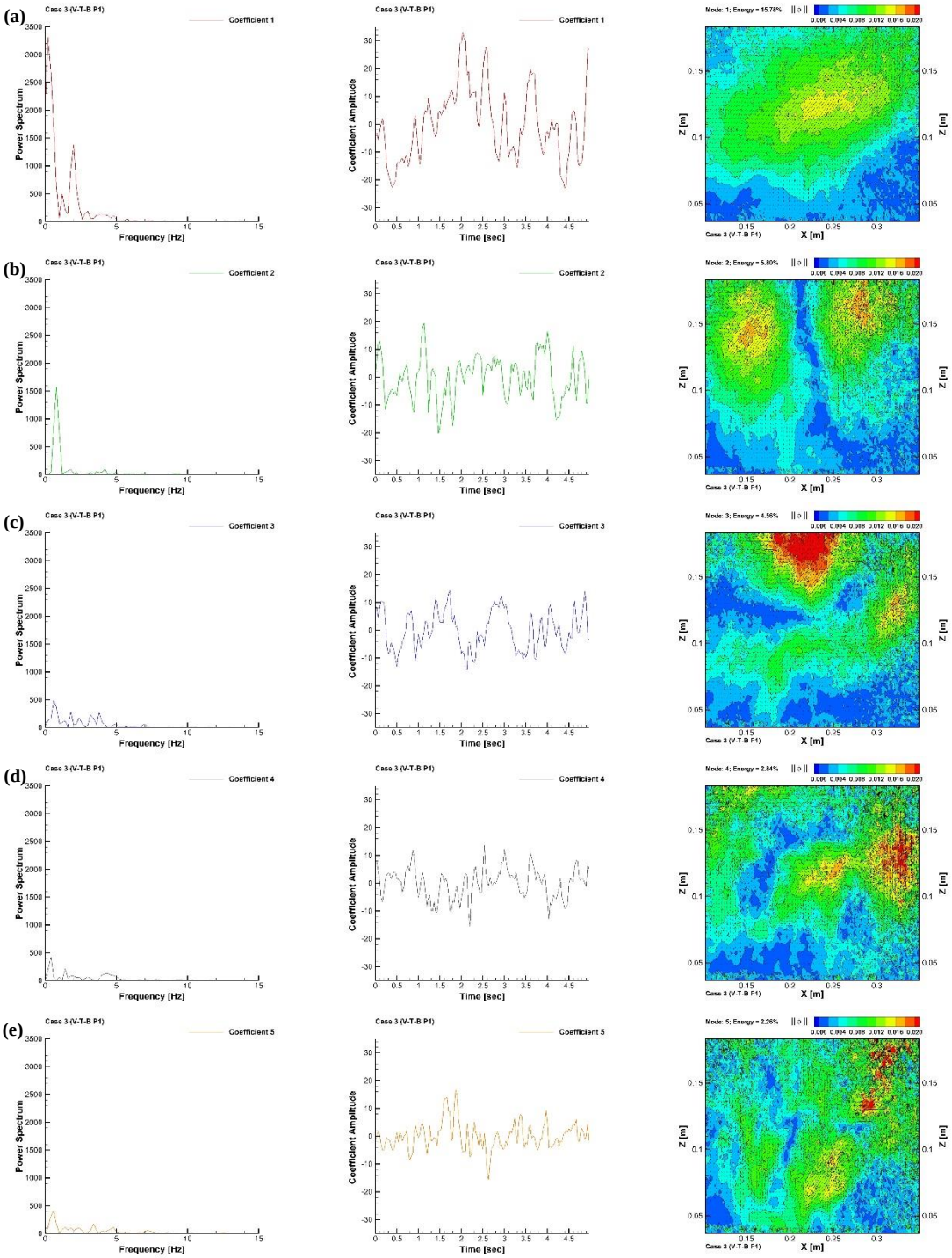

Figure 204. The time histories and frequencies of POD mode coefficients and contour plots of POD modes magnitudes for the V-T-B P1 of Case 3: (a) 1st mode, (b) 2nd mode, (c) 3rd mode, (d) 4th mode, (e) 5th mode.

X.6.3. POD Reconstructed Fields

In this section, a random instantaneous snapshot was chosen and the flow fields were reconstructed using multiple POD modes. Since most of the kinetic energy of the flow field was stored in the first few POD modes, only a few POD modes were needed to capture the maximum large-scale coherent structures or a large scale behavior from complex flow field. It was known that the behavior of these large-scale coherent structures were often concealed by the presence of fine or small-scale coherent structures within the flow field. In other words, the power of POD fast convergence permitted the large-scale coherent structures to be isolated from the fine or small-scale coherent structures in the turbulence flow.

Figure 205 and Figure 206 show the instantaneous and POD reconstructed velocity plots and contour plots of vorticity at the V-T-A P1 for Case 3a and Case 3a. Those figures displays the progression of the POD mode reconstruction using the first two, fifth, tenth, fiftieth, and hundredth POD modes. It was obvious that the instantaneous contour plot of vorticity without POD reconstruction was clouded with the fine or small-scale vortical patterns throughout the field. Meanwhile, the POD reconstructed vorticity fields represent a cleaner view of the velocity vectors and vorticity map by filtering the smaller scale coherent structure. The POD modes convergence was faster for the adiabatic case (Case 3a) as compared with the heated case (Case 3).

The presence of the four jets issued from the four risers was apparent in the POD reconstruction using two modes for the adiabatic case whereas for the heated case, the jets

were seen only at the reconstruction with the five POD modes. The visibility of the jets at these two conditions corresponding to the total kinetic energy of approximately 10%. Reconstruction with 50 modes has the high relative energy significance clearly established for both cases, which translated to 59% for Case 3a and 51% for Case 3a. Large vortical structures were also seen in the outer layer of each jet particularly for the first three reconstructed vorticity maps. The existence of the large vortical structures near each jet shear layer suggested: (1) the presence of the Kelvin-Helmholtz instability as a result of the shear force between the high velocity air jet and the surrounding stagnant air, and (2) the ambient fluid entrainment phenomena.

Instantaneous and POD reconstructed velocity plots and vorticity fields at the V-T-B P1 for Case 3a and Case 3a are portrayed in Figure 207 and Figure 208. The POD was fruitful in capturing the large-scale coherent structures from the flow field and representing the dominant flow features. The POD reconstructed fields emphasize on the larger vortical structures by eliminating the small-scale vorticity patterns from the flow field. The POD reconstruction with 35 modes has the high relative energy significance clearly seen for Case 3a (73%) whereas for Case 3, the high relative energy significance (68%) occurred at the POD reconstruction of 50 modes. However, unlike the case of the V-T-A P1 where the large vortical structures could be predicted to be near each jet shear layer, there was no specific guideline to forecast the presence of the large vortical structure for the V-T-B P1 case.

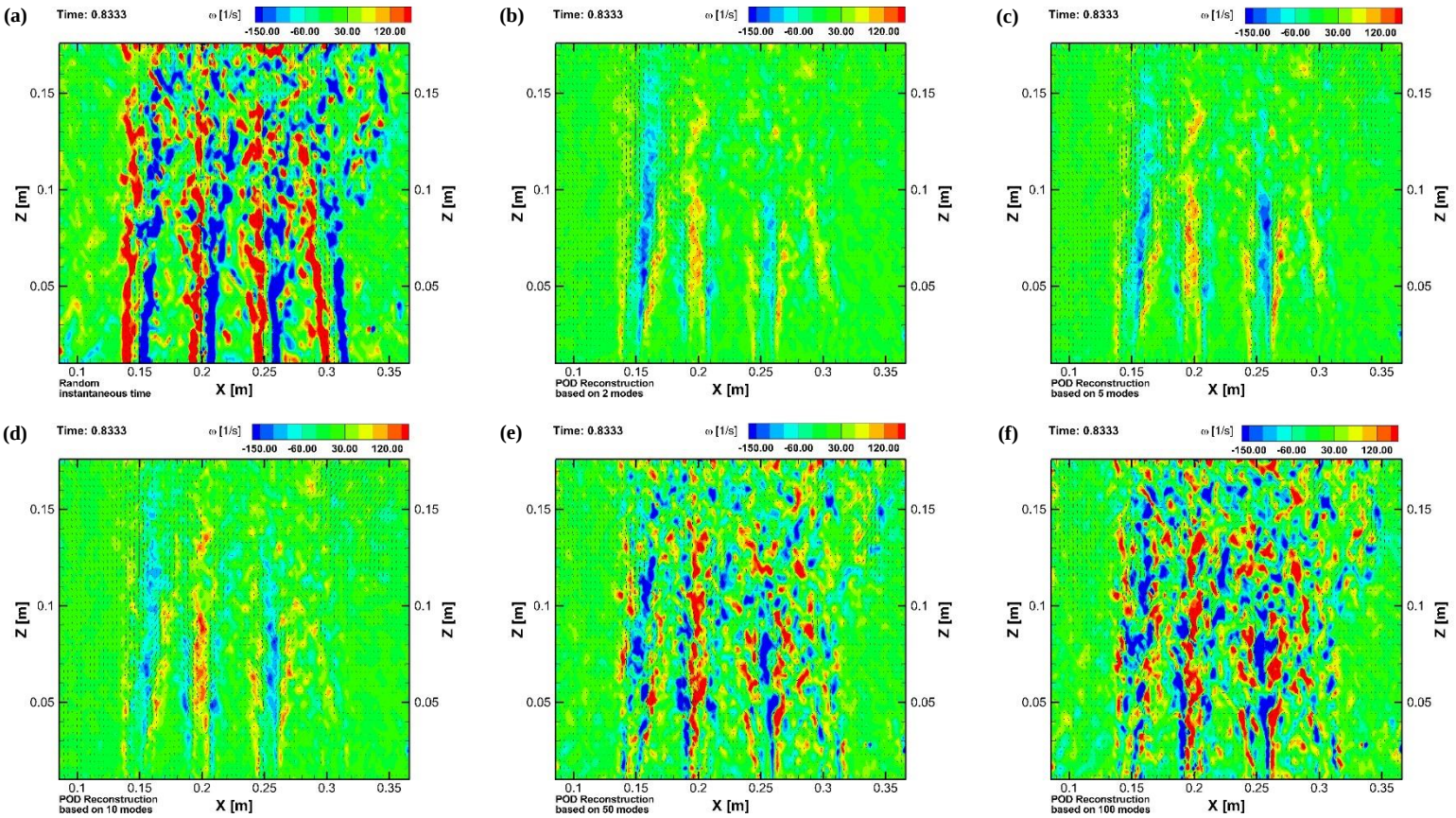

Figure 205. The POD modes reconstructed vector plots and contour plots of vorticity for the V-T-A P1 of Case 3a: (a) a random instantaneous time, (b) 2 modes, (c) 5 modes, (d) 10 modes, (e) 50 modes, and (f) 100 modes.

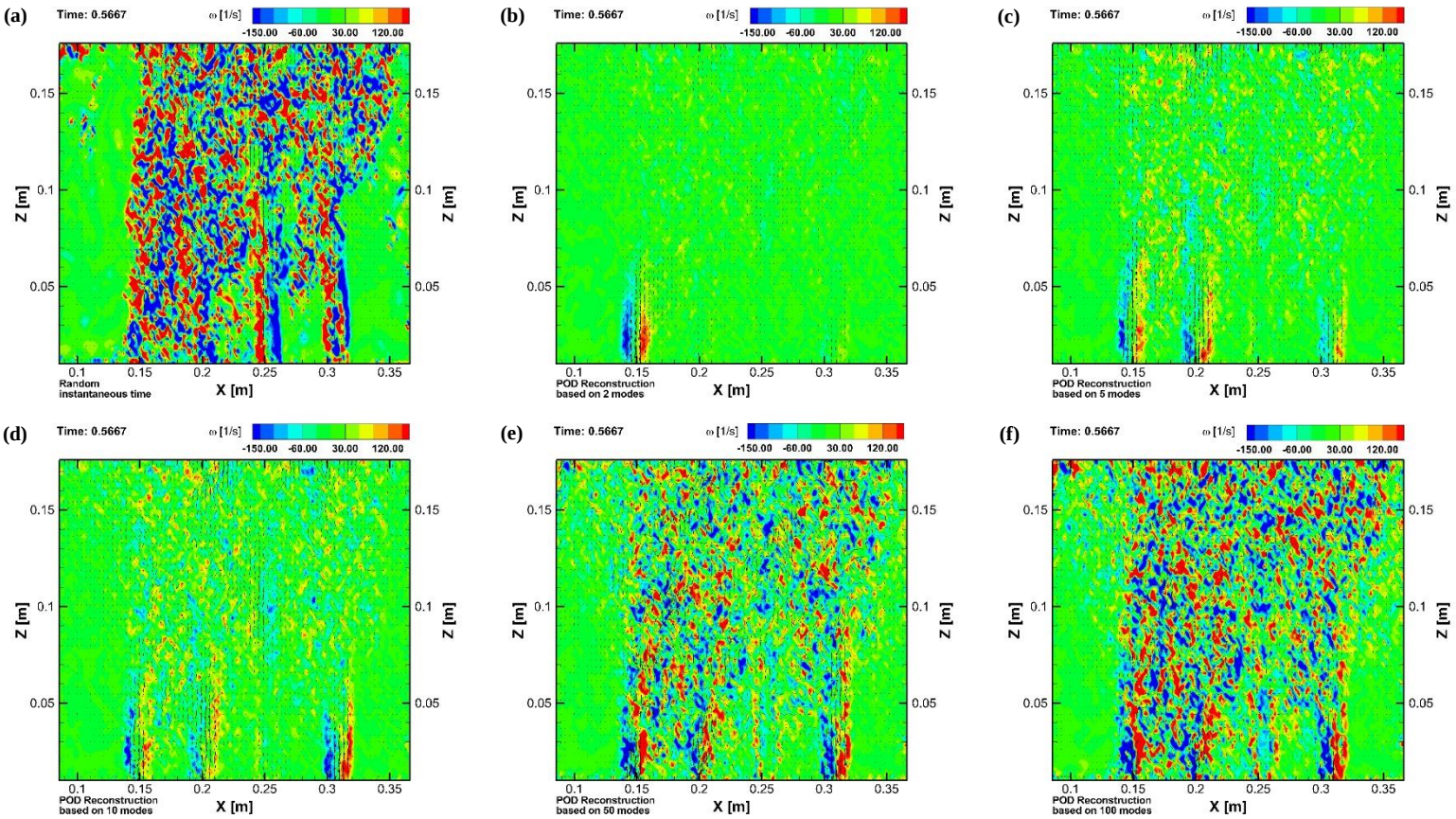

Figure 206. The POD modes reconstructed vector plots and contour plots of vorticity for the V-T-A P1 of Case 3: (a) a random instantaneous time, (b) 2 modes, (c) 5 modes, (d) 10 modes, (e) 50 modes, and (f) 100 modes.

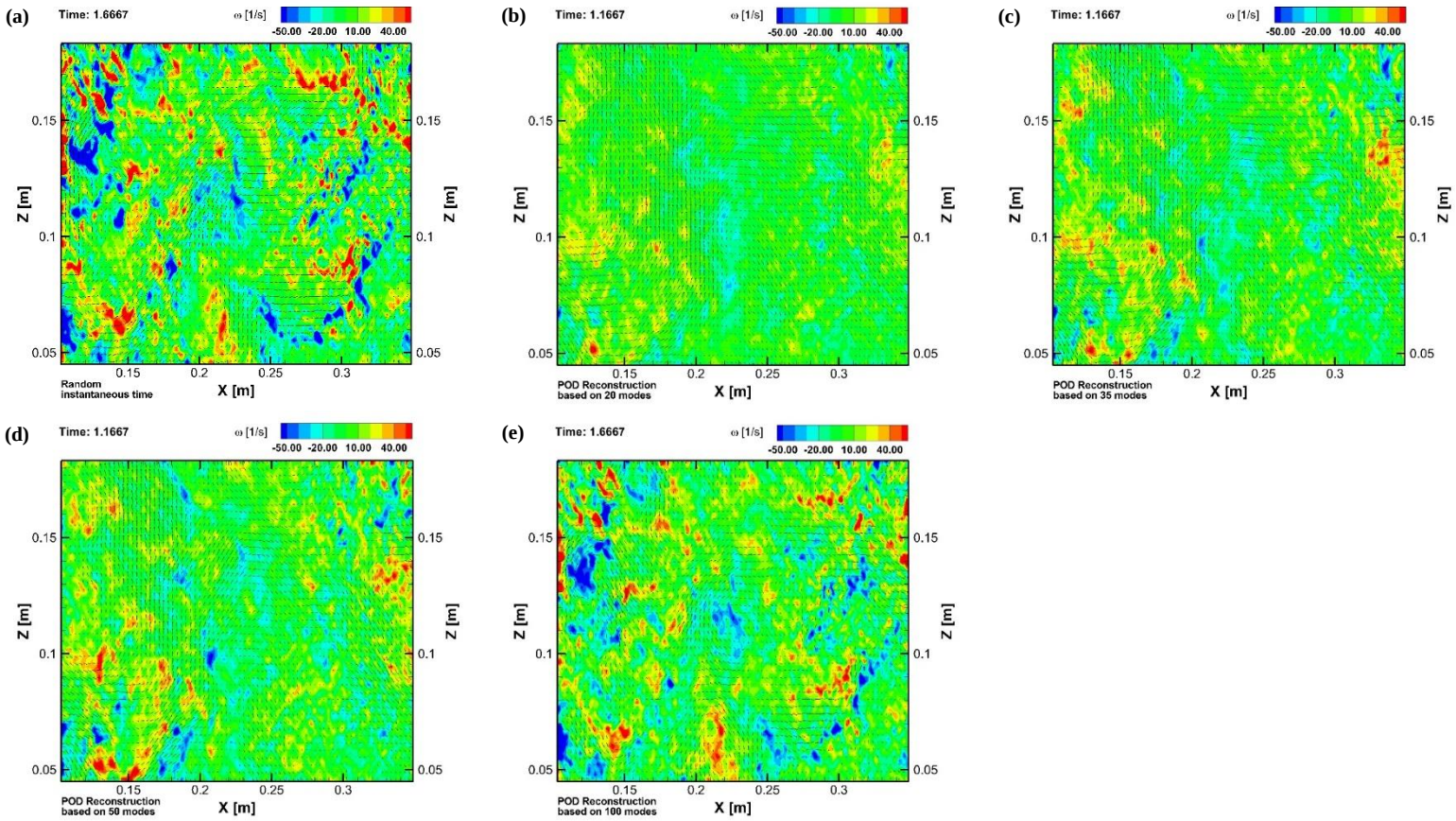

Figure 207. The POD modes reconstructed vector plots and contour plots of vorticity for the V-T-B P1 of Case 3a: (a) a random instantaneous time, (b) 20 modes, (c) 35 modes, (d) 50 modes, (e) 100 modes, and (f) 100 modes.

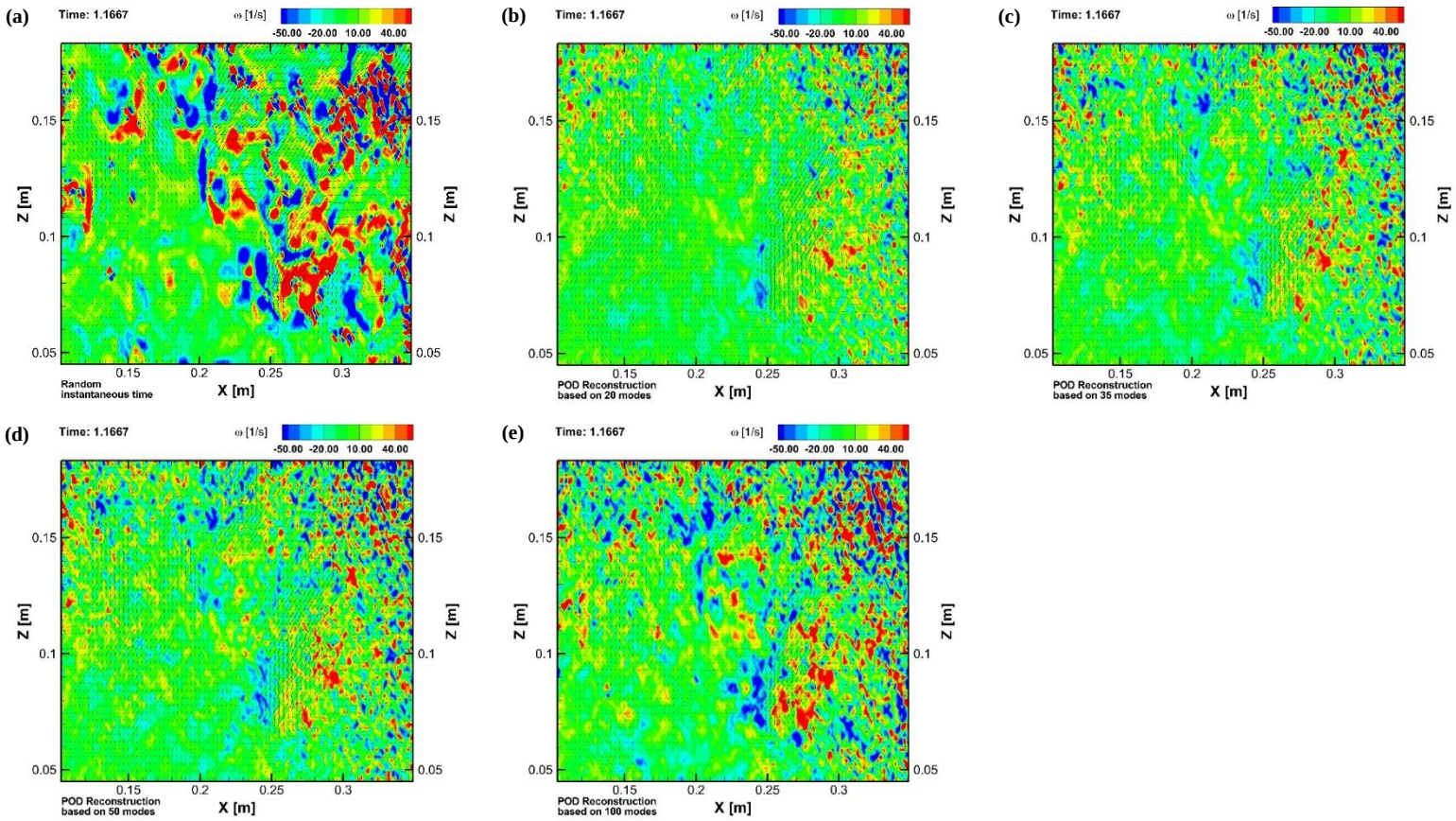

Figure 208. The POD modes reconstructed vector plots and contour plots of vorticity for the V-T-B P1 of Case 3a: (a) a random instantaneous time, (b) 20 modes, (c) 35 modes, (d) 50 modes, (e) 100 modes, and (f) 100 modes.

Table 38. The POD modes reconstruction at 70% R.E. for Case 3a and Case 3 at the respective positions.

Case	Position	POD modes reconstruction at 70% R.E.
Case 3a	V-T-A P1	69
	V-T-B P1	30
	V-T-C P1	24
Case 3	V-T-A P1	83
	V-T-B P1	54
	V-T-C P1	34

The POD technique is a robust tool that enables one to produce lower dimensional models of high dimensional systems due to the fact that the POD eigenmodes are the optimal decomposition for the flow. In other words, the flow fields' reconstruction utilizing these primary eigenmodes represent the spatial and temporal evolution of the dominant or most energetic coherent structures in the flow field. Assuming that at 70% of the total energy in the fluctuating motion or relative energy (R.E.) are satisfactory for the flow to retain its primary features and characteristics, an analysis was carried out to determine the corresponding POD modes required at the V-T-A P1 and V-T-B P1 for both Cases 3a and Case 3, respectively (Table 38). Figure 209 shows that the velocity vectors and vorticity contour plots of a random instantaneous snapshot reconstructed with 70% R.E. and reconstruction using full POD modes (150 modes) at the V-T-A P1 for Case 3a and Case 3. It was seen that most of principal features and characteristics of the

reconstructed flow fields using 150 modes were captured by the POD reconstruction with 70% R.E.

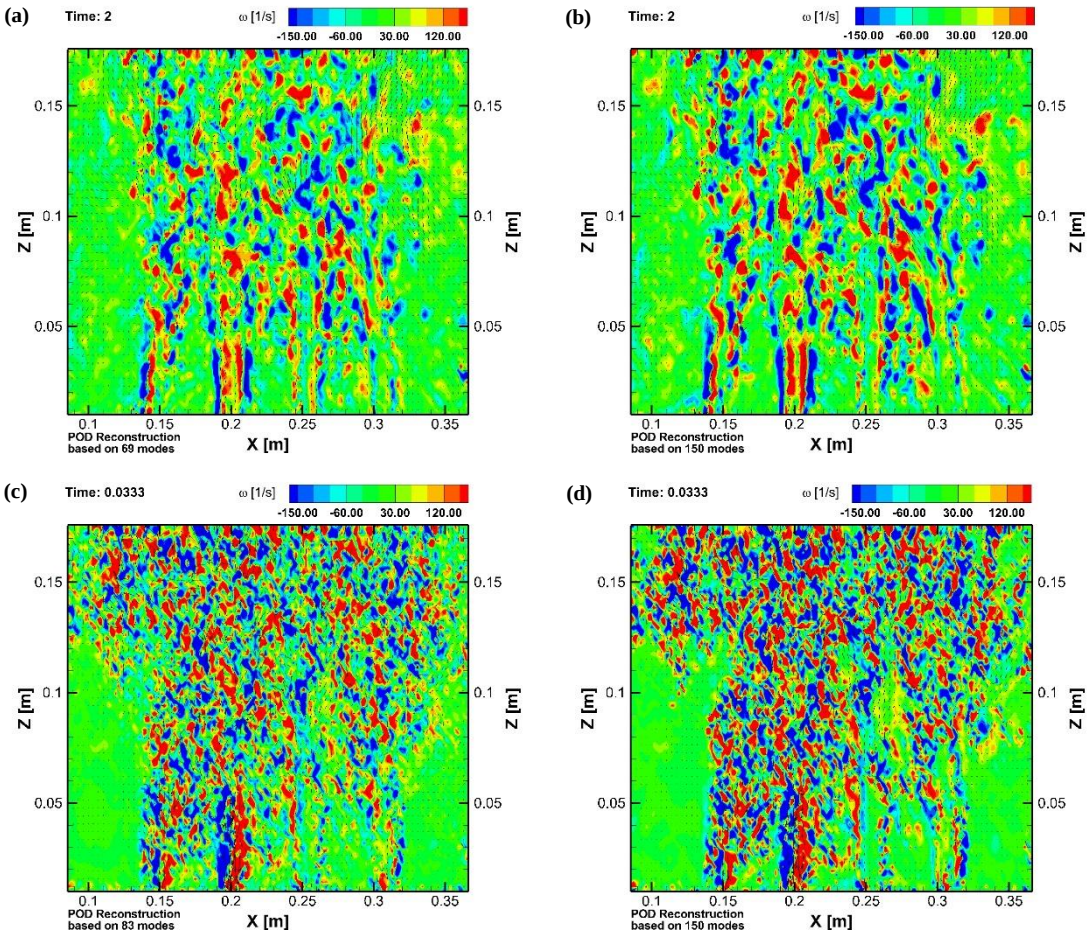

Figure 209. Comparison of the POD modes reconstructed velocity vector plots and contour plots of vorticity for the V-T-A P1 (for a random instantaneous file); Top: Case 3a: (a) 69 modes (70% R.E. energy), (b) 150 modes (full POD modes); Bottom: Case 3: (c) 83 modes (70% R.E.), and (d) 150 modes (full POD modes).

As mentioned previously, less number of POD modes was entailed for reconstruction at the adiabatic condition than the heated condition due to different intensity level of turbulence mixing. These reduced dimensional models were utilized to identify vortical structures which allowed for rough approximation of the size of turbulence length scale at the V-T-A P1 and V-T-B P1 for both Case 3a and Case 3. Turbulence length scale, l, is a physical quantity which represents the size of the large eddies (energy containing eddies) in turbulent flows.

Vortices of different length scales occurred in the flow. Each turbulent length scale was associated with its corresponding time scale. Smallest turbulent length scale has the smallest time scale. The large eddies broke down into smaller eddies. Smaller eddies broke down into still smaller eddies, and so forth (cascade of energy). The small scales (energy dissipating eddies) could be approximated from the circumstance that the energy was dissipated into heat. The viscous forces were dominant at very small scales. Knowledge of different turbulent length scale would enable turbulence modeling for CFD simulations to become more accurate and realistic. In this investigation, the streamtraces computed by Tecplot 360 were used to locate vortical structures in each contour plot of vorticity. The size of each vortex was estimated as a perfect circle in the flow field. These vortices were labelled and counted in sequential manner. Their sizes (i.e. based on the diameter of a circle) were recorded and the average size was computed accordingly.

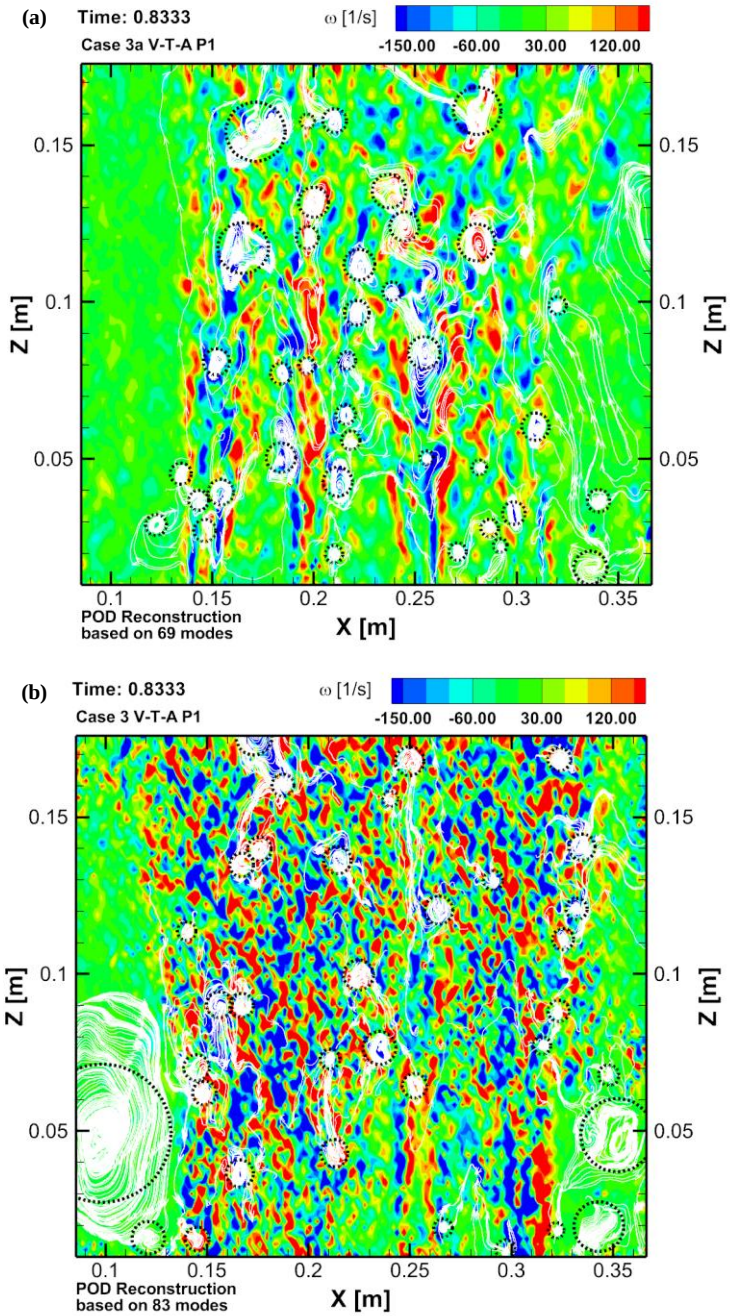

Figure 210. POD modes reconstruction at 70% R.E.: (a) Case 3a V-T-A P1 (69 modes), and (b) Case 3 V-T-A P1 (83 modes).

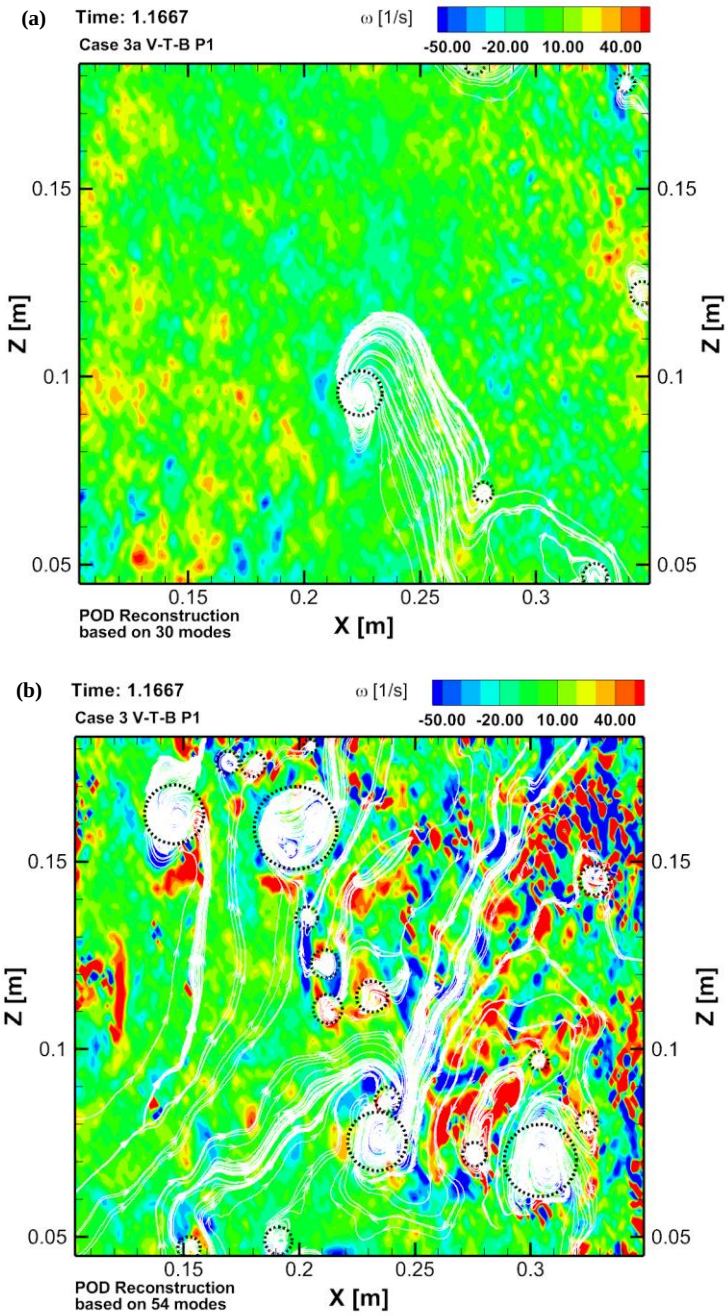

Figure 211. POD modes reconstruction at 70% R.E.: (a) Case 3a V-T-B P1 (30 modes), and (b) Case 3 V-T-B P1 (54 modes).

Table 39. Rough approximation of turbulence length scale at the V-T-A P1 for Case 3a and Case 3.

Case 3a V-T-A P1							
Count	**Skewness**	**Std. Dev. (mm)**	**Min. (mm)**	**Max. (mm)**	**Mean (mm)**	**Median (mm)**	**Mode (mm)**
38	1.6	5.0	7.7	29.1	12.4	10-12.5	10-12.5
Case 3 V-T-A P1							
Count	**Skewness**	**Std. Dev. (mm)**	**Min. (mm)**	**Max. (mm)**	**Mean (mm)**	**Median (mm)**	**Mode (mm)**
35	4.2	10.6	6.9	68.0	14.5	10-12.5	10-12.5

Several interesting observations were found based in this simple analysis. Figure 210 shows the contour of vorticity plots of the reconstructed POD modes at 70% R.E. for Case 3a and Case 3 at the V-T-A P1. Each black dotted line circle signified the location and size of the identified vortex. It was found that more vortical structures were discovered at the adiabatic condition than the heated condition (Table 39). The computed average turbulence length scale at the adiabatic condition (12.4 mm) was less than its counterpart at the heated condition (14.5 mm). In fact, there was a huge gap in vortices sizes for the heated case as compared with the adiabatic case.

An identical analysis was carried out at the V-T-B P1 for Case 3a and Case 3 (Figure 211). For Case 3a, a similar trend exhibited at the V-T-A P1 was observable at the V-T-B P1 with respect to the mean vortex size with different magnitude. However, a huge drop of number of vortices was seen for the adiabatic case of which only six number of

vortices were identified at the V-T-B P1. More vortices were found at the heated condition than the adiabatic condition. The maximum size of the vortices at the V-T-B P1 was smaller than the V-T-A P1 for Case 3a and Case 3 (Table 40).

Table 40. Rough approximation of turbulence length scale at the V-T-B P1 for Case 3a and Case 3.

Case 3a V-T-B P1							
Count	**Skewness**	**Std. Dev. (mm)**	**Min. (mm)**	**Max. (mm)**	**Mean (mm)**	**Median (mm)**	**Mode (mm)**
6	2.1	4.4	7.8	19.4	10.8	7.5-10	7.5-10
Case 3 V-T-B P1							
Count	**Skewness**	**Std. Dev. (mm)**	**Min. (mm)**	**Max. (mm)**	**Mean (mm)**	**Median (mm)**	**Mode (mm)**
18	1.5	8.3	6.1	35.8	14.4	10-12.5	10-12.5

Vortices sizes for both Case 3a V-T-A P1 and Case 3 V-T-A P1 have a “skewed right” or “positively skewed” distribution of which the tail of the data was lying on the right side or a longer upper tail (McCluskey and Lalkhen, 2007) (Figure 212). Case 3a V-T-B P1 has a skewed right or positively skewed distribution as well whereas Case 3 V-T-B P1 has a “skewed left” or “negatively skewed” distribution of which the tail data was located on the left side or a longer lower tail (McCluskey and Lalkhen, 2007). For a skewed distribution, mean, median, and mode could be used for typical value metrics. It was observed that the mean, median, and mode for Case 3a V-T-A P1 have fallen into the

same range (10-12.5 mm) whereas for other cases, their median and mode have the similar range. Subsequently, it is prudent to conclude that the representative range for Case 3a V-T-A P1 is 10-12.5, 10-12.5 mm for Case 3 (V-TA P1 and V-T-B P1), and 7.5-10 mm for Case V-T-B P1.

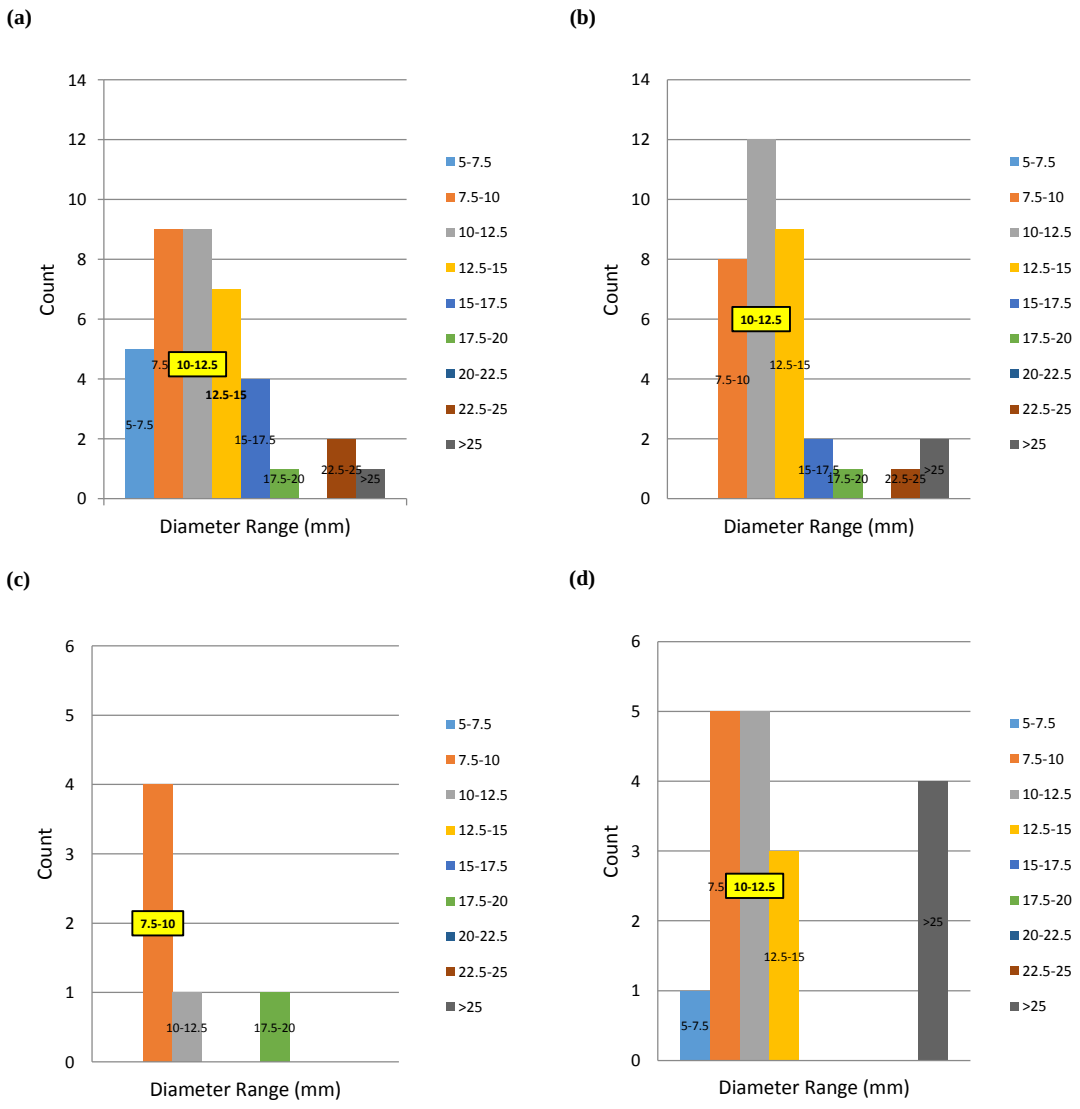

Figure 212. The tabulation of vortices size based on 2.5 mm interval range. The representative value of the vortices range is denoted by the yellow box: (a) Case 3a V-T-A P1, (b) Case 3 V-T-A P1, (c) Case 3a V-T-B P1, (d) Case 3a V-T-B P1.

X.7. Uncertainty Analysis

X.7.1. Temperature Measurement Uncertainty

Alhashimi (2014) carried out the uncertainty analysis for the temperature measurements based on a model developed by Sandia National Lab (SNL) of which both systematic and random errors were incorporated in the analysis, respectively. It was seen that the systematic error had a much bigger influence than the random error due to the presence of large sample (900 measurements per thermocouple in each location) acquired for each temperature measurements. As such, the maximum uncertainty of the temperature measurements was ±1.6ºC or $(\pm 1.33 \times 10^{-2})\ T_{max}$.

X.7.2. Velocity Measurements Uncertainty

X.7.2.1. PIV System Uncertainty

For the uncertainty analysis, the guidelines outlined by the Visualization Society of Japan (VSJ) were implemented. The guidelines for uncertainty analysis were established as an outcome of an organized project on PIV standardization (Nishio, Okamoto, Kobayashi, and Saga, 1999; Nishio and Murata, 2003). The root-sum-square was adopted to evaluate the uncertainties build-up. Table 41 summarizes the principal dimension of target measurements which comprises the following sub-systems: (1)

Calibration, (2) Flow Visualization, (3) Image Detection, and (4) Data Processing. Table 42 encapsulates the propagation and build-up of uncertainties for measurement parameters $\alpha, \Delta X, \Delta t,$ and $\delta u,$ and its correspondent combined measurement uncertainty velocity u. Table 43 shows the uncertainty propagation to the measurement target position x and time t. The uncertainties of u, X and t were analyzed separately. When collection for total performance of the measurement system by the uncertainty for the flow speed was desirable, the following summation can be applied,

$$u_c = \sqrt{u_u^2 + \left(\frac{u_x \partial u}{\partial x}\right)^2 + \left(\frac{u_t \partial u}{\partial t}\right)^2} \tag{X-15}$$

where u_u, u_x, and u_t denote the uncertainties of velocity, position, and time, respectively. When the combined uncertainties were evaluated, the major uncertainty sources may be determined.

The highest uncertainty sources pinpointed in this investigation was the normal view angle and optical magnification factor. The position of the beam delivering arm was fixed so that the only movement involved during measurement only in the y-direction of the BiSlide positioning system. The calibration errors contributing to the magnification factor α were quantified using in-situ calibration images for each measured plane. The V-T-A plane for Case 1 was used for the computation of the uncertainties.

Case 1 was chosen since it was the heated case with the high inlet velocity (5 m/s) of which the probability of highest uncertainty would be highly likely. The V-T-A plane was selected chiefly due to its location which was directly above the risers' outlets where the jets were issued from the nozzles into the inside of the upper plenum and it has the longest distance from the high-resolution digital camera. As such, it was prudent to assume that the V-T-A plane of Case 1 has the highest error than the other planes; therefore, it was utilized to determine the values tabulated in Table 41 to Table 43.

Table 41. Principal dimensions of PIV measurement.

Target Flow of Measurement		
Target flow		2-D air flow
Measurement facility		Upper plenum
Measurement area		419.1 x 431.8
Uniform flow speed		5
Calibration		
Distance of reference points	l_r	10
Distance of reference image	L_r	45
Magnification factor	α	0.22
Flow Visualization		
Tracer particle		Spherical olive oil particle
Average diameter dp	d_P	7.45E-07 m
Standard deviation of diameter	s_P	6.00E-09 m
Average specific gravity		0.913 g/cm^3
Light source		Double Pulse Vlite-200 Laser
Laser power		200 mJ
Thickness of laser light sheet		1 mm
Time interval	Δt	500 μs
Image Detection		
Camera		Vision Research Miro M310 Phantom 12 GB
Spatial resolution		1280 x 800 pixels
Sampling frequency		30 Hz
Gray scale resolution		8-bit
Sensor size		25.6 mm x 16.0 mm
Optical system		
Distance from the target	l_t	42.375 mm
Length of focus		50 mm (Carl Zeiss)
F number of lens		f/2-f/22
Perspective angle	θ	6º
Data Processing		
Pixel unit analysis		Cross correlation method
Correlation area size (multi-pass)		64 x 64 pixels
Search area size		16 x 16 pixels
Sub-pixel analysis		Gauss 2x3 point

Table 42. Summary of uncertainties for velocity $\boldsymbol{u}$.

Parameter	Category	Error sources	$u(x_i)$	(unit)	c_i	(unit)	$c_i u(x_i)$	u_c
α (mm/pix)	Calibration	Reference image (digital error, non-uniformity of distribution)	7.00E-01	(pix)	-4.94E-03	(mm/pix^2)	-3.46E-03	1.14E-02
		Physical distance	2.00E-02	(mm)	2.22E-02	1/px	4.44E-04	
		Image distortion by lens	2.25E-01	(pix)	-4.94E-03	(mm/pix^2)	-1.11E-03	
		Image distortion by CCD	5.60E-03	(pix)	2.22E-02	(mm/pix^2)	1.24E-04	
		Reference position	2.00E+00	(mm)	5.24E-03	(1/pix)	1.05E-02	
		Parallel board	1.05E-01	(rad)	-2.33E-02	(mm/pix)	-2.45E-03	
ΔX (pix)	Acquisition	Laser power fluctuation	7.10E-03	(mm)	4.50E+00	pix/mm	3.20E-02	4.83E-02
		Image distortion by CCD	5.60E-03	(px)	2.20E-01		1.23E-03	
		Normal view angle	1.05E-01	(rad)	-2.33E-02	(mm/pix)	-2.45E-03	
	Reduction	Mismatching error (cross correlation and centroid location)	2.00E-02	(pix)	1.00E+00		2.00E-02	
Δt (s)	Acquisition	Sub-pixel analysis	3.00E-02	(pix)	1.00E+00		3.00E-02	1.41E-08
		Delay generator	1.00E-08	(s)	1.00E+00		1.00E-08	
		Pulse time	1.00E-08	(s)	1.00E+00		1.00E-08	
δu (mm/s)	Experiment	Particle trajectory (lag)	5.96E-09	(mm/s)	1.00E+00		5.96E-09	2.26E-03
		3-D effects	2.26E-03	(mm/s)	1.00E+00		2.26E-03	

Parameter	Category	Error sources	$u(x_i)$	(unit)	c_i	(unit)	$c_i u(x_i)$	(unit)
α		Magnification factor	1.14E-02	(mm/pix)	140.69	(pix/s)	1.60E+00	(mm/s)
ΔX		Image displacement	4.83E-02	(pix)	0.444444	(mm/px/s)	2.14E-02	(mm/s)
Δt		Image interval	1.41E-08	(s)	182.90	(mm/s^2)	2.59E-06	(mm/s)
δu		Experiment	2.26E-03	(mm/s)	1.0		2.26E-03	(mm/s)
			Combined uncertainty		u_u		1.60	(mm/s)

Standard uncertainty: $u(x_i)$; Sensitivity coefficient: $c_i = \partial f / \partial x_i$

Table 43. Summary of uncertainties for position, $\boldsymbol{x}$, and time, $\boldsymbol{t}$.

Parameter	Category	Error sources	$u(x_i)$ (unit)	c_i (unit)	$c_i u(x_i)$ (unit)
X_s, X_e	Acquisition	Digital error (center position of correlation area)	0.005 (pix)	0.22 (mm/pix)	1.11E-03
		Non-uniformity of tracer particle distribution	16.0 (pix)	0.22 (mm/pix)	3.56E+00
X_0	Calibration	Origin correlation	2 (pix)	0.22 (mm/pix)	4.44E-01
α		Magnification factor	400 (mm/pix)	1.14E-02 (pix)	4.55E+00
			Combined uncertainty	u_x	5.79 (mm)

Parameter	Category	Error sources	$u(x_i)$ (unit)	c_i (unit)	$c_i u(x_i)$ (unit)
t_s, t_e	Acquisition	Delay generator	1.00E-08 (s)	1.0	1.00E-08
		Pulse time	1.00E-08 (s)	1.0	1.00E-08
			Combined uncertainty	u_t	1.41E-08 (s)

Standard uncertainty: $u(x_i)$; Sensitivity coefficient: $c_i = \partial f / \partial x_i$

Combined uncertainty, $u_c = \sqrt{u_u^2 + \left(u_x \frac{\partial u}{\partial x}\right)^2 + \left(u_t \frac{\partial u}{\partial t}\right)^2} = \pm 57.94\ mm/s = \pm 0.058\ m/s = (\pm 1.16 \times 10^{-2}) U_{max}$

X.7.2.2. Statistical Uncertainty

An adequate and satisfactory number (N) of PIV images must be recorded and processed in light to meet statistical requirements for the mean and fluctuation velocity component measurements. When the number of N is sufficiently large, the probability distribution function (PDF) of measured velocity magnitudes follows a Gaussian distribution. Additionally, when N is sufficiently large, the ensemble averaged or mean value verges onto a true mean as N goes to infinity. In the event of finite N-samplings of fluctuating property, i.e. instantaneous velocity vectors, their ensemble average shoulders an uncertainty from the true value. In accordance to the central limit theorem (CLT), the uncertainty can be estimated as equal to the standard deviation of measured values (σ) divided by $\sqrt{N}$, i.e. the standard error of mean value, $\varepsilon = \sigma/\sqrt{N}$.

Table 44 and Table 45 show errors calculated from measured data for the velocity component $\bar{U}$, $\bar{V}$ and $\overline{U'V'}$ averaged from 150 PIV pair images at the V-T-A P1 position for both Case 1a and Case 1, respectively. The tabulated uncertainties were approximated at the positions of maximum standard deviation of individual components (i.e. the V-T-A P1), and they were equivalent to 95% confidence interval, which translated to $\pm 1.96\sigma$.

Table 44. Uncertainties of assemble averaged flow components of the V-T-A P1 of Case 1a.

Variable	Standard Error
$\langle U \rangle$	$(\pm 4.74 \times 10^{-2})\, U_{max}$
$\langle V \rangle$	$(\pm 4.38 \times 10^{-2})\, U_{max}$
$\langle U'V' \rangle$	$(\pm 3.15 \times 10^{-2})\, U_{max}^2$

Table 45. Uncertainties of assemble averaged flow components of the V-T-A P1 of Case 1.

Variable	Standard Error
$\langle U \rangle$	$(\pm 4.05 \times 10^{-2})\, U_{max}$
$\langle V \rangle$	$(\pm 2.83 \times 10^{-2})\, U_{max}$
$\langle U'V' \rangle$	$(\pm 1.42 \times 10^{-2})\, U_{max}^2$

CHAPTER XI

CONCLUSIONS AND FUTURE WORK

In this dissertation, a fully functional scaled experimental test facility for the air RCCS has been designed, constructed and operated. This facility allows for the simulation of a wide range of experimental conditions and allows for the collection of various and extensive types of data, including full field temperature and velocity.

Turbulent flow behavior and characteristics inside the upper plenum of a scaled air-cooled RCCS have been investigated at the adiabatic (inlet = room temperature) and heated (inlet = 120º C) conditions using either one or four active risers. Two different velocities (2.25 m/s and 5 m/s) were used as part of inlet boundary conditions. Temperature measurements data was collected using movable, custom-made thermocouple racks and velocity measurements data was acquired using PIV, and the data has been post-processed and analyzed.

Based on the findings of the experimental test matrix, it was proven that the existence of anticipated thermal stratification layers inside the upper plenum is closely linked to the inlet boundary conditions of the risers. It was observed that the flow reversal may lead to thermal stratification layers inside the upper plenum. As a result, natural circulation driven flow may be inhibited by the establishment of stratified layers inside the upper plenum, which in turn could reduce the overall effectiveness of decay and residual heat removal, leading to a departure of the RCCS from its design conditions.

The air-cooled RCCS cooling performance is highly sensitive to boundary conditions. It was noted that the flow reversal phenomenon did not occur at the adiabatic condition for all cases (i.e. Case 1a, Case 2a, Case 3a, and Case 4a). In fact, for one riser case (i.e. Riser ④), the air flow from the upper plenum exits the nearest outlet after mixing, i.e. the inlet of right chimney. Based on the experimental test matrix, three out of four cases at the heated condition have demonstrated flow reversal phenomenon; that is, only Case 1 shows symmetric flow and does not exhibit any flow reversal characteristics. The triggering mechanism of the flow reversal has yet to be identified and this could be a part of the future research.

The experimental data shows that buoyancy effects are more prominent in four-jet cases than 1-riser jet cases. Moreover, the buoyancy flux is reduced greatly as the jets travel downstream in streamwise direction. The buoyancy effects playing less role surpassing the axial distance between the riser outlets and the middle line across the two exits of the upper plenum. Therefore, buoyancy effects must be taken into consideration into the CFD modeling for near-field (i.e. zone of flow establishment, ZFE where the jets' motion and physical characteristics are characterized by its initial momentum and discharge conditions & zone of established flow where the flow characteristics where its initial momentum, buoyancy, and ambient stratification and ambient conditions) and far-field (the jets' initial momentum has negligible effect, and the jet may passively convected by ambient motions).

The POD technique helps in giving some insights to quantify and characterize the structure and the physics of the flow field. The snapshot POD method was utilized to study

the behavior of the coherent structures within the flow field of selected positions of one of the flow reversal cases. The POD analysis helped to determine the large-scale coherent structures from the flow field and more importantly it allowed for the reconstruction of lower-order models of the highly complex turbulence flow fields. The results of the POD analysis indicate that the first few POD eigenmodes encompass the majority of the energy of the flow field. Rough approximation of the turbulent length scale representative values were obtained for a random instantaneous snapshot reconstructed using the optimal POD modes for several specific cases.

The novel data acquired through this experimental study could be applied as a benchmark for the validation of the existing CFD codes modeling the flow behavior inside the upper plenum. The result of the investigation could also be served as a CFD-grade experimental database for validation of the numerical model used for prediction of the thermal stratification and flow reversal phenomena.

For the future research, extension of the experimental test matrix to include more cases at different inlet boundary conditions (uniform and non-uniform velocities and temperatures) is highly necessary in order to gain better understanding on the flow physical characteristics. Close interaction between the measuring and modeling activities is imperative in order to seek close agreement between measurement and prediction. The triggering mechanism of the flow reversal should be investigated more rigorously by conducting more tests that force the reverse flow in one of the chimneys, and appropriate measurement techniques should be installed for the capture to capture the flow fields at transient and steady-state conditions.

Augmentation of the existing measurements facility to include state-of-the-art measurement techniques are recommended. An advanced PIV method such as Time-Resolved PIV (TR-PIV) of which a high power/high repetition laser is coupled with a high speed/high resolution CMOS camera will provide higher temporal and spatial resolution of the velocity fields compared with normal PIV. Usage of stereoscopic PIV method to obtain three-component of velocity would furnish detailed 3D information on turbulence mixing. The Planar Laser Induced Florescence (PLIF) technique can be utilized to acquire the temperature fields inside the upper plenum. Furthermore, the PLIF method can be used in conjunction with the TR-PIV to obtain simultaneous velocity and temperature fields.

In terms of numerical simulations, 3D CFD, employing in minimum unsteady (time-dependent) RANS analyses (URANS), and possibly Large-Eddy Simulation (LES), are highly required to investigate multi-layered thermal-hydraulic phenomena that are coupled together, such as thermal stratification, flow reversal, buoyant jet impinging to the wall, flow stratification, formation of wall jet and its interaction, complex turbulent mixing due to adjacent jet interactions, and so forth. Post-processing using advanced techniques to decompose spatial and temporal characteristics of the flow using the POD technique, wavelet, or any equivalent techniques, should be carried out for both physical and numerical experiments, which can later be used to benchmark.

REFERENCES

Adrian, R. J. (1991). Particle-image techniques for experimental fluid mechanics. *Annual Review of Fluid Mechanics, 23,* 261–304. http://doi.org/10.1146/annurev.fl.23.010191.001401.

Adrian, R. J. (1996). Laser Velocimetry. In R. Goldstein (Ed.), *Fluid Mechanics Measurements* (2nd ed.). Philadelphia: Taylor & Francis.

Alhashimi, T. (2014). *Measurement of temperature profile in the reactor cavity cooling system*. Master's Thesis, Texas A&M University, College Station.

Amini, N. (2011). *Turbulent flow analysis and coherent structure identification in experimental models with complex geometries*. PhD. Dissertation, Texas A&M University, College Station.

Baccaglini, G., Ball, S., & Shaber, E. (2003). *Very high temperature reactor (VHTR) survey of materials research and development needs to support early deployment*. *INEELlEXT03-00141*. Idaho Falls.

Beamtech Optronics Co. Ltd. (2013). Vlite series laser system - Vlite-200 user's manual. Beijing, China: Beamtech Optronics Co. Ltd.

Bechtel National, Inc., Combustion Engineering, Inc., Dept. of Energy, EG&G Idaho, Inc., GA Technologies, Inc., Gas-cooled Reactor Associates, … Stone & Webster Engineering Cor. (1992). *Preliminary safety information document for the standard MHTGR (HTGR-86-024) - Volume 1, Amendment 13*. Washington, D. C.

Beitelmal, A. H., Shah, A. J., & Saad, M. A. (2006). Analysis of an impinging two-dimensional jet. *Journal of Heat Transfer*, *128*(3), 307–310. http://doi.org/10.1115/1.2150841.

Berkooz, G., Holmes, P., & Lumley, J. L. (1993). The proper orthogonal decomposition in the analysis of turbulent flows. *Annual Review of Fluid Mechanics*, *25*, 539–575. http://doi.org/10.1146/annurev.fl.25.010193.002543.

Biagioli, F., Lachaux, T., & Narendran, S. (2014). Investigation of the Dynamic Response of Swirling Flows Based on LES and Experiments. *Flow, Turbulence and Combustion*, *93*(3), 521–536. http://doi.org/10.1007/s10494-014-9564-2.

Blandford, E., Moheet, A., Seifried, J., & Thomas, E. (2007). *Preliminary safety analysis report for the General Atomic gas-turbine modular helium reactor (NE 167/267 final report)*. Retrieved from http://www.uxc.com/smr/Library/Design Specific/GT-MHR/Papers/2007 - Preliminary Safety Analysis Report for the GA GT_MHR.pdf\npapers3://publication/uuid/1D9FB5D5-ABC4-44D8-A8ED-0A25E50E7492.

Bradshaw, P. (1966). The effect of initial conditions on the development of a free shear layer. *Journal of Fluid Mechanics*, *26*(2), 225–236. http://doi.org/10.1017/S0022112066001204.

Brossard, C., Monnier, J.-C., Barricau, P., Vandernoot, F.-X., Sant, Y. Le, Champagnat, F., & Besnerais, G. Le. (2009). Principles and applications of particle image velocimetry. *Onera AerospaceLab Journal*, *AL01-03*(1), 1–11.

Cartwright, W. G., & Russell, P. J. (1967). Characteristics of a turbulent slot jet impinging on a plane surface. In *Proceedings of the Institution of Mechanical Engineers* (Vol. 182, pp. 309–319). http://doi.org/10.1243/PIME.

CD-Adapco. (2013). User guide: STAR-CCM+ version 8.06.005. New York: CD-Adapco.

CD-Adapco. (2014). Introduction to STAR-CCM+ - CD-Adapco webinar. Houston: CD-Adapco.

CD-Adapco. (2014). User guide: STAR-CCM+ version 9.04.009. New York: CD-Adapco.

Chapin, D., Kiffer, S., & Nestell, J. (2004). *The very high temperature reactor: A technical summary*. Alexandria. Retrieved from http://www.mpr.com/uploads/news/very-high-temperature-reactor.pdf.

Chen, C. J., & Chen, C. H. (1979). On Prediction and Unified Correlation for Decay of Vertical Buoyant Jets. *Journal of Heat Transfer*, *101*(3), 532–537. http://doi.org/10.1115/1.3451023.

Chen, C. J., & Nikitopoulos, C. P. (1979). On the near field characteristics of axisymmetric turbulent buoyant jets in a uniform environment. *International Journal of Heat and Mass Transfer*, *22*(2), 245–255. http://doi.org/10.1016/0017-9310(79)90148-0.

Chua, L. P., & Lua, A. C. (1998). Measurements of a confined jet. *Physics of Fluids*, *10*(12), 3137–3144. http://doi.org/10.1063/1.869841.

Corradini, M., Feltus, M., & Wei, T. (2012). *Experimental studies of NGNP reactor cavity cooling system with water*. *Project No. 09-781*. Madison.

Dantec Dynamics, Inc. (2012). Traversing mechanism. *Publication No.: pi_193_v10*. New York. Retrieved from http://www.josts.com/userfiles/files/Traversing System.pdf.

Dilling, D. A., Ghose, S. K., & Berkoe, J. M. (1992a). Modeling and analysis of heat transfer from the MHTGR core through a steel reactor vessel to the reactor cavity cooling system. In *Proceeding of a specialists meeting on decay heat removal and heat transfer under normal and accident conditions in gas cooled reactors (IAEA-TECDOC-757)* (pp. 111–116). Jülich, Germany: International Atomic Energy Agency.

Dilling, D. A., Ghose, S. K., & Berkoe, J. M. (1992b). Passive decay and residual heat removal in the MHTGR. In *Proceeding of a specialists meeting on decay heat removal and heat transfer under normal and accident conditions in gas cooled reactors (IAEA-TECDOC-757)* (pp. 75–89). Jülich, Germany: International Atomic Energy Agency.

Durve, A., Patwardhan, A. W., Banarjee, I., Padmakumar, G., & Vaidyanathan, G. (2012). Numerical investigation of mixing in parallel jets. *Nuclear Engineering and Design*, *242*, 78–90. http://doi.org/10.1016/j.nucengdes.2011.10.051.

Erdem, D., & Atli, V. (2002). Interaction of two parallel rectangular jets. In *Proceedings from the 23rd Congress of International Council of the Aeronautical Sciences* (pp. 1–1). Toronto: Optimage Ltd. Retrieved from http://www.icas.org/ICAS_ARCHIVE/ICAS2002/PAPERS/R15.PDF.

Estrada-Perez, C. E. (2004). *Analysis, comparison and modification of various particle image velocimetry (PIV) algorithms*. Master's Thesis, Texas A&M University, College Station.

Fitzgerald, J. A., & Garimella, S. V. (1998). A study of the flow field of a confined and submerged impinging jet. *International Journal of Heat and Mass Transfer*, *41*(8-9), 1025–1034. http://doi.org/10.1016/S0017-9310(97)00205-6.

Frisani, A., Hassan, Y. A., & Ugaz, V. M. (2010). Computation fluid dynamics analysis of the Reactor Cavity Cooling System for Very High Temperature Gas-Cooled Reactors. *Nuclear Technology*, *176*, 238–259. http://doi.org/10.1016/j.anucene.2014.04.039.

Frisani, F. (2010). *Analysis of the reactor cavity cooling system for very high temperature gas-cooled reactors using computational fluid dynamics tools*. Master's Thesis, Texas A&M University, College Station.

Fujimoto, N., Nojiri, N., Tachibana, Y., & Mizushima, T. (2009). Operation of the high-temperature engineering test reactor. In *Proceedings of an international conference on non-electric applications of nuclear Power: Seawater desalination, hydrogen production and other industrial applications* (p. 509). Vienna, Austria: International Atomic Energy Agency. Retrieved from http://www-pub.iaea.org/MTCD/Meetings/PDFplus/2007/cn152/cn152p/HTTR WS 1 Fujimoto.pdf.

Garimella, S. V., & Rice, R. A. (1995). Confined and submerged liquid jet impingement heat transfer. *Journal of Heat Transfer*, *117*(4), 871–877. http://doi.org/10.1115/1.2836304.

Gebhart, B., Hilder, D. S., & Kelleher, M. (1984). The diffusion of turbulent buoyant jets. *Advances in Heat Transfer*, *16*, 1–57.

General Atomics. (1996). *Gas turbine-modular helium reactor (GT-MHR) conceptual design description report (910720 Revision 1)*. San Diego.

Generation IV International Forum. (2002). *A technology roadmap for generation IV nuclear energy systems*. Washington, D. C. Retrieved from http://scholar.google.com/scholar?hl=en&btnG=Search&q=intitle:A+Technology+Roadmap+for+Generation+IV+Nuclear+Energy+Systems#0.

Generation IV International Forum. (2005). *Generation IV nuclear energy systems ten-year program plan fiscal year 2005* (Vol. I). Idaho Falls. Retrieved from http://nuclear.in, l.gov/deliverables/docs/gen-iv-10-yr-program-plan.pdf.

Hassan, Y. A., Blanchat, T. K., & Seeley Jr., C. H. (1992). PIV flow visualization using particle tracking techniques. *Measurement Science and Technology*, *3*, 633–642.

Hecht, M. M. (1989). MHTGR - nuclear engine for world development. *Executive Intelligence Review*, *16*(49), 22–28.

Hill, W. G., Jenkins, R. C., & Gilbert, B. L. (1976). Effects of the Initial Boundary-Layer State on Turbulent Jet Mixing. *AIAA Journal*, *14*(11), 1513–1514. http://doi.org/10.2514/3.61491.

International Atomic Energy Agency. (2001). *Current status and future development of modular high temperature gas cooled reactor technology (IAEA-TECDOC-1198)*. Vienna, Austria. Retrieved from http://www-pub.iaea.org/MTCD/Publications/PDF/te_1198_prn.pdf.

International Atomic Energy Agency. (2008). *Accident analysis for nuclear power plants with modular high temperature gas cooled reactors*. *Safety Reports Series 54*. Vienna, Austria. Retrieved from http://www-pub.iaea.org/MTCD/publications/PDF/pub1318_web.pdf.

International Atomic Energy Agency. (2013). *Evaluation of high temperature gas cooled reactor performance: Benchmark analysis related to the PBMR-400, PBMM, GT-MHR, HTR-10 and the ASTRA critical facility (IAEA-TECDOC-1694)*. Vienna, Austria. Retrieved from http://www-pub.iaea.org/MTCD/Publications/PDF/TE-1694_web.pdf.

JAERI. (1994). *Design of high temperature engineering test reactor (HTTR)*. Oarai-machi, Higashiibaraki-gun, Japan. Retrieved from http://httr.jaea.go.jp/G/jaeri_1332.html.

Jahanmiri, M. (2011). *Particle Image Velocimetry : Fundamentals and Its Applications Particle Image Velocimetry : Fundamentals and Its Applications*. Göteborg, Sweden. Retrieved from http://webfiles.ita.chalmers.se/~chernora/files/MJahanmiri_ParticleImageVelocimetry.pdf.

Johannessen, S. R. (2012). *Use of CFD to study hydrodynamic loads on free-fall lifeboats in the impact phase - a verification and validation study*. Master's Thesis, Norwegian University of Science and Technology, Trondheim, Norway.

Keane, R. D., & Adrian, R. J. (1992). Theory of cross-correlation analysis of PIV images. *Applied Scientific Research*, *49*(3), 191–215. http://doi.org/10.1007/BF00384623.

Kerschen, G., Golinval, J.-C., Vakakis, A. F., & Bergman, L. A. (2005). The method of proper orthogonal decomposition for dynamical characterization and order reduction of mechanical systems: an overview. *Nonlinear Dynamics*, *41*, 147–169.

Konefal, J., Kauffman, S., Graf, D., Rackiewicz, D., Chapin, D., Marrone, N., & Lubnow, T. (2009). *Evaluation of high temperature reactors for potential application to thermal in-situ recovery of oil sand* (No. MPR-3254). Calgary, Canada.

Krothapalli, A., Baganoff, D., & Karamcheti, K. (1980). Development and structure of a rectangular jet in a multiple jet configuration. *AIAA Journal*, *18*(8), 945–946.

Krothapalli, A., Baganoff, D., & Karamcheti, K. (1981). On the mixing of a rectangular jet. *Journal of Fluid Mechanics*, *17*, 201–220. http://doi.org/10.1017/S0022112081001730.

Lai, A. C. H., & Lee, J. H. W. (2012). Dynamic interaction of multiple buoyant jets. *Journal of Fluid Mechanics*, *708*, 539–575. http://doi.org/10.1017/jfm.2012.332.

Lisowski, D. D. (2013). *Thermal hydraulic analysis of an experimental reactor cavity cooling system with water: Performance and stability*. PhD. Dissertation, University of Wisconsin- Madison, Madison.

Lisowski, D. D., Moses, M. A., Andersen, M. A., & Corradini, M. L. (2013). Design consideration for a scaled reactor cavity cooling system with air for the VHTR (NURETH15-484). In *15th International Topical Meeting on Nuclear Reactor Thermal-hydraulics (NURETH-15)*. Pisa, Italy.

Lomperski, S. Pointer, W. D., Tzanos, C. P., Wei, T. Y. C., & Krauss, A. R. (2011). *Generation IV Nuclear Energy System Initiative. Air- Cooled Option RCCS Studies and NSTF Preparation (ANL-GenIV-179).* Retrieved from http://www.ipd.anl.gov/anlpubs/2012/11/71292.pdf.

Lumley, J. L., (1967). The structure of inhomogeneous turbulent flows. In *Atmospheric Turbulence and Radio Wave Propagation* (pp. 166-178). Moscow, Russia.

McCluskey, A., & Lalkhen, A. G. (2007). Statistics II: Central tendency and spread of data. *Continuing Education in Anesthesia, Critical Care and Pain*, *7*(4), 127–130. http://doi.org/10.1093/bjaceaccp/mkm020.

Menon, R. K. (1999). Laser Anemometry. In J. G. Webster (Ed.), *The measurement instrumentation and sensors handbook*. Boca Raton: CRC Press LLC.

Nasr, A., & Lai, J. (2010). Applicability of Reichardt's hypothesis to the prediction of velocity field of multiple parallel plane jets. *Journal of Mechanics*, *26*(02), N17–N22. http://doi.org/10.1017/S1727719100003117.

Nasr, A., & Lai, J. (2011). An investigation on applying Reichardt's hypothesis to flow prediction of ventilated two parallel plane jets. *Advances in Aerospace Science and Applications*, *1*(1), 1–6.

Nishio, S., Okamoto, K., Kobayashi, T., Saga, T. (1999). Evaluation of System Performance and Uncertainty Analysis of PIV (PIV-STD project). In *Proceedings of the 3rd International Workshop on Particle Image Velocimetry* (pp. 465–470). Santa Barbara.

Nishio, S., Murata, S. (2003). A Numerical Approach to the Evaluation of Error Vector Appearance Possibility in PIV. In *Proceedings of the 5th International Symposium on Particle Image Velocimetry* (pp. 3321.1–3321.9). Busan, South Korea.

Nobach, H., Tropea, C., Cordier, L., Bonnet, J.-P., Delville, J., Lewalle, J., … Adrian, R. J. (2014). Review of some fundamentals of data processing. In C. Tropea, A. L. Yarin, & J. F. Foss (Eds.), *Springer Handbook of Experimental Fluid Mechanics* (pp. 1337–1398). Berlin - Heidelberg, Germany: Springer. Retrieved from http://link.springer.com/referencework/10.1007/978-3-540-30299-5/page/2.

Oh, C. H., Park, G. C., & Davis, C. (2009). RCCS experiments and validation for high temperature gas-cooled reactor. *Nuclear Technology*, *167*, 107–117.

Oh, C., Kim, E., Schultz, R., Patterson, M., Petti, D., & Kang, H. (2010). Comprehensive thermal hydraulics research of the very high temperature gas cooled reactor. *Nuclear Engineering and Design*, *240*(10), 3361–3371. http://doi.org/10.1016/j.nucengdes.2010.07.007.

Park, G. C., Cho, Y. J., & Cho, H. K. (2006). Assessment of a new design for a reactor cavity cooling system in a very high temperature gas-cooled reactor. *Nuclear Engineering and Technology*, *38*(1), 45–60.

Quantum Composers, Inc. (2012). 9600+ series digital delay pulse generators. Bozeman: Quantum composers. Retrieved from https://www.valuetronics.com/Manuals/QC-9600-PLUS.pdf.

Raffel, M., Willert, C., Wereley, S. T., & Kompenhans, J. (2007). *Particle image velocimetry - a practical guide* (2nd ed.). New York: Springer.

Reichardt, H. (1942). Gestzmassigkeiten Der Freien Turbulens, *Forschungsheft, 414, Verien Deutscher Ingenieure*.

San, J. Y., & Chen, J. J. (2014). Effects of jet-to-jet spacing and jet height on heat transfer characteristics of an impinging jet array. *International Journal of Heat and Mass Transfer*, *71*, 8–17. http://doi.org/10.1016/j.ijheatmasstransfer.2013.11.079.

Saripalli, K. R. (1983). Visualization of multijet impingement flow. *AIAA Journal*, *21*(4), 483–484. http://doi.org/10.2514/3.8102.

Sirovich, L. (1987). Turbulence and the dynamics of coherent structures. Part I: Coherent structures. *Quarterly of Applied Mathematics*, *45*, 561–571.

So, R. M. C., & Aksoy, H. (1993). On vertical turbulent buoyant jets. *International Journal of Heat and Mass Transfer*, *36*(13), 3187–3200. http://doi.org/10.1016/0017-9310(93)90003-O.

Sulaiman, S. A., Dominguez-Ontiveros, E. E., Alhashimi, T., Budd, J. L., Matos, M. D., & Hassan, Y. A. (2015). Design considerations and experimental observations for the TAMU air-cooled reactor cavity cooling system for the VHTR. *AIP Conference Proceedings*, *1659*, 030002. http://doi.org/10.1063/1.4916850.

Sulaiman, S. A., Dominguez-Ontiveros, E. E., Wang, H., & Hassan, Y. A. (2014). Design of TAMU air-cooled reactor cavity cooling system experimental test facility. *Transactions of the American Nuclear Society*, *110*, 708–711.

Sun, Y., & Zhang, Y. (2007). An Overview of Room Air Motion Measurement: Technology and Application. *HVAC&R Research*, *13*(6), 929–950. http://doi.org/10.1080/10789669.2007.10391463.

Tanaka, E. (1970). The interference of two-dimensional parallel jets (1st report, experiments on dual jet). *Bulletin of the JSME*, *13*(56), 272–280.

Tanaka, E. (1974). The interference of two-dimensional parallel jets (2nd report, experiments on the combined flow of dual jet). *Bulletin of the JSME*, *17*(109), 920–927.

Tektronix, Inc. (2012). TDS 210 & TDS 220 digital real-time oscilloscopes user manual.pdf. Wisonville: Tektronix, Inc. Retrieved from http://mmrc.caltech.edu/Oscilliscope/TDS210 Digital Os User Manual.pdf.

Thielicke, W., & Stamhuis, E. J. (2014). PIVlab – Towards user-friendly, affordable and accurate digital particle image velocimetry in MATLAB. *Journal of Open Research Software*, *2*(e30). http://doi.org/http://dx.doi.org/10.5334/jors.bl.

Tirunagari, S. (2011). *Implementation of POD, NIPALS and image processing methods in the analysis of turbulent flows*. Otaniemi. Retrieved from http://www.academia.edu/3835528/Implementation_of_POD_NIPALS_and_Image_Processing_Methods_in_the_Analysis_of_Turbulent_Flows.

Tokuhiro, A., & Kimura, N. (1999). Experimental investigation on thermal striping. Mixing phenomena of a vertical non-buoyant jet with two adjacent buoyant jets as measured by ultrasound Doppler velocimetry. *Nuclear Engineering and Design*, *188*(1), 49–73. http://doi.org/10.1016/S0029-5493(99)00006-0.

Törnblom, O. (2004). Introduction course in particle image velocimetry. Stockholm, Sweden: Kungliga Tekniska högskolan (KTH) Royal Institute of Technology. Retrieved from http://www2.mech.kth.se/~olle/pivkurs/Intro_to_PIV.pdf.

TSI, Inc. (2012). Model 3321. Aerodynamic particle sizer spectrometer - Operation and service manual. Shoreview: TSI, Inc. Retrieved from http://webx.ubi.pt/~goa/Manuals/APS3321/3321_APS_1930092G.pdf.

TSI, Inc. (2014). Six-jet atomizer model 9306 - owner's manual. Shoreview: TSI, Inc.

Turner, J. S. (1966). Jets and plumes with negative or reversing buoyancy. *Journal of Fluid Mechanics, 26*(4), 779–792. http://doi.org/10.1017/S0022112066001526.

Tzanos, C. P., & Farmer, M. T. (2006). *Feasibility study for use of the natural convection shutdown heat removal test facility (NSTF) for VHTR water-cooled RCCS shutdown (ANL-GenIV-079)*. Argonne. Retrieved from http://www.ipd.anl.gov/anlpubs/2007/08/59753.pdf.

Velmex, Inc. (2001). Bislide positioning system - manual and motorized, high precision linear motion cmponents (catalog b-01). Bloomfield: Velmex, Inc. Retrieved from http://www.bislide.com/pdf/bislidelit.pdf.

Velmex, Inc. (2004). VXM stepping motor controller user's manual (extended version) models VXM-1, 2, 3, 4 (document # VXM-UM-E5). bloomfield: Velmex, Inc. Retrieved from http://www.velmex.com/controls/vxm/downloads/documentation/users_manual/vxm2_users_man.pdf.

Vision Research, Inc. (2012). Phantom miro digital high-speed cameras – data sheet (Rev Aug 2012). Wayne: Vision Research, Inc. Retrieved from http://www.visionresearch.com/uploads/Docs/Products/DS_WEB-MIRO_M-LC_Series.pdf.

Wang, H., Sulaiman, S. A., & Hassan, Y. A. (2014). Computational fluid dynamics analysis of NGNP reactor cavity cooling system with air. *Transactions of the American Nuclear Society*, *110*, 675–677.

Williams, P. M., Silady, F. A., Dunn, T. D., Noren, R. C., McEachern, D. W., Dilling, D. A., … Reid, C. L. (1994). MHTGR development in the United States. *Progress in Nuclear Energy*, *28*(3), 265–346.

APPENDIX A: PHASE I DESIGN DRAWINGS

The Solidworks drawings for the Phase I of the experimental test facility are furnished in this section.

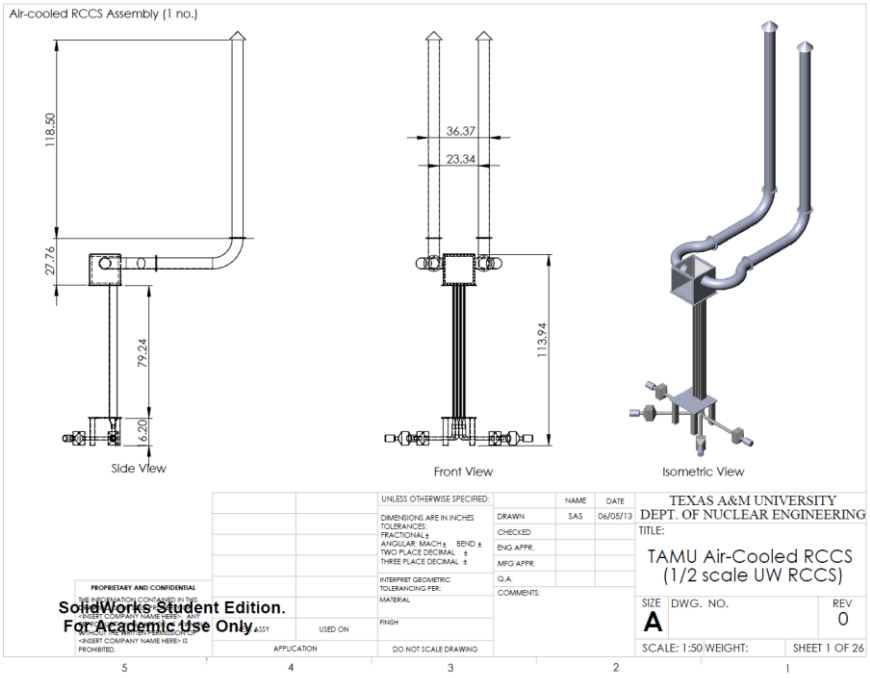

Figure 213. Overall dimensions of the TAMU Air-Cooled RCCS.

(a)

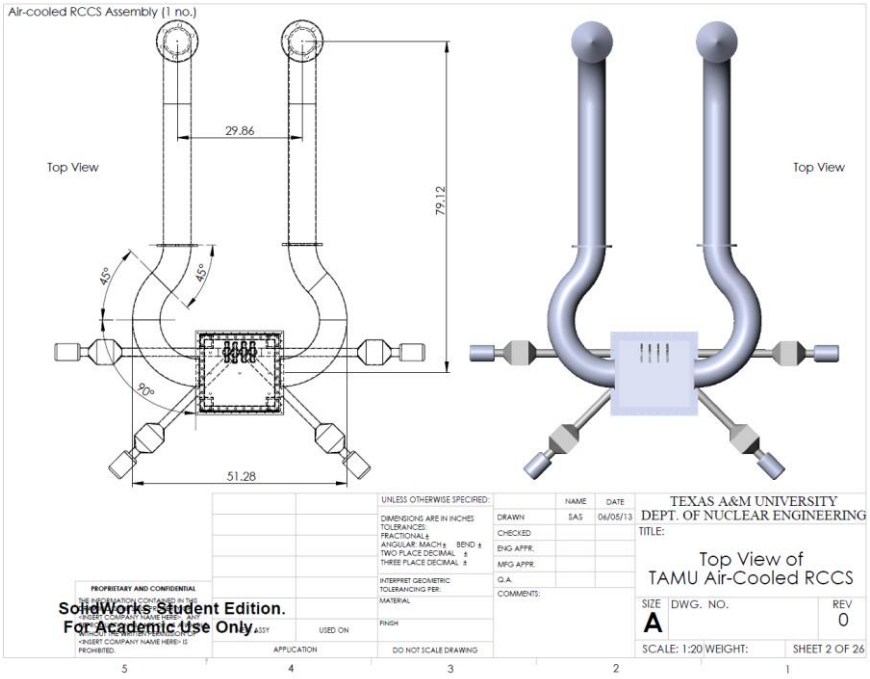

(b)

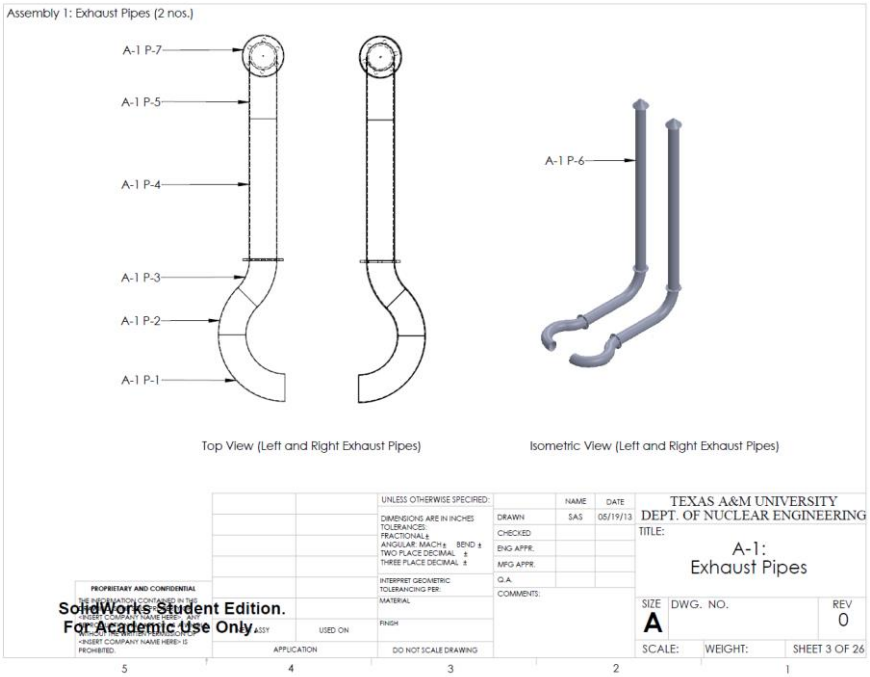

Figure 214. (a) Top view of The TAMU Air-Cooled RCCS, (b) A-1: Exhaust pipe assembly (2 units) and parts.

(a)

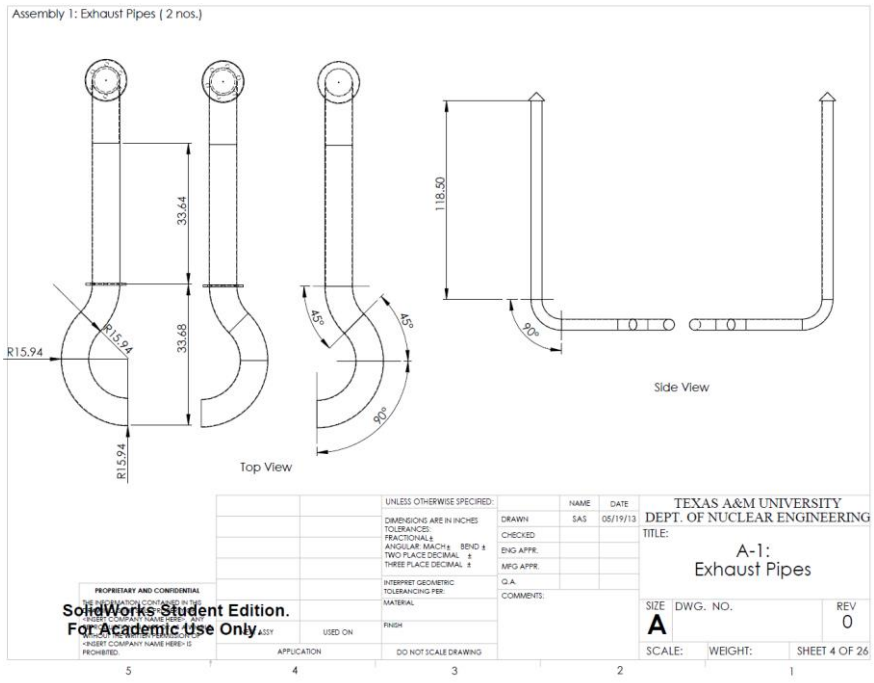

(b)

Figure 215. (a) Exhaust pipes assembly: Main components dimensions (A-1), (b) Exhaust pipe assembly: 90º bend pipe (2 units) (A-1 P-1).

(a)

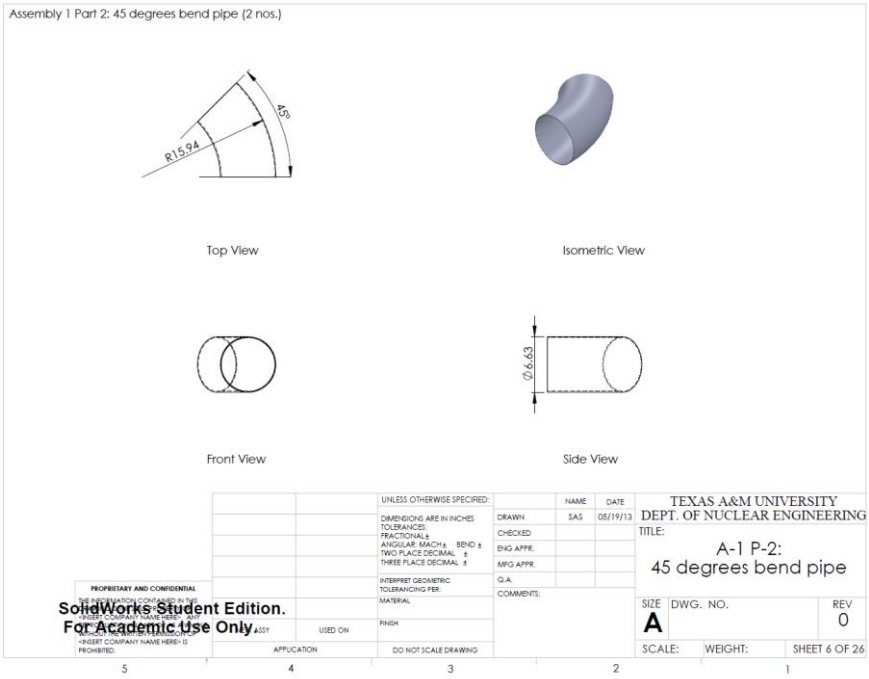

(b)

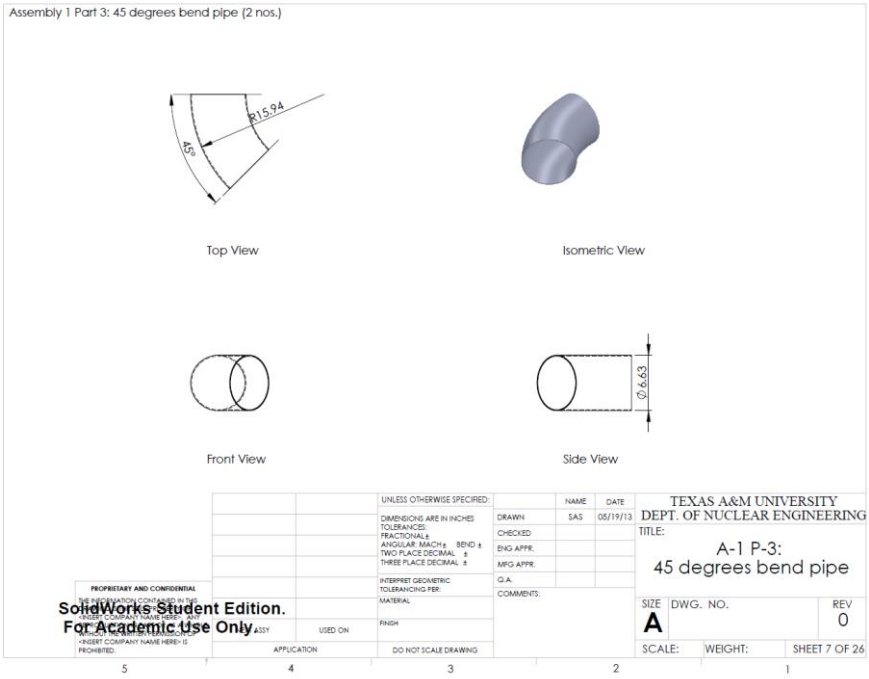

Figure 216. (a) Exhaust pipe assembly: 45º bend pipe (2 units) (A-1 P-2), (b) Exhaust pipe assembly: 45º bend pipe (2 units) (A-1 P-3).

(a)

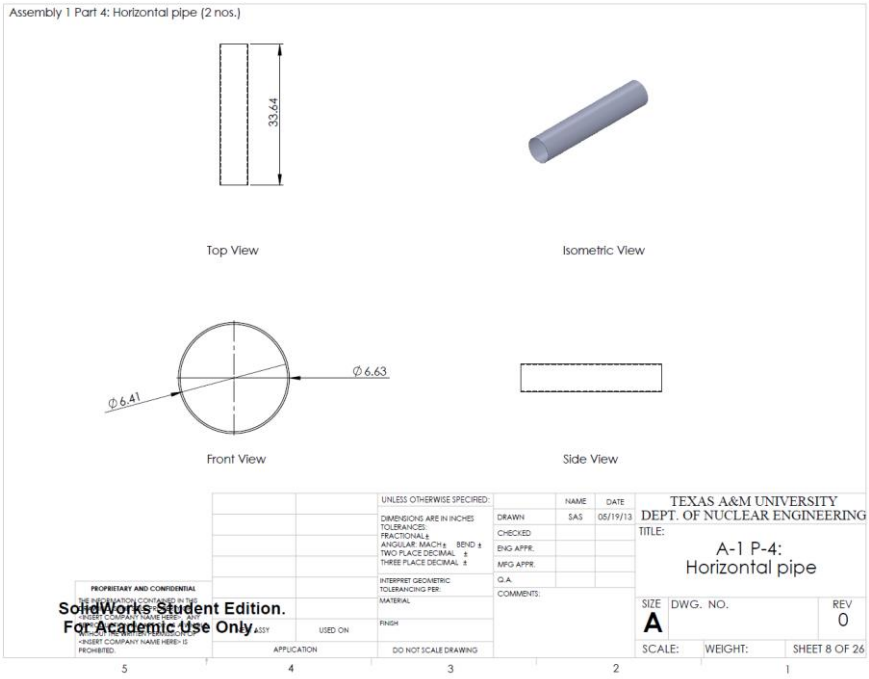

(b)

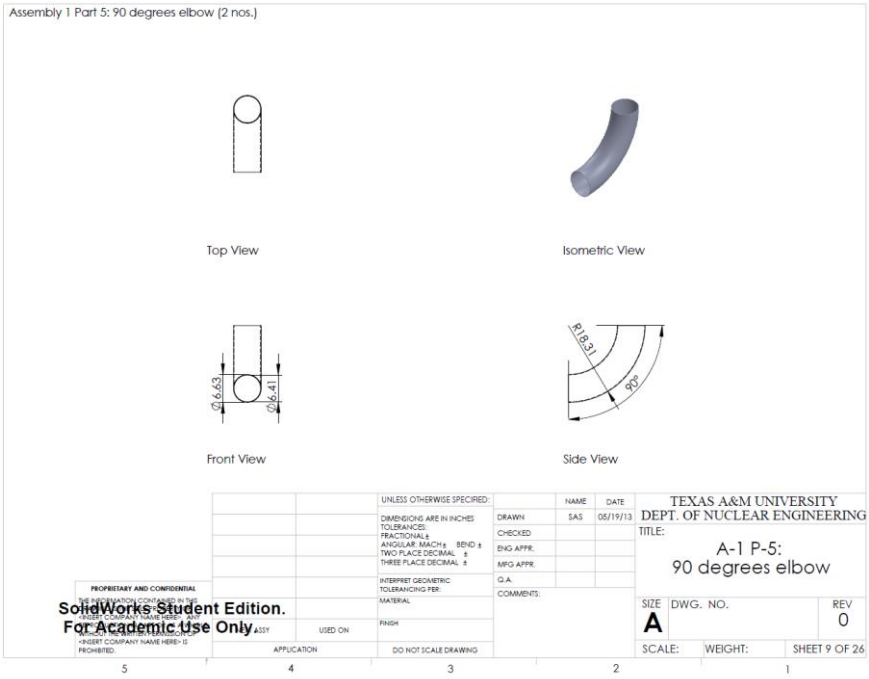

Figure 217. (a) Exhaust pipe assembly: Horizontal pipe (2 units) (A-1 P-4), (b) Exhaust pipe assembly: 90º elbow (2 units) (A-1 P-5).

(a)

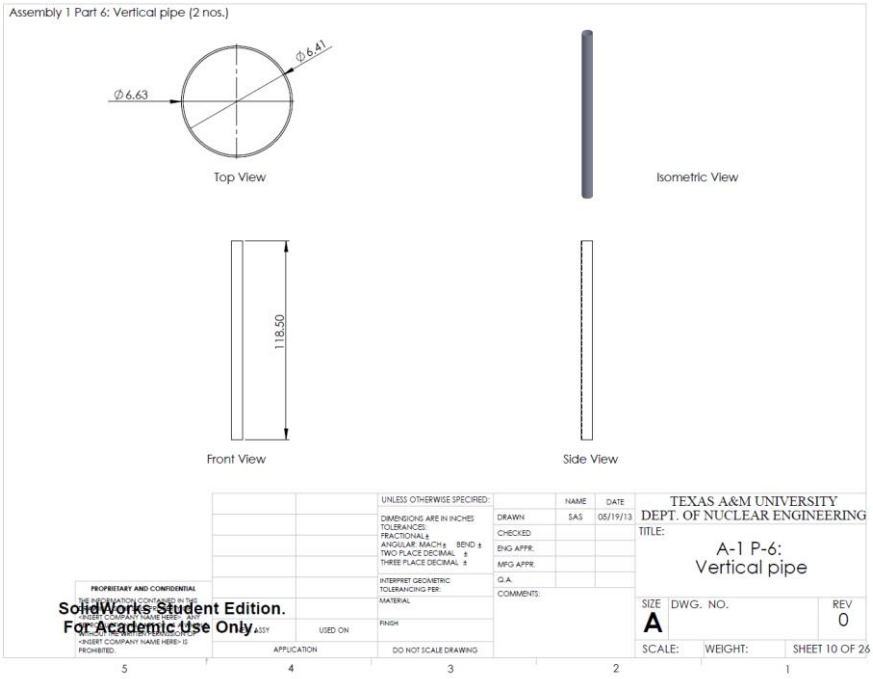

(b)

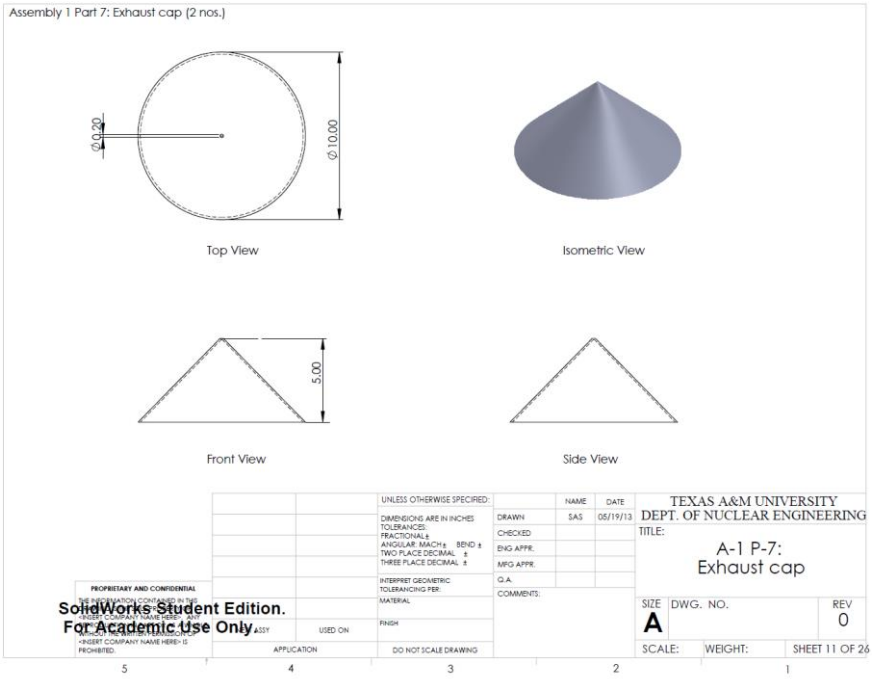

Figure 218. (a) Exhaust pipe assembly: Vertical pipe (2 units) (A-1 P-6), (b) Exhaust pipe assembly: Exhaust cap (2 units) (A-1 P-7).

(a)

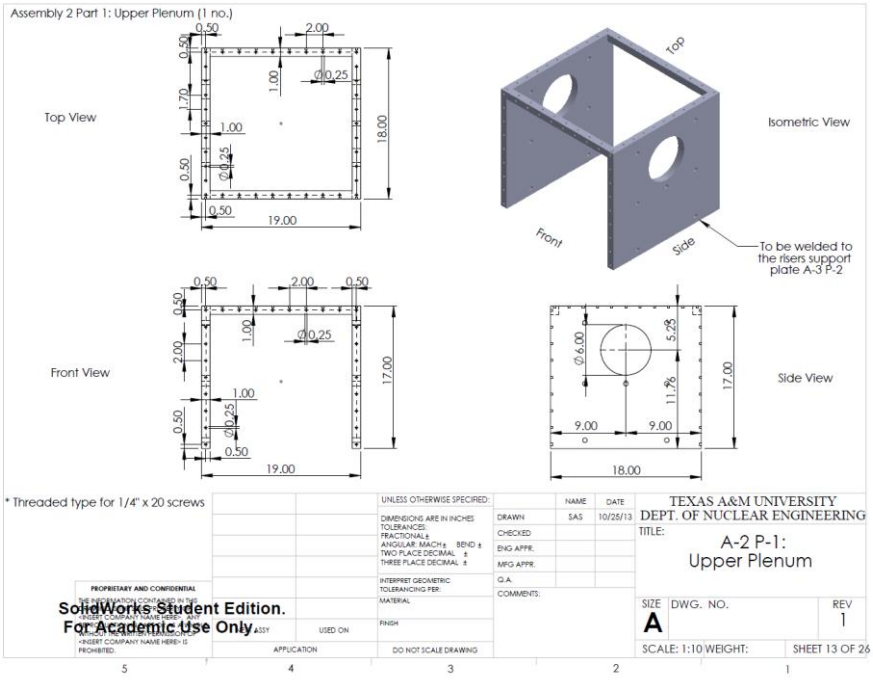

(b)

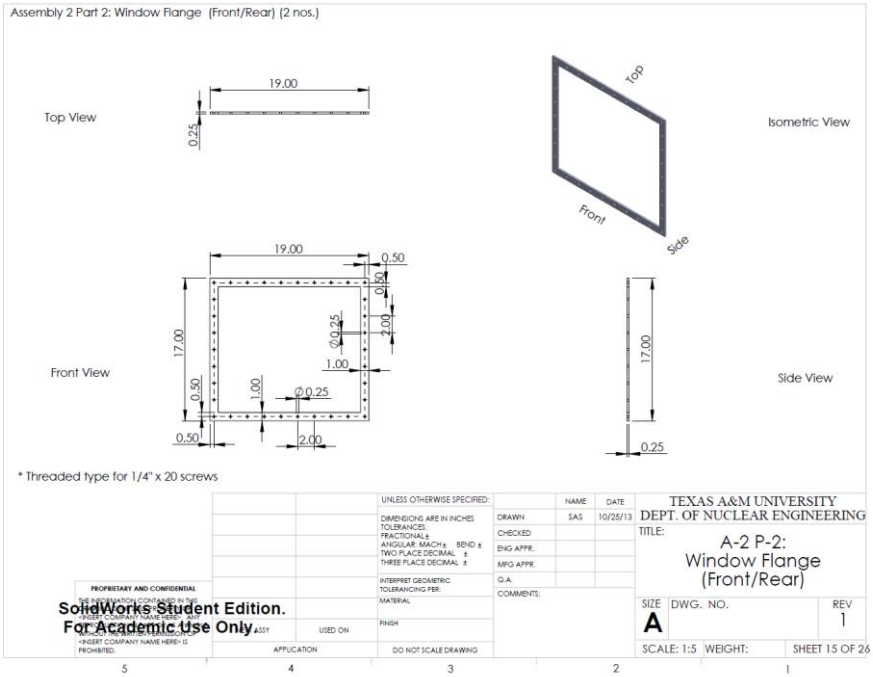

Figure 219. (a) Upper plenum with glass windows assembly: Main component (1 unit) (A-2 P-1), (b) Upper plenum with glass windows assembly: Window flange – front/rear (1 unit each) (A-2 P-2).

(a)

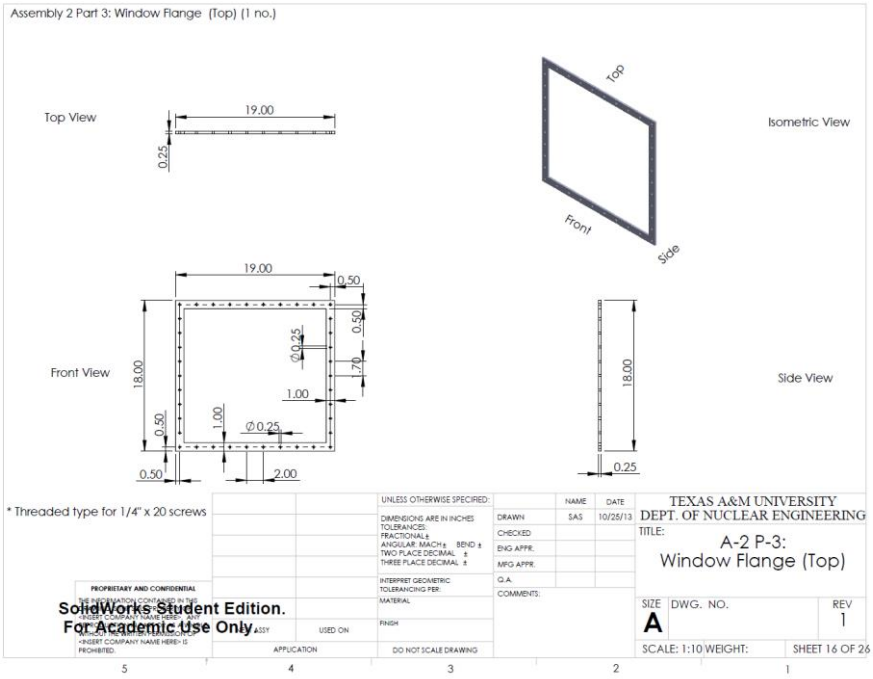

(b)

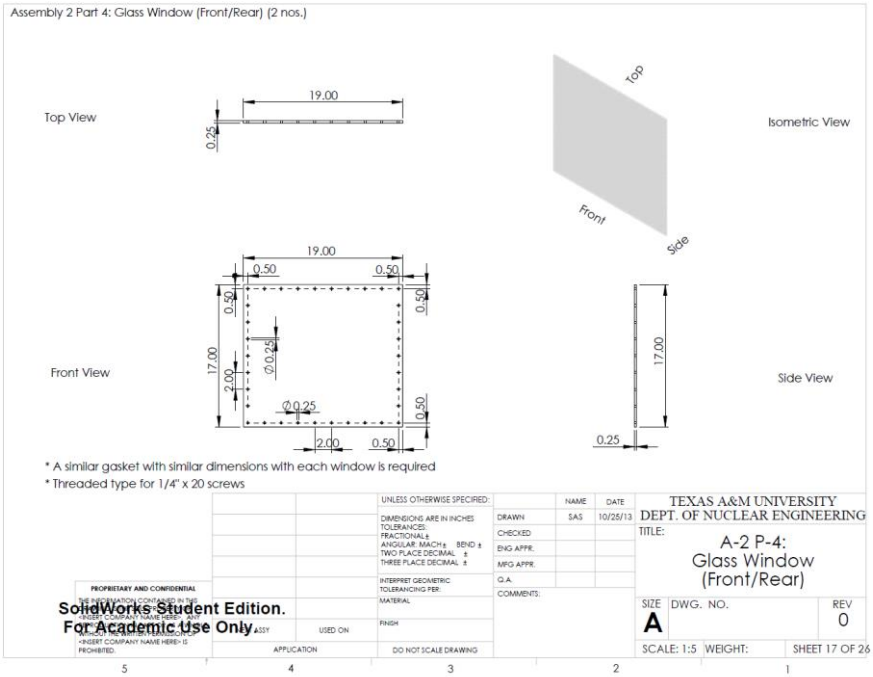

Figure 220. (a) Upper plenum with glass windows assembly: Window flange - top (1 unit) (A-2 P-3), (b) Upper plenum with glass windows assembly: Glass window – front/rear (1 unit each) (A-2 P-4).

(a)

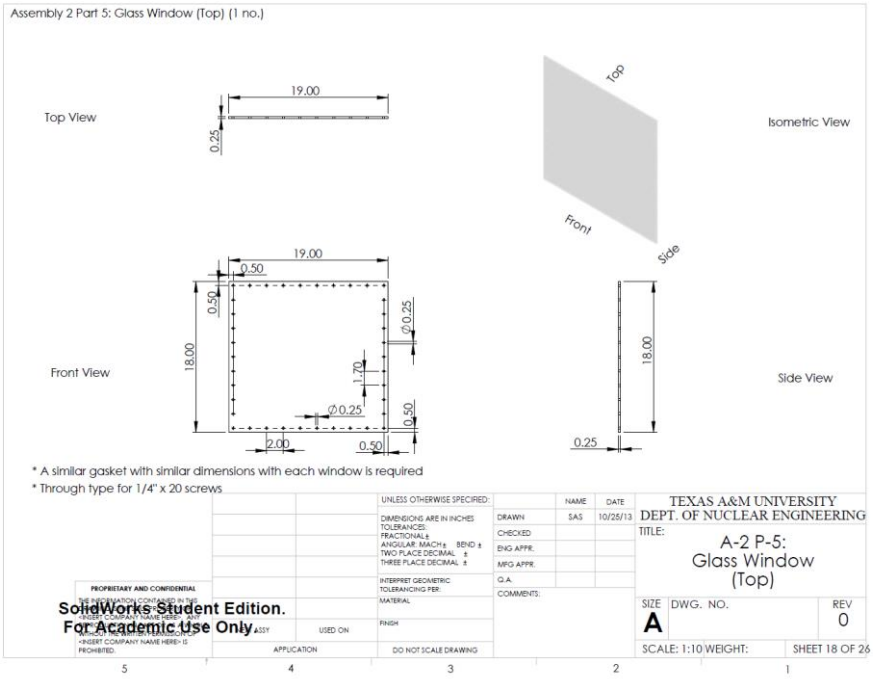

(b)

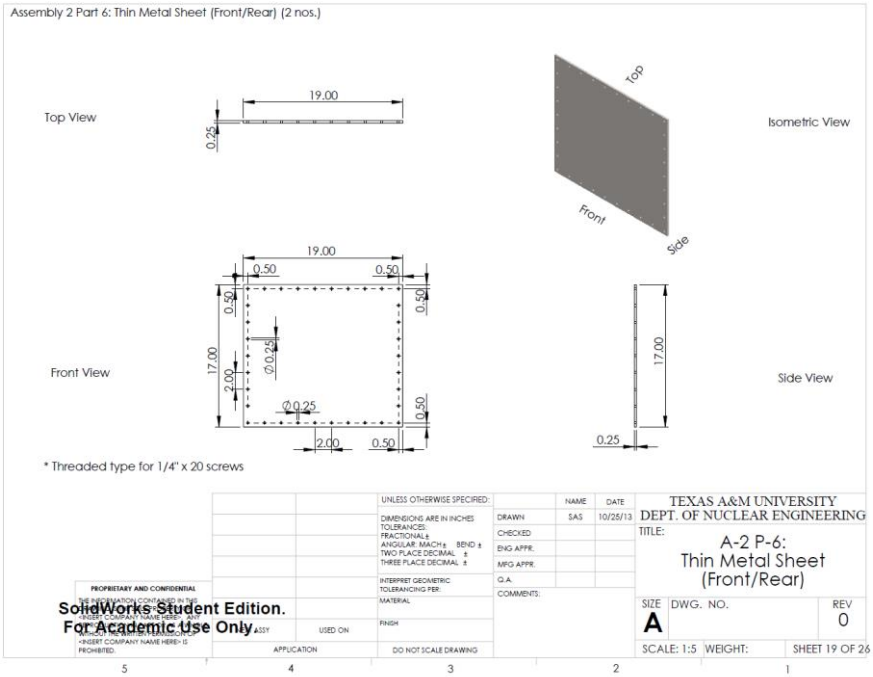

Figure 221. (a) Upper plenum with glass windows assembly: Glass window - top (1 unit) (A-2 P-5), (b) Upper plenum with glass windows assembly: Thin metal sheet – front/rear (1 unit each) (A-2 P-6).

(a)

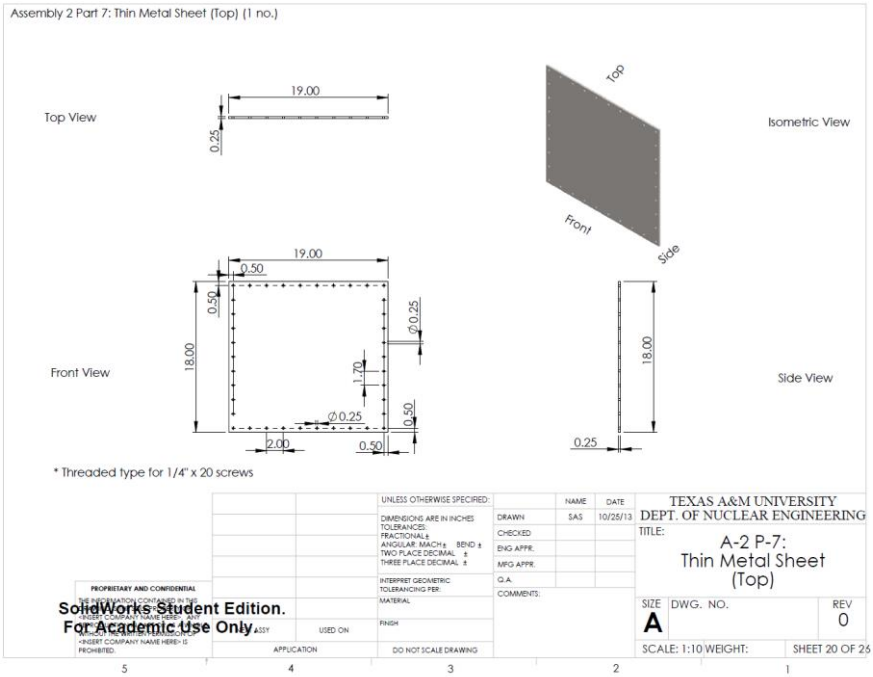

(b)

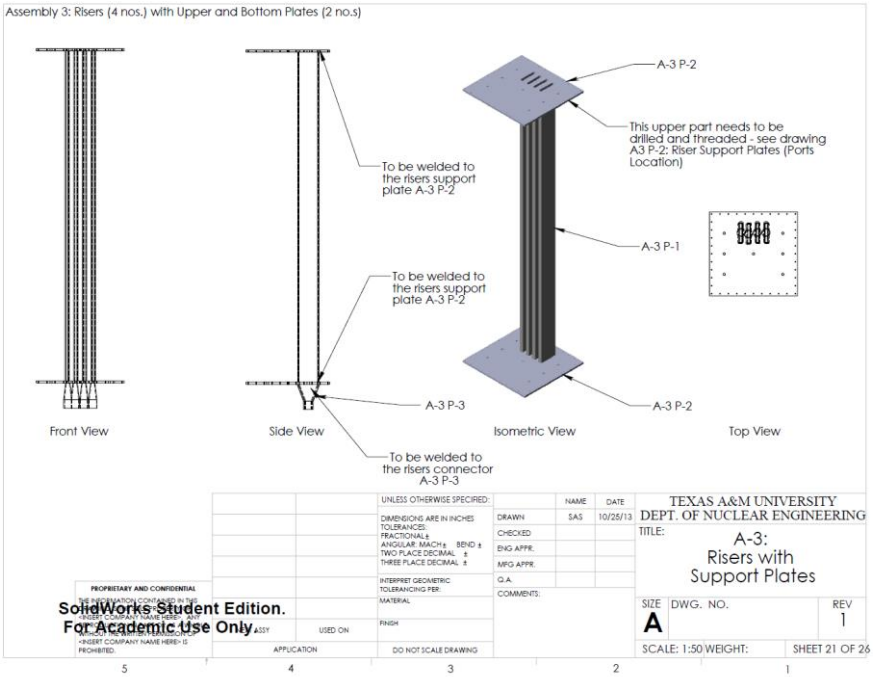

Figure 222. (a) Upper plenum with glass windows assembly: Thin metal sheet - top (1 unit) (A-2 P-7), (b) Risers with support plates assembly (A-3).

(a)

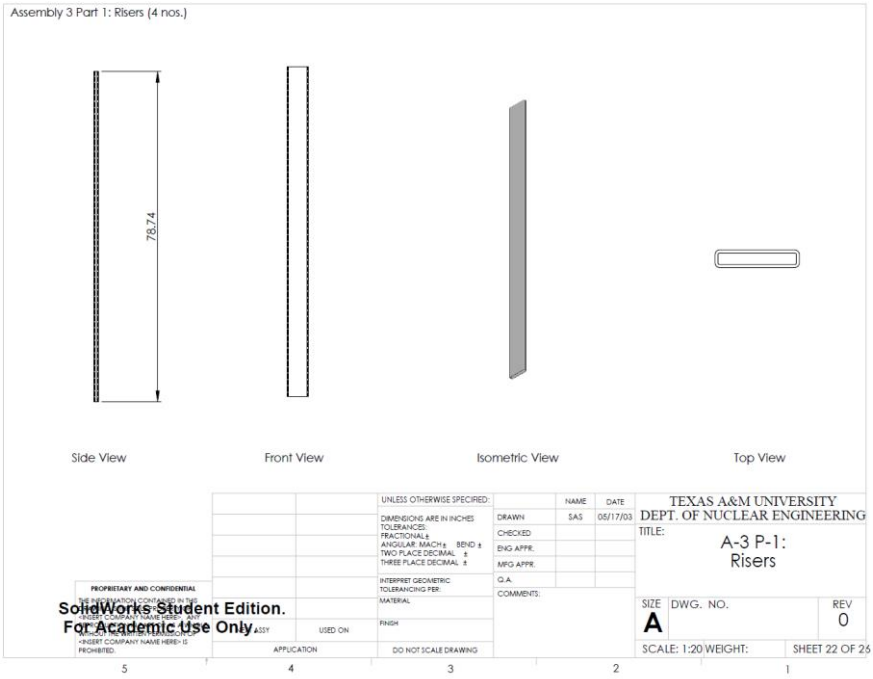

(b)

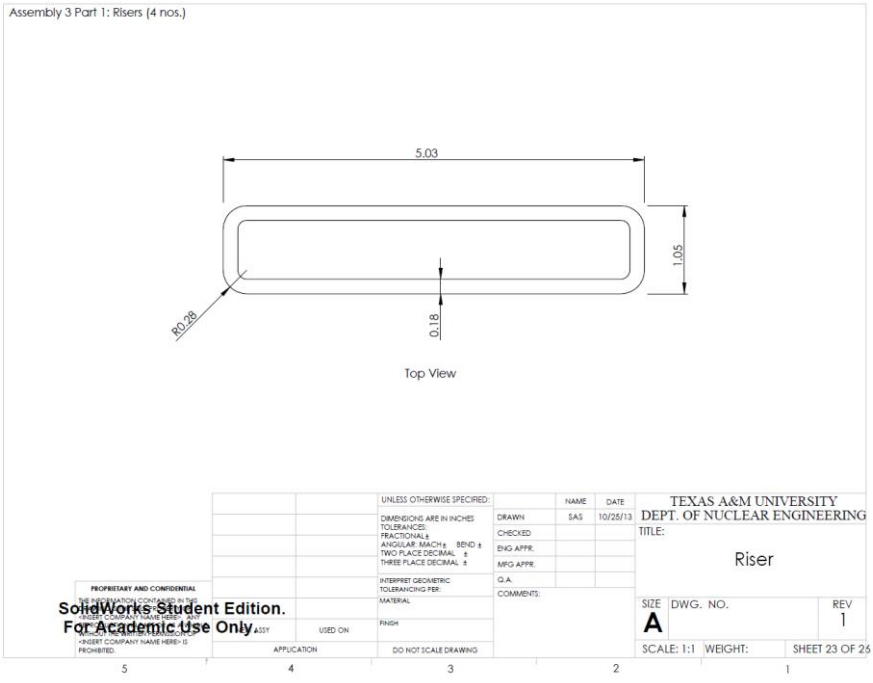

Figure 223. (a) Risers with support plates assembly: Risers (4 units) (A-3 P-1), (b) Risers with support plates assembly: Riser cross section dimension.

(a)

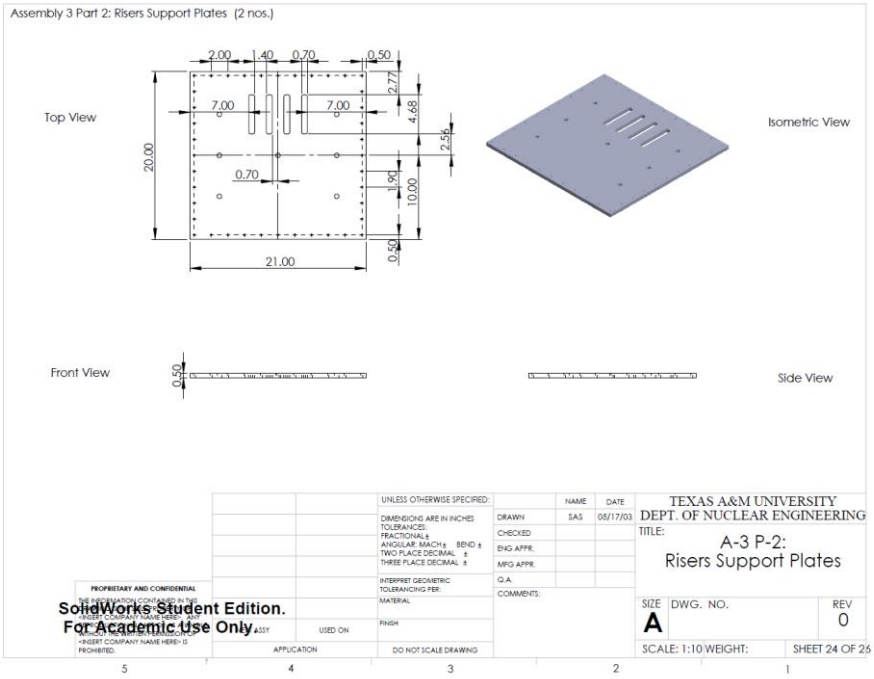

(b)

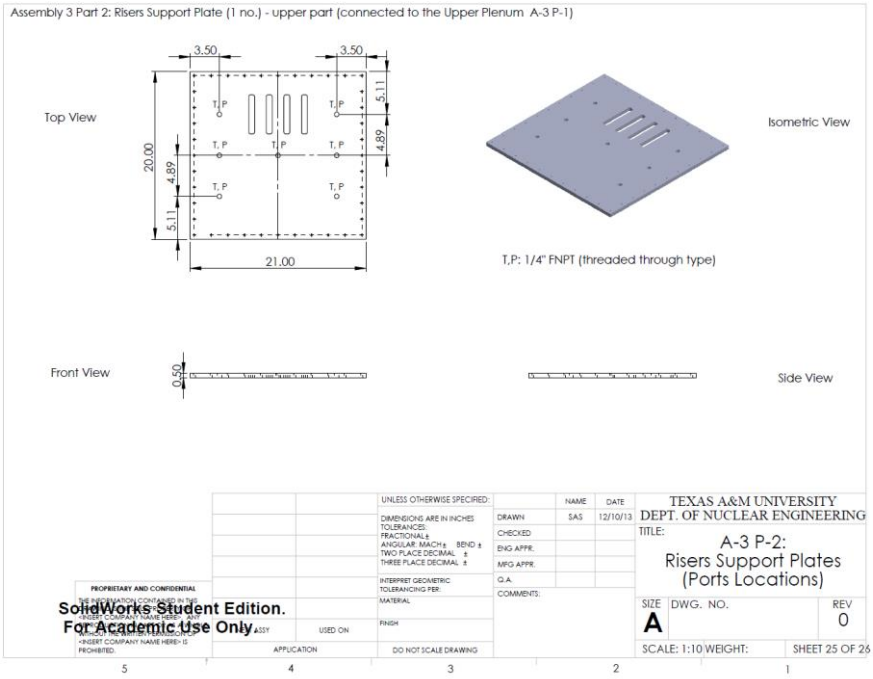

Figure 224. (a) Risers with support plates assembly: Risers support plate (2 units) (A-3 P-2), (b) Risers with support plates assembly: Riser support plates (ports locations).

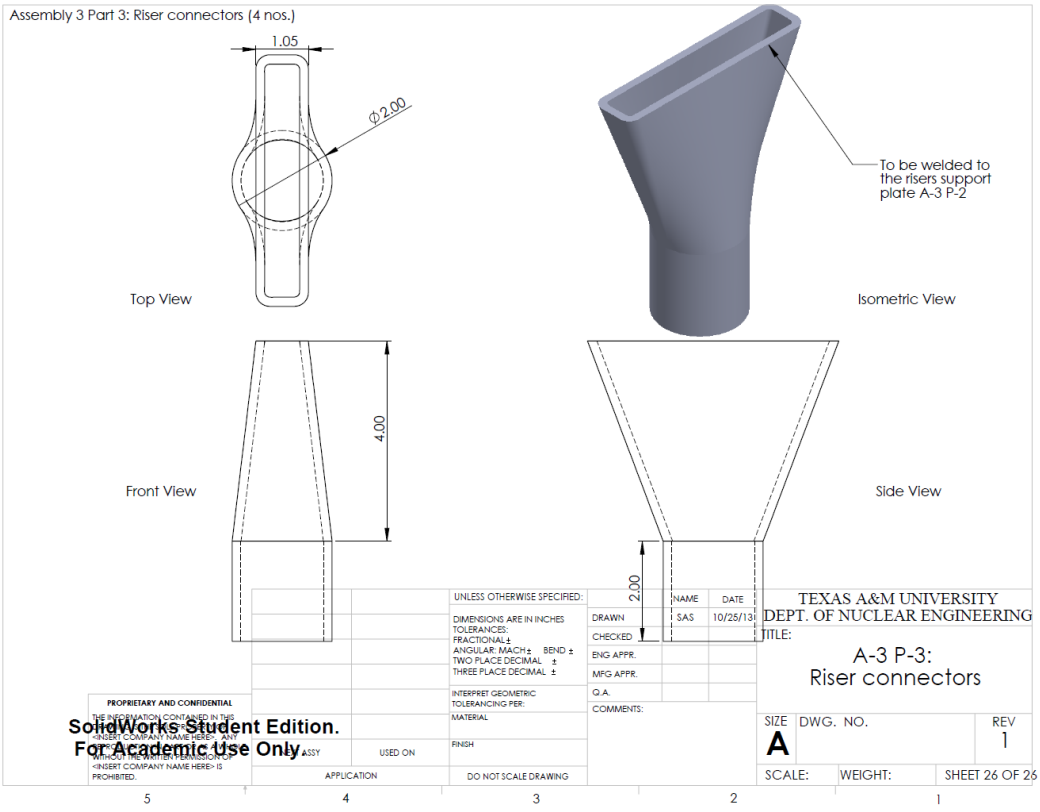

Figure 225. Risers with support plates assembly: Risers connector (4 units) (A-3 P-3).

APPENDIX B: OLIVE OIL AEROSOL MEASUREMENT

A small experiment to verify the manufacturer's specification on the aerodynamic diameter size of the olive oil was carried out (Figure 226). The aerodynamic diameter, by definition is the physical diameter of a unit density sphere that settles through the air with a velocity match to that of the particle in question. It is an essential aerosol size parameter due to the fact that it governs the particle's behavior whilst airborne. Irrespective of their physical density, size, shape or composition, particles demonstrating the similar airborne behavior have the similar aerodynamic diameter.

Case 1a (4 active risers, 5 m/s, 25 ºC) was utilized for the verification. A TSI Aerodynamic Particle Sizer (APS) Model 3321 (particle size range: 0.5 to 1.2 μm aerodynamic sizing) was used for the measurement (Figure 226). A transparent rubber hose was inserted into the upper plenum via an opening of the front window of the upper plenum. A painter's tape was utilized to cover up the top and bottom opening of the front window. Sufficient settling time was allocated prior to conduct the measurement so that the measurement fluctuation could be minimized. Figure 227 shows the normalized frequency functions for the near-monodisperse olive oil aerosol particle, which were generated by the TSI Six-Jet Atomizer and sized with the TSI APS. It was found that the near-monodisperse olive oil samples have geometric means from 0.50 to 1.2 μm aerodynamic diameter, and the average was 0.745 μm, which was approximately very

close to the given manufacturer's specification (< 0.6 μm). The average value of the mono-disperse olive oil samples was used in the calculation of the PIV system uncertainty.

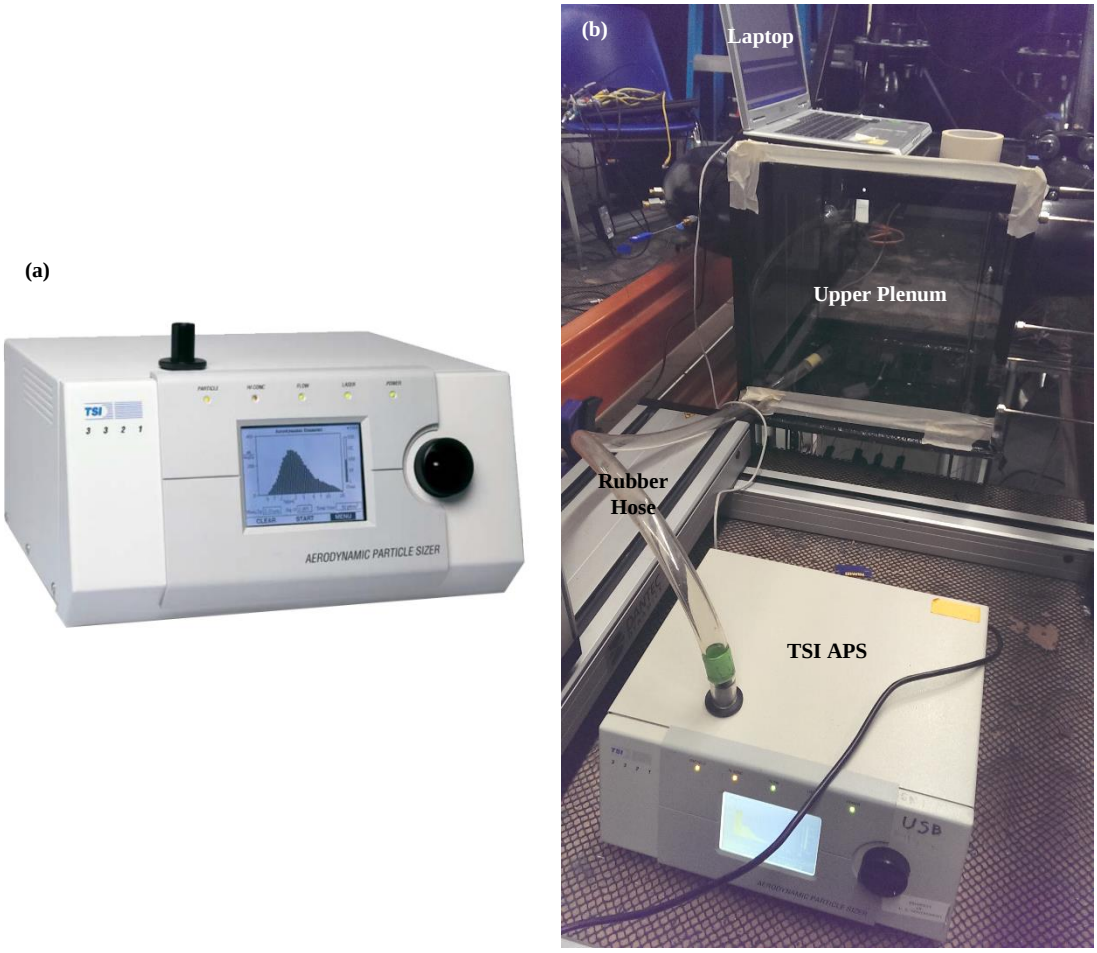

Figure 226. (a) TSI Aerodynamic Particle Sizer (APS) Model 3321 (TSI, Inc., 2012), (b) Experimental set-up at the second floor of the experimental facility.

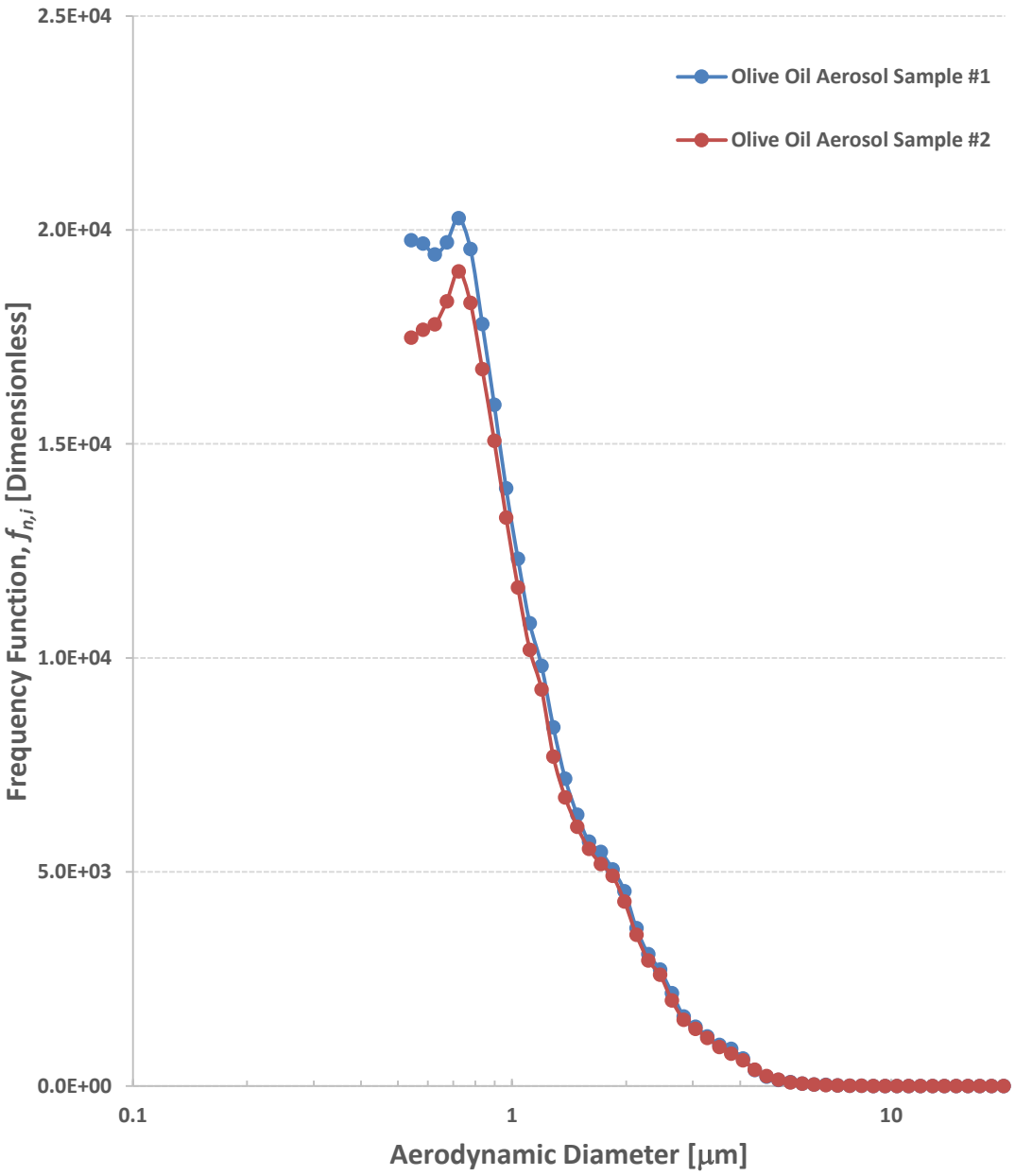

Figure 227. Size distributions measured with the TSI APS Model 3321: Normalized frequency functions for the near-monodisperse aerosol particles.